



HAL
open science

Emerging roles for natural and artificial lipids in shaping the catalytic function, stability and oligomeric state of membrane proteins.

Batoul Srour

► To cite this version:

Batoul Srour. Emerging roles for natural and artificial lipids in shaping the catalytic function, stability and oligomeric state of membrane proteins.. Other. Université de Strasbourg, 2015. English. NNT : 2015STRAF068 . tel-01304805

HAL Id: tel-01304805

<https://theses.hal.science/tel-01304805>

Submitted on 20 Apr 2016

HAL is a multi-disciplinary open access archive for the deposit and dissemination of scientific research documents, whether they are published or not. The documents may come from teaching and research institutions in France or abroad, or from public or private research centers.

L'archive ouverte pluridisciplinaire **HAL**, est destinée au dépôt et à la diffusion de documents scientifiques de niveau recherche, publiés ou non, émanant des établissements d'enseignement et de recherche français ou étrangers, des laboratoires publics ou privés.

ÉCOLE DOCTORALE DES SCIENCE CHIMIQUES

UMR 7140, Chimie de la matière complexe

THÈSE

présentée par :

Batoul SROUR

soutenue le : **24 Avril 2015**

pour obtenir le grade de

Docteur de l'université de Strasbourg

Discipline/ Spécialité : Chimie

Emerging roles for natural and artificial lipids in shaping the catalytic function, stability and oligomeric state of membrane proteins.

Rôles émergents des lipides naturels et artificiels dans l'élaboration de la fonction catalytique, la stabilité et l'état d'oligomérisation des protéines membranaires.

THÈSE dirigée par :

Prof. Dr. HELLWIG Petra

Université de Strasbourg

RAPPORTEURS :

Prof. Dr. SüSS Regine

Albert-Ludwig universität de Freiburg

Prof. Dr. ANDRADE Susana

Albert-Ludwig universität de Freiburg

AUTRES MEMBRES DU JURY:

Prof. Dr. BECHINGER Burkhard

Université de Strasbourg

*“If you can't fly then run
if you can't run then walk
if you can't walk then crawl
but whatever you do you have to keep moving forward.*

Martin Luther King Jr.

ACKNOWLEDGEMENTS

Coming to the end of these three unforgettable years, lots of memories flash back into my mind where lots of people have played a major role and without their care and love, this thesis would not have been possible.

I would like first to express my sincere appreciation and respect to my thesis director Prof. Petra Hellwig for her supervision, kindness and continuous help. It was a great pleasure for me to work within your team.

I would also like to thank Prof. Regine Süß, Prof. Susane Andrade and Prof. Burkhard Bechinger for accepting the task of evaluating my thesis work and be my committee members.

I want also to express my sincere thanks to the laboratory members: to Frederic, Thomas, Sinan, Sebastien, Michelle, Zahia, Alicia, Nathalia, Soumia, and especially for Mireille for the support and extra encouragement you gave. Thank you all for creating this lovely working ambiance.

A special thanks to my Lebanese friends: To Rania Noureldeen, Joelle Magarian, Ola Srour, and Zeinab Wehbe for the nice moments we spent together and for being my support during the hard moments I passed especially in the last few months. Thanks to Nedal Taha, Joelle Mezher, Marianne Ibrahim, Fatima Ibrahim, Malak Abbas, Iman Abdallah, Nancy Watfa and Haifa Mokbel for their kindness.

Thanks to Mohamad Rajab, Amal Mcheik, Dalia Fakih, Wassim Jaber and Ali Said for your continuous listening and motivation. Hussein Awada deserves extra thanks for being beside during this journey; your support is much appreciated.

Special thanks to Hassan Hammoud, Ali and Hamed Wehbe for the good moments we shared together. Thanks to everyone who has participated either directly or indirectly in this accomplishment.

My deepest thanks go to my family for being beside and for all the sacrifices you have made on my behalf. This work is dedicated to my father Ali, my mother Hala, my beloved sister Hawraa, and my two brothers Hassan and Hussein.

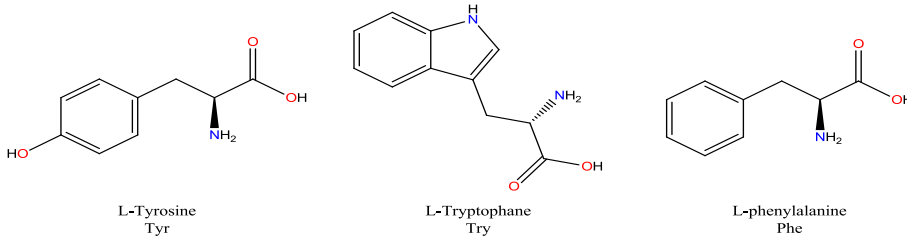
List of abbreviations

Å	Angstrom
ATR	Attenuated total reflection
Abs	Absorbance
ATP	Adenosine triphosphate
Ag/AgCl	Silver/silver chloride
BCP	Block copolymer
CL	Cardiolipin
DTGS	Deuterated triglycine sulfate
DDM	n-Dodecyl β -D-maltoside
Da	Dalton
DSC	Differential scanning calorimetry
DQ	Decylubiquinone
<i>E. coli</i>	Escherichia coli
Em	Midpoint potential
EPR	Electron paramagnetic resonance
Fe-S	Iron sulfur cluster
FMN	Flavin mononucleotide
FTIR	Fourier transform infrared
IRE	Internal reflection element
IR	Infrared
MCT	Mercury cadmium telluride
MES	2-(N-morpholino) ethanesulfonic Acid
MIR	Mid infrared
MD	Molecular dynamic
mV	mili-volts
NMR	Nuclear magnetic resonance
NADH	Nicotinamide adenine dinucleotide
NDF	NADH dehydrogenase fragment
Nuo	NADH: ubiquinone oxidoreductase subunit
Ox-red	oxidized minus reduced
PDB	Protein data bank
PC	Phosphatidylcholine
PE	Phosphatidylethanolamine
PG	Phosphatidylglycerol

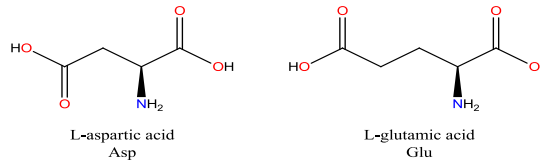
PMOXA	Polymethyloxazoline
PDMS	Polydimethylsiloxane
Q	Quinone (oxidized)
QRF	Quinone reductase fragment
QH2	Reduced quinone
QCM	Quartz crystal microbalance
RE	Reference electrode
ROS	Reactive oxygen species
RR	Resonance Raman
SHE	Standard hydrogen electrode
SERS	Surface enhanced resonance Raman spectroscopy
SQ	Semiquinone
UV	Ultraviolet
TM	Transmembrane
T_m	Transition temperature
vis	Visible
v	Stretching vibrations
δ	Bending vibrations
ε	Molar absorption coefficient

The twenty amino acids

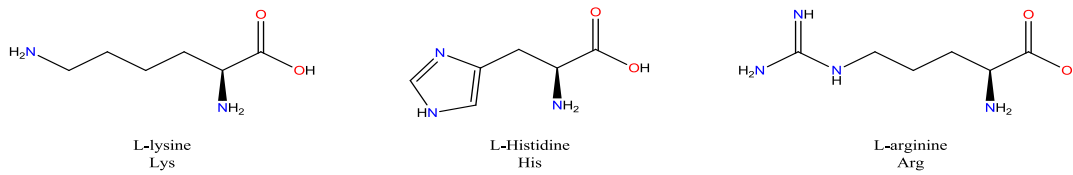
Aromatic amino acids



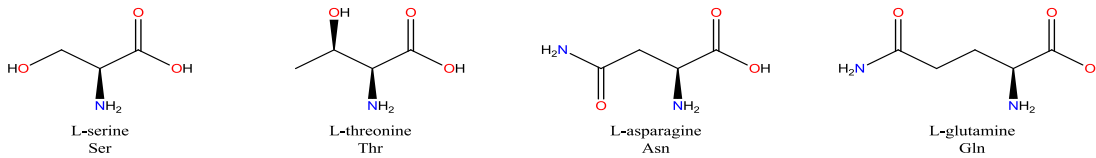
Acidic amino acids



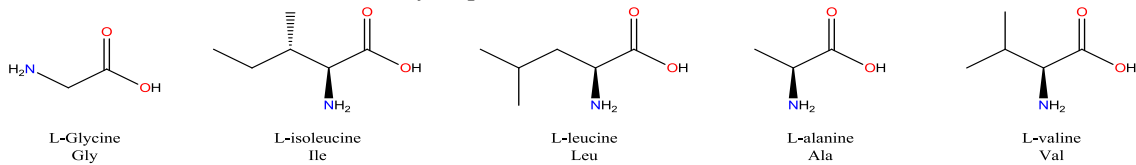
Basic amino acids



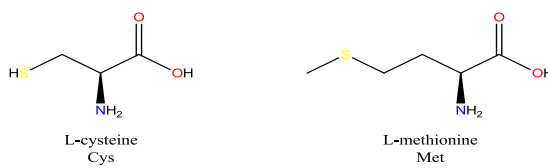
Hydrophilic amino acids



Hydrophobic amino acids



Sulfur containing amino acids



Special structure amino acid

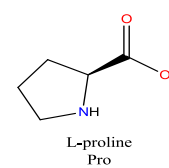


Table of contents

1	Introduction.....	2
1.1	<i>The cell membrane.....</i>	2
1.1.1	Lipids	3
1.1.2	Properties of lipids	6
1.1.3	Experimental studies on lipids	9
1.1.4	Computational studies.....	11
1.1.5	Lipids with cholesterol (experimental and simulation studies)	12
1.2	<i>Liposomes</i>	15
1.2.1	Liposomes stability on solid surfaces	17
1.2.2	pH sensitive liposomes	18
1.3	<i>Role of lipids in proteins.....</i>	20
1.4	<i>The respiratory chain.....</i>	21
1.4.1	The NADH: ubiquinone oxidoreductase (complex I).....	22
1.4.2	NuoL mutants.....	32
1.4.3	Complex I and zinc	32
1.4.4	Complex I and synthetic lipids (polymer)	33
1.5	<i>Aims of the thesis</i>	35
2	Characterization techniques and sample preparation	37
2.1	<i>Introduction to spectroscopy.....</i>	37
2.2	<i>UV-visible spectroscopy.....</i>	38
2.3	<i>IR spectroscopy.....</i>	39
2.3.1	Fourier transform infrared spectroscopy (FTIR)	43
2.3.2	IR spectroscopy of proteins	45
2.3.3	Transmission mode	48
2.3.4	Difference spectroscopy.....	48
2.3.5	Attenuated total reflection (ATR) spectroscopy	50
2.4	<i>Raman spectroscopy</i>	52
2.4.1	Resonance Raman spectroscopy (RR).....	53

2.4.2	Surface enhanced resonance Raman spectroscopy (SERS).....	54
2.5	<i>Sample Preparation</i>	54
2.5.1	Preparation of complex I protein and its variants	54
2.5.2	Preparation of lipids and liposomes.....	57
2.6	<i>Experimental conditions</i>	61
2.6.1	Infrared absorbance spectra of lipids	61
2.6.2	Study of liposomes.....	62
2.6.3	Spectroelectrochemisrty.....	63
2.6.4	Resonance Raman Spectroscopy	68
3	Results and discussions	71
3.1	<i>The temperature dependence of lipids in the mid infrared domain</i>	71
3.1.1	Spectral features characteristics of the tail part	72
3.1.1.1	CH stretching vibration.....	72
3.1.1.2	Phase transition temperature	74
3.1.1.3	Bending modes: CH ₂ wagging, rocking and scissoring vibrational modes .	80
3.1.2	Spectral features characteristics of the lipid head group	82
3.1.2.1	CO vibration.....	82
3.1.2.2	Phosphate region.....	90
3.2	<i>The temperature dependence of lipids in the far infrared domain</i>	96
3.3	<i>Raman spectroscopic study of lipids</i>	101
3.3.1	Raman spectroscopic study of mixture of lipids with cholesterol	104
3.3.2	Surface enhanced Raman spectroscopy	106
3.4	<i>The far infrared spectroscopic properties of EPC/EPE mixtures</i>	108
3.4.1	Far infrared ATR absorbance spectra of EPC, EPE and EPC/EPE mixtures	108
3.4.2	Temperature dependent far infrared absorbance spectra of pure phospholipids (DMPC and DMPE in comparison to EPC and EPE respectively).	110
3.4.3	Temperature dependent far infrared absorbance spectra of mixture of phospho- lipids	111
3.4.4	Temperature dependent mid infrared absorbance spectra of mixture of phospholipids	114
3.4.5	Temperature dependence of the water mode in mixed phospholipids.....	117

3.5	<i>Liposomes</i>	118
3.5.1	pH sensitive liposomes	118
3.5.1.1	DOPE/CHEMS liposomes	119
3.5.1.2	Mid infrared ATR absorbance spectra of CHEMS	119
3.5.1.3	Mid infrared ATR absorbance spectra of DOPE/CHEMS	121
3.5.1.4	Effect of pH on phosphate head group	123
3.5.1.5	Effect of pH on the CO band	126
3.5.1.6	Far infrared ATR absorbance spectra of DOPE/CHEMS	127
3.6	<i>Conclusion</i>	129
4	Complex I	132
4.1	<i>Complex I protein and polymer</i>	132
4.1.1	Electrochemical cell	134
4.1.2	Far infrared spectroscopic investigation	135
4.2	<i>NuoL mutants</i>	137
4.2.1	Zinc inhibition	141
4.3	<i>NuoB mutants</i>	144
4.3.1	UV-visible titration	146
4.3.2	Raman spectroscopy of Complex I wild type and NuoB mutants	149
4.3.2.1	Fe-S modes for Complex I and NuoB mutants at different pH	150
5	Conclusion and future work	155
6	Appendix	158
6.1	<i>Results and discussion appendix</i>	158
7	References	163

List of Figures

Figure 1. Schematic representation of the fluid mosaic model according to Singer and Nicolson (1972)	2
Figure 2. Abundance of each type of lipid adapted from lipid MAPS	3
Figure 3. Representation of the structure of a phospholipid molecule	4
Figure 4. Schematic representation of the cholesterol structure.	4
Figure 5. The organization of phospholipids in aqueous environment.	6
Figure 6. The phospholipid bilayer transition from a gel phase to a liquid crystalline phase. The two phases differ in the packing density of the hydrocarbon chains.	8
Figure 7. Models of the phospholipid bilayer with different phases and the temperature-composition phase diagram for DMPC/cholesterol.....	13
Figure 8. The computed phase diagram of DMPC lipid as function of cholesterol and temperature. The color gives the condensation effect and the lines indicate the phase boundaries of the different phases.....	14
Figure 9. Schematic drawing of liposome structure.....	15
Figure 10. Illustration of liposomes of different size and number of lamellae.	16
Figure 11. A proposed mechanism for liposomes adsorption on hydrophobic surfaces	17
Figure 12. Interaction between liposomes and solid surfaces	18
Figure 13. Schematic drawing of the release of pH sensitive liposomes after pH change	18
Figure 14. Main constituents of pH sensitive liposomes and their structural representation: cholesteryl hemisuccinate (CHEMS) in deprotonated and natural forms and DOPE lipid.	19
Figure 15. Representative model of the respiratory chain.	22
Figure 16. Schematic representation of complex I from <i>T. thermophilus</i>	24
Figure 17. Schematic drawing of the different subunits of complex I.	26
Figure 18. Representation of the binuclear and tetranuclear iron sulfur cluster structures.	27
Figure 19. Scheme of the electron transfer between N2 and the UQ.....	28
Figure 20. The chain of the iron sulfur clusters in the <i>T. thermophilus</i> Complex I and their midpoint potentials	29
Figure 21. Representation of the different subunits of the membrane arm of <i>E. coli</i> complex I.	30
Figure 22. Schematic representation of the coupling between the electron transfer and proton transfer of <i>T. thermophilus</i> complex I.	31
Figure 23. Representation of the inhibition of the proton translocation pathways in the membrane arm of the complex I in the presence of zinc	33
Figure 24. Representation of the electromagnetic spectrum as function of the wavelength (m), frequency (Hz) and energy (eV)	37
Figure 25. Lambert-Beer's Law.....	38
Figure 26. Change in the dipole moment of a heteronuclear diatomic molecule.	39
Figure 27. Scheme of a molecule composed of two atoms representing the harmonic oscillator.....	40
Figure 28. Different normal vibrational modes.	41
Figure 29. Stretching and bending vibrations of a tetrahedral carbon atom.	42

Figure 30. Schematic representation of the Michelson interferometer.	44
Figure 31. The interferogram and its corresponding absorbance spectrum obtained after Fourier transformation	44
Figure 32. Linking of amino acid together by amide bond.....	45
Figure 33. Representation of the different secondary structural elements: α helix and β sheet	46
Figure 34. Amide I band second derivative and secondary structure components	47
Figure 35. Scheme of the different parts of the absorbance cell.	48
Figure 36. The mid infrared absorbance spectrum of protein in solution.	49
Figure 37. The absorption spectra in the reduced and the oxidized states and difference spectrum.....	49
Figure 38. Scheme of an attenuated total reflectance unit.	50
Figure 39. Diagram of the Rayleigh and Raman scattering processes.....	52
Figure 40. Diagram of the Raman and resonance Raman scattering	53
Figure 41. Chemical structures of DMPC, DMPE, EPC, EPE, CL and cholesterol	58
Figure 42. The crucial steps involved in the preparation of liposomes.....	59
Figure 43. Extruder used for producing LUV.....	60
Figure 44. Liposomes solution on TiO ₂ modified Si/ZnSe crystal.	62
Figure 45. The spectroelectrochemical cell and its different compartments before and after assembly.....	63
Figure 46. Schematic representation of the role of mediators.....	64
Figure 47. The steps used to immobilize lipids for signal enhancement in Raman.	69
Figure 48. The mid infrared absorption spectra of EPC, EPE, CL and cholesterol.	72
Figure 49. Temperature dependent ATR absorbance spectra of pure EPE, EPE/cholesterol (2:1), EPC, EPC/cholesterol (2:1), CL and CL/cholesterol (2:1).	73
Figure 50. Plot of CH ₂ wavenumber as function of temperature of pure EPE and EPE/cholesterol (2:1).....	75
Figure 51. Description of the different lipid phases: the gel phase, the liquid crystalline phase and the hexagonal non-bilayer structure of EPE lipid	76
Figure 52. Plot of CH ₂ wavenumber as function of temperature of pure EPC and EPC/cholesterol (2:1).....	77
Figure 53. Plot of CH ₂ wavenumber as function of temperature of pure CL and CL/cholesterol (2:1).....	79
Figure 54. The CH bending region of EPE, EPE/cholesterol (2:1), EPC, EPC/cholesterol (2:1), CL, CL/cholesterol (2:1) under the effect of temperature.....	81
Figure 55. The temperature dependent C=O band of EPE, EPE/cholesterol (2:1), EPC, EPC/cholesterol (2:1), CL, CL/cholesterol (2:1).....	83
Figure 56. Schematic representation of cholesterol insertion between acyl chains of lipids.	84
Figure 57. Comparison of the carbonyl band of EPC and EPC/cholesterol at 5 and 40 °C.....	85
Figure 58. Comparison of the carbonyl band of EPE and EPE/cholesterol at 5, 40 and 80 °C	87
Figure 59. Comparison of the carbonyl band of CL and CL/cholesterol at 5 and 40 °C	89
Figure 60. Enlarged view of the temperature dependent $\nu_{as}(\text{PO}_2^-)$ and $\nu_s(\text{PO}_2^-)$ stretching modes of EPC and EPC/cholesterol (2:1).	91
Figure 61. Enlarged view of the temperature dependent $\nu_{as}(\text{PO}_2^-)$ and $\nu_s(\text{PO}_2^-)$ stretching modes of EPE and EPE/cholesterol (2:1).....	93
Figure 62. The intramolecular hydrogen bonding of cardiolipin structure (18:0).	94

Figure 63. Enlarged view of the temperature dependent $\nu_{as}(\text{PO}_2^-)$ and $\nu_s(\text{PO}_2^-)$ stretching modes of CL and CL/cholesterol (2:1).....	95
Figure 64. Far IR absorbance spectra as a function of temperature of EPC and EPC/cholesterol (2:1)	96
Figure 65. Far IR absorbance spectra as a function of temperature of EPE and EPE/cholesterol (2:1).....	98
Figure 66. Far IR absorbance spectra as a function of temperature of CL and CL/cholesterol (2:1).....	99
Figure 67. Raman spectra from 400 to 1800 cm^{-1} of EPC, EPE, CL and cholesterol with an excitation of 514 nm.	102
Figure 68. Raman spectra from 400 to 1800 cm^{-1} of EPC, EPC/cholesterol, EPE, EPE/cholesterol, CL and CL/cholesterol	104
Figure 69. The low frequency region and CH stretching region of EPC, EPE, and CL after SERS.....	107
Figure 70. Far infrared absorbance spectra of EPE, EPC and the mixture of EPC/EPE of (1:1), (2:1) and (4:1) ratios	109
Figure 71. Temperature dependent far infrared absorbance spectra of DMPC, EPC, DMPE, and EPE lipids upon heating	110
Figure 72. Temperature dependent far infrared absorbance spectra of EPC/EPE mixture of (1:1), (2:1) and (4:1) ratios	112
Figure 73. Temperature dependent mid IR absorbance spectra and the transition temperature of EPC/EPE mixture of (1:1), (2:1) and (4:1) ratios.....	115
Figure 74. Enlarged view of the studied spectral range 900-1800 cm^{-1} of EPC /EPE mixture of (1:1), (2:1) and (4:1) ratios	116
Figure 75. Temperature dependent behaviour of the mid infrared spectra of the (OH) stretching vibration from 3700 to 3050 cm^{-1} and δ (HOH) bending vibrations from 1700 and 1550 cm^{-1} of EPC/EPE mixture of (1:1), (2:1) and (4:1) ratios	117
Figure 76. pH sensitive liposomes: fusion with endosomal membrane.	119
Figure 77. The mir ATR absorbance spectra of CHEMS at pH 7.4 and pH 4.5.....	120
Figure 78. An enlarged view of the carbonyl band of CHEMS at pH 7.4 and pH 4.5.....	121
Figure 79. The mid ATR absorbance spectra of the DOPE/CHEMS liposomes, DOPE lipid and CHEMS at different pH	122
Figure 80. The phosphate region of DOPE/CHEMS liposomes and its pH dependence.	124
Figure 81. Schematic diagram of the different kinds of interaction between CHEMS and DOPE lipid.	125
Figure 82. Deconvolution of the CO stretching band of DOPE/CHEMS liposomes at pH 4.5 and pH 7.4.....	126
Figure 83. ATR far infrared absorbance spectra of DOPE/CHEMS liposomes at different pH values.....	127
Figure 84. The far infrared spectra of DOPE/CHEMS liposomes, DOPE lipid and CHEMS at pH 7.4.	128
Figure 85. Enlarged view of the hydrogen bonding continuum of DOPE/CHEMS liposomes at different pHs	129
Figure 86. Graphical representation of complex I incorporated in copolymer membrane.....	134
Figure 87. Oxidized minus reduced FTIR difference spectra of the delipidated wild type complex I with and without polymer.....	135
Figure 88. Far infrared absorbance spectra of delipidated complex I treated with polymer	136
Figure 89. The subunits NuoL, M, N of the membrane arm of complex I from <i>E. coli</i> and the D563 residue..	137

Figure 90. Oxidized minus reduced FTIR spectra of complex I, D563E, D563N and Y594F from -650 to 0 mV.	139
Figure 91. The fully oxidized minus fully reduced difference spectra of untreated and Zn ²⁺ incubated D563N complex I mutant for the step from -650 to 0 mV.	141
Figure 92. Double difference spectra of complex I <i>minus</i> complex I treated with Zn ²⁺ of the wild type protein and the D563N variant.....	142
Figure 93. The tetranuclear iron sulphur cluster N2.	145
Figure 94. The tetranuclear iron sulfur cluster N2 showing the different sites of mutation.	146
Figure 95. UV-vis titrations of the NuoB mutants at pH 7 and 6.5	147
Figure 96. Low frequency resonance Raman spectra of Nuo B mutants	150

List of Tables

Table 1. Different kinds of phospholipids with their polar group R and net charge	5
Table 2. Packing parameters and possible structures	6
Table 3. Phase transition temperature of PC lipid according to the length of the two fatty acid chains and degree of unsaturation	8
Table 4. Nomenclature of the 14 core subunits of bacterial complex I with their bound cofactors and proposed function of the subunit.....	25
Table 5. Degrees of freedom for linear and non-linear molecules	40
Table 6. The effect of isotope labelling on the vibrational frequencies of some groups.....	41
Table 7. Equipment used in the infrared measurement according to the different spectral range.....	43
Table 8. Amide vibrations, frequencies and description of the peptide backbone	46
Table 9. Assignment of protein secondary structural elements according to the amide I band	47
Table 10. ATR crystal characteristics for FTIR sampling.	51
Table 11. DOPE/CHEMS (3:2) liposomes at 6 different pH buffers.....	60
Table 12. List of mediators used for spectroelectrochemical experiments.	65
Table 13. The transition temperatures of EPC, EPE lipids and their mixtures with cholesterol.....	79
Table 14. Positions of the low and high frequency components of carbonyl band obtained by deconvolution at a temperature of 5 °C and 40 °C for EPC and EPC/cholesterol.	86
Table 15. Positions of the low and high frequency components of carbonyl band obtained by deconvolution at a temperature of 5 °C, 40 °C and 80 °C for EPE and EPE/cholesterol.	88
Table 16. Positions of the low and high frequency components of carbonyl band obtained by deconvolution at a temperature of 5 °C and 40 °C for CL and CL/cholesterol.....	90
Table 17. Summary of the tentative assignments of EPC, EPC/cholesterol, EPE, EPE/cholesterol, CL, CL/cholesterol studied in the mid and far infrared region	100
Table 18. Assignments of Raman modes in EPC, EPE, CL and cholesterol.	103

Table 19. Tentative assignments of phospholipids vibrations in the mid, far infrared as well as Raman domains.	105
Table 20. The assignments of EPC, EPE and CL vibrations after SERS.	108
Table 21. The tentative assignments of DMPC, DMPE and EPC/ EPE of (1:1), (2:1) and (4:1) (studied in the far infrared region)	113
Table 22. Detailed band assignments of DOPE/CHEMS liposomes, DOPE lipid, CHEMS at pH 7.4.	123
Table 23. Different peaks obtained by the deconvolution of the CO vibration of DOPE/CHEMS liposomes at pH 4.5 and 7.4.	126
Table 24. The activity measurements of delipidated complex I protein in the presence of <i>E. coli</i> polar lipids (PL), cardiolipin (CL) and block copolymer (BCP).	133
Table 25. Detailed band assignments of the FTIR electrochemically induced oxidized <i>minus</i> reduced difference spectra of the complex I from <i>E. coli</i> , D563N, D563E and Y594F mutants	140
Table 26. Tentative attribution of the signals of the oxidized <i>minus</i> reduced FTIR difference spectra of the WT complex I and D563N in presence of Zn ²⁺	143
Table 27. The estimated midpoint potentials of FMN and iron sulfur redox cofactors of the NuoB mutants at pH 7 and 6.5 versus SHE.	148
Table 28. Frequencies modes (cm ⁻¹) of the different samples and their assignments.	153

Résumé

Les membranes constituent une barrière naturelle pour les cellules qui séparent l'intérieur de l'extérieur et permettent la formation de divers compartiments cellulaires internes. Elles sont essentielles pour la vie, car elles exécutent un certain nombre de processus cellulaires, y compris la communication cellulaire, la respiration, la transduction du signal et la motilité. Les membranes peuvent être décrites selon le modèle de la mosaïque fluide, où la bicouche phospholipidique est considérée comme deux liquides bidimensionnels incorporant un assemblage globulaire des protéines et des glycoprotéines.

Le travail présenté au cours de cette thèse s'articule autour de trois parties principales:

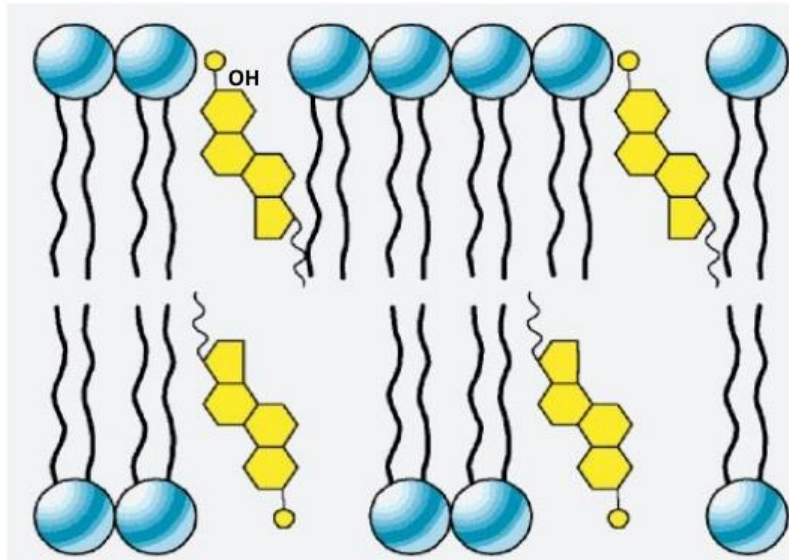
1) Interaction lipide-lipide

La première partie est consacrée à l'étude des lipides qui forment les membranes biologiques. Ces lipides sont constitués de groupes hydrophiles ainsi que de chaînes grasses hydrophobes, ils s'auto-assemblent en milieu aqueux dans des structures différentes comme des micelles, des bicouches lipidiques et des liposomes. En outre, ils présentent une propriété intéressante sous l'effet de la température; ils passent d'une phase de gel ordonnée à une phase désordonnée. Ces deux phases diffèrent par leur densité d'auto-association des chaînes d'hydrocarbure.

La structure et l'organisation des lipides dans les différentes phases sont étudiées par spectroscopie infrarouge (FTIR). Le moyen infrarouge (MIR) ($4000-800\text{ cm}^{-1}$) donne des informations sur la température de transition de phase et les propriétés conformationnelles des lipides. En revanche, la région de l'infrarouge lointain (FIR) ($600-50\text{ cm}^{-1}$) permet de voir la contribution du groupe principal PO_2^- du phosphate, les mouvements de torsion des vibrations de la chaîne d'hydrocarbure aussi bien que l'interaction des liaisons hydrogènes.

La caractérisation des systèmes lipidiques purs et lipide/cholestérol permet l'examen de l'influence du cholestérol sur le comportement thermotropique et le polymorphisme de ces mélanges de lipides. Pour obtenir une meilleure compréhension de l'effet du cholestérol sur la phosphatidylcholine, phosphatidyléthanolamine issue de l'œuf et la cardiolipine, la région carbonyle ($1700-1800\text{ cm}^{-1}$) est examinée. Cette région est importante pour l'étude des systèmes lipide/cholestérol, puisque le cholestérol n'a pas de contribution dans cette gamme

spectrale et tous les effets observés peuvent être corrélés à l'interaction entre le cholestérol et les lipides, soit de manière directe par la formation de liaisons hydrogène entre le groupement CO des lipides et de l'hydroxyle OH du cholestérol ou d'une manière indirecte par des effets de conformation.



Représentation du groupement hydroxyle (-OH) du cholestérol (en jaune) associés avec le groupe de tête polaire des lipides (en bleu).

En outre, les mesures réalisées par la spectroscopie infrarouge sur la dépendance de la température des mélanges lipidiques de différents ratio (phosphatidylcholine/ phosphatidyl-éthanolamine) dans la région de l'infrarouge lointain sont effectuées dans le but de déterminer la composition du groupe principal (choline et éthanolamine) qui affecte les interactions des liaisons hydrogène et la température de transition de phase.

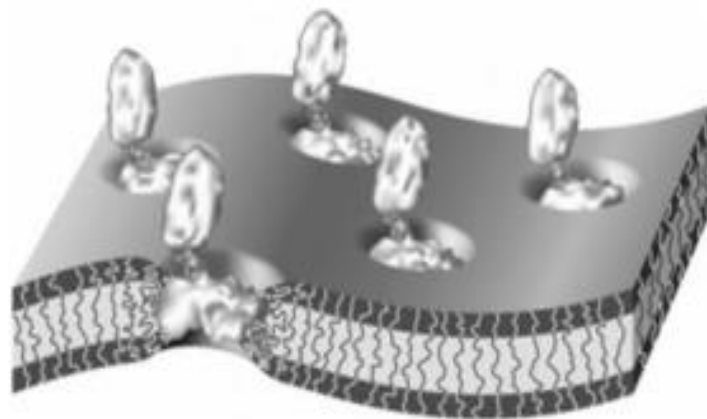
Enfin dioleoylphosphatidyléthanolamine/cholesteryl hemisuccinate (DOPE/CHEMS) liposomes à différents pH sont étudiés afin d'examiner la dépendance du pH. Le changement de pH induit un changement clair dans la vibration de l'étirement asymétrique du phosphate et dans le continuum de liaison hydrogène. Ainsi, les conclusions de la spectroscopie infrarouge moyen et lointain nous ont permis de proposer un mécanisme d'interaction entre le DOPE et CHEMS via les liaisons hydrogène et les interactions électrostatique.

2) Interaction lipide-protéine

La protéine NADH ubiquinone oxydoréductase (complexe I) constitue le premier complexe de la chaîne respiratoire; elle couple l'oxydation du NADH en NAD^+ et la réduction de l'ubiquinone en ubiquinol accompagnées par la translocation de quatre protons à travers la membrane.

Ce complexe enzymatique de 500 KDa est à la fois le plus grand et le moins bien connu des complexes de la chaîne respiratoire. En dépit de récentes avancées structurales, le mécanisme de couplage de l'oxydation de NADH à la translocation de protons reste sujet à discussion. Il est suspecté que des modifications de la fonction ou de la structure de cette enzyme mènent à une variété de pathologies humaines courantes, telles que les maladies de Parkinson et d'Alzheimer ou encore la neuropathie optique héréditaire de Leber.

La seconde partie de la thèse porte sur l'étude du rôle d'un lipide artificiel (copolymère séquencé de polyméthylsiloxane-polyméthylloxazoline-polyméthylloxazoline) dans la protéine complexe I. Les résultats obtenus sur les mesures d'activités indiquent que le lipide artificiel (copolymère mentionné ci-dessus) est capable d'activer le complexe I de manière similaire à celle des phospholipides et de fournir un milieu approprié pour la conformation active de la protéine. La spectroscopie infrarouge couplée à l'électrochimie a montré que ce polymère a induit des changements majeurs au niveau de la bande amide I et amide II. D'autres expériences telles que la spectroscopie Raman et l'échange cinétique hydrogène-deutérium (H/D) ont dû être effectuées afin de mieux comprendre le mécanisme de l'interaction entre ce copolymère et le complexe I.



Représentation du Complexe I incorporé dans la membrane du copolymère.

3) Complexe I et ces différents mutants

Le complexe I a une structure en forme de L dont la partie périphérique s'étend dans le cytoplasme là où se trouve un mononucléotide de flavine (FMN) et une série de clusters binucléaires et tétranucléaires de fer-soufre. En revanche, la partie membranaire est incorporée dans la bicouche lipidique et ne contient pas de cofacteurs. Cette partie est impliquée dans le mécanisme de pompage des protons, où certains résidus d'acides aminés sont proposés d'intervenir dans les chemins de protons.

Pour cette raison, des études sur différents mutants du complexe I situés au niveau de la sous-unité NuoL ont été effectuées. Les résultats observés révèlent de faibles changements de conformation de la bande amide I et amide II dans ces mutants, ce qui est cohérent avec leur taux de transfert d'électrons légèrement modifié. L'étude de ces mutants permet de déterminer le rôle de cette sous-unité dans le pompage de proton afin d'obtenir une meilleure compréhension du mécanisme de fonctionnement de cette protéine.

L'ion Zn^{2+} est un inhibiteur du pompage de protons pour le complexe I. Ceci, induit des changements dans la signature spectrale de certains résidus d'acides aminés connus pour participer au transfert de protons. Les mesures effectuées en spectroscopie infrarouge différentielle induite par électrochimie ont permis de conclure que le blocage du pompage de protons avait une influence sur les changements conformationnels lors du fonctionnement de la protéine.

Enfin, les mutants NuoB à différentes valeurs de pH ont été étudiés. Les modes de vibrations « bridging et terminaux » des clusters fer-soufre, ainsi que leurs potentiels redox ont été sondés en utilisant la spectroscopie Raman et l'UV-visible. Le potentiel redox (E_m) du cluster N2 a été déplacé de 70 mV par rapport à la protéine sauvage (wild type). En revanche, le potentiel redox de la FMN n'a pas été affecté. Ceci pourrait être expliqué par la distance entre le site de la mutation et le cofacteur. Les résultats Raman nous ont permis de conclure que les modes de vibrations bridging ($Fe-S_b$) ont été déplacés vers des fréquences plus basses ce qui implique que la mutation a induit une perturbation ainsi qu'un changement conformationnel du cluster fer-soufre.

Chapter I

**General introduction about lipids and
NADH ubiquinone oxidoreductase protein**

1 Introduction

1.1 The cell membrane

The cell is considered as the smallest structural and functional unit of all known living organisms. Cells are classified based on their cellular characteristics into two types: eukaryotic cells that have nucleus and prokaryotic cells that do not have. Both types are surrounded by permeable thin membranes that separate the inside from the outside and allow the formation of various internal cellular compartments. The study of these membranes attracted scientist's interest and became a primary target in both basic and applied research since they are involved in various cellular processes including cell communication, respiration, signal transduction and motility.

In 1972, Singer *et al.* ⁽¹⁾ designed the fluid mosaic model that explains various observations regarding the structure of functional cell membrane. According to this model, the phospholipid bilayer can be considered as a two dimensional liquid incorporating globular assembly of proteins and glycoproteins (Figure 1). This model was subjected to many developments in terms of composition and molecular organization. For instance, Simons *et al.* and Brown *et al.* suggested that membrane lipids are organized into lateral micro domains or lipid rafts which possess a specific composition and molecular dynamic ⁽²⁻⁴⁾.

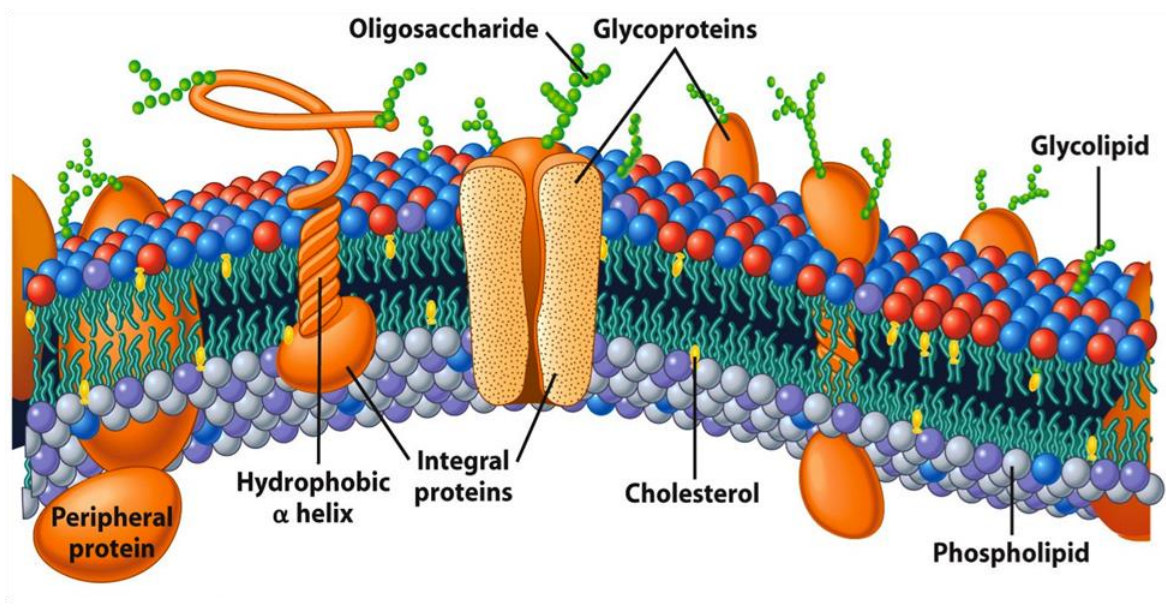


Figure 1. Schematic representation of the fluid mosaic model according to Singer and Nicolson (1972) ⁽⁵⁾.

As illustrated in Figure 1, a biological membrane is mainly made of three major components: sugars (5%), proteins (45%) and lipids (50%) ⁽⁶⁾. The sugars are found on one side of the membrane and they are attached by covalent bonds to the protein and lipid molecules. Protein and lipid molecules are held together through non covalent interactions ⁽⁷⁾.

1.1.1 Lipids

Lipids are amphiphilic molecules composed of hydrophilic head groups and hydrophobic tails ⁽⁸⁾. The lipid head groups are polar, zwitterionic or charged. Three types of lipids are found mainly in biological membranes: phospholipids, glycolipids and cholesterol. Besides, there are many other types of lipids classified by Lipid Metabolites and Pathways Strategy (Lipid MAPS) according to their chemical structures ⁽⁸⁾. The abundance of each type of lipid is presented in Figure 2 ⁽⁹⁾.

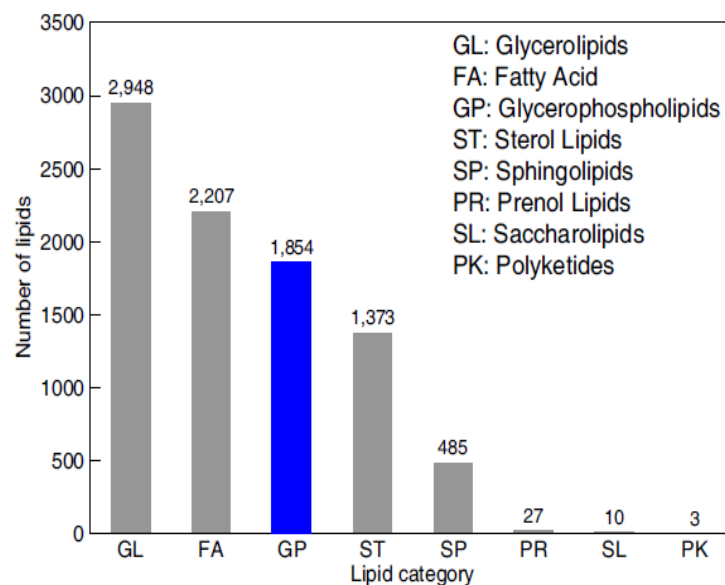


Figure 2. Abundance of each type of lipid adapted from lipid MAPS ⁽⁹⁾.

- **Phospholipids**

The most abundant class of lipid molecules found in cell membranes is phospholipids. The phospholipid molecule is made up of a polar head which contains phosphate group and two nonpolar fatty acid chains as the tail, usually one chain is unsaturated (Figure 3). The nature of the R group attached to the phosphate usually determines the lipid type (see Table 1).

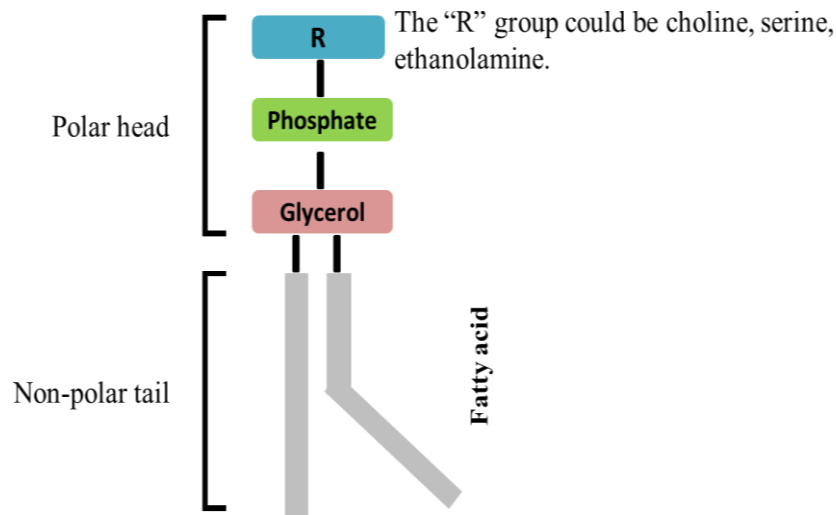


Figure 3. Representation of the structure of a phospholipid molecule.

- **Glycolipids**

The main difference between phospholipids and glycolipids is that the latter have a sugar group as glucose or galactose instead of the phosphate group. Glycolipids exist in animal and plant membranes with sphingosine and glycerol groups respectively.

- **Cholesterol**

Cholesterol constitutes the third type of lipids; the structure is made up of four steroid rings together with a hydroxyl group and a small hydrocarbon side chain (Figure 4). Cholesterol is present in some mammalian membranes in contrast to bacterial and plant membranes ⁽⁷⁾. Cholesterol does not have the ability to form bilayer by itself however it is incorporated into the phospholipid bilayer to fill the flickering spaces among the acyl chains ^(10, 11).

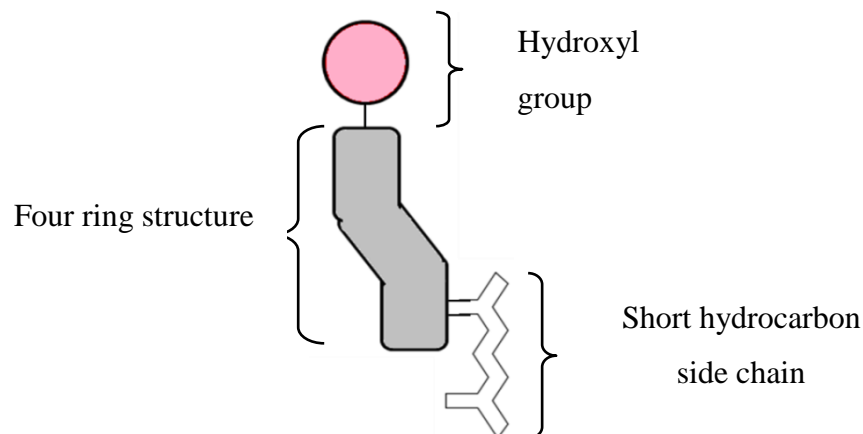
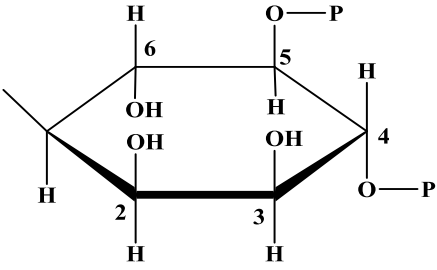
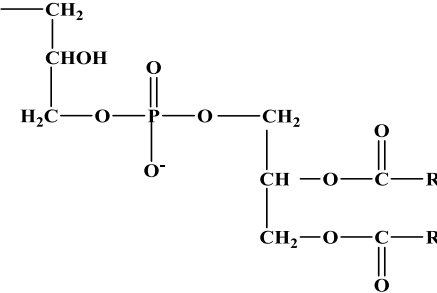


Figure 4. Schematic representation of the cholesterol structure.

Table 1. Different kinds of phospholipids with their polar group R and net charge ^(12, 13).

Name of phospholipid	Name of R	Formula of R	Net charge at pH 7
Phosphatidic acid	—	—H	-1
Phosphatidylethanolamine	Ethanolamine	—H ₂ C—CH ₂ —NH ₃ [⊕]	0
Phosphatidylcholine	Choline	—H ₂ C—CH ₂ —N(CH ₃) ₃ [⊕]	0
Phosphatidylserine	Serine	—H ₂ C—CH—NH ₃ [⊕] COO ⁻	-1
Phosphatidylglycerol	Glycerol	—CH ₂ —CH—C—OH OH H ₂	-1
Phosphatidylinositol 4,5-bisphosphate	Inositol 4,5-bisphosphate		-4
Cardiolipin	Phosphatidylglycerol		-2

According to the nature of the polar group R, lipids are classified into zwitterionic like phosphatidylcholine and phosphatidylethanolamine or negatively charged such as cardiolipin, phosphatidylserine and phosphatidylglycerol.

1.1.2 Properties of lipids

In aqueous medium, lipid molecules self-assemble into different organized structures as micelles, liposomes and phospholipid bilayers (Figure 5) in order to minimize the contact between hydrophobic parts of lipids and water molecules.

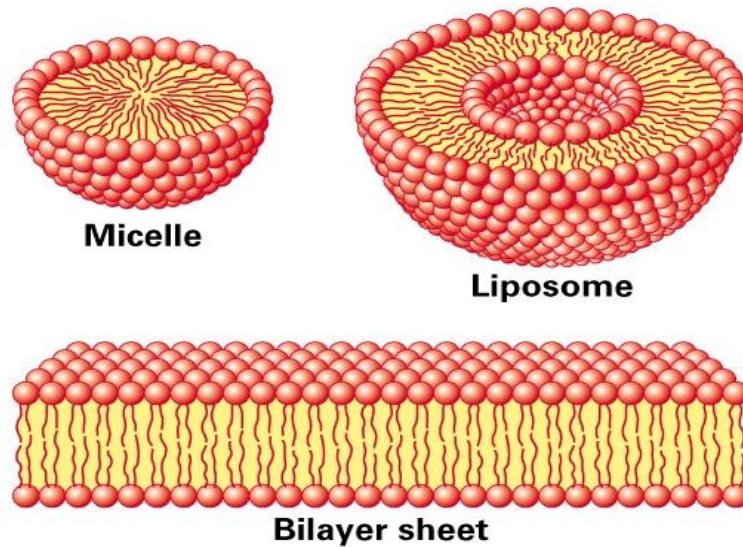


Figure 5. The organization of phospholipids in aqueous environment.

The morphology of the phases formed depends not only on the concentration of the amphiphilic molecules but also on the geometrical shape of the molecules under consideration. The ratio between the volume of the hydrophobic portion (v) and the product of the area of the polar head (a_0) by the length of the molecule (l_c) is called the shape factor or packing parameter ($P=v/a_0l_c$). This factor determines the topology of the self-assembled structure as can be seen in Table 2⁽¹⁴⁾.

Table 2. Packing parameters and possible structures⁽¹³⁾.

Packing parameter (v/a_0l_c)	Formed structure
$P < 1/3$	Spherical micelles
$1/3 < P < 1/2$	Cylindrical (rod like micelles)
$1/2 < P < 1$	Bilayers (if a_0 is small and hydrocarbon chains are bulky)
$P > 1$	Inverted micelles
$1/2 < P < 1$	Vesicles

The structures formed are sensitive to the environment and conditions. Transitions between them occur due to: temperature change (where a_0 and l_c are altered), presence of ions, chain unsaturation and branching ⁽¹⁵⁾.

The phospholipid bilayer is considered as a two dimensional fluid, so proteins and lipid molecules are able to diffuse freely in the matrix. The lateral diffusion is very rapid so the phospholipid molecule is able to move from one end to the other within few seconds. In addition, these lipid molecules can rotate rapidly along their head to tail axes. In comparison, the mobility of membrane proteins is different from those of phospholipids ⁽⁷⁾.

In contrast to the rapid lateral diffusion, lipid molecules rarely move from one side of the monolayer into the opposite side. This process of transfer is known as flip-flop or transverse diffusion and it occurs rarely because the hydrophilic head group of the lipid molecule should enter into the hydrophobic core of the bilayer. The measurements done on labelled phospholipids in artificial vesicles showed that one phospholipid molecule undergoes transverse diffusion only once in several hours.

Nevertheless, the flip-flop movement is slow and energetically unfavourable. The diffusion coefficient associated with this process is of the order of $10^{-8} \text{ cm}^2 \cdot \text{s}^{-1}$ ⁽¹⁶⁾. Binder *et al.* ⁽¹⁷⁾ revealed that these dynamic phenomena can occur either spontaneously or as a result of external stimuli. Concerning proteins, no flip-flop has been observed yet. This is mainly due to their large size and the extensive polar region which makes it difficult to move from one layer to another.

- **Fluidity**

One of the most important features of the phospholipid bilayer is the fluidity. It is affected by the temperature, lipid composition and cholesterol content. At low temperatures, the lipid exists in the gel phase where the fatty acid chains are tightly packed with all *trans* conformation. As temperature increases, the lipids vibrate more rapidly causing the transition of the bilayer to a more loosely packed system where the chains exist in *gauche* conformation.

The temperature at which the bilayer melts is called the transition temperature and it corresponds to the transition from an ordered phase (gel phase) to a disordered phase (liquid crystalline phase) (Figure 6) ⁽¹⁸⁻²⁰⁾. The fluidity is influenced by the transition temperature: when the transition temperature is lower the bilayer is more fluid.

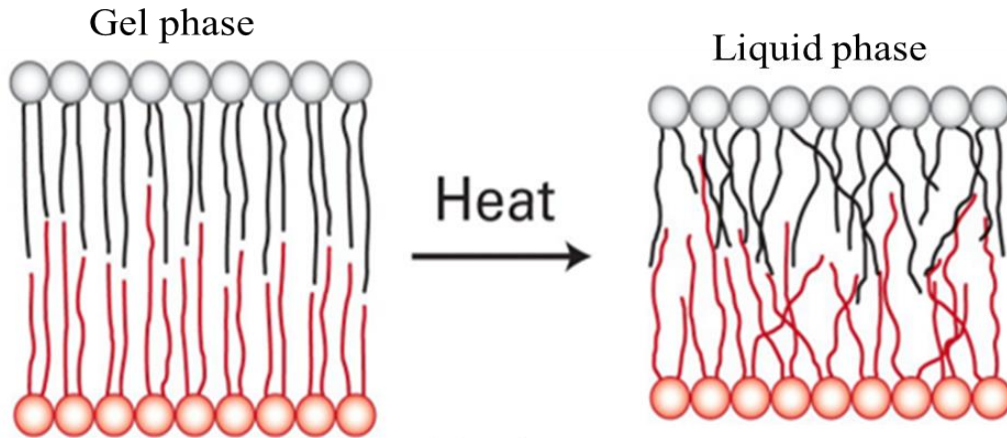


Figure 6. The phospholipid bilayer transition from a gel phase to a liquid crystalline phase. The two phases differ in the packing density of the hydrocarbon chains.

The second factor affecting bilayer fluidity is the presence of cholesterol. Cholesterol fits between the phospholipid molecules with its steroid rings between tails and hydroxyl group between heads leading to a more rigid and stiff system, thus the membrane is less fluid and it needs higher transition temperature to be melted ⁽⁷⁾.

Furthermore, the bilayer fluidity is influenced by the lipid composition. Lipid tails with short chains or double bonds cause higher fluidity. Since short tails interact less with one another in comparison with the long chains, this weak interaction necessitates lower transition temperature to melt the bilayer containing them. In addition, double bonds put bends in the hydrocarbon chain leading to a less packed system and more fluid bilayer (Table 3) ⁽⁷⁾.

Table 3. Phase transition temperature of PC lipid according to the length of the two fatty acid chains (where number of carbon atoms varies between 16 and 18) and degree of unsaturation where 0 (no double bond), 1 (one double bond) and 2 (two double bonds) ⁽²¹⁻²³⁾.

Saturated		Mono-unsaturated		Poly-unsaturated	
Lipid Tail	T_m (°C)	Lipid Tail	T_m (°C)	Lipid Tail	T_m (°C)
16:0-18:0	49	16:0-18:1	0	16:0-18:2	-19.5
18:0-18:0	55	18:0-18:1	6	18:0-18:2	-13.7
		18:1-18:0	9	18:1-18:1	-20

From Table 3, it is obvious that the increase in the degree of unsaturation (number of double bonds) leads to the decrease of the transition temperature. For instance, the transition temperature is 49 °C for (16:0-18:0) and 0 °C for (16:0-18:1). Additionally, the comparison between (16:0-18:0) and (18:0-18:0) shows that the transition temperature increases as the length of the fatty acid chain increases by two carbon atoms. As a result, beside the lipid head groups, the lipid tails affect the structural properties of membranes as transition temperature, hydrophobicity, reactivity and stability.

1.1.3 Experimental studies on lipids

This thesis is oriented around the study of particular lipid molecules as phosphatidylcholine (PC), phosphatidylethanolamine (PE) and cardiolipin (CL). In general, PC and PE are two of the most important neutral lipids found in all living organisms. The abundance of PE is variable among cell types and organisms. For instance, it exists in low concentration in animal cells, moderate concentration in blood cells (6%) and high concentration in bacteria (70-80% in *E. coli*)⁽²⁴⁾. PE is distributed unequally between the inner and outer leaflets of the membranes and it plays an important role in vesicle formation and membrane fusion^(25, 26). On the other hand, PC lipid is dominating in animal cells and is considered as a key for building and maintaining integrity of membranes^(27, 28).

The major difference between PC and PE is the nature of the head group namely the choline group for PC and the amine group for PE. The head group of PE allows the formation of intermolecular and intramolecular hydrogen bonding where the amine group acts as a hydrogen donor and the phosphate/carbonyl group as a hydrogen acceptor⁽²⁹⁾. These interactions affect the transition temperature, membrane permeability, stability, etc.

Beside PC and PE lipids, cardiolipin (CL) is an anionic phospholipid with two protonable phosphate groups⁽³⁰⁾. It is found mainly in the plasma membrane of many types of *Gram positive* and *Gram negative* bacteria and in the mitochondrial and chloroplast inner membranes of eukaryotes⁽³¹⁻³⁴⁾. CL plays important roles in promoting cell growth, mitochondrial function, anaerobic metabolism and structural stabilization.

The physical properties of lipids provide fundamental information which help in the determination of the structural and functional properties of biomembranes. For this reason, pure and mixtures of lipids were subjected to different kinds of characterization and simulation studies. For instance, dipalmitoyl-phosphatidylcholine (DPPC), a pure PC system,

was used as a model membrane to investigate the lipid-lipid and lipid-water interactions which mimics the interaction between membranes and extracellular matter. The structural and dynamic properties of DPPC such as 1) the area per lipid, 2) volume per lipid, 3) lamellar repeated spacing, 4) bilayer thickness, 5) order parameter, 6) diffusion coefficient and 7) transition temperature were analyzed using X ray diffraction ⁽³⁵⁻³⁸⁾, nuclear magnetic resonance (NMR) ^(39, 40) and neutron diffraction ⁽⁴¹⁾. Other types of lipids such as dioleoyl-phosphatidylcholine (DOPC) ^(42, 43), dimyristoyl-phosphatidylcholine (DMPC) ^(44, 45) and palmitoyl-oleoyl-phosphatidylcholine (POPC) ⁽²²⁾ were studied as well to investigate the properties and the structure of the model cell membrane.

On the other hand, the physical properties of PE membranes had also been characterized by using different techniques. For example, Hitchcock *et al.* ⁽⁴⁶⁾ used the X ray diffraction technique to probe the structure and arrangement of dimyristoyl-phosphatidylethanolamine (DMPE) molecules. Mantsch *et al.* ⁽⁴⁷⁾ used the Fourier transform infrared (FTIR) spectroscopic technique to analyze the thermotropic behaviour of PE and monitor the changes during the transition from a bilayer lamellar phase to a non-lamellar hexagonal phase. Furthermore, Popova *et al.* ⁽⁴⁸⁾ characterized the phase behaviour of dry membranes containing egg PE (EPE) or monogalactosyldiacylglycerol (MGDG) using differential scanning calorimetry (DSC) and FTIR spectroscopy.

For mixed PC and PE systems, most studies focused on the mechanism of interaction due to the formation of intermolecular and intramolecular hydrogen bonding and its consequences on the structure. Blume *et al.* ⁽²⁹⁾ determined the phase equilibria and dynamic structure of binary mixtures of DPPC and dipalmitoyl-phosphatidylethanolamine (DPPE) using solid state ¹³C and ²H NMR. Dyck *et al.* ⁽⁴⁹⁾ used surface sensitive X ray scattering to understand the lipid conformation of diacyl-phosphatidylethanolamine (PE) with its mono, di and trimethylated diacyl-phosphatidylcholine (PC). Quinn *et al.* ⁽⁵⁰⁾ reported the study of dynamic phase transition of (DMPC) and (DMPE) in water in a 4:1 molar mixture using time resolved X ray diffraction. Mendelschon *et al.* ⁽⁵¹⁾ used Raman spectroscopy to construct the phase diagram for the binary phospholipid systems of DPPC/DPPE and DPPC-d₆₂/DPPE in order to see the effect of chain perdeuteration on the phase behaviour of the system. Moreover, Blume *et al.* ⁽⁵²⁾ used DSC to study lipid phase transitions in aqueous dispersions of PC and PE systems.

In addition, many studies have been reported on the cardiolipin model membranes. The thermotropic phase behaviour of cardiolipin (18:0) using FTIR spectroscopy was described

by Hubner *et al.* ⁽⁵³⁾, where they suggested that the glycerol head group of cardiolipin is involved in strong intramolecular interactions. Another study by Lewis *et al.* ⁽⁵⁴⁾ showed the characterization of the thermotropic phase behaviour, the structure and organization of the various lamellar phases of the tetramyristoyl cardiolipin (TMCL) using FTIR spectroscopy, DSC, X ray diffraction and ³¹P NMR. Powel *et al.* ⁽⁵⁵⁾ studied the polymorphic phase behaviour of cardiolipin derivatives using X ray diffraction and ³¹P NMR indicating the importance of head group interactions in determining the lipid phase behaviour.

Most of the mentioned studies are concerned with the phase behavior of pure lipids in the fully hydrated form or even at different degrees of hydration. However, little work has specifically focused on mixed lipids and in particular on their specific interactions in the dry state.

1.1.4 Computational studies

Beside experimental studies carried on pure and mixtures of lipids, several computational studies have been performed including molecular dynamic (MD) simulation studies on lipids like DMPC ⁽⁵⁶⁻⁵⁸⁾, DPPC ⁽⁵⁹⁻⁶¹⁾, POPC ^(62, 63), and DOPC ⁽⁶⁴⁾. Simulation calculates some of the structural and dynamic properties as membrane thickness, area per lipid, density profiles, head group hydration, and lipid tail order parameter. Additionally, the simulation of PE lipid and mixed PE bilayers had attracted a great deal of attention in order to get a further understanding about the mechanism of hydrogen bonding of PE and to identify the changes of the membrane properties. Damodaran *et al.* ⁽⁶⁵⁾ applied a MD simulation to investigate the water structure around DMPC and dilauroyl-phosphatidylethanolamine (DLPE) head groups. Another MD simulation was applied by Murzyn *et al.* ⁽⁶⁶⁾ to examine the properties of a bilayer built of palmitoyl-oleoyl-phosphatidylethanolamine (POPE) and palmitoyl-oleoyl-phosphatidylglycerol (POPG). They were able to identify specific interaction including hydrogen bonds between lipids, water bridges, and lipid water hydrogen bonds in addition to the examination of the affinity of interaction of PE towards PG. Furthermore, Shi *et al.* ⁽⁶⁷⁾ used a coarse grained model with MD simulation to examine phase separation in binary mixed lipid bilayers of DPPC and DPPE lipids.

The behaviour of the cardiolipin bilayers was studied using the coarse grained model and atomistic molecular dynamic simulations. Dahlberg *et al.* ^(68, 69) modelled the nature of the phases formed by CL derivatives at both neutral and low pH and presented new aspects for

the mechanism of conversion from lamellar (bilayer phase) to non-lamellar forms (hexagonal forms).

1.1.5 Lipids with cholesterol (experimental and simulation studies)

It is well known that cholesterol causes important changes in the physical properties of membranes. It reduces the passive permeability and increases the mechanical strength of membranes and affects the transition temperature. Cholesterol/phospholipid mole ratios vary from values approaching 1 for plasma membranes to values closer to 0.3 for membranes of intracellular organelles ⁽⁷⁰⁾. However, based on data from a variety of physical techniques, it has been concluded that ideal packing occurred at a mole ratio of cholesterol/phospholipid of 0.5 or 33 mol % which is approximately 4 fatty acyl chains/cholesterol molecule ⁽⁷⁰⁾. Several experimental and theoretical studies are reported on the lipid-cholesterol interactions. For example, Ipsen *et al.* ⁽⁷¹⁾ constructed the phase equilibria in the PC/cholesterol system using thermodynamic and microscopic interaction model. Vist *et al.* ⁽⁷²⁾ used the DSC and ²H NMR spectroscopy to determine the phase boundaries of DPPC/cholesterol system. McMullen *et al.* ⁽⁷³⁾ investigated the effect of cholesterol on the thermotropic phase behaviour and they proposed a complete phase diagram of DPPC/cholesterol using the high sensitivity DSC.

Furthermore, McIntosh *et al.* ⁽⁷⁴⁾ used X ray diffraction methods to probe the effect of cholesterol on the structure of phosphatidylcholine bilayers by comparing electron density profiles and hydrocarbon chain packing parameters for phosphatidylcholine in the gel and liquid crystalline states with and without cholesterol. Lippert *et al.* ⁽⁷⁵⁾ used Raman spectroscopy to see the influence of the cholesterol on the conformational changes in dipalmitoyl-lecithin multilayers. In addition, Todd *et al.* ⁽⁷⁶⁾ studied the effect of increasing concentration of cholesterol on the thermotropic behaviour of a homologous series of linear saturated phosphatidylcholine by using DSC. They found that cholesterol stabilizes the gel phase of short chains PC and destabilizes the PC with long chains.

Moreover, Almeida *et al.* ⁽⁷⁷⁾ investigated the phase diagram of DMPC/cholesterol using fluorescence recovery after photobleaching showing the formation of liquid ordered phase which shares the characteristics of liquid crystalline and gel phases (Figure 7). The liquid ordered phase (Lo) exhibits hydrocarbon chains with a highly ordered structure and fast translational diffusion. In contrast, the two other phases possess either fast translational diffusion (the liquid crystalline phase) or a highly ordered structure (the gel phase). The

liquid ordered phase is considered of particular interest since it is proposed to be more representative of plasma membrane organization.

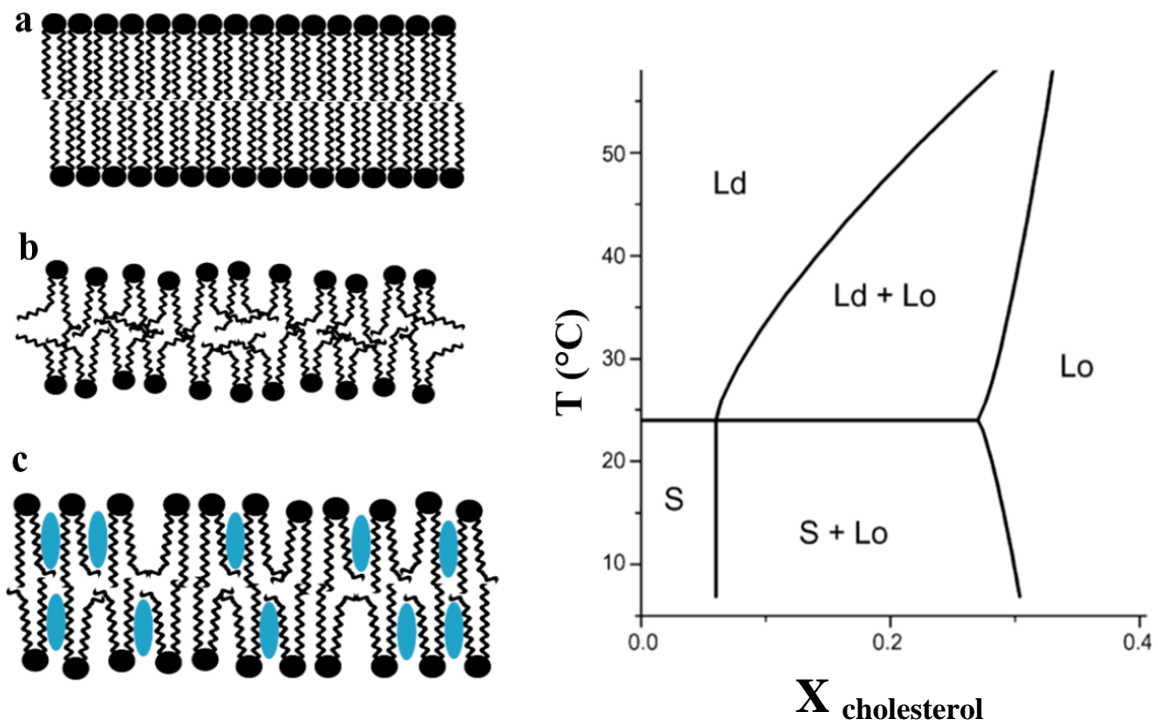


Figure 7. Models of the phospholipid bilayer (left) with gel phase (a), liquid crystalline phase (b) and liquid ordered phase (c). Blue ellipses are cholesterol molecules. The temperature-composition phase diagram for DMPC/cholesterol (right) with S, Ld, Lo representing gel, liquid disordered and liquid ordered phases respectively. The lines correspond to the phases boundaries between different phases and the horizontal line is where the main phase transition occurs ^(77, 78).

Furthermore, De Meyer *et al.* ⁽⁷⁹⁾ applied a mesoscopic water-lipid-cholesterol model to examine the phase diagram of DMPC/cholesterol by using dissipative particle dynamics. The main advantage of this model is that it predicts many of the different phases that have been observed experimentally. In addition, it explained the condensation effect where the area per lipid decreases more than one would expect from ideal mixing. This condensation effect is maximal near the main phase transition as can be seen clearly in Figure 8.

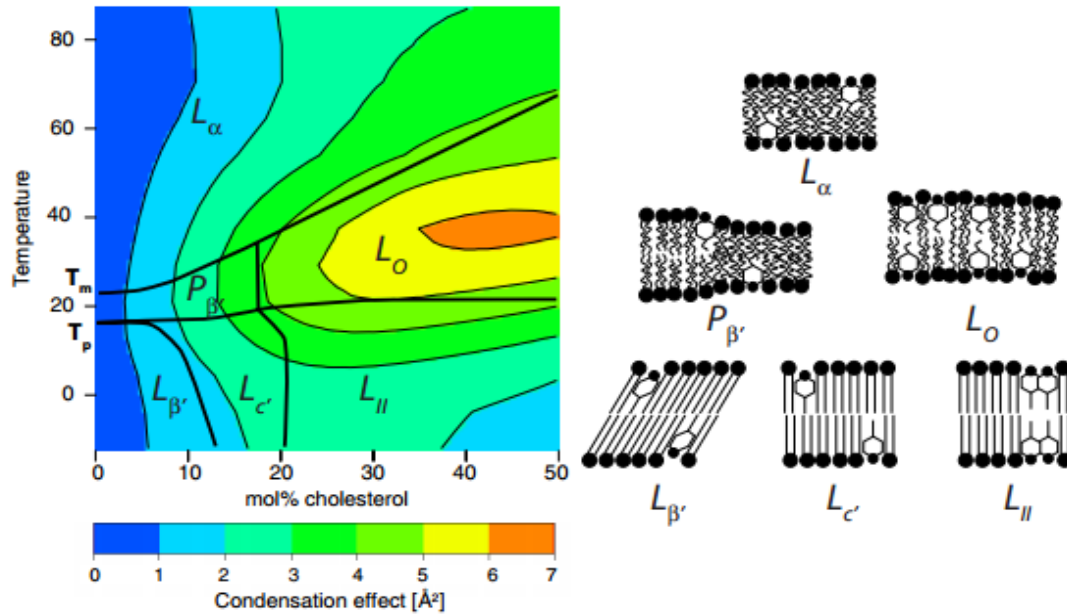


Figure 8. The computed phase diagram of DMPC lipid as function of cholesterol and temperature (left). The color gives the condensation effect and the lines indicate the phase boundaries of the different phases. Schematic representation of different phases (right), L_{α} lipids in the liquid phase; $P_{\beta'}$ ripple phase; $L_{\beta'}$ gel phase with tilted lipid chains; $L_{c'}$ gel phase with lipid chains not tilted; L_{II} gel phase similar to $L_{c'}$ containing small cholesterol clusters; L_o liquid-ordered phase ⁽⁷⁹⁾.

Concerning the PE/cholesterol mixtures, Paré *et al.* ⁽⁸⁰⁾ examined the influence of cholesterol on phosphatidylethanolamine polymorphisms using ^2H NMR and infrared spectroscopic investigation and proposed a temperature-composition diagram for POPE/cholesterol. This study revealed that cholesterol induces the formation of liquid ordered phase similar to what have been observed before for PC/cholesterol systems. Todd *et al.* ⁽⁸¹⁾ analyzed the effect of cholesterol on the thermotropic phase behaviour and organization of a homologous series of linear saturated phosphatidylethanolamine bilayers using DSC, FTIR spectroscopy and ^{31}P NMR. Epanand *et al.* ⁽⁸²⁾ described the phase transition behaviour of phosphatidylethanolamine by cholesterol and oxysterols using DSC studies. They probed the effect of cholesterol on the bilayer to hexagonal phase transition temperature of POPE and dielaidoyl-phosphatidylethanolamine (DEPE). In addition, Blume *et al.* ⁽⁸³⁾ determined the thermotropic behaviour of PE/cholesterol mixtures using DSC and they found that incorporation of cholesterol downshifted the gel to liquid phase transition temperature of phosphatidylethanolamine.

As compared to PC/cholesterol and PE/cholesterol, for which many data are available, very little is known about CL/cholesterol interaction. Gally *et al.* ⁽⁸⁴⁾ used steady state and time resolved fluorescence anisotropy to see the effect of cholesterol on the acyl chain order and dynamics of the cardiolipin membranes in the liquid crystalline state. Boggs *et al.* ⁽⁸⁵⁾ applied electron spin resonance spectroscopy to investigate the structural characteristics of lipids as cardiolipin in the presence of cholesterol. In addition, Lu *et al.* ⁽⁸⁶⁾ studied the effect of cholesterol on the phase behaviour and polymorphisms of cardiolipin liposomes using freeze fracture electron microscope.

1.2 Liposomes

Liposomes are vesicles formed of a lipid bilayer enclosing an aqueous compartment at the center. The polar head groups are exposed toward the outer and the inner aqueous media protecting the hydrophobic part from the polar environment (Figure 9). Liposomes were first produced in England by Bangham *et al.* ⁽⁸⁷⁾ and they have attracted a great deal of attention because of their importance in the pharmaceutical field. Liposomes were studied using different techniques to investigate the role of lipid composition/distribution and factors such as temperature, pH, ionic strength on the membrane stability and permeability ^(88, 89).

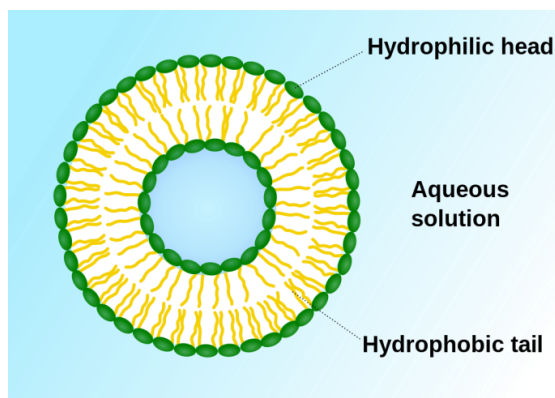


Figure 9. Schematic drawing of liposome structure.

Liposomes are classified according to two criteria: the size of the vesicle and the number of the lamella (Figure 10):

- (i) Small unilamellar vesicles (SUV): 20–100 nm;
- (ii) Large unilamellar vesicles (LUV): >100 nm;
- (iii) Giant unilamellar vesicles (GUV): >1000 nm;
- (v) Multilamellar vesicles (MLV): >500 nm.

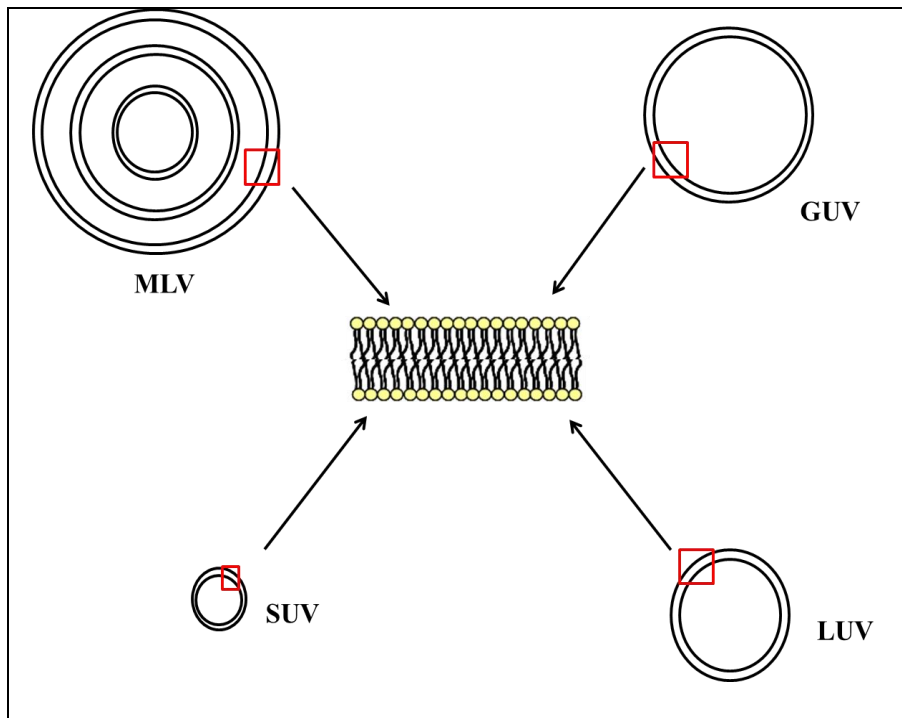


Figure 10. Illustration of liposomes of different size and number of lamellae.

As seen in Figure 10, the multilamellar vesicle is made up of several phospholipid bilayers whereas the unilamellar is formed of a single phospholipid bilayer. The number of lamella is usually obtained using ^{31}P -NMR^(90, 91) and it is considered of particular importance since it affects the encapsulation efficiency and the flowing rate of the encapsulated material.

The size and type of liposome depends on the method of preparation which in turn is selected according to the targeted research objective. For instance, small unilamellar vesicles are produced from the disruptions of multilamellar vesicles by sonication. Whereas large unilamellar vesicles are obtained by reverse-phase evaporation followed by extrusion. These LUV vesicles are the most used for drug delivery⁽⁹²⁾ and for studying membrane proteins by forming proteoliposomes⁽⁹³⁾. On the other hand, giant unilamellar vesicles are produced by electroformation or microinjection and multilamellar vesicles by shaking the lipid film in the aqueous solution.

The size and distribution of liposomes are usually obtained using dynamic light scattering (DLS) (also known as photo-correlation spectroscopy), size exclusion chromatography (SEC) and a variety of microscopic techniques^(94, 95).

1.2.1 Liposomes stability on solid surfaces

The big challenge with studying liposomes is to keep them stable on the surface of crystals without subsequent rupture. This depends on the interactions between vesicles and solid substrates. For example, liposomes do not directly adsorb on hydrophobic surface because of their hydrophilic head groups and as a result the liposomes rupture to allow the contact between hydrophobic tails and the surface according to the mechanism shown in Figure 11 (96, 97).

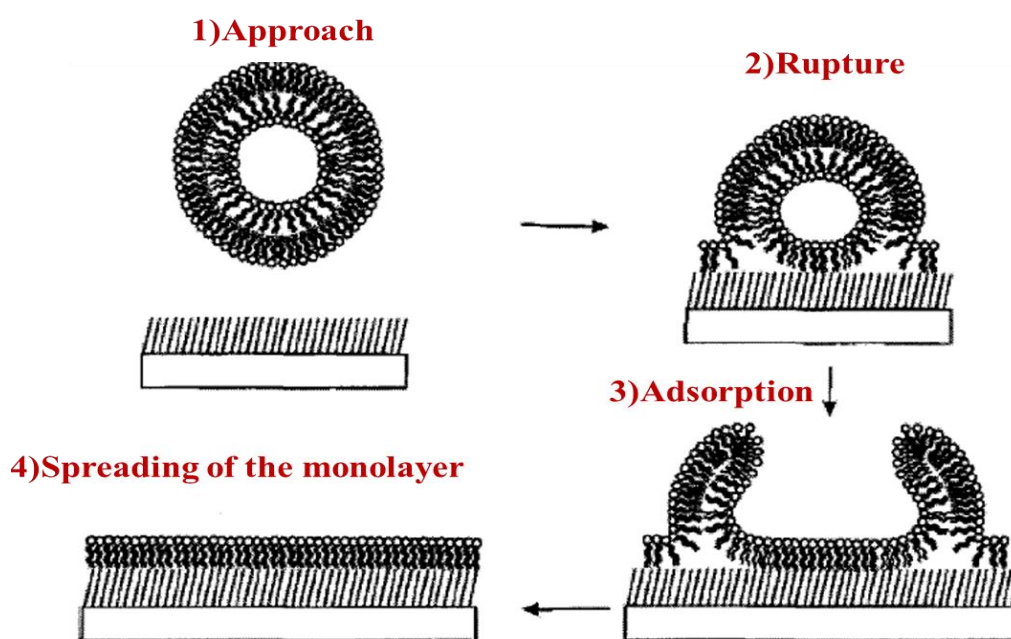


Figure 11. A proposed mechanism for liposomes adsorption on hydrophobic surfaces (96, 97).

A considerable amount of studies focused on the morphology of vesicles on solid surfaces. Sofou *et al.* (98) studied the behaviour of phospholipid vesicles on glass, gold and modified gold with chemisorbed acetyl-cysteine by using fluorescence microscopy. They found that the best substrate for adhesion of intact vesicle is the acetyl-cysteine modified gold surface. Jung *et al.* (99) used atomic force microscope to investigate the performance of liposomes from three different preparation methods and they noticed that the liposomes with thiol groups remained intact. Jiang *et al.* (100) used the attenuated total reflection FTIR spectroscopy on zinc selenide crystal coated with TiO₂ to study the structure of liposome membranes.

In addition, Reimhult *et al.* (88) used the quartz crystal microbalance (QCM) to probe the stability of EPC liposomes on different surfaces. They observed that vesicles remain intact on

oxidized gold, oxidized platinum and TiO_2 surfaces whereas on SiO_2 and Si_3N_4 , the vesicles are intact at low coverage followed by bilayer transformation at a critical coverage (Figure 12). Furthermore, Reimhult *et al.* ⁽¹⁰¹⁾ measured the kinetics of vesicle adsorption on gold surface and vesicle to bilayer transformation on SiO_2 using QCM and surface plasmon resonance.

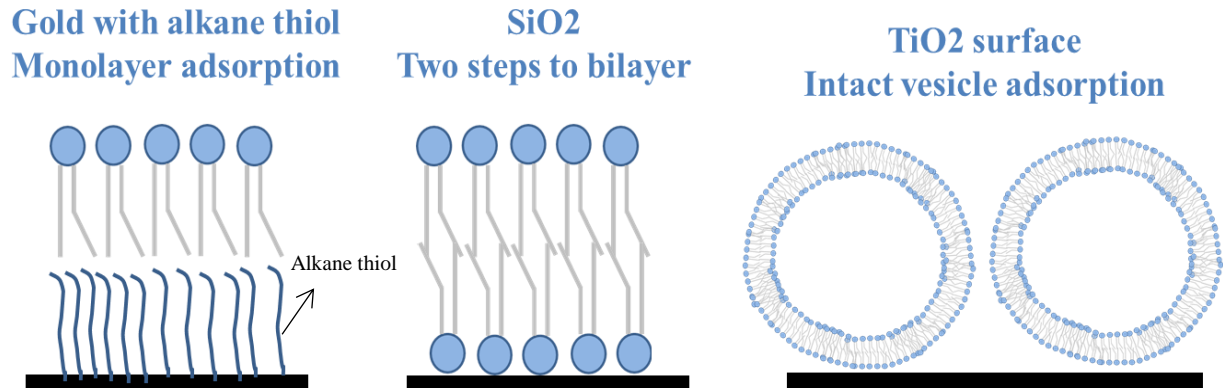


Figure 12. The interaction between liposomes and solid surface can produce monolayer, bilayer and vesicle.

1.2.2 pH sensitive liposomes

pH sensitive liposomes are lipid compositions that can be destabilized when the external pH is changed. They are mainly used in pharmaceutical fields where certain drugs are incorporated in these liposomes and the release is triggered by changing the pH (Figure 13). There exist different classes of pH sensitive liposomes based on the mechanism of triggering pH sensitivity ^(89, 102). The most intensively studied involved polymorphic lipids such as phosphatidylethanolamine with an acidic amphiphile that acts as a stabilizer at neutral pH.



Figure 13. Schematic drawing of the release of pH sensitive liposomes after pH change.

- **DOPE/CHEMS liposomes**

Most reported pH sensitive liposomes are made up of DOPE lipid which has a small head group and occupies a small volume as compared to its hydrocarbon chain part (Figure 14C). It exhibits conical shape geometry and tends to form a non-bilayer structure. In order to form a bilayer structure, it requires the presence of complementary molecules to fill the spaces between the head groups of DOPE. The weakly acidic amphiphile cholesteryl hemisuccinate (CHEMS) is used as the complementary molecule and it confers stability to the DOPE bilayer at physiological pH (Figures 14A, 14B) ⁽¹⁰³⁻¹⁰⁷⁾.

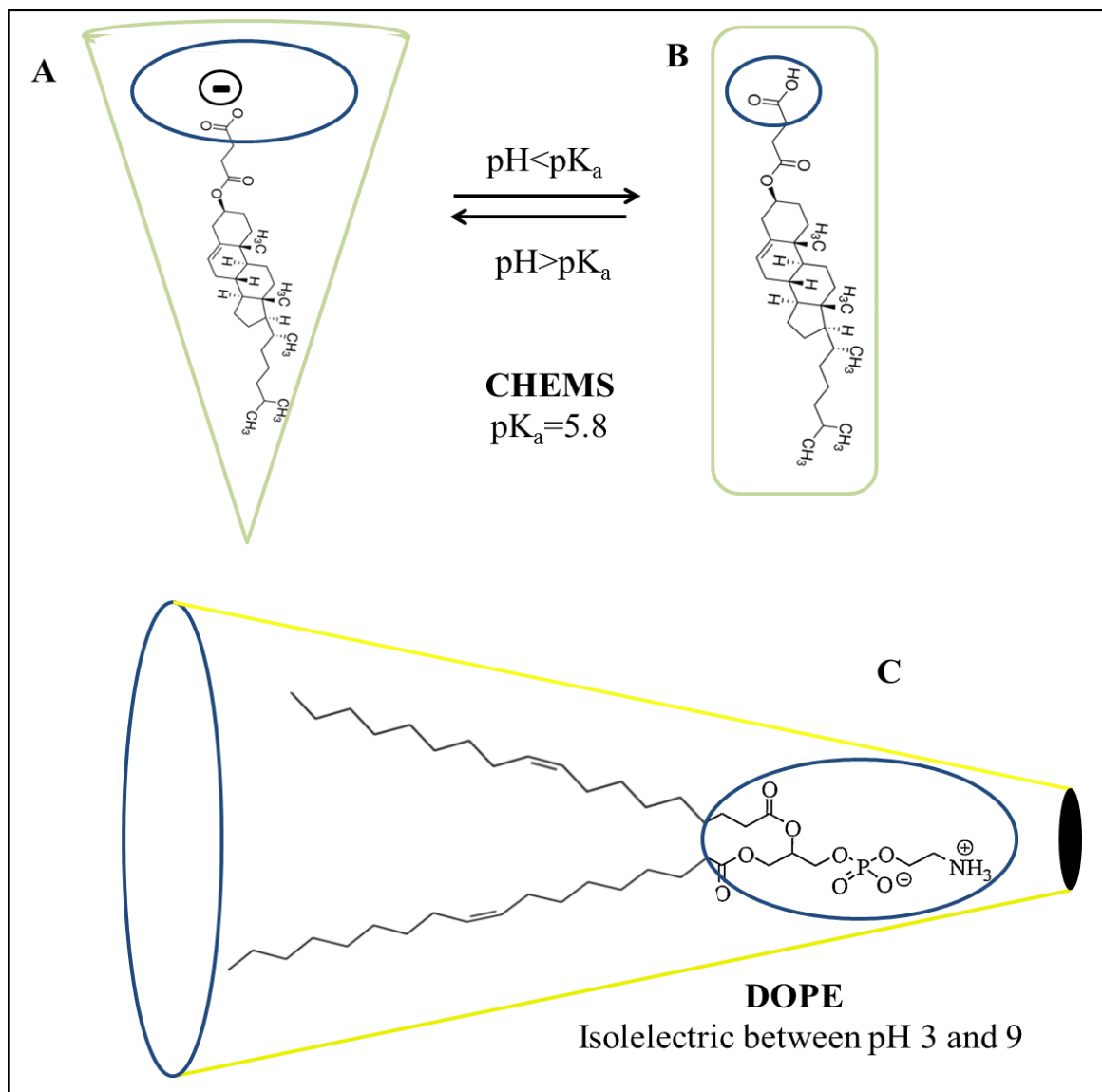


Figure 14. Main constituents of pH sensitive liposomes and their structural representation: cholesteryl hemisuccinate (CHEMS) in deprotonated and natural forms (A and B) and DOPE lipid (C).

The DOPE/CHEMS liposomes are stable at physiological pH (pH 7.4) but acidic conditions trigger the protonation of the carboxylic group of the amphiphile reducing their stabilizing

effect. Thus these liposomes undergo destabilization and acquire fusogenic properties leading to the release of their contents.

The choice of the amphiphilic stabilizer as well as its molar percentage with respect to the PE content is determined according to the desired properties of the liposomes. For example, Sudimack *et al.* ⁽¹⁰⁸⁾ reported the design and evaluation of pH sensitive liposomes based on the use of oleyl alcohol (OAlc) as the membrane destabilizing component and the results indicated that pH sensitive liposomes based on OAlc are promising for membrane impermeable therapeutic agents.

Simoës *et al.* ⁽¹⁰⁹⁾ incorporated a low percentage of polyethylene glycol conjugated lipid into pH sensitive liposomes in order to enhance the circulation times of these liposomes in the blood stream. Zignani *et al.* ⁽¹¹⁰⁾ reported the introduction of N-isopropylacrylamide (NIPA) copolymers in liposomal membranes and the results showed that the addition of pH sensitive copolymers of NIPA represents a promising strategy for improving liposomal drug delivery. In addition, Liu *et al.* ⁽¹⁰⁵⁾ designed pH sensitive liposomes from DOPE and dipalmitoyl-succinylglycerol (DPSG) and they found that they have prolonged circulation times thus making them significant drug carriers.

1.3 Role of lipids in proteins

Membrane proteins are responsible for many functions carried out by the membrane. They act as transporters, channels, sensors and receptors ⁽¹¹¹⁻¹¹³⁾. Their amounts and types differ from one membrane to another and they are associated with the lipid bilayer in different forms. The transmembrane type can anchor the lipid bilayer through their hydrophobic regions to be embedded inside it whereas their hydrophilic regions extend into outside the bilayer. On the other hand, the peripheral proteins are weakly bound to the membrane through non covalent interactions with other membrane proteins without spanning the lipid bilayer.

Many membrane proteins require specific lipids for folding ⁽¹¹⁴⁾, thermal stability ⁽¹¹⁵⁾, transporter function ⁽¹¹⁶⁾, supercomplexes formation ⁽¹¹⁷⁾, structural integrity and their oligomeric state ^(24, 118). However, the molecular details of the protein/lipid interactions, their dynamics and the general principles underlying these interactions are poorly understood. A wealth of biochemical and biophysical studies explained the assigned role of phospholipids in membrane proteins. Evidence emerged that lipids may play a crucial role in the catalytic

activity of the integral membrane proteins which are highly influenced by the lipid molecules that surround them ⁽¹¹⁹⁾. Furthermore, it was reported that lipids as phosphatidylglycerol are involved in the proton translocation across *E. coli* inner membranes ⁽¹²⁰⁾. Lipids also determine the topology of membrane proteins, where the interaction between the negatively charged phospholipids and positively charged amino acids affects the orientation of membrane proteins ⁽¹²¹⁾.

Hielscher *et al.* ^(122, 123) used FTIR spectroscopy to examine the effect of phospholipids on the function of the cytochrome *bc*₁ complex (see respiratory chain section 1.4). They found that delipidation leads to the loss of catalytic activity and the change of the redox properties of the hemes *b* and *c*. Chicco *et al.* ⁽¹²⁴⁾ explained the importance of cardiolipin in the structural and functional support to several proteins involved in mitochondrial bioenergetics. They indicated that the lack of cardiolipin is associated with the Barth syndrome. In addition, Hakizimana *et al.* ⁽¹²⁵⁾ examined the importance of phosphatidylethanolamine lipid on the activity of a multidrug transporter Lmrp and they revealed the contribution of just the hydrophilic part of the lipid to the function of the membrane protein. Bertero *et al.* ⁽¹²⁶⁾ reported a specific interaction of the anionic lipid phosphatidylglycerol with the nitrate reductase A. This protein builds a specific binding pocket for the lipid made up of all three subunits of the reductase.

Furthermore, the role of lipids in the NADH ubiquinone oxidoreductase (see section 1.4.1) was examined by Sazanov *et al.* ⁽¹²⁷⁾. They found that lipids play important role in the stabilization and the crystallization of the protein. Shinzawa-Itoh *et al.* ⁽¹²⁸⁾ revealed that the functional form of the mitochondrial enzyme from bovine heart contains 8 PC, 16 CL, 23 PE and 8 PG per molecule of complex I.

1.4 The respiratory chain

The production of nucleotide adenosine triphosphate (ATP) is considered of particular importance because it is the main energy unit of the living cell. The synthesis is catalyzed by ATP synthase protein which is a part of the respiratory chain. The mechanism correlating the energy generating electron transfer to the production of ATP by ATPase was described by Mitchell *et al.* ⁽¹²⁹⁾ where they proposed that the energy from the electron transfer is coupled to proton pumping within the respiratory complexes. The protons then flow back along their gradient and through the ATP synthase, which uses this energy to produce ATP. This process is called oxidative phosphorylation and it takes place in the inner membrane of mitochondria of eukaryotes and in the plasma membrane of photosynthetic bacteria. Figure 15 shows a

schematic representation of the bacterial respiratory chain. It includes five complexes; each has its own characteristics and functions.

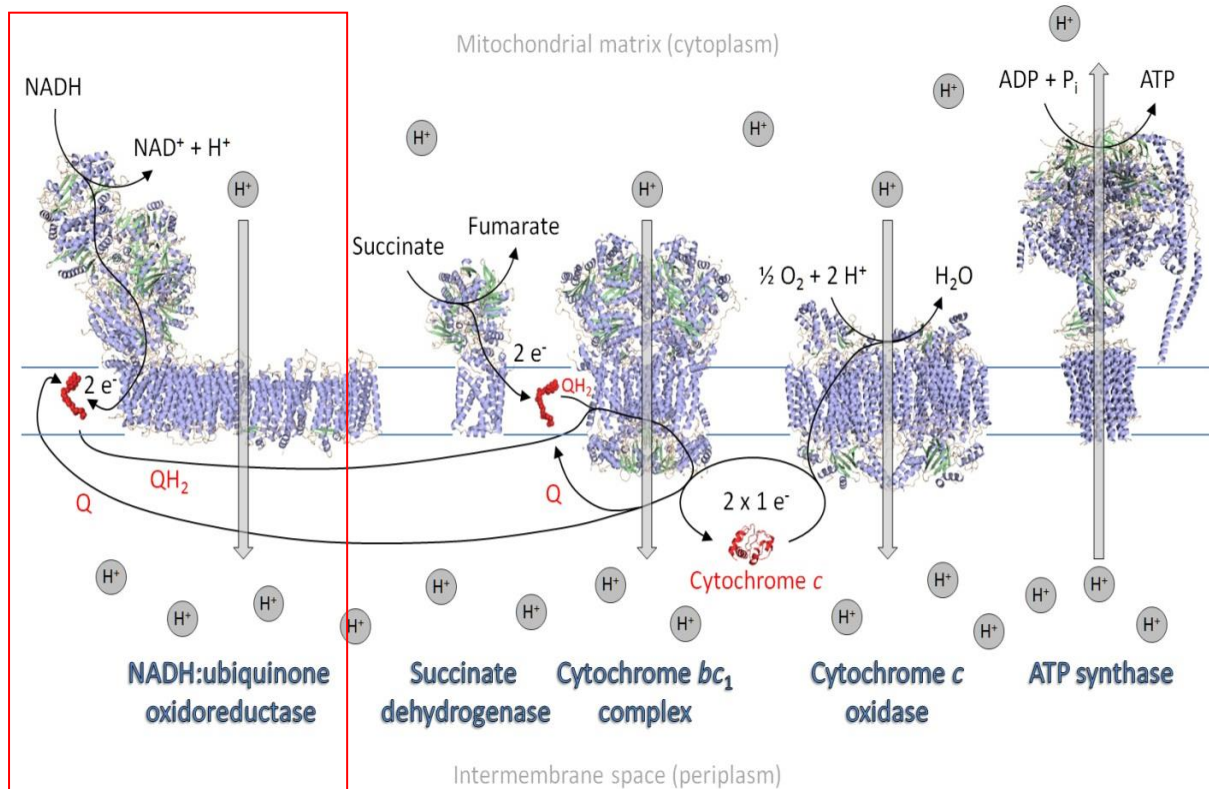
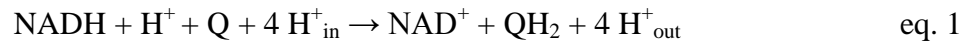


Figure 15. Representative model of the respiratory chain. From left to right: NADH:ubiquinone oxidoreductase from *Thermus thermophilus* (PDB:4HEA), Succinate dehydrogenase (quinone) from *Sus scrofa* (PDB:3AEF); Cytochrome bc₁ complex from *Bos taurus* (PDB:2A06); Cytochrome c oxidase from *Bos taurus* (PDB: 2DYR); ATP synthase - Central stalk from *Saccharomyces cerevisiae* (2WPD) and stator from *Bos taurus* (PDB: 2CLY); Cytochrome c from *Bos taurus* (PDB: 2B4Z). Adapted from Kriegel⁽¹³⁰⁾.

1.4.1 The NADH: ubiquinone oxidoreductase (complex I)

The proton pumping NADH ubiquinone oxidoreductase (also known as complex I) is the first enzyme of the respiratory chain of mitochondria and several bacteria (Figure 15). It is considered the main entry point of electrons into the respiratory chain. In addition, it has a central role in energy production providing around 40% of the proton motive force needed for the synthesis of ATP⁽¹³¹⁾. This protein is one of the main sources of reactive oxygen species (ROS) in mitochondria which can damage mitochondrial DNA and may be one of the causes of Parkinson's disease⁽¹³²⁾ and ageing⁽¹³³⁾.

This enzyme catalyzes the oxidation of NADH into NAD⁺ and the reduction of ubiquinone to ubiquinol accompanied by the translocation of four protons across the bacterial or inner mitochondrial membrane (equation 1) by a mechanism involving long conformational changes ⁽¹³⁴⁾. The process is not fully understood although a recent X ray structure ⁽¹³⁵⁾ revealed that it seems to function in a piston like manner.



(in = mitochondrial matrix/ cytoplasm ; out = intermembrane space / periplasm; Q refers to ubiquinone)

Complex I protein has been under study for more than 50 years since it was first isolated by Hatefi *et al.* ⁽¹³⁶⁾. Considerable progress has been made in order to investigate the structure and functional details of this protein ⁽¹³⁷⁻¹⁴¹⁾. However, the coupling mechanism between redox reaction and proton translocation within this large molecular machine is currently unknown.

- **Genes**

The genes coding for subunits of complex I in *E. coli* and *Rhodobacter capsulatus* are named *nuo* operons from NADH ubiquinone oxidoreductase. Whereas, in *Paracoccus denitrificans* and *Thermus thermophilus*, they are organized in the so called *nqo* operon from NADH quinone oxidoreductase. In general, 14 genes of the *nuo* operons from NuoA to NuoN or *nqo*1 to *nqo*14 code for the subunits in the complex I protein.

- **Structure**

Complex I is one of the largest membrane protein complexes known so far. It has L shaped structure constituted of a peripheral part (hydrophilic) that is connected to a hydrophobic part (Figure 16). This hydrophilic arm protrudes into the mitochondrial matrix or the bacterial cytoplasm whereas the hydrophobic part is embedded in the membrane ^(131, 142). The mitochondrial enzyme consists of 45 subunits with a mass of 1 MDa ⁽¹⁴³⁾. In comparison the prokaryotic enzyme is simpler, it consists of 14 subunits of mass 0.5 MDa. All the subunits of complex I presented in the membrane arm and the peripheral part are encoded by mitochondrial and nuclear DNA respectively. According to the homology between the mitochondrial and bacterial form of complex I protein, the bacterial enzyme is considered as a minimal model of complex I ^(144, 145).

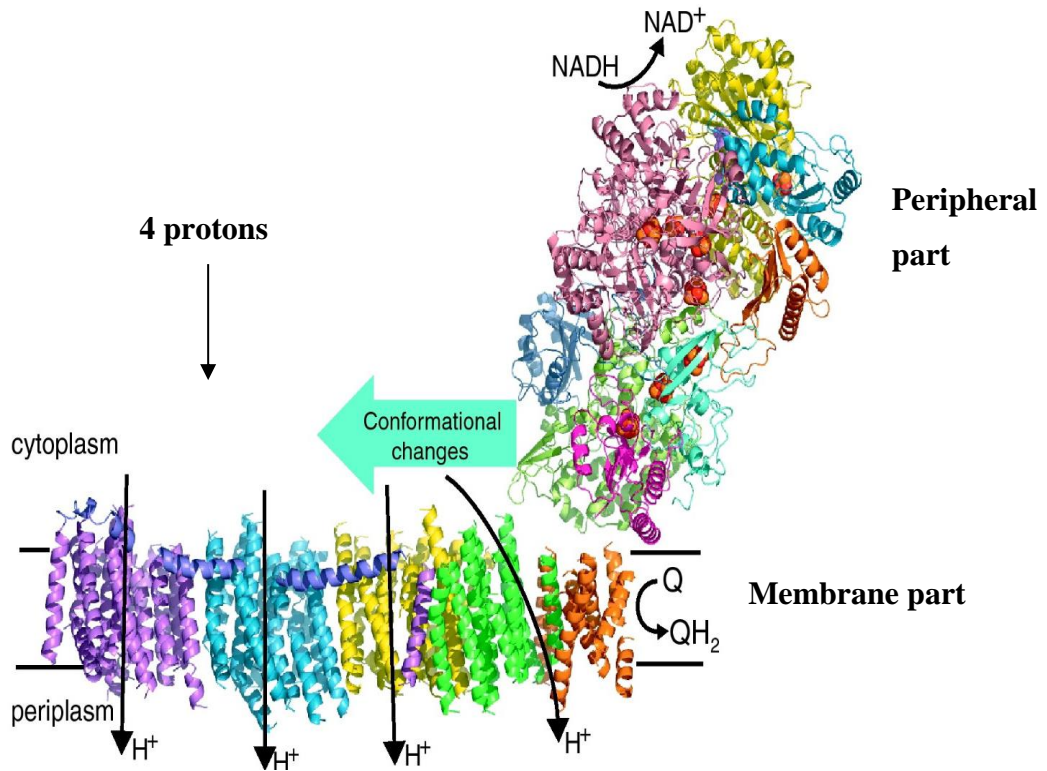


Figure 16. Schematic representation of complex I from *T. thermophilus*. Adapted from Sazanov *et al.* ⁽¹³⁵⁾ (PDB: 4HEA).

The membrane arm is about 180 Å long whereas the peripheral arm is about 130 Å and it extends into the cytoplasm ⁽¹⁴⁶⁾. The hydrophilic part is made up of seven subunits: NuoE, F, G, B, C, D, I and the membrane part contains the other 7 subunits NuoL, M, N, J, H, K and A. So far, no cofactor has been detected in the membrane part. This part is mainly involved in the proton pumping mechanism and quinone binding. In comparison, the peripheral part contains all the known cofactors (active sites) of complex I. There is a non-covalently bound Flavin Mononucleotide (FMN) and a series of binuclear and tetranuclear iron sulfur clusters. Depending on the organism, the number of iron sulfur clusters detected in the peripheral part varies between eight to ten, seven of which are involved in the electron transfer pathway among all the studied species ⁽¹⁴⁷⁾ and the others are needed for the structural stabilization of the protein. In *E. coli* and *T. thermophilus*, there exists seven tetranuclear clusters [4Fe-4S], named N2, N3, N4, N5, N6a, N6b and N7 and two binuclear Fe-S clusters [2Fe-2S], named N1a and N1b (Table 4).

Table 4. Nomenclature of the 14 core subunits of bacterial complex I with their bound cofactors and proposed function of the subunit ^(148, 149).

Enzyme domain	<i>T. Thermophilus</i>	<i>E. coli</i>	Proposed function
Hydrophilic arm	Nqo3	NuoG	N1b[2Fe-2S], N4,N5,N7[4Fe-4S]
	Nqo1	NuoF	FMN, N3[4Fe-4S] NADH binding
	Nqo4	NuoD	Quinone binding
	Nqo5	NuoC	Quinone binding
	Nqo2	NuoE	N1a[2Fe-2S]
	Nqo6	NuoB	N2[4Fe-4S]
	Nqo9	NuoI	N6a, N6b[4Fe-4S]
Membrane arm	Nqo15		Unique to <i>T.thermophilus</i>
	Nqo8	NuoH	Quinone binding
	Nqo14	NuoN	H ⁺ translocation
	Nqo7	NuoA	
	Nqo13	NuoM	H ⁺ translocation
	Nqo12	NuoL	H ⁺ translocation
	Nqo10	NuoK	H ⁺ translocation (involve NuoA/H/J/K)
	Nqo11	NuoJ	

The hydrophilic domain of complex I from *T. thermophilus* contains an additional subunit called Nqo15 (Table 4). This was demonstrated by the study of Barradaran *et al.* ⁽¹⁴⁶⁾ who resolved the structure of the entire bacterial complex I from *T. thermophilus* at 3.3 Å resolution using X ray crystallography. The crystal structure of the complex I from *E. coli* was first solved by Efremov *et al.* ⁽¹³⁵⁾ who reported the crystal structure of the membrane domain at 3.0 Å resolution. Furthermore, the structure of complex I from *Yarrowia lipolytica* (an aerobic yeast) was determined using three dimensional electron microscopy by Radermacher *et al.* ⁽¹⁵⁰⁾ where they showed some additional density outside the membrane.

In the context of this work, the NADH ubiquinone oxidoreductase from *E. coli* is studied because *E. coli* is the most well-known prokaryotic model organism. Additionally, it can be easily purified in high quantity, purity and be genetically modified. If not specified, the subunit nomenclature used hereafter thus refers to the *E. coli* enzyme.

- **Subunits**

The 14 core subunits of the NADH ubiquinone oxidoreductase of *E. coli* are arranged into three different categories (Figure 17).

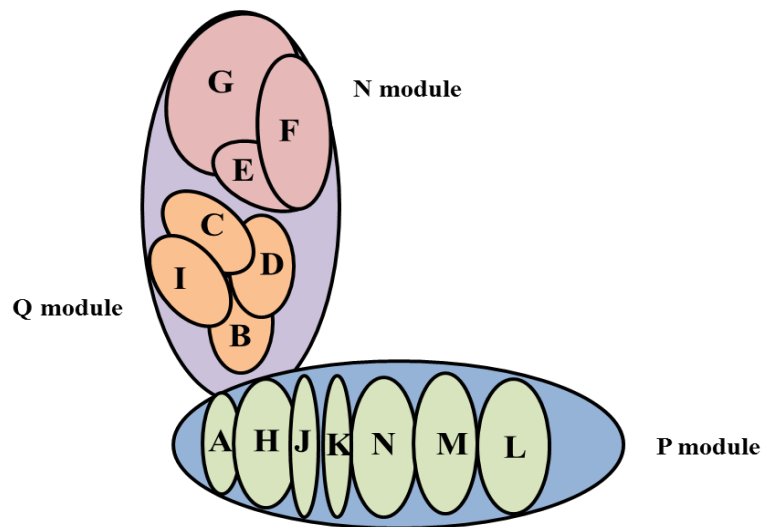


Figure 17. Schematic drawing of the different subunits of complex I.

- 1) Subunits NuoE, F, G called the N-module since they harbour the NADH oxidase activity.
- 2) Subunits NuoB, C, D, I termed the Q-module because it is the site of quinone reduction.
- 3) Subunits NuoA, J, K, L, M, N named the P-module since they host the proton pumping activity and they are close to the class of membrane potential Na^+/H^+ antiporters ⁽¹⁵¹⁾.

- **Iron sulfur clusters**

As indicated before, complex I protein contains a series of iron sulfur clusters which are considered as a major class of electron transfer cofactors. Interestingly beside their major role in the electron transfer, they provide structural support and stability for the protein. The Fe-S clusters of complex I are classified into binuclear and tetranuclear according to the number of Fe and S that compose them.

These clusters are usually bounded to the protein by amino acid side chains that have an additional coordination site usually cysteine and histidine residues⁽¹⁵²⁾. The tetranuclear iron sulfur cluster exhibits four short and eight long Fe-S^b bridge bonds as well as four terminal Fe-S^t stretching (Figure 18).

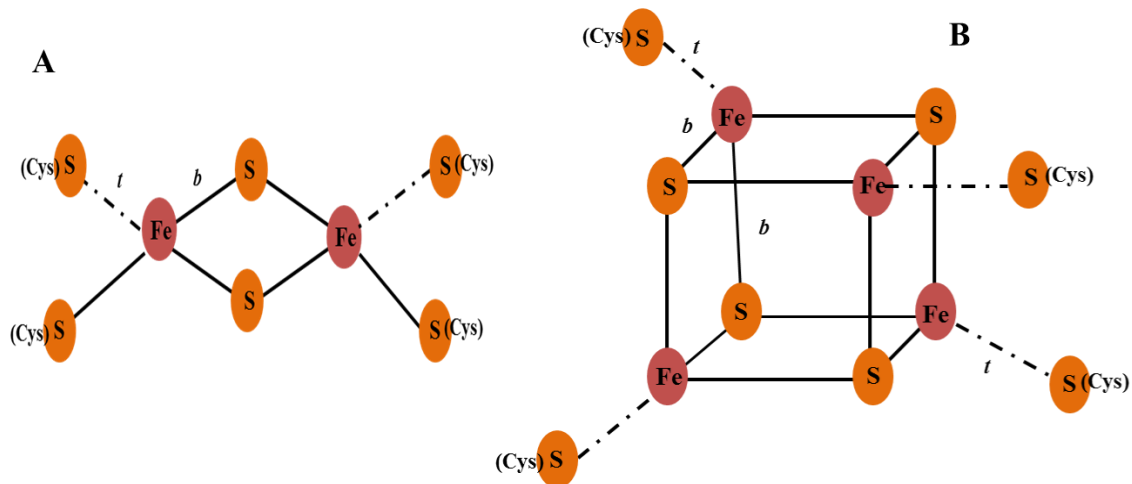


Figure 18. Representation of the binuclear (A) and tetranuclear (B) iron sulfur cluster structures.

- **Redox cofactors and electron transfer**

The electron transfer pathway involves a chain of redox active cofactors located in the peripheral part starting from the FMN to a series of iron sulfur clusters. This chain connects the NADH binding site which is located in the NuoF subunit with the ubiquinone binding site located 20-25 Å above the membrane surface^(153, 154), this means that the two sites are separated by around 100 Å.

The electrons from NADH are accepted by the first cofactor FMN via a hydride transfer⁽¹⁵³⁾ so it becomes FMNH₂. The two electrons are transferred one by one to the iron sulfur clusters which are one electron acceptors; thus one electron is transferred to the first cluster of the main chain (N3) while the other is donated to N1a. The midpoint potential of FMN/FMNH₂ is -320 mV^(155, 156) and that of cluster N3 is -270 mV⁽¹⁵⁷⁻¹⁶⁰⁾ versus standard hydrogen electrode (SHE). Therefore, the transfer of the first electron probably takes place to the N3 cluster and then it moves along the iron sulfur chain N1b, N4, N5, N6a, N6b to reach the N2 cluster. The resulting FMN/flavosemiquinone exhibits a -380 mV midpoint potential^(161, 162) causing the reduction of the cluster N1a of midpoint potential -330 mV. This mechanism was confirmed using the EPR spectroscopy which proposed that one electron from the reduced flavin is deposited on N1a⁽¹⁶¹⁾. The process of electron transfer between FMN and N2 occurs in a microsecond timescale^(155, 163) due to the geometrical arrangement of the cofactors and their favorable midpoint potentials. In turn, these electrons reduce the ubiquinone into ubiquinol in a two one electron steps by passing through a semiquinone (SQ) intermediate (Figure 19)⁽¹⁴⁹⁾.

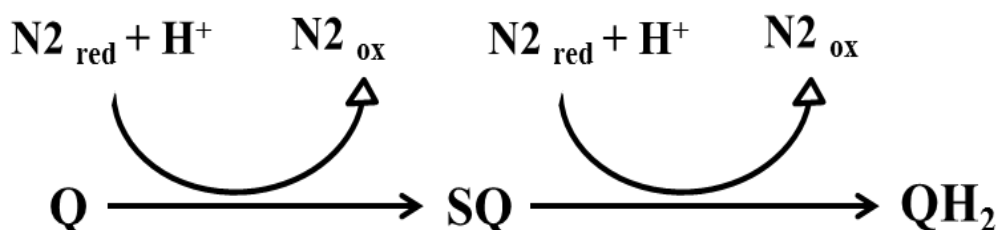


Figure 19. Scheme of the electron transfer between N2 and the UQ⁽¹⁶⁴⁾.

The distance between the different iron sulfur clusters is less than 14 Å indicating that all the clusters are found to be within efficient electron tunneling distance to their neighbors⁽¹⁶⁵⁾ and electrons can be transferred easily between the clusters. However, the distance between clusters N5 and N6a is on the limit (Figure 20), thus the electron transfer is explained by the involvement of the aromatic amino acids⁽¹⁶⁶⁾. In addition, the distance between clusters N3 and N4 is close to 16 Å so the electron transfer has necessarily to take the route via N1b. Moreover, the cluster N7 is not involved in electron transfer, N7 is found only in bacterial organisms and its presence confers stability to the structure^(167, 168).

The midpoint potentials of iron sulfur clusters N3, N1b, N4, N5, N6a are similar (range from -300 to -250 mV versus SHE), they are considered as isopotential clusters^(157, 167, 169). These potentials are close to the FMN favouring the rapid electron tunneling. N2 has the highest midpoint potential because of its highly polar environment as well as it is characterized by its unusual geometry and high flexibility. In addition, N2 plays a specific role in coupling the proton translocation to the electron transfer.

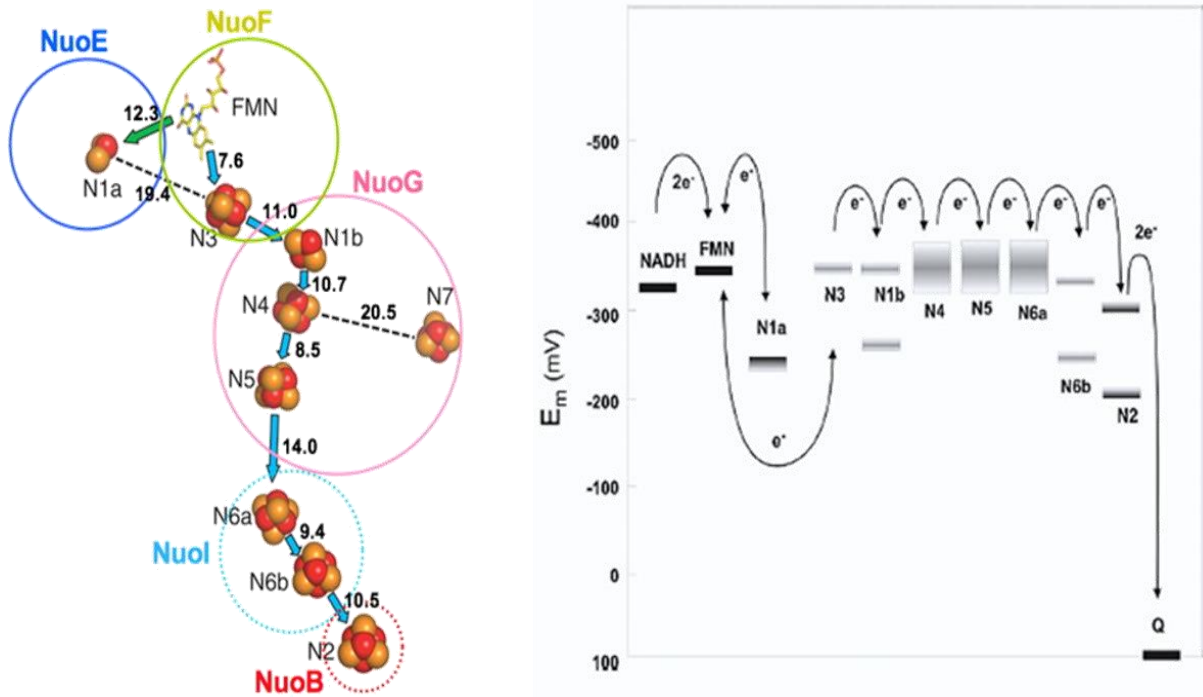


Figure 20. The chain of the iron sulfur clusters in the *T. thermophilus* complex I (left). Midpoint potential profile of the Fe-S clusters from *E. coli* complex I (right)^(139, 149). Edge-to-edge distances between adjacent clusters are given in Å, the blue arrows indicate the main electron path and the green one indicates the side path (left). The potentials are presented by bars (right).

- **Membrane part**

Subunits NuoL, M, N, A, J, K in the membrane part are involved in proton translocation. These subunits consist of 55 transmembrane helices (TM)⁽¹³⁵⁾ where the subunits NuoA and NuoK are predicted to contain three helices each, whereas NuoJ includes five (Figure 21). The subunits NuoN, M, L are separated from the peripheral arm by the 11-helix bundle formed by the NuoA, J, K subunits which are involved in coupling mechanism. These hydrophobic subunits are homologous to each other and to the Na⁺ or K⁺/H⁺ antiporter family^(170, 171). Subunit NuoL exhibits a carboxy-terminal extension, absent in NuoM and N, with

two TM helices predicted at the beginning and the end of the extension. This subunit is constituted by 15 TM helices holding a 110 Å long amphipathic helix (HL) extending along nearly the entire length of the membrane domain (Figure 21)⁽¹³⁵⁾. This helix is also found in the mitochondrial complex I and has a length of 60 Å. It exhibits an amphipathic nature, consistent with its position near the expected surface of the lipid bilayer. Helix HL stabilizes the complex and it is tightly anchored to NuoN, J, K, M and L⁽¹³⁵⁾.

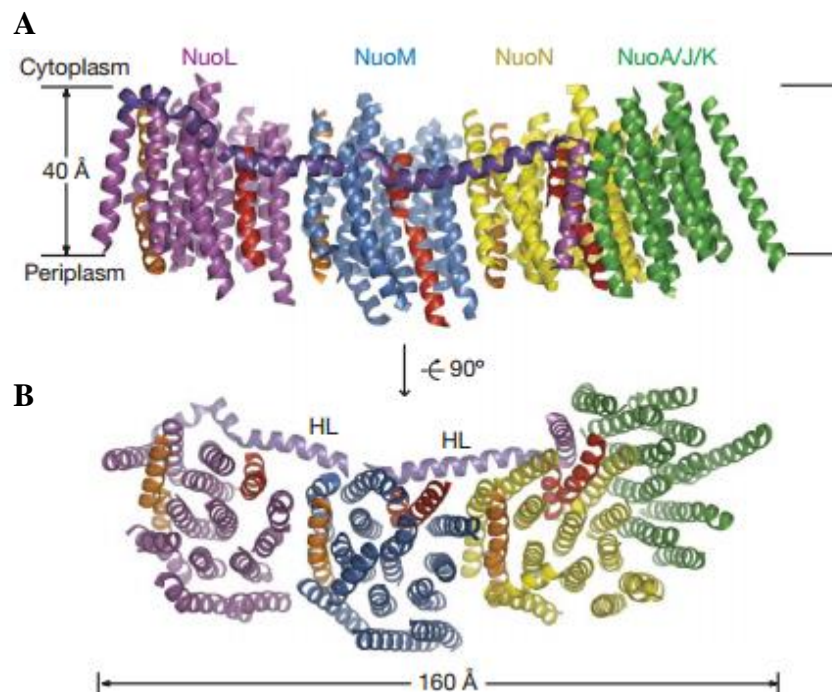


Figure 21. Representation of the different subunits of the membrane arm of *E. coli* complex I. Side view in the membrane plane (A). View from the periplasm into the membrane (B)⁽¹³⁵⁾.

- **Proton translocation**

The coupling process between electron transfer and proton pumping is still unknown. Two mechanisms were proposed: one is direct (redox-driven) and the other is indirect (conformation-driven)^(148, 172).

As mentioned above, the three major subunits NuoL, NuoM and NuoN, which are homologues to monovalent cation/H⁺ antiporters, are mainly involved in proton translocation. Three protons are translocated through these three channels however a fourth proton per cycle is translocated at the interface of NuoN, K and J. It has been proposed by Barradaran *et al.*⁽¹⁴⁶⁾ that the quinone binding causes conformational changes that are transmitted to the

long horizontal helix from the NuoL subunit. This helix acts as a kind of piston to transmit the redox energy released by the redox reaction and to drive the concerted long-range conformational changes in the four antiporters like domains, resulting in translocation of four protons per cycle. These conformational changes lead to an opening and closing of proton translocation channels in the antiporter like subunits NuoL, M and N in the oxidized and reduced state (Figure 22).

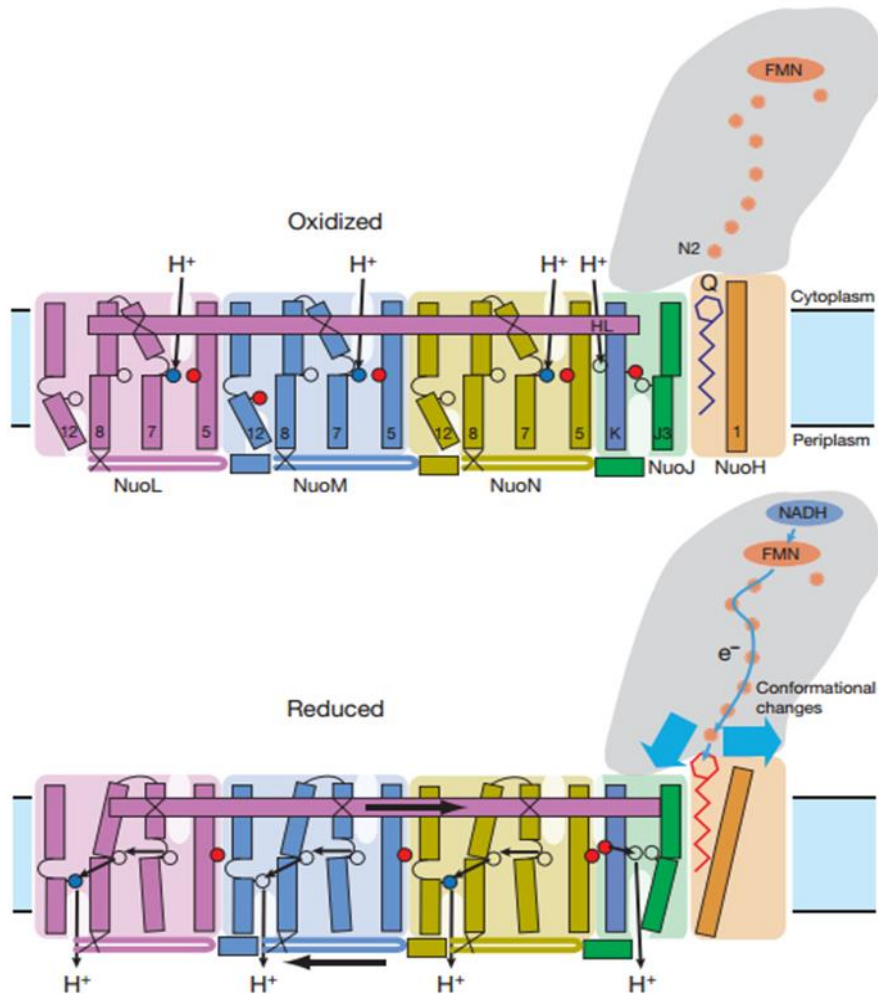


Figure 22. Schematic representation of the coupling between the electron transfer and proton transfer of *T. thermophilus* complex I. Adapted from Efremov *et al.* ⁽¹³⁵⁾.

The suggestion about the work of complex I as a conformation driven pump was determined by the work of Hellwig *et al.* ⁽¹⁵⁹⁾ using electrochemically induced FTIR spectroscopy. They found large reorganizations of the polypeptide backbone accompanied by the reaction of complex I which are relevant at the level of amide I and amide II indicating great

conformational changes. Furthermore, Efremov *et al.* ⁽¹³⁵⁾ proposed that a network of conserved polar residues are involved in the proton translocation mechanism. They suggested that lysines rather than carboxylate residues act as the main elements of the proton pump in the NuoL, NuoM and NuoN subunits. Friedrich *et al.* ⁽¹⁷³⁾ proposed that the protonation of acidic amino acids associated with the oxidation of N2 (studied by Hellwig *et al.* ⁽¹⁵⁹⁾) is the molecular switch involved in proton translocation and represents a conserved device for redox-driven mechanism.

1.4.2 NuoL mutants

NuoL seems to be involved in proton translocation. Steimle *et al.* ⁽¹⁷⁴⁾ investigated the electron transfer and proton translocation of complex I wild type protein and the complex I in a mutant with depleted NuoL subunit. They found that NuoL is involved in the translocation of two protons which is in contrast to the structural data where it was proposed that NuoL is involved in the translocation of one proton.

This NuoL subunit is characterized by the presence of the 110 Å long amphipathic helix which is anchored on the NuoL subunit by two additional TM helices. The deletion of this helix leads to reduced H^+/e^- stoichiometry demonstrating its functional importance in proton translocation. The question if specific amino acid residues of the horizontal helix are needed for the function was discussed by the work reported by Steimle *et al.* ⁽¹⁷⁵⁾, where the charged residues D542, D546 and D563 have been mutated. It was shown that the H^+/e^- stoichiometry varies significantly in the D563N indicating its functional role in the proton pumping in *E. coli* complex I.

1.4.3 Complex I and zinc

The redox reaction and the proton translocation in complex I protein can be inhibited. For instance, NADH-OH is a known inhibitor for the NADH binding site thus blocking the electron transfer. In addition, several inhibitors were reported for the quinone binding sites such as piericidin A and rotenone. However until now, only one inhibitor (Zn^{2+}) is known for proton pumping. Sharpley *et al.* and Link *et al.* ^(176, 177) showed that zinc perturbs the proton translocation and reduction of quinone in complexes I and III.

Schulte *et al.* ⁽¹⁷⁸⁾ used the zinc inhibition in complex I to elucidate the coupling between redox reaction and proton translocation processes (Figure 23). They found that blocking the

proton channels in the membrane part induces a partial block in the electron transfer in the peripheral arm. In addition they proved, using enzyme kinetics, that complex I exhibits at least two high affinity binding sites for Zn^{2+} . They also found that the interaction of Zn^{2+} with specific residues leads to small perturbation in the conformational changes using FTIR difference spectra of complex I in the absence and presence of zinc.

In conclusion, the proton translocation machinery appears to be particularly perturbed by the presence of zinc. However in order to get insight into the exact position where zinc binds to complex I, mutagenesis of conserved charged residues in the membrane arm is required.

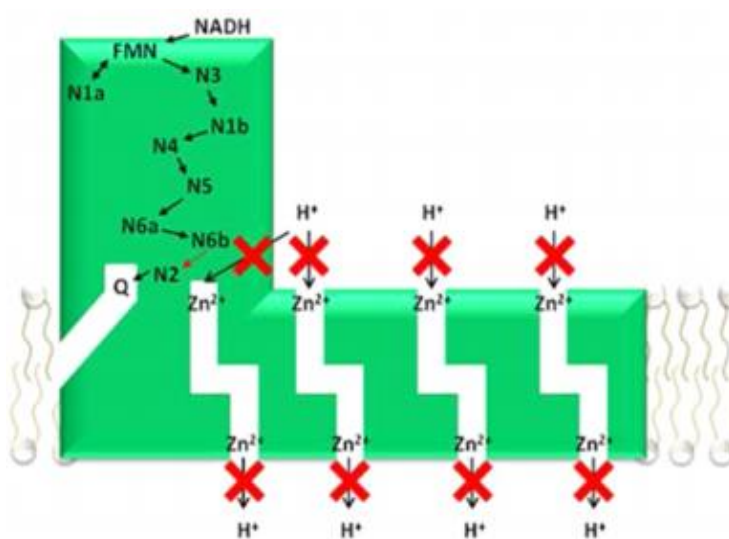


Figure 23. Representation of the inhibition of the proton translocation pathways in the membrane arm of complex I in the presence of zinc ⁽¹⁷⁸⁾.

1.4.4 Complex I and synthetic lipids (polymer)

The enzymatic activity of the respiratory complex I from bovine heart mitochondria is only maintained in the presence of lipids as cardiolipin, phosphatidylethanolamine and phosphatidylcholine as demonstrated by Sharpley *et al.* ⁽¹⁷⁹⁾. Previous studies performed in our laboratory suggested that lipids bind specifically to complex I ^(180, 181). The effect of lipids with different head groups and acyl chains on the complex I protein activity and function was estimated. The phospholipids present in *E. coli* have zwitterionic (PE) or anionic head groups (CL and PG) and they interact with the positively charged areas on the surface of the protein whereas the acyl chains interact with the nonpolar patches on the surface ⁽¹³⁰⁾.

Since complex I protein is not functional in the absence of lipids, potentially limiting its application. Thus the search for a certain material which has the ability to substitute the predicted molecular requirements of natural lipids attracted a great deal of attention. In this respect, amphiphilic copolymers are of great interest because of their distinct chemical properties. These properties can be designed by chemical synthesis such as the length of the hydrophobic part, the volume and charge of the hydrophilic part and the ratio between hydrophobic and hydrophilic domains. Thus, the participation of individual moieties of the polymer with the membrane proteins is revealed. Compared to natural lipids, polymers exhibit long term stability arising from the combination of chemical inertness and high mechanical stability making them favorable for technological applications.

Recently, Graff *et al.* ⁽¹⁸²⁾ determined the behaviour of complex I devoid of most of its endogenous lipids (delipidated) in a polymer media. They synthesized a library of various polymethyloxazoline-polymethylsiloxane-polymethyloxazoline (PMOXA-PDMS-PMOXA) (for chemical structure see appendix 1) followed by activity and EPR measurements. The activity was strongly influenced by the molar mass and the block length of the (PMOXA-PDMS-PMOXA) copolymers. Here, we attempted to see the effect of a (PMOXA-PDMS-PMOXA) copolymer of different ratio than studied before on the complex I activity.

1.5 Aims of the thesis

This project describes the application of infrared and Raman spectroscopies to study different kinds of natural and synthetic lipids and their interactions with proteins. The goals of the study are summarized by the following points.

1) Lipid-lipid interaction

- * Study pure lipids and mixtures of lipids with cholesterol in the mid and far infrared regions in order to investigate the role of cholesterol on the phase transition temperature and on hydrogen bonding behaviour.
- * Characterize phospholipid interactions between EPC and EPE in the far infrared domain below 600 cm^{-1} to probe the effect of the head group composition on the hydrogen bonding behavior and to show the potential use of the far IR spectroscopy for the study of lipids.
- * Study pH sensitive liposomes DOPE/CHEMS at different pH in order to get a better understanding about the interaction of the lipids within these liposomes.

2) Lipid-protein interaction

- * Investigate the effect of $\text{PMOXA}_{16}\text{-PDMS}_{72}\text{-PMOXA}_{16}$ copolymer (synthetic lipid) on the delipidated complex I protein using electrochemically-induced FTIR difference spectroscopy.

3) Complex I mutants

- * Study NuoL mutants using electrochemically induced FTIR difference spectroscopy to elucidate the proton translocation mechanism and to probe the inhibition of complex I mutants by Zn^{2+} .
- * Use Raman spectroscopy to study the metal-ligand vibrations of the Fe-S clusters in the low frequency region in NuoB mutants.

Chapter II

**Technical approach - characterization
techniques and sample preparation**

2 Characterization techniques and sample preparation

2.1 Introduction to spectroscopy

Spectroscopy is a method for the study of the interaction between electromagnetic radiation (EM) and matter. This electromagnetic radiation has a particle nature and each photon carry a quantum of energy (E) related to the frequency (ν) (equation 2) ^(181, 183).

$$E = h\nu \quad c = \lambda \cdot \nu \quad E = \frac{hc}{\lambda} \quad \text{eq. 2}$$

Where h is the Planck's constant (6.626×10^{-34} J.s), c is the speed of light (3×10^8 m.s⁻¹) and λ is the wavelength (nm).

Electromagnetic radiation exists as continuous and wide spectrum. It is typically classified by the wavelength region and include Microwave, Terahertz, Infrared, Visible, Ultraviolet, X-ray and Gamma spectroscopy (Figure 24).

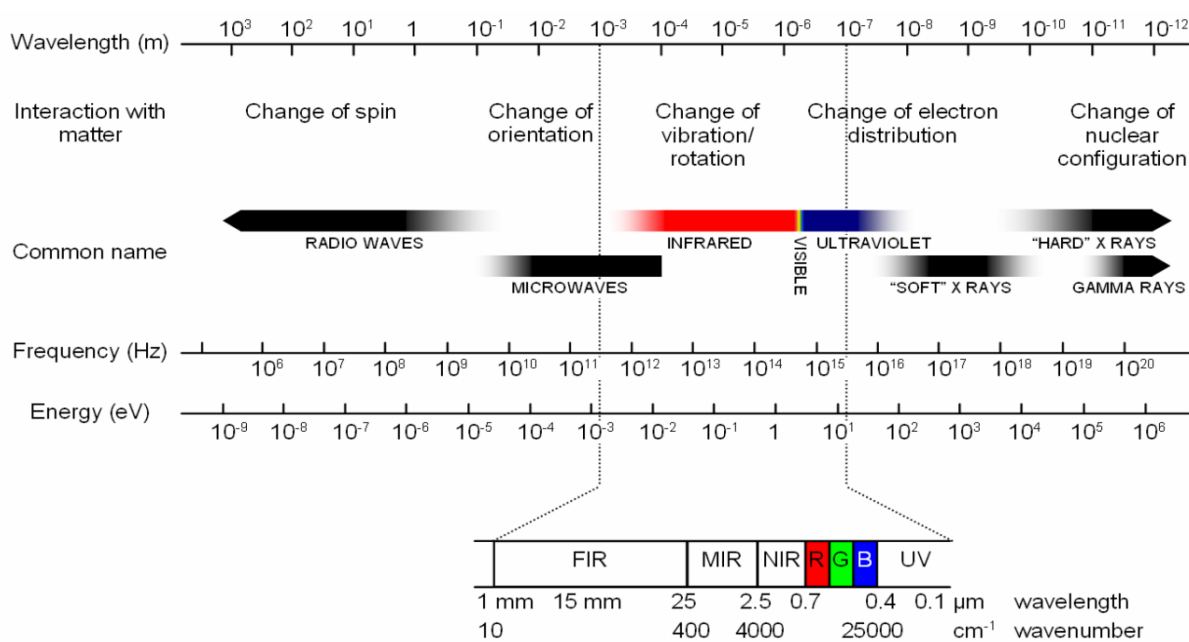


Figure 24. Representation of the electromagnetic spectrum as function of the wavelength (m), frequency (Hz) and energy (eV) ⁽¹⁸¹⁾.

The interaction between EM and the matter can produce different processes. For instance, high energy gamma rays change the nuclear configuration; microwave causes the change of orientation whereas radio waves change the spin. In this manuscript, infrared (mid and far),

UV-visible and Raman spectroscopies were applied in order to investigate the properties of lipids and proteins.

2.2 UV-visible spectroscopy

UV-visible spectroscopy uses the absorption of the UV-visible light by a molecule inducing the excitation of electrons from an occupied molecular orbital (n , σ , π) to an unoccupied molecular orbital (σ^* , π^*) of higher energy^(184, 185). Typically, the observed transitions are electronic transitions and they are detected between the near ultraviolet (200-400 nm) and the entire visible light range (400-800 nm).

In UV-visible spectroscopy, the absorption of a sample is measured by plotting the absorbance as function of wavelength λ . The absorption band is characterized by its maximum absorbance A , and its molar extinction coefficient ϵ and this is given by the Lambert-Beer's law that is applicable for monochromatic light and dilute solutions (Figure 25).

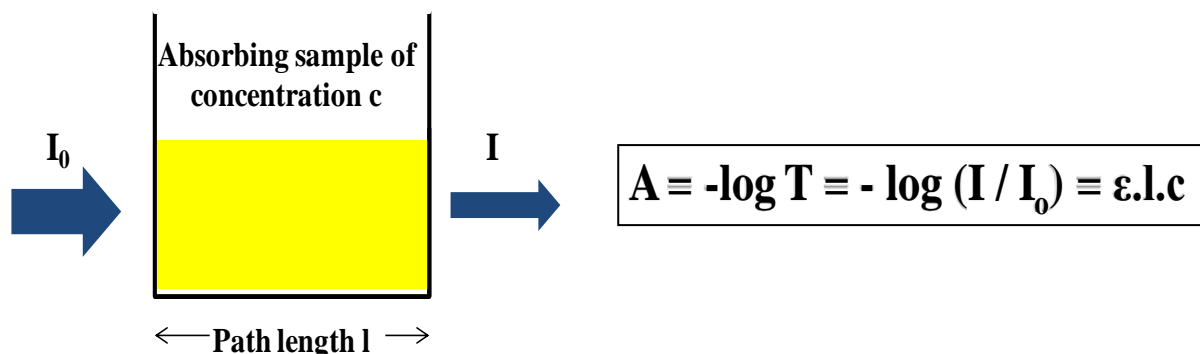


Figure 25. Lambert-Beer's Law; where A is the absorbance, I_0 is the intensity of the initial beam, I is the intensity of the transmitted light, ϵ is the molar extinction coefficient ($\text{mol}^{-1}.\text{L}.\text{cm}^{-1}$), l is the path length (cm), c is the molar concentration of the sample ($\text{mol}.\text{L}^{-1}$)⁽¹⁸⁶⁾.

This technique is mainly used for quantitative analysis *i.e* to determine the concentration of samples using Lambert-Beer's law. In addition, it has large sensibility with certain limits of detection (10^{-5} M) and precision with 1 to 5 % error.

UV-visible spectroscopy proved to be a powerful tool to investigate the properties of proteins containing hemes in order to distinguish between the different types of hemes and to see their individual contributions^(187, 188). UV-visible spectroscopy was used to measure the activity of

complex I protein by following the progressive diminution of the NADH-characteristic peak at 340 nm⁽¹⁸⁹⁾. Additionally, coupling UV-visible to electrochemistry was used to determine the redox properties of the following cofactors: FMN and the iron sulfur clusters of complex I protein^(190, 191). These cofactors have distinctive molar absorption coefficient at 450 and 525 nm. At 450 nm, FMN has a higher extinction coefficient ($\epsilon_{450 \text{ nm}} = 12.800 \text{ M}^{-1} \cdot \text{cm}^{-1}$) than iron sulfur clusters ($\epsilon_{450 \text{ nm}} = 4.100 \text{ M}^{-1} \cdot \text{cm}^{-1}$).

2.3 IR spectroscopy

Infrared spectroscopy is considered as one of the most important techniques used for the identification of compounds and for structural determination. The resulting spectrum represents a molecular fingerprint of the sample (no two molecular structures give the same infrared spectrum). One of the main advantages of IR is that a sample in any state (liquid, powder, or film) can be studied⁽¹⁹²⁾. The infrared radiation is found between the microwave region and the visible light (Figure 24) and it is divided into three main domains: the near infrared (13000-4000 cm^{-1}), the mid infrared (MIR) (4000-600 cm^{-1}) and the far infrared (FIR) (600-10 cm^{-1}).

- **Selection rules**

For an “infrared active” such as the case of a heteronuclear diatomic molecule, the electric dipole moment must change during the vibration as the bond contracts or expands (Figure 26). In contrast, a homonuclear diatomic molecule is “infrared inactive” because its dipole moment remains zero regardless of the bond length⁽¹⁹³⁾.

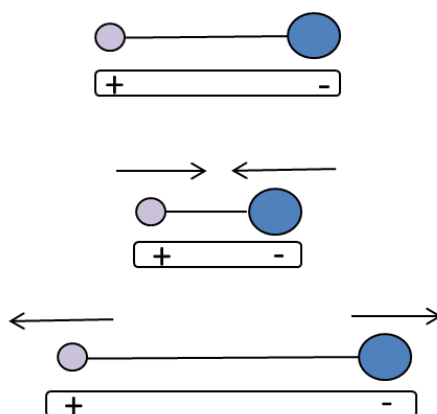


Figure 26. Change in the dipole moment of a heteronuclear diatomic molecule.

- **Normal modes of vibration**

The infrared spectroscopy technique is based on the absorption of infrared radiation by the molecule which results in changes of the vibrational or rotational modes of atomic bonds. For a linear and a non-linear molecule of N atoms, there exists $3N-5$ and $3N-6$ vibrational modes respectively (Table 5) ⁽¹⁹⁴⁾. For example H_2O , which is a non-linear molecule, has $3 \times 3 - 6 = 3$ degrees of vibrational freedom or modes.

Table 5. Degrees of freedom for linear and non-linear molecules ⁽¹⁹⁴⁾.

Types of degrees of freedom	Linear	Non-Linear
Translational	3	3
Rotational	2	3
Vibrational	$3N-5$	$3N-6$
Total	$3N$	$3N$

For a molecule composed of two atoms A and B, the vibration can be represented by the means of a harmonic oscillator. These two atoms are connected by chemical bond which is considered as a spring that obeys Hooke's law (Figure 27) ^(130, 195-197).



Figure 27. Scheme of a molecule composed of two atoms representing the harmonic oscillator.

The restoring force F (N) is needed to return the spring to its initial state and it is equal to

$$F = k.d \quad \text{eq. 3}$$

Where k is the force constant ($N.cm^{-1}$) which indicates the stiffness of the bond and d is the displacement of the spring in (cm). To express the frequency of this vibration and relate the reduced mass μ with the force constant, equation 4 is applied.

$$\nu = \frac{1}{2\pi} \sqrt{\frac{k}{\mu}} \quad \frac{1}{\mu} = \frac{1}{m_A} + \frac{1}{m_B} \quad \mu = \frac{m_A \cdot m_B}{m_A + m_B} \quad \text{eq. 4}$$

This equation is modified to calculate the wavenumber instead of frequency (equation 5).

$$\tilde{\nu} = \frac{\nu}{c} \quad \tilde{\nu} = \frac{1}{2\pi c} \sqrt{\frac{k}{\mu}} \quad \text{eq. 5}$$

From this relation, the wavenumber is inversely proportional to the reduced mass and proportional to k. This indicates that the single bond which has lower k value absorbs at lower frequency than double and triple bonds. Concerning the mass, the molecule with heavier atoms is lower in frequency than bonds involving hydrogen. μ is influenced by isotope labeling where the change in the mass induces an observable shift in the frequency (Table 6) whereas the bond strength k is modified upon interaction with different environments.

Table 6. The effect of isotope labelling on the vibrational frequencies of some groups ⁽¹⁸⁶⁾.

Bond	Vibrational Mode	Frequency (cm ⁻¹)
C–H; C– ² H (D)	$\nu(\text{C–H})$; $\nu(\text{C–}^2\text{H})$	3000; 2120
¹² C=O; ¹³ C=O	$\nu(^{12}\text{C=O})$; $\nu(^{13}\text{C=O})$	1700; 1650
N– ⁵⁶ Fe; N– ⁵⁴ Fe	$\nu(\text{N–}^{56}\text{Fe})$; $\nu(\text{N–}^{54}\text{Fe})$	350; 356
¹⁴ NH ₂ ; ¹⁵ NH ₂	$\nu(^{14}\text{NH}_2)$; $\nu(^{15}\text{NH}_2)$	3400; 3000

The normal modes of vibration can be classified based on two different criteria (Figure 28).

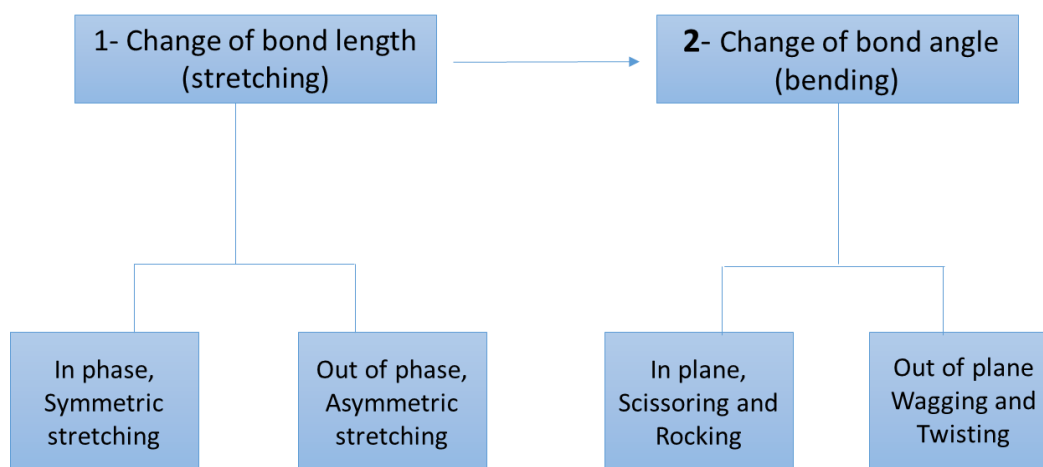


Figure 28. Different normal vibrational modes.

The typical vibrations of CH₂ atoms in a CH₂X₂ group (X can represent any other atom) are displayed in Figure 29. In general, the bending frequencies are lower than stretching frequencies since it is easier to bend a bond than to stretch or compress it. For instance, the CH₂ symmetric/asymmetric stretching and bending modes appear in the region 2800-3000 cm⁻¹ and 1000-1500 cm⁻¹ respectively. Other important features for infrared spectroscopy are the hydrogen bonding and conjugation that shift the vibration to lower frequencies.

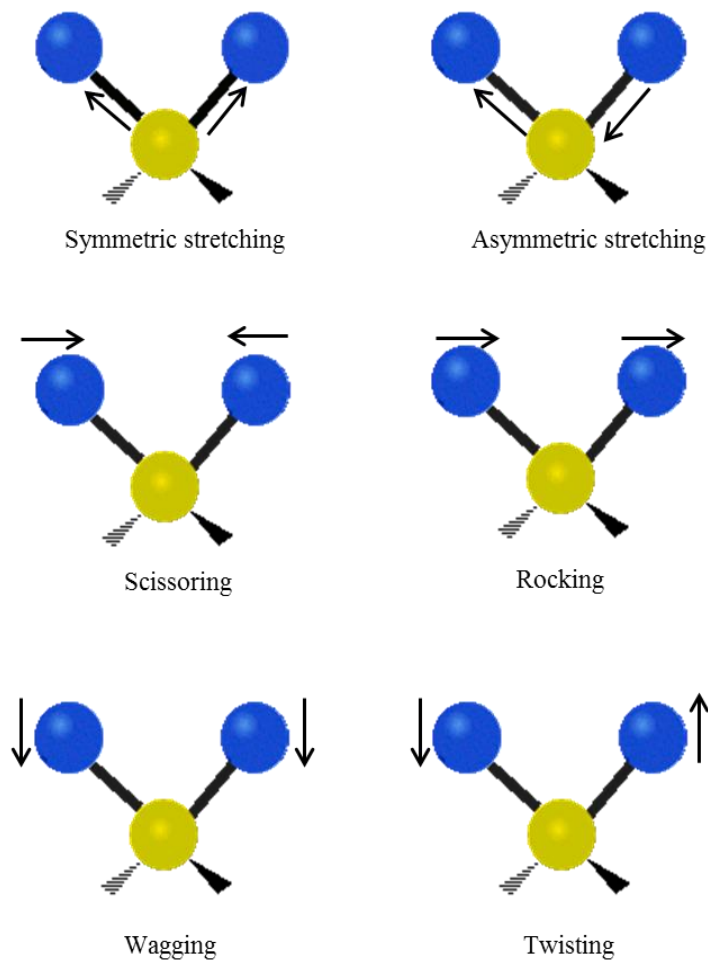


Figure 29. Stretching and bending vibrations of a tetrahedral carbon atom.

2.3.1 Fourier transform infrared spectroscopy (FTIR)

FTIR is the preferred method in infrared spectroscopy. FTIR instruments possess several advantages in comparison to dispersive instruments. The improvement of the signal to noise ratio per time unit leads to a higher quality spectrum. In addition, the ability of the mirror to move short distances quite rapidly makes it possible to obtain spectra on a millisecond timescale. Furthermore, FTIR is highly precise and accurate since a laser is controlling the movement of the mirror⁽¹⁹³⁾. This technique is based on the interference of the radiation between two beams giving an interferogram. It mainly consists of three parts: the detector, the interferometer and the IR light source. These parts differ according to the studied region of the infrared spectrum (Table 7)⁽¹⁹⁸⁾.

Table 7. Equipment used in the infrared measurement according to the different spectral range.

Source	MIR	FIR
Spectral range	4000 - 600 cm ⁻¹	600 - 50 cm ⁻¹
Source	Globar	Mercury vapor / synchrotron
Beam splitter	Potassium Bromide (KBr)	Silicon / Mylar
Detector	Liquid nitrogen mercury cadmium telluride (LNMCT)	Deuterated triglycine sulfate (DTGS) / Bolometer

- **Michelson interferometer**

The most common interferometer used in FTIR spectrometry is a Michelson interferometer⁽¹⁹⁹⁾. It consists of two perpendicularly oriented plane mirrors, one is fixed and the other is moving. The detection starts when an infrared light from the source hits the beam splitter, then half percentage of the light intensity is reflected on the movable mirror and the rest is transmitted on the fixed mirror. After that, the two beams are reflected back to the beam splitter to be combined. In the last step, the beam is divided again equally into two fractions; one is reflected back in the direction of the source while the second passes through the sample to the detector (Figure 30).

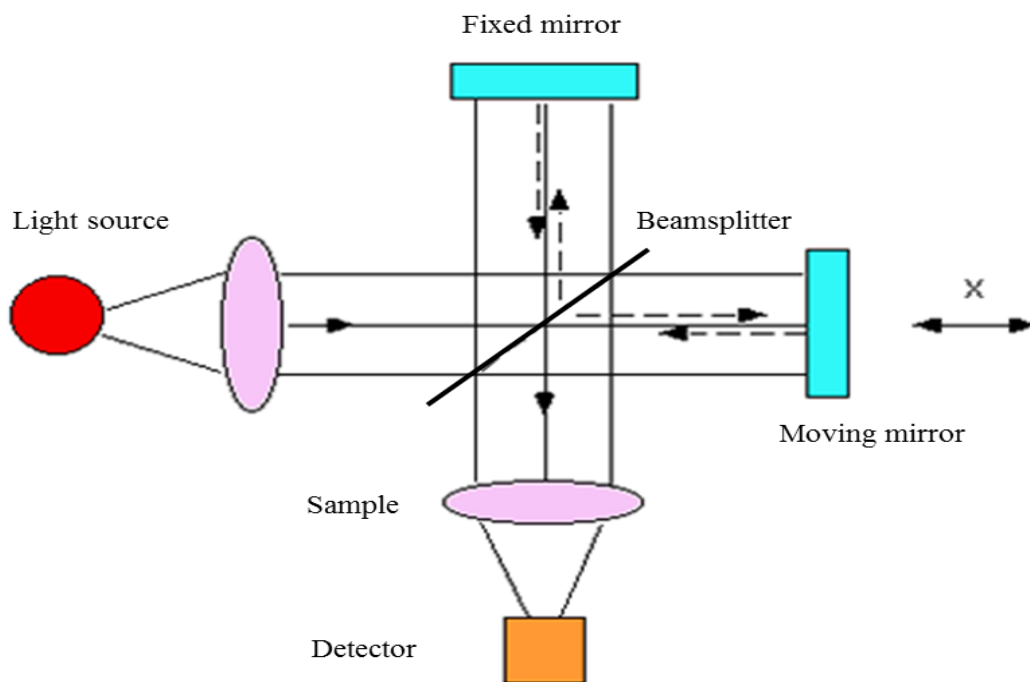


Figure 30. Schematic representation of the Michelson interferometer.

The movable mirror is the most important component of the interferometer and its velocity is controlled using a Helium-Neon (He-Ne) laser. Depending on the mirror position, the infrared radiation will be under constructive or destructive interference when it recombines at the beam splitter producing an interferogram plot (Figure 31). Finally, Fourier transformation is used to transform the interferogram into a spectrum given in wavenumber.

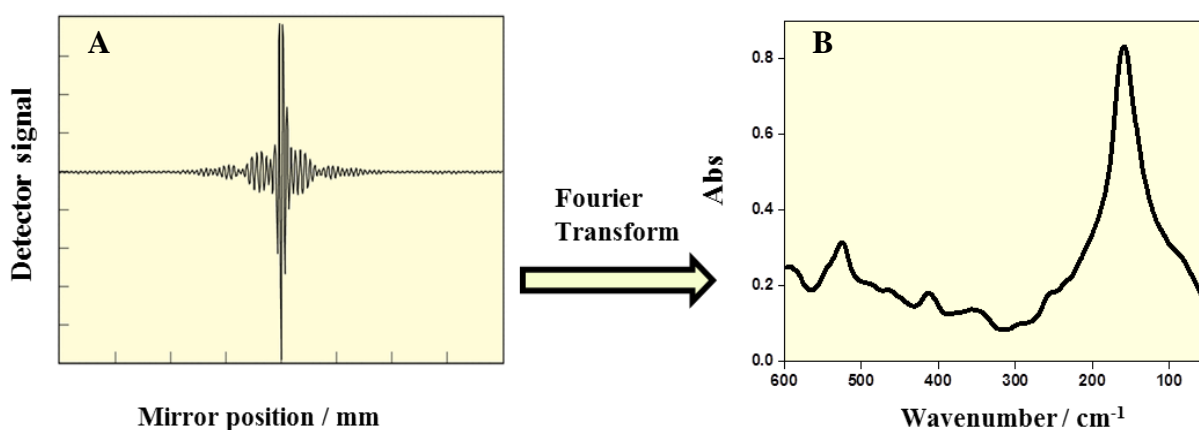


Figure 31. The interferogram (A) and its corresponding absorbance spectrum (B) obtained after Fourier transformation ⁽¹⁹⁵⁾.

The essential equations for Fourier transformation are as follows:

$$I(\delta) = \int_0^{\infty} B(\tilde{\nu}) \cos(2\pi\delta\tilde{\nu}) d\tilde{\nu} \quad \text{eq. 6}$$

$$B(\tilde{\nu}) = \int_{-\infty}^{+\infty} I(\delta) \cos(2\pi\delta\tilde{\nu}) d\delta \quad \text{eq. 7}$$

Where $\tilde{\nu}$ is the wavenumber (cm^{-1}), I is the intensity of the interferogram, δ is the optical path difference between the two beams and $B(\tilde{\nu})$ is the spectral power density. The first equation (eq. 6) describes the variation in intensity as a function of the difference in path length, which is an interference pattern. The second equation (eq. 7) shows the variation in intensity as a function of wavenumber. Each can be converted into the other by the mathematical method of Fourier transformation.

2.3.2 IR spectroscopy of proteins

Proteins are biological polymers constituted of monomeric units which are the amino acids (Figure 32) ⁽²⁰⁰⁾. There exist twenty different amino acids that are distinguished by the identity of the side chain group (R). These amino acids are linked together by an amide bond (peptide bond).

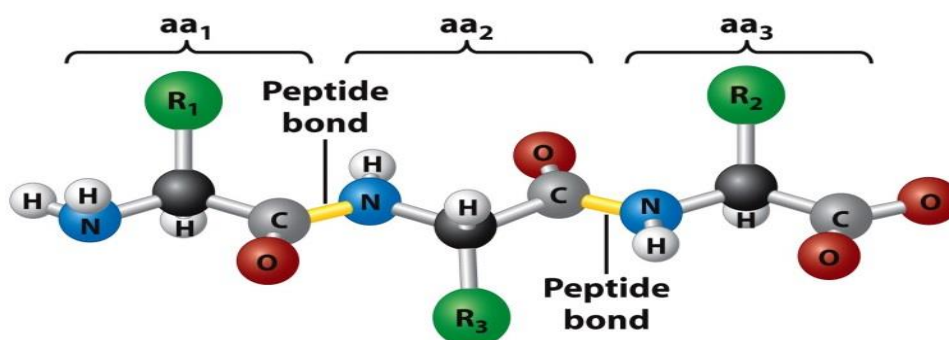


Figure 32. Linking of amino acid together by amide bond ⁽²⁰¹⁾.

Applying infrared spectroscopy to proteins is of great interest as every chemical bond in the protein is infrared active. Thus information about structure, ligands, cofactors ^(202, 203) and amino acid side chains will be provided ^(204, 205). Amide bands are the characteristic signals found in the infrared spectra of proteins and polypeptides. Their correlated vibrations are presented in Table 8.

Table 8. Amide vibrations, frequencies and description of the peptide backbone ^(206, 207).

Amide	Wavenumber (cm ⁻¹)	Vibrations
A	3500-3200	$\nu(\text{N-H})$, $\nu(\text{O-H})$
B	3200-3030	$\nu(\text{C-H})$
I	1700-1600	80% $\nu(\text{C=O})$, $\nu(\text{C-N})$, $\delta(\text{N-H})$ and $\delta(\text{C-CN})$
II	1590-1480	Coupled 60% $\delta(\text{N-H})$ with 40% $\nu(\text{C-N})$, Coupled $\delta(\text{C=O})$ and $\nu(\text{C-C})$
III	1400-1200	$\delta(\text{N-H})$, $\nu(\text{C-N})$, $\delta(\text{C=O})$ and $\nu(\text{C-C})$
IV	780-650	$\delta(\text{C=O})$ in-plane, $\nu(\text{C-C})$
V	600-540	$\delta(\text{C-N})$ torsion
VI	540-500	$\delta(\text{C=O})$ in-plane and out-of-plane (C-C-N) deformations
VII	290-250	$\delta(\text{N-H})$ out-of-plane

The amide I signal is the most studied spectral range in the protein infrared spectra and it originates mainly from the C=O stretching vibration, whereas amide II is associated mainly with N-H bending vibration coupled to C-N stretching. Since both amide I and amide II are involved in the hydrogen bonding interaction occurring between the different elements of the secondary structures (Figure 33), the exact position of the amide bands allows the determination of the secondary structure composition of the protein ⁽²⁰⁸⁾.

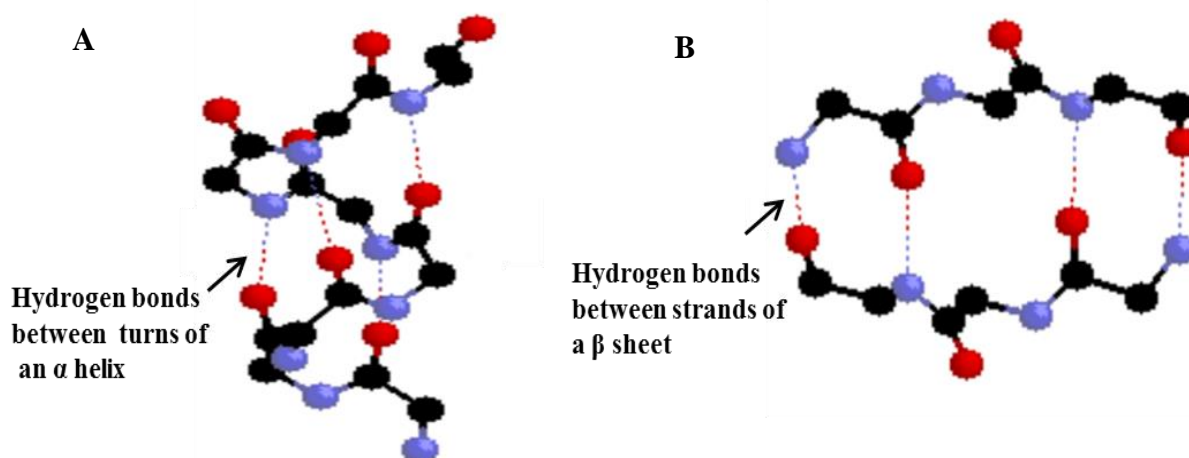


Figure 33. Representation of the different secondary structural elements: α helix (A), β sheet (B) ⁽²⁰⁰⁾. Carbon is black, oxygen is red and nitrogen is blue.

Previous studies done on proteins with known structures have been used to correlate the position of amide I to secondary structure content (Table 9).

Table 9. Assignment of protein secondary structural elements according to the amide I band ⁽²⁰⁶⁾.

H_2O (cm^{-1})	D_2O (cm^{-1})	Assignment
1624–1642	1624–1637	β -sheet
1648	1645	Random coils
1656	1653	α -helix
1663	1641	3_{10} -helix
1667–1685	1663–1671 / 1683–1689	β -turns
1691–1696	1675	β -sheet

The analysis of the secondary structure is based on the deconvolution of the amide I band. First, the amide I band is normalized and the baseline corrected before the second derivative is calculated. The negative peaks in the second derivative correspond to the secondary structure components. Using the position of these peaks, the origin program calculates the deconvolution (Figure 34). The relative percentage of each structure is calculated by integrating the area under each peak to the total area of the amide I band.

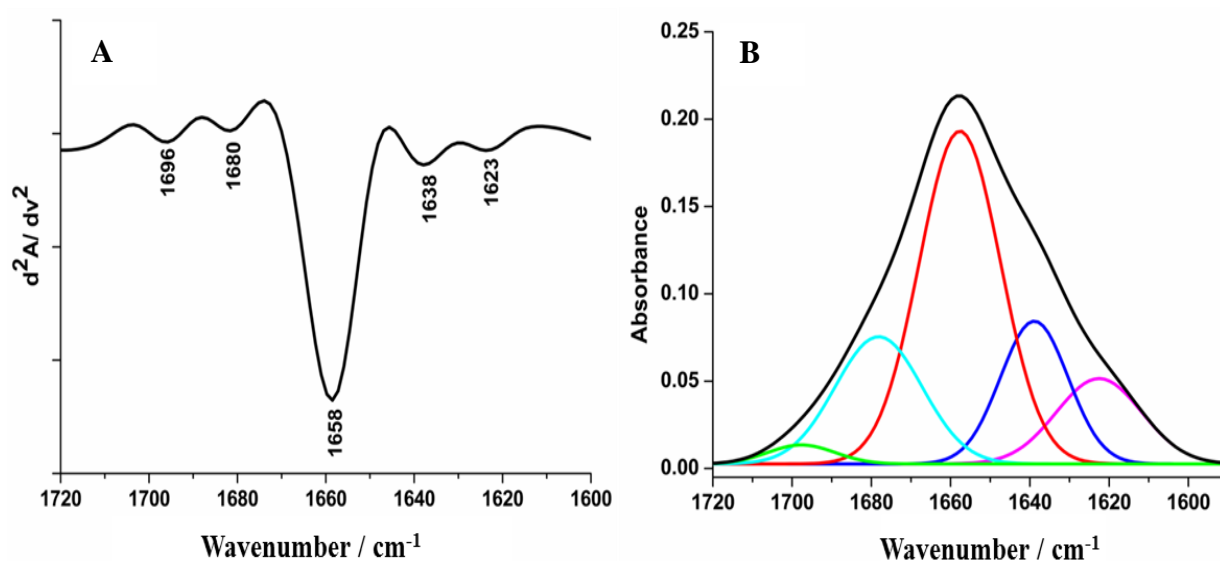


Figure 34. Amide I band second derivative (A) and secondary structure components (B).

2.3.3 Transmission mode

FTIR spectroscopy in transmission mode is obtained by placing the sample on an infrared transmitting window in the optical path of the spectrometer. This method allows studying samples in solution. The window is chosen according to the studied range. For instance, silicon or polyethylene windows are used for far infrared region whereas calcium fluoride (CaF_2) and barium fluoride (BaF_2) for mid infrared. Two different cell types are used in this thesis; the first one is the absorbance cell which is used to study the temperature dependence of lipids in the far infrared (Figure 35). The second cell using the transmission mode is called the optically transparent thin layer electrochemical cell (section 2.6.3).

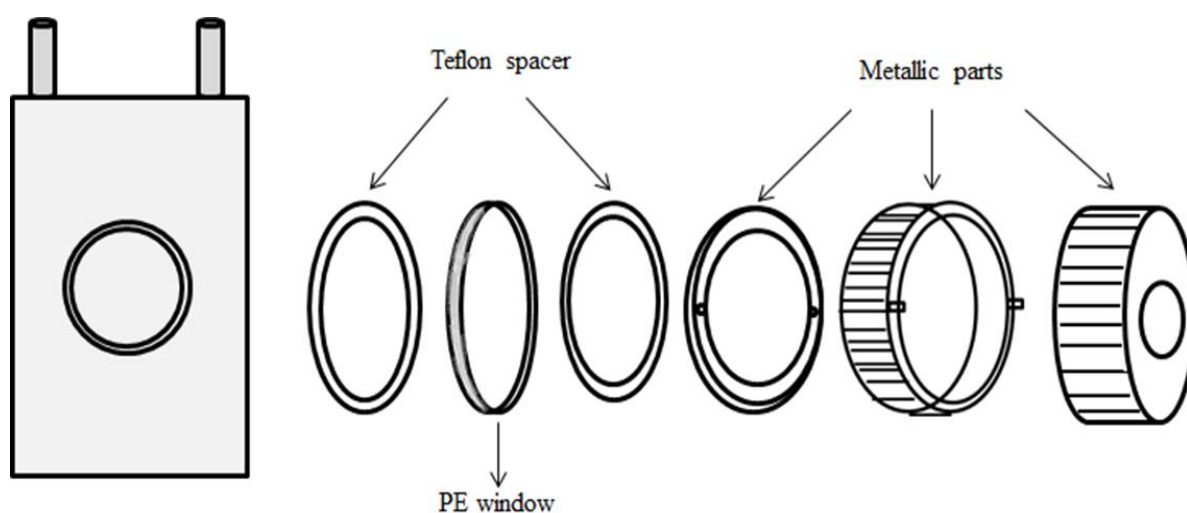


Figure 35. Scheme of the different parts of the absorbance cell.

2.3.4 Difference spectroscopy

As mentioned before, the absorption spectrum of a protein is characterized by the presence of several amide bands, where the amide I includes the different secondary structural elements. Unfortunately, amide I and amide A bands of proteins overlap with the stretching and bending modes of water (Figure 36). Thus to remove the contribution of water and buffer and to probe the functional and the structural changes taking place in the protein, difference spectroscopy was developed^(130, 209).

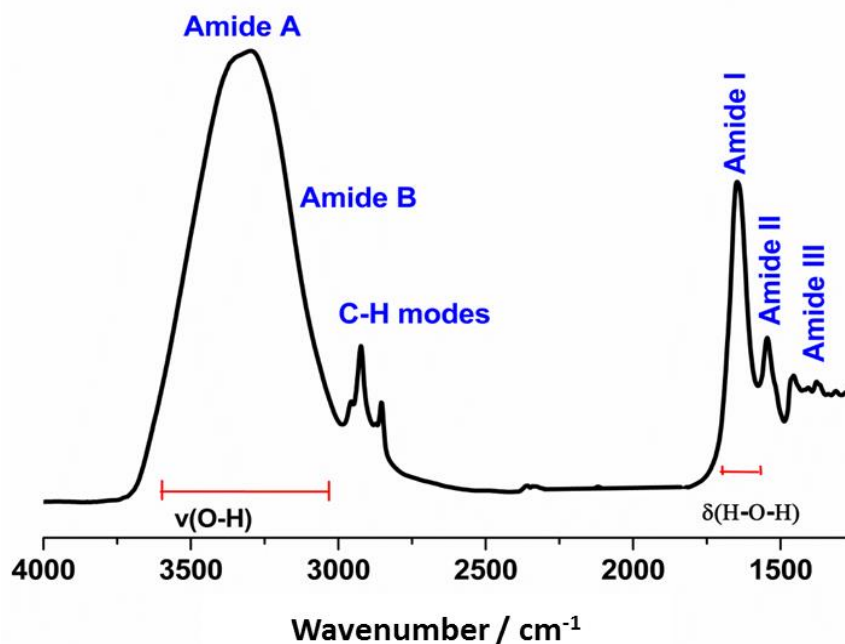


Figure 36. The mid infrared absorbance spectrum of protein in solution.

The principle of difference spectroscopy is to study the sample in the oxidized and reduced forms; however these two spectra look very similar (Figure 37A). The subtraction of one spectrum from the other leads to a difference spectrum of the protein (oxidized minus reduced difference spectrum (Figure 37B)). This ox-red spectrum is usually obtained using the electrochemical cell (section 2.6.3) with small path length of around 10 μm .

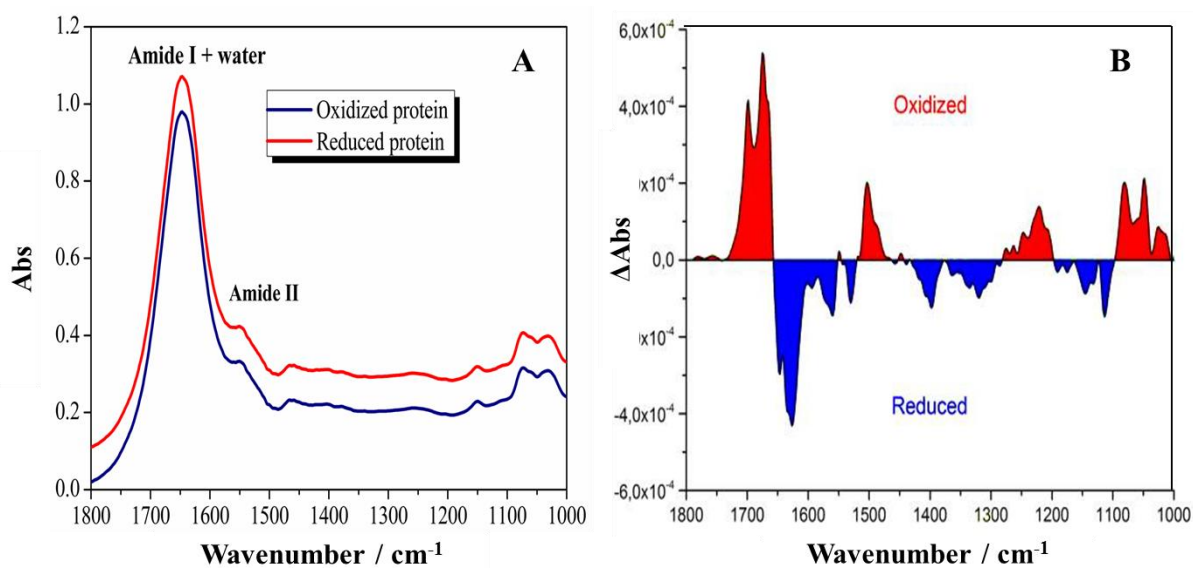


Figure 37. The absorption spectra in the reduced and the oxidized states (A) and difference spectrum (B).

The differential spectrum shows positive (red) and negative (blue) signals that are attributed to oxidation and reduction respectively (Figure 37B)^(210, 211). The analysis of these signals is made with the help of infrared data previously obtained for individual amino acids, isolated cofactors, as well as model compounds^(207, 212).

The difference spectrum provides information concerning the conformational changes taking place during the studied reaction and the modification of the secondary structural elements which are relevant at the level of amide I and amide II bands. In addition, the protonation/deprotonation of acidic residues and environmental changes around the cofactors can be detected between 1700-1750 cm^{-1} and 1600-1500 cm^{-1} respectively.

The main problem that should be taken into consideration is the low intensity of the differential spectrum which is 1000 times lower than the absorption spectrum. Thus, to get precise and accurate results, 50 cycles are performed and averaged to get the final spectrum (increasing signal to noise ratio).

2.3.5 Attenuated total reflection (ATR) spectroscopy

This technique was developed by Harrick *et al.* in the 1960's and it is based on the phenomena of total internal reflection^(209, 213, 214). Its working principle is illustrated in Figure 38.

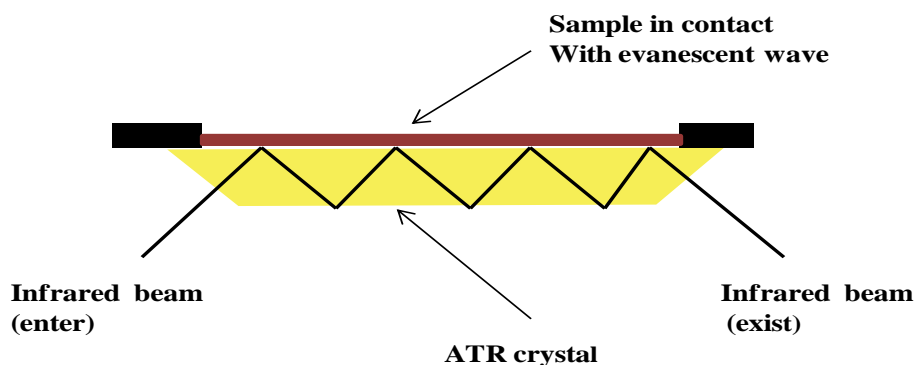


Figure 38. Scheme of an attenuated total reflectance unit.

Two parameters should be achieved to generate total reflection with an evanescent wave extending through the sample:

- 1) The refractive index n_1 of the transparent crystal (also called the internal reflection element IRE) is higher than the refractive index of the sample placed on this crystal n_2 ;

$$n_1 > n_2.$$

- 2) The angle of incidence θ at the interface between the sample and the crystal is greater than the critical angle θ_c ;

$$\theta > \theta_c.$$

The penetration depth of the evanescent wave d_p is given by the relation below ⁽²¹⁵⁾ where λ : wavelength, n_1 : refractive index of the IRE, n_2 : refractive index of the sample and θ angle of incidence.

$$d_p = \frac{\lambda/n_1}{\sqrt{2\pi(\sin^2\theta - (n_2/n_1)^2)}} \quad \text{eq. 8}$$

The crystals used in the attenuated total reflection mode such as diamond, zinc selenide and germanium ⁽¹⁹³⁾ are characterized by their high refractive index, low solubility in water and useful range of detection (Table 10).

Table 10. ATR crystal characteristics for FTIR sampling ⁽¹⁹³⁾.

Crystal	Useful range (cm ⁻¹)	Refractive index	Properties
ZnSe	20000-500	2.4	Insoluble in water, cheap
Ge	5000-550	4	Insoluble in water, very brittle
Diamond	45000-2500; 1800-50	2.4	Insoluble in water, expensive, robust and durable

This technique is well adapted for the study of films on the surface since it overcomes the problem of contribution of water. Only a small quantity of the sample (1-2 μL) is needed and it is more accessible than a sealed sample used in the transmission mode.

Furthermore, the multiple reflections taking place at the interface lead to the enhancement of the signal with better signal to noise ratio. On the other hand, the crystal by itself has a polarizing effect which leads to spectral differences when compared to other methods. The

measurement of dry samples causes small secondary structural changes which arise either from drying or the interaction with the crystal.

2.4 Raman spectroscopy

Raman spectroscopy is a complementary technique to infrared spectroscopy. IR measures the change of dipole moment, whereas Raman measures the change of polarizability. The polarizability of the bond determines the frequency and intensity of the Raman shift. Raman possesses several advantages over IR; 1) it is well suited for the study of aqueous solution because of the low diffusion of water, 2) it is non-destructive and 3) requires no sample preparation. Unfortunately, the drawback of this technique lies in the disability of measuring low concentrated samples as few photons undergo elastic scattering. To overcome this problem, resonance Raman spectroscopy is used.

Basically, when light interacts with a molecule it could be either absorbed, scattered or not interact. Raman spectroscopy is a light scattering technique where there is no need for the photons to be absorbed. Thus, it focuses on scattering where two cases are distinguished; either the scattered light would have the same energy as the incident light or it gains/loses energy during the interaction with molecule resulting in elastic (Rayleigh shift) or inelastic scattering (Stokes/Antistokes shift) respectively (Figure 39) ⁽²¹⁶⁻²¹⁸⁾.

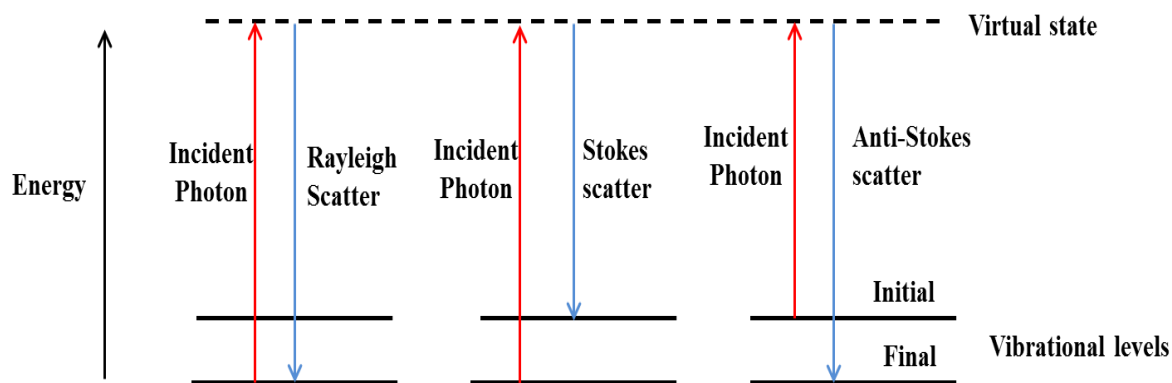


Figure 39. Diagram of the Rayleigh and Raman scattering processes.

These virtual states are created due to the interaction between the laser and the electrons which causes polarization. The energy of these states is determined by the frequency of the light source used.

2.4.1 Resonance Raman spectroscopy (RR)

Raman effect gives weak signal intensities. One of the strategies used to enhance the signals by several orders of magnitude (10^2 - 10^4) and increases the precision of detection and analysis is the resonance Raman spectroscopy (RR). In resonance Raman, the molecule is excited to the first electronic state whereas it is excited to virtual energy state in case of Raman spectroscopy (Figure 40) ⁽²¹⁷⁾.

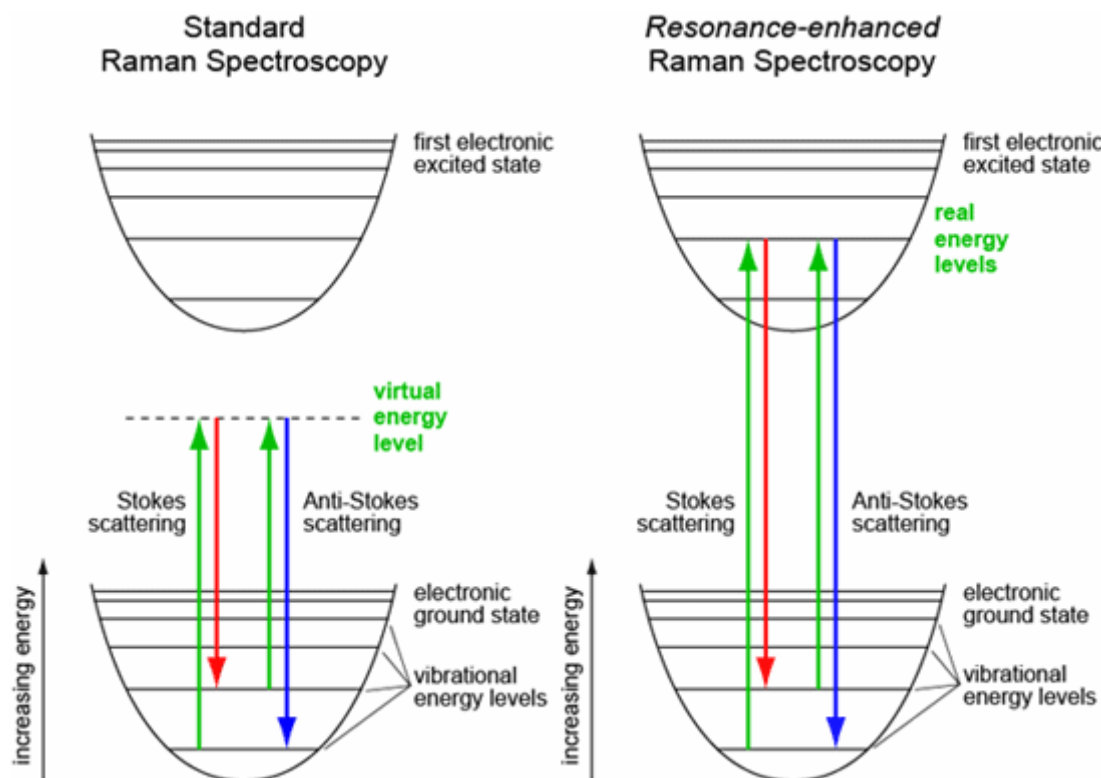


Figure 40. Diagram of the Raman and resonance Raman scattering ⁽²¹⁶⁾.

This method has the advantage of being able to selectively excite a specific part of the molecule in a complex and therefore makes sense for the study of proteins possessing chromophores. On the contrary, the main disadvantages of resonance Raman are due to the increasing risk of fluorescence (broad and more intense than in Raman scattering) and photo-degradation of the sample due to the increased energy of the incoming laser light.

This technique is well adapted to the study of biological systems. Several studies have been reported on the Raman of heme proteins as hemoglobin ^(219, 220) and myoglobin ⁽²²¹⁻²²³⁾ where they identified the spin state and the coordination states of the hemes using marker bands. In addition, resonance Raman is used to probe the iron sulfur proteins ⁽²²⁴⁻²³⁰⁾ where certain

peaks are associated with the bridging (Fe-S^b) and terminal (Fe-S^t) modes. Furthermore, it gives valuable information about the cluster ligation, the symmetry, and the environment of each iron sulfur cluster. In this manuscript, the resonance Raman spectroscopy of complex I protein and some mutants are reported to have a better understanding about the contribution and environment of each cluster.

2.4.2 Surface enhanced resonance Raman spectroscopy (SERS)

SERS was discovered in 1974 by Fleischmann *et al.* ⁽²³¹⁾ who detected enhanced Raman scattering from pyridine adsorbed on electrochemically roughened silver. SERS is a Raman spectroscopic technique that is based on highly enhanced Raman signals coming from active analyte molecules adsorbed on metal surfaces as gold, copper, silver and lithium. The enhancement factor usually depends on the nature of the adsorbed molecule, the structure and morphology of the metal surface. This technique is sensitive to study the surface of a material with an improved signal intensity to the order $10^4 - 10^6$ and sometimes higher to $10^8 - 10^{14}$ for some systems ⁽²³²⁾.

Electromagnetic and chemical theories have been suggested in the literature to explain the enhancement effect ^(233, 234). The presence of roughness features on the metal surface and the changes of the adsorbate electronic state due to chemisorption of the analyte reflect the parameters that affect electromagnetic and chemical enhancement respectively. The electromagnetic contribution in the enhancement usually dominates over the chemical effect ⁽²³²⁾.

Two drawbacks of such technique should be mentioned: the difficulty to obtain reproducible SERS active substrates and calibration curve for the analyte. This technique has been widely used for the study of biological molecules. Cotton *et al.* ⁽²³⁵⁾ reported the study of proteins from the respiratory chain such as cytochrome c by using this technique.

2.5 Sample Preparation

2.5.1 Preparation of complex I protein and its variants

- **Preparation of wild type complex I from *E. coli***

The preparation of the samples was performed in the laboratory of Prof. Dr. Thorsten Friedrich (Institute of organic chemistry and Biochemistry, Albert-Ludwigs-Universität,

Freiburg, Germany). All the steps were made according to the protocol described in the literature of Pohl *et al.* ⁽²³⁶⁾ to obtain complex I. The first step was the cell growth followed by the preparation of the cytoplasmic membranes and then a two-step purification process.

For isolation of complex I, around 30 g of cells were mixed with 150 ml of buffer composed of 50 mM sodium chloride (NaCl), 100 μ M phenylmethylsulfonyl fluoride (PMSF). Traces of Dnase I and lysozyme were added to the suspension and then homogenized in a mixer. Foam was removed by using antifoam (Sigma Aldrich). Then a French press cell (SLM Aminco) at 110 Mpa was used to break these cells. All these steps were carried out at 4 °C. After that, the solution was distributed equally in the tubes of centrifuge (RC-5 SR centrifuge, Sorvall instruments). Cell debris was removed after centrifugation at 36000 g for 20 min. The cytoplasmic membranes were obtained by centrifugation at 250000 g for one hour (L8-M, Beckman Coulter). The membranes were collected and suspended in 50 mM MES/NaOH, 50 mM NaCl, 5 mM MgCl₂, pH 6 and 100 μ M PMSF at 1 g per mL of suspension. n-Dodecyl β -D- maltoside (DDM, Sigma) from 20% stock solution in water was added to the membrane suspension to a final concentration of 3% and then the solution was homogenized using a glass-Teflon homogenizer and incubated 15 min on ice. Unsolubilized material was removed by ultracentrifugation at 250000 g for 15 min. The supernatant solution was applied to a 60 mL anion exchange chromatography column (Fractogel, EMD, Merck) which was equilibrated in 50 mM MES/NaOH, 50 mM NaCl, 0.1% DDM and pH 6. The column was washed with the same buffer. Furthermore, the column was washed with 35 mL of 150 mM NaCl in 50 mM MES/NaOH, 0.1% DDM, 30 μ M PMSF pH 6. Proteins were eluted with a 75 mL linear salt gradient from 150 to 350 mM NaCl in 50 mM MES/NaOH, 0.1% DDM and pH 6 at a flow rate of 5 mL.min⁻¹. Fractions exhibiting NADH/ferricyanide oxidoreductase activity were collected together. Then imidazole was added to have a final concentration of 20 mM and the sample was loaded on a 10 mL ProBond Ni²⁺-IDA column (Invitrogen) which was equilibrated in 50 mM MES/NaOH, 200 mM NaCl, 20 mM imidazole, 0.1% DDM, pH 6.3 at a flow rate of 1.1 mL.min⁻¹. The column was washed with the same buffer until the absorbance at 280 nm decreased to the initial value. Proteins were eluted with a step gradient from 20 to 500 mM of imidazole in 50 mM MES/NaOH, 200 mM NaCl, 0.1% DDM, pH 6.3 at a flow rate of 1.1 mL.min⁻¹, then fractions exhibiting NADH/ferricyanide oxidoreductase activity were pooled together and washed at least three times with the 50 mM MES/NaOH, 50 mM NaCl, 0.1% DDM, pH 6.0 and concentrated by ultrafiltration (100 kDa

MWCO Amicon, Millipore) to remove the imidazole. The samples were submitted to shock freezing in liquid nitrogen and stored at -80 °C until used.

For some experiments, the sample should be highly concentrated. This can be achieved with the help of ultrafiltration (100 kDa MWCO Amicon) of volume 500 µL (Millipore, Billerica, MA 01821, USA) and centrifuge 5804 R (Eppendorf, Le Pecq, France). The concentration was performed at a rate of 5000 rpm.min⁻¹ for 20 min. The final concentration obtained for the sample was around 100 µM.

- **Preparation of wild type complex I from *E. coli* with reduced lipid content (delipidated sample)**

The same procedures described above (section 2.5.1) were followed for the preparation of the delipidated complex I samples. The main difference involves a longer washing step during the Probond Ni²⁺-IDA affinity column chromatography in order to remove higher amount of phospholipids.

- **Preparation of NuoL and NuoB mutants**

The purification of NuoL mutants (D563N, D563E, Y594F) were done by Stefan Steimle^(174, 175) whereas NuoB mutants (C64AG100C with respect to *E. coli*) at pH 6, 6.5, 7 were prepared by Patricia Hegger and Ina Parsjow in the laboratory of Prof. Dr. Thorsten Friedrich. As described before, membrane proteins were extracted with *n*-dodecyl-β-D-maltoside (DDM, Sigma) and separated by anion exchange chromatography on Fractogel EMD TMAE Hicap (Merck). Fractions exhibiting NADH/ferricyanide oxidoreductase activity were pooled and loaded on to affinity chromatography on Probond Ni²⁺-IDA (Invitrogen). Bound proteins were eluted with an imidazole step gradient. Peak fractions with NADH/ferricyanide oxidoreductase activity were pooled and concentrated.

- **Preparation of ABA triblock copolymer PMOXA₁₆-PDMS₇₂-PMOXA₁₆**

Polymethyloxazoline-Polydimethylsiloxane-Polymethyloxazoline of molar mass 7988 g.mol⁻¹⁽¹⁸²⁾ was prepared in the laboratory of Prof. Dr. Wolfgang Meier in department of chemistry, University of Basel. 1 mL of the ABA polymer in chloroform at concentration of 1mg.mL⁻¹ (125 µM) was used.

- **Determination of NADH/ferricyanide oxidoreductase activity**

The enzymatic activity of complex I was obtained by following the reduction of ferricyanide by NADH at 410 nm at room temperature⁽¹⁸⁹⁾. The measurement was performed using a 1 cm x 1 cm cuvette with a final volume of 1 mL containing 50 mM MES/NaOH, 50 mM NaCl, 1 mM $K_3[Fe(CN_6)]$, 0.2 mM NADH, pH 6 with 5 μ L of the sample. The NADH/ferricyanide oxidoreductase activity in units of μ mol.min⁻¹.mL⁻¹ or (U.mL⁻¹) was determined by using the equation of Lambert-Beer's law where the molar absorption coefficient of $K_3[Fe(CN_6)]$ is $\epsilon_{410} = 1 \text{ mM}^{-1}.\text{cm}^{-1}$.

- **Determination of complex I concentration through UV-visible spectroscopy**

The concentration of the complex I was determined using a Diode-Array UV-vis Spectrophotometer (TIDAS II, J&M), where 1 cm path length quartz cuvette filled with 5 μ L of the sample and diluted in 245 μ L of the buffer (MES 50 mM, NaCl 50 mM, 5 mM $MgCl_2$, 0.1 % DDM) is used. The concentration was calculated using Lambert-Beer's law where the molar extinction coefficient for complex I (MW 535.4 kDa) is $\epsilon_{280} = 781 \text{ mM}^{-1}.\text{cm}^{-1}$ ⁽²³⁷⁾. One important thing that should be taken into consideration was the contribution from lipids and detergents which usually appear at 310 nm, thus the absorbance at 310 should be subtracted from the absorbance of the protein at 280 nm.

2.5.2 Preparation of lipids and liposomes

- **Phospholipids**

Lyophilized L- α phosphatidylcholine from egg yolk EPC (fatty acid composition: 33% 16:0, 13% 18:0, 31% 18:1 and 15% 18:2), lyophilized L- α phosphatidylethanolamine from egg yolk EPE (fatty acid composition: 22.0% 16:0, 37.4% 18:0, 29.4% 18:1 and 11.2% 18:2), 1,2-dimyristoyl-sn-glycero-3-phosphocholine DMPC (100%, 14:0), 1,2-dimyristoyl-sn-glycero-3-phosphatidylethanolamine DMPE (100%, 14:0), cardiolipin from bovine heart (CL) (fatty acid composition: 0.5% 16:0, 0.4% 16:1, 0.2% 18:0, 6.7% 18:1 and 92.2% 18:2) and cholesterol were purchased from Sigma Aldrich and used without further purifications (Figure 41).

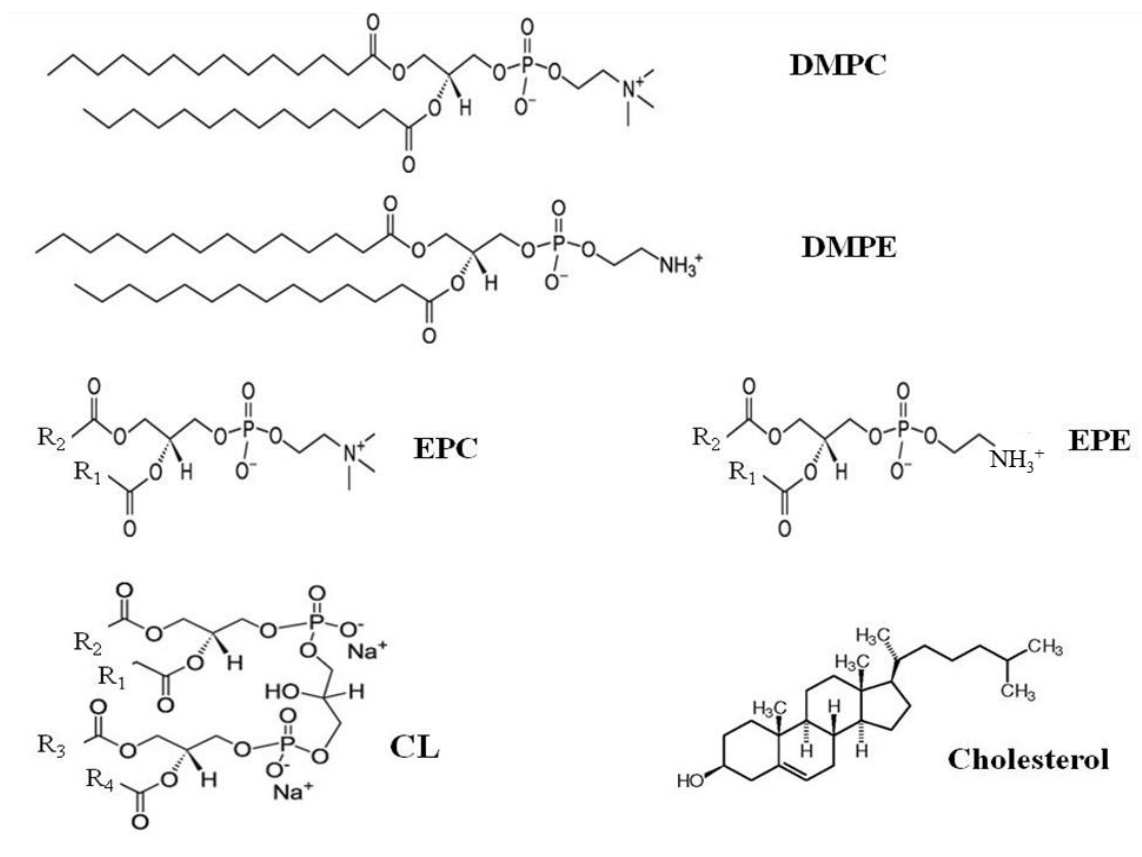


Figure 41. Chemical structures of DMPC, DMPE, EPC, EPE, CL and cholesterol. R₁, R₂, R₃, R₄ are fatty acid residues.

The samples were dissolved in chloroform (Fluka, 99.5% purity and 0.5% ethanol as a stabilizer) with a concentration of 20 mg.mL⁻¹. The lipid DMPE is soluble in a mixture of organic solvents (80% chloroform, 20% methanol) with a little sonication. Lipid mixtures of EPC and EPE of different ratios 1:1, 2:1 and 4:1 (mole ratio) were prepared.

- **Liposomes**

Liposomes were prepared by Birgit Erhard in the laboratory of Prof. Dr. Regine Süss in the faculty of pharmacy, Freiburg. The production of liposomes involves 3-4 basic steps (Figure 42)⁽⁹⁶⁾.

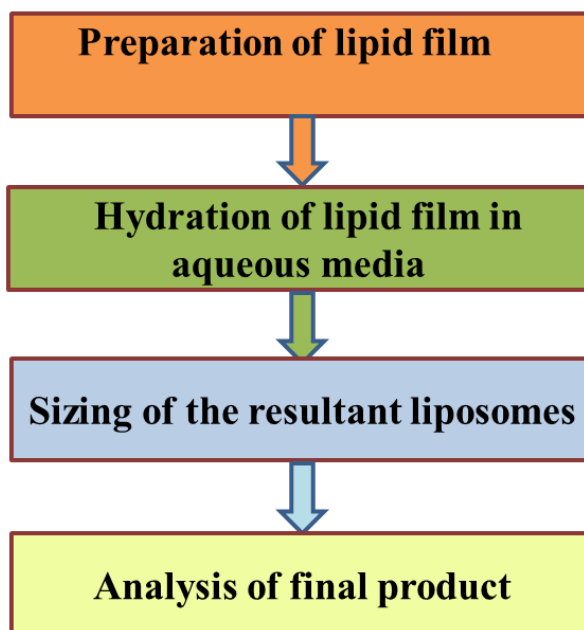


Figure 42. The crucial steps involved in the preparation of liposomes.

Preparation of lipid film: The lipid sample was dissolved in chloroform until a clear lipid solution was observed. It was then placed in a round bottom flask which was connected to rotary evaporator using an argon stream in a fume hood. After the evaporation of the organic solvent, the lipid film was obtained.

Hydration of lipid film: The lipid film was hydrated in aqueous media and allowed to stand for 2 hours at room temperature in order to form the liposomes.

Sizing of lipid suspensions: The final step was to have a homogenous distribution of the liposomes and this is achieved using a variety of techniques including sonication, detergent depletion, reverse phase evaporation, extrusion, and microinjection⁽²³⁸⁻²⁴⁰⁾. Extrusion was the approach used in our preparation because it is well known to generate LUV with uniform size between 100-200 nm. This can be done by passing the sample through a polycarbonate membrane with a defined pore size which then yields vesicles with diameter similar to that of filter (Figure 43). The size and polydispersity were measured using the dynamic light scattering method (DLS).

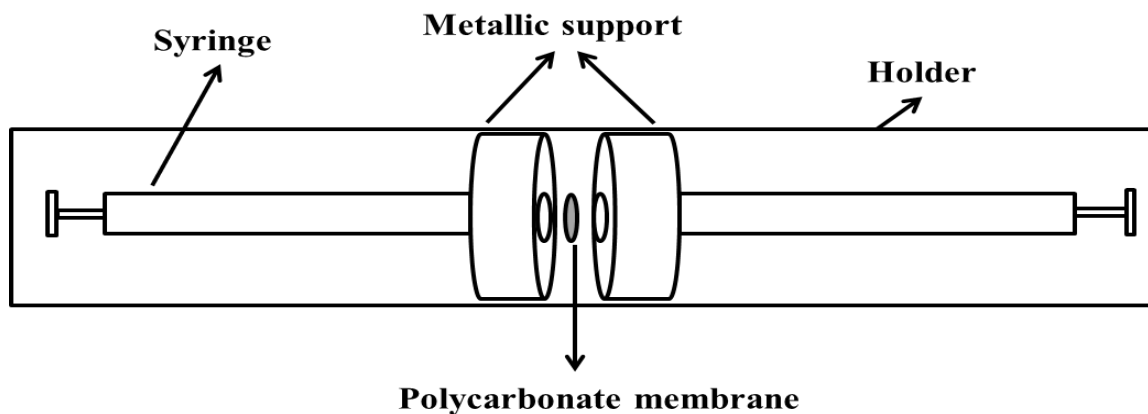


Figure 43. Extruder used for producing LUV.

- **pH sensitive liposomes DOPE/CHEMS (3:2)**

Dioleoylphosphatidylethanolamine (DOPE) was mixed with cholesteryl hemisuccinate (CHEMS) and the lipid film formed was hydrated with HEPES buffer 10 mM + 150 mM NaCl at given pH. Six samples of DOPE/CHEMS liposomes of 3:2 ratio at different pH were prepared and studied.

Table 11. DOPE/CHEMS (3:2) liposomes at 6 different pH buffers.

DOPE/CHEMS (3:2) pH	Size (nm)	Polydispersity
7.4	125	0.082
6.5	137	0.041
6	142	0.042
5.5	308	0.194
5	1533	0.149
4.5	1088	0.186

2.6 Experimental conditions

2.6.1 Infrared absorbance spectra of lipids

The ATR absorbance spectra of lipids were carried out by depositing 2-3 μL of the lipid sample on the surface of the crystal. Each time the detector, beamsplitter and IR source were chosen according to the studied spectral range (section 2.3.1). The far infrared absorbance spectra were recorded between 600-50 cm^{-1} using the diamond ATR crystal, whereas the Si/ZnSe crystal was used for the mid infrared region from 4000 to 900 cm^{-1} ⁽²⁴¹⁾.

MIR data were obtained using a Bruker IFS 28 FTIR spectrometer equipped with a KBr beamsplitter and deuterated triglycine sulphate (dTGS) detector. On the other hand, a Bruker Vertex 70 FTIR spectrometer supplied with a removable silicon beamsplitter and room temperature dTGS detector was used for the far infrared absorbance spectra. These spectrometers were purged with dry air. Generally, five spectra with 128 scans were averaged to have the final far infrared spectra. The resolution was 4 cm^{-1} with a scan velocity 2.5 kHz whereas ten mid infrared spectra with 256 scans were averaged using a mirror velocity of 10 kHz and resolution 2 cm^{-1} . Water vapour compensation and smoothing of 2 to 5 points were performed when necessary. Each measurement was repeated at least three times to assure reproducibility.

- **Temperature-dependent behaviour of phospholipids**

For the temperature dependent measurements in the mid infrared region, the lipid solution was deposited on the surface of the Si/ZnSe crystal and left to dry. The temperature was slowly decreased to the desired temperature starting at 5 $^{\circ}\text{C}$ and after an equilibration time of an hour infrared, measurements were performed in function of increasing/decreasing temperature as previously described ⁽²⁴¹⁾. An external bath containing water/ethanol was used to control the temperature. The infrared spectra were recorded between 5 and 60 $^{\circ}\text{C}$ and the samples were equilibrated for at least 30 minutes at the respective temperature before data acquisition.

The same experiments were done for the far infrared measurements but in this case the absorbance cell was used (section 2.3.3). A 2 mm thick polyethylene (PE) window was used and the sample was prepared as a dried film on the surface of the window. The experiments on DMPC, DMPE, EPC and EPE were realized using a Bruker Vertex 70 FTIR with a

conventional light source whereas the measurements on the lipid mixtures EPC/EPE at different ratios and the lipid/cholesterol mixtures were carried on a Bruker IFS 66 FTIR spectrometer and mylar beamsplitter and a helium cooled bolometer as detector, using the synchrotron light at the ANKA IR Beamline Karlsruhe. The two main advantages of such experiments are summarized by the high brilliance of the synchrotron light in the low frequency region and the vacuum condition in the spectrometer which reduces the contribution of humidity. The final spectrum was obtained after averaging seven spectra with 256 scans, 4 cm^{-1} resolution and 20 kHz scan velocity and subtracting the PE spectrum.

2.6.2 Study of liposomes

- **Modification of the Si/ZnSe crystal**

The Si/ZnSe crystal was modified by TiO_2 solution to promote the adsorption of liposomes. TiO_2 was selected because it allows keeping liposomes intact^(96, 100). TiO_2 solution was prepared by dissolving 30 mg of fumed TiO_2 (P25) powder (Sigma Aldrich, particle size of about 20 nm) in 25 mL of methanol and placing it for 30 min in an ultrasonic bath. Then 100 μL of the TiO_2 suspension in methanol was deposited on the surface of the Si/ZnSe followed by the evaporation of the solvent⁽²⁴²⁾. A layer of dry TiO_2 was formed on the surface (Figure 44).

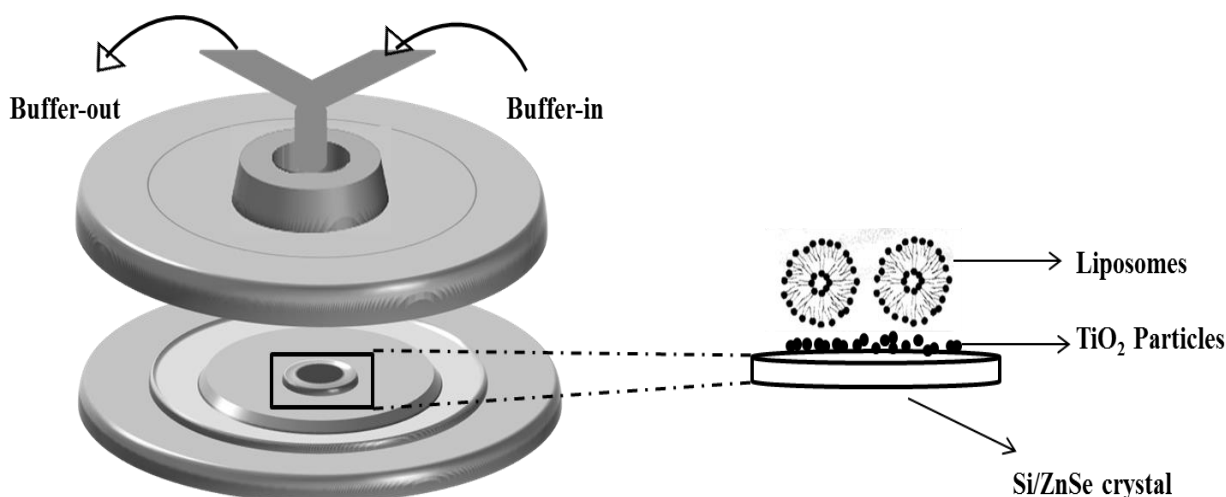


Figure 44. Liposomes solution on TiO_2 modified Si/ZnSe crystal.

After coating the crystal, the buffer Hepes at given pH was pumped until a stable background was obtained. Then the MIR absorbance spectra of liposome samples at different pH were

recorded. The experiments were carried out at room temperature and the flow rate of the pump was $1 \text{ mL}\cdot\text{min}^{-1}$ and 20 spectra with 256 scans and 2 cm^{-1} resolution were averaged in order to get the final spectrum.

2.6.3 Spectroelectrochemistry

- **Thin layer electrochemical cell**

For the electrochemistry experiments, the optically transparent thin layer electrochemical cell designed by David Moss in 1990 was used⁽²⁴³⁾. This cell is composed of three electrodes: 1) a gold grid (35 x35 μm mesh width, optical transparency of 55%, from Buckbee, USA) used as a working electrode, 2) platinum film used as a counter electrode and 3) silver/silver chloride (3M KCl) as a reference electrode (+208 mV versus SHE) (Figure 45A).

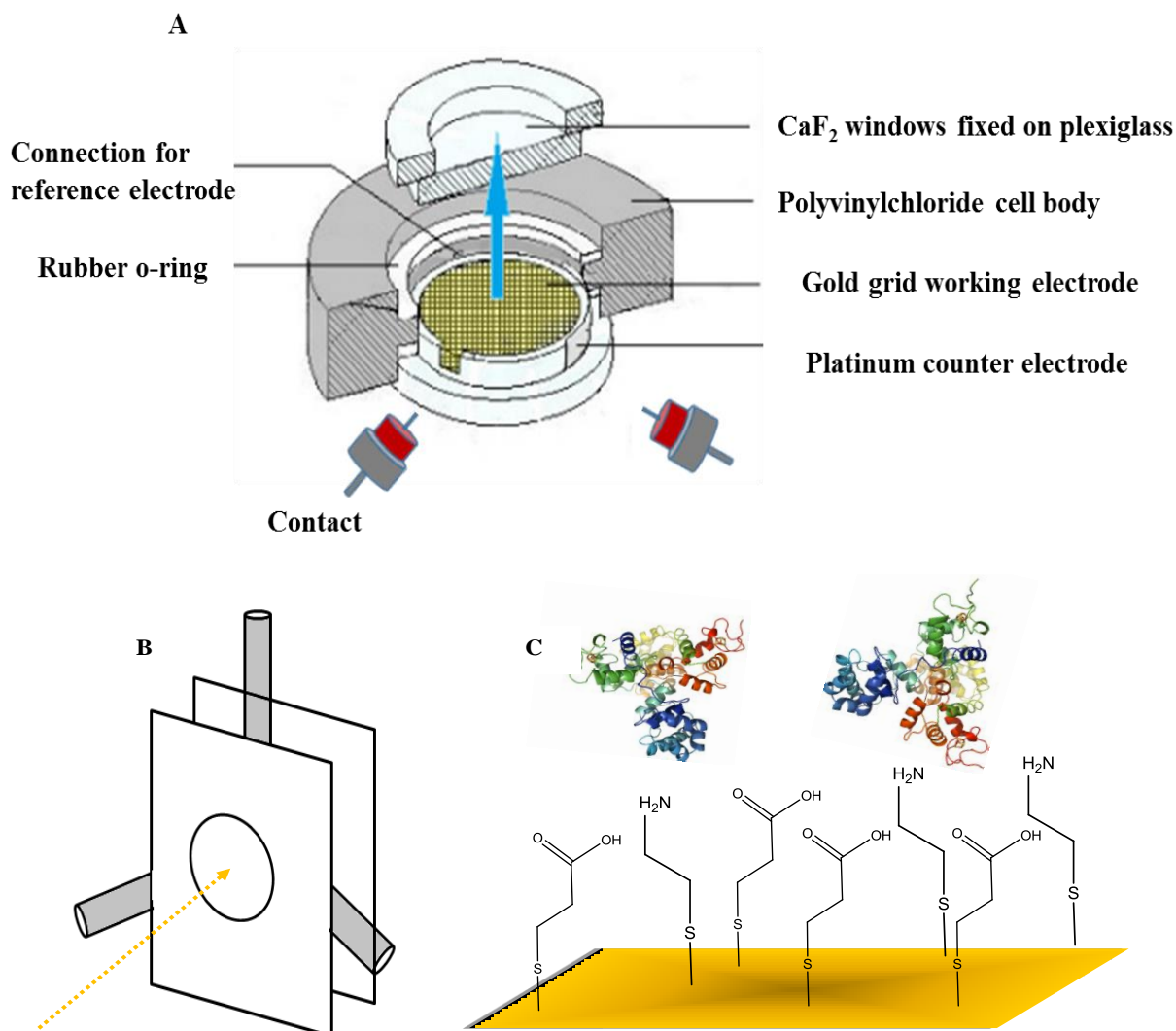


Figure 45. The spectroelectrochemical cell and its different compartments⁽²⁴³⁾ before (A) and after (B) assembly, the yellow arrow indicates the optical pathway, representation of the gold grid modification with cysteamine and mercaptopropionic acid (C).

After closing the cell, the corresponding buffer was added in order to ensure the connection between the electrodes. The cell was maintained inside a metallic support that helps to control the temperature during the measurement (Figure 45B). After that, it was transferred to the spectrometer and connected to a potentiostat which regulates the potential applied to the working electrode.

The gold grid was pre-treated with a solution of modifiers of 2 mM cysteamine and 2 mM mercaptopropionic acid for at least one hour (Figure 45C) to avoid denaturation of protein upon contact. These modifiers are covalently attached to the gold surface from the sulfur part and they form a self-assembled monolayer (SAM) of $-\text{COO}^-$ and $-\text{NH}_3^+$ groups from the other part that electrostatically interact with the protein. It is important to mention that the grid was washed with distilled water in order to remove the noncovalently bound thiols before adding the sample.

The proteins usually have cofactors which are embedded inside their structure. For this reason, a mixture of 19 electrochemical mediators (Table 12) which act as a shuttle that accelerate the rate of electron transfer between the cofactors and the working electrode were used (Figure 46).

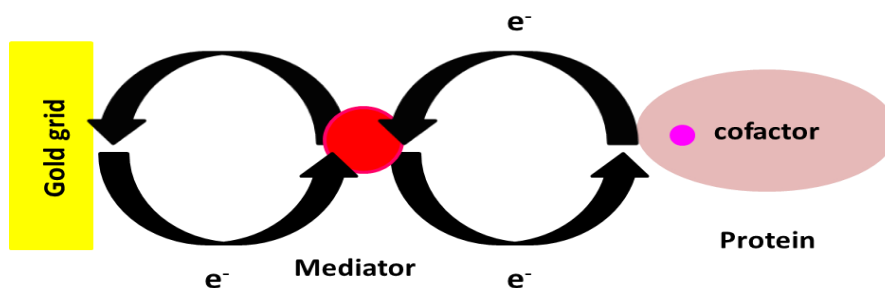


Figure 46. Schematic representation of the role of mediators.

Table 12. List of mediators used for spectroelectrochemical experiments.

Mediator	E_m(mV) vs. Ag/AgCl (3M KCl)	Source	Solvent
Ferrocenylmethyltrimethylammoniumiodide	607	Stern chemicals	Ethanol
1-1-ferrocenedicarboxylic acid	436	Fluka	Ethanol
Potassiumhexacyanoferrate (II) trihydrate	212	Riedel-de-Haën	Water
1-1-dimethylferrocene	133	Sigma Aldrich	Ethanol
Quinhydrone	70	Fluka	Ethanol
Tetrachloro-1.4-benzoquinone (<i>p</i> -Chloranil)	72	Sigma Aldrich	Acetone
N,N,N,N-Tetramethyl- <i>p</i> -phenylenediamine dihydrochloride	62	Fluka	Water
2,6-dichlorophenolindophenol sodium salt hydrate	9	Biochemika	Ethanol
Hexaamminerythenium (III) chloride	-8	Sigma Aldrich	Water
Anthraquinone-2-sulfonic acid sodium salt	-23	Sigma Aldrich	Water
1.4 naphthoquinone hydrate	-63	Sigma Aldrich	Water
Trimethylhydroquinone	-108	Sigma Aldrich	Ethanol
Anthraquinone	-108	Sigma Aldrich	Ethanol
5-Hydroxy-1,4-naphthiquinone	-158	Sigma Aldrich	Ethanol
Duroquinone	-198	Sigma Aldrich	Ethanol
Menadione	-220	Sigma Aldrich	Acetone
2-Hydroxyl-1,4-naphthoquinone	-333	Sigma Aldrich	Ethanol
9,10-Anthraquinone-2,6-disulfonic acid disodium salt	-433	Sigma Aldrich	Ethanol
Neutral red	-515	Sigma Aldrich	Ethanol
1,1-Dimethyl-4,4-bypyridium dichloride hydrate	-628	Sigma Aldrich	Water

Each of these mediators has a different midpoint potential, but all together they are capable of mediating electron transfer over a range of potentials ⁽²⁴⁴⁾ from -600 to +600 mV versus

Ag/AgCl (3M KCl). These mediators have a final concentration of 25 μM so they do not contribute much to the visible absorption spectrum as seen previously⁽²⁴⁵⁻²⁴⁷⁾.

- **Study of complex I and NuoL mutants**

The electrochemical cell described above was used where 10 μL of the sample of concentration around 125 μM was placed on a mixture of mediators for 35 minutes to promote electron transfer between the cofactors of protein and the working electrode. Then the sample was deposited on the gold grid and the cell was closed and filled with buffer (50 mM NaCl, 50 mM MES, 0.01 % DDM, pH 6). Undesired air bubbles were eliminated and the pathlength should not exceed 10 μm ^(130, 183).

The cell was connected to a thermostat with a temperature fixed at 5 °C. The potentials applied for the oxidized state and the reduced states were 0 and -650 mV respectively versus Ag/AgCl (3M KCl). The equilibration times were 3 min for the oxidized state and 5 min for the reduced state.

The measurements were carried out using the Bruker Vertex 70 spectrometer (KBr beamsplitter, liquid nitrogen MCT detector, global source). The spectra were recorded in the oxidized and reduced states at 40 kHz scan rate, 4 cm^{-1} resolution and 256 scans. The opus program then calculated the ox-red and red-ox spectra. The final spectrum obtained was an average of around 60 cycles.

- **Interaction of complex I with ABA block copolymer**

30 μL of the polymer PMOXA₁₆-PDMS₇₂-PMOXA₁₆ of concentration 1 $\text{mg}\cdot\text{mL}^{-1}$ were placed in an eppendorf and left to evaporate, then 6 μL buffer (50 mM NaCl, 50mM MES, 0.01 % DDM, pH 6) were added to dissolve the 30 μg of polymer and they are shaken for around one week at 4°C using the thermomixer (compact, Eppendorf). 4 μL were left due to evaporation and mixed with around 9 μL of delipidated complex I sample for 3 hours at 4 °C. The final molar ratio was around 30:1 polymer/complex I.

- **Interaction of complex I and the NuoL mutant with zinc (II)**

1 μL of ZnSO_4 solution of concentration 150 mM was added to 9 μL of D563N mutant of concentration around 150 μM in order to obtain a 100:1 ZnSO_4 /D563N ratio. Then they were mixed for 3 hours at 4 °C and the mixture was incubated on the mediators for 35 min. The electrochemical cell was assembled as described before (section 2.6.3); the main difference

was the equilibration time which was extended to 9 min for oxidation and 10 min for reduction.

- **UV-visible redox titration of NuoB mutants**

UV-visible spectroscopy coupled to thin layer electrochemical cell was used for the titration of cofactors. For the study of NuoB mutants, titrations were performed using a Diode-Array UV-vis Spectrophotometer (TIDAS II, J&M) in order to probe the effect of the mutated residues and pH on the midpoint potential of each cofactor present in the enzyme. The procedures followed were identical to the one described above (section 2.6.3) except that two gold grids were used instead of one in order to increase the optical path length, and the mediators concentration was doubled. The thermostat was placed at 10 °C in order to avoid the condensation of water inside the spectrometer. The titration was started by measuring a reference in the oxidized state and then the potential was shifted to the reduced state to take a full red-ox spectrum. This step was repeated in the other direction in order to get the ox-red spectrum. If the two spectra were reversible and mirror images to each other, this indicates that the experimental setup is functioning well. The data were recorded by applying a potential between 0 and -650 mV (vs. Ag/AgCl). The potential was changed in -25 mV steps from -400 to -650 mV and -50 mV from -400 to 0 mV. The equilibration time was between 10 to 30 min, and every 5 min a spectrum was recorded and compared to the previous one. When no more changes were observed, the potential was shifted to the next one.

- **Determination of the redox midpoint potential (E_m)**

To estimate the midpoint potential of a certain cofactor, the difference in absorbance at a given wavelength was plotted against the applied potential (ΔA as a function of potential) then the curve was fitted to Nernst equation.

$$A(p) = \Sigma \frac{A_{max}}{1 + e^{(p - E_m) \frac{nF}{RT}}} \quad \text{eq. 9}$$

E_m is the midpoint potential of the cofactor, p is the applied potential, R universal gas constant (8.3144 J.K⁻¹.mol⁻¹), n correspond to the number of electrons transferred, F is the Faraday constant (96485.3 C.mol⁻¹) and T corresponds to the temperature in Kelvin, A_{max} is the maximal change in the absorbance. This method usually works when one or two components absorb at this specific wavelength in a redox dependent manner. But in the case

of complex I protein, around nine cofactors (FMN and iron sulfur clusters) are involved in the same spectral region, so fitting to Nernst equation gives inaccurate results. For this reason the first derivative of the difference in absorbance was plotted against the applied potential (δA as a function of potential). Then the resulting curve was fitted by simple Gaussian equations. The height of each Gaussian peak depends on the molar extinction coefficient and the half width depends on the number of electron transferred during the reaction ⁽¹⁸³⁾.

2.6.4 Resonance Raman Spectroscopy

Raman Spectroscopy was used to compare the complex I wild type with NuoB mutants at different pH. The measurements were performed using a Renishaw InVia Reflex Raman microprobe with a multi-wavelength facility equipped with a CCD (charge coupled device) as a detector. The sample was dried on a polyethylene window (2 mm) under argon. Then a 50 x objective lens was used to focus the laser onto a certain position. The experiments were conducted using an argon ion laser with a power of 12.5 mW and an excitation wavelength 514 nm. The spectrum was obtained after 50 accumulations with an exposure time of 10 s and resolution 1 cm⁻¹. All Raman spectra were calibrated using silicon window as a reference.

- **Surface enhanced Raman Spectroscopy on lipid**

The Raman spectra of EPC, EPE, cardiolipin and lipid/cholesterol mixtures were recorded using CaF₂ window with an excitation of 514 nm. On the other hand for the SERS experiments on these lipids, a Si substrate was coated with silver nanoparticles and modified with a 1mM thiol solution (Figure 47) then the lipid sample was deposited on the surface.

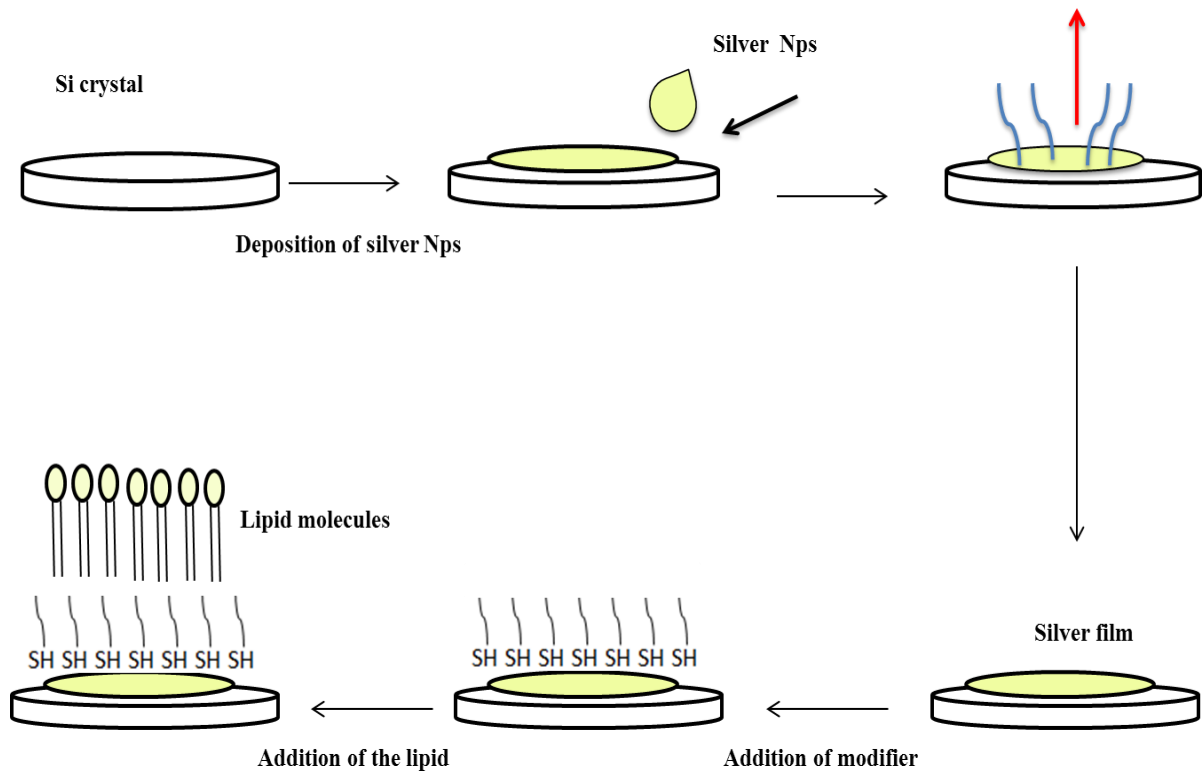


Figure 47. The steps used to immobilize lipids for signal enhancement in Raman.

Chapter III

**Mid and Far infrared properties of lipids
and pH sensitive liposomes**

3 Results and discussions

In the last decade, a significant progress in the understanding of lipid interaction was achieved by applying Fourier transform infrared spectroscopy⁽²⁴⁸⁾. This technique is a powerful tool for studying the structure and organization of membrane lipids in their various phases. The conformational properties and the phase transition temperature of lipids have been mostly studied in the mid infrared region (4000-800 cm^{-1}). In the far infrared region (600-50 cm^{-1}), the contribution of the head group (600-480 cm^{-1}), the torsion motion of the hydrocarbon chain/skeleton vibrations (460-180 cm^{-1}) and the hydrogen bonding continuum ($\leq 300 \text{ cm}^{-1}$) can be probed as shown recently⁽²⁴¹⁾.

Several kinds of phospholipid model compounds as phosphatidylcholine⁽²⁴⁹⁻²⁵²⁾, phosphatidylethanolamine⁽⁴⁸⁾, cardiolipin⁽⁵³⁾ as well as asolectin⁽²⁴¹⁾ have been well characterized using IR spectroscopic methods. Lipid/cholesterol systems have been examined using different techniques like X-ray^(253, 254), neutron diffraction⁽²⁵⁵⁾, NMR⁽²⁵⁶⁻²⁵⁹⁾, ESR⁽²⁶⁰⁾, Raman^(75, 261) and IR spectroscopies^(262, 263). However, the interaction mechanism of cholesterol with membranes is not yet fully understood and is still under investigation. In this chapter, the temperature dependence of thin films composed of pure and mixed phospholipids with cholesterol are probed by means of mid and far infrared spectroscopies. To the best of our knowledge, this is the first description of the hydrogen bonding behaviour of mixture of phospholipids together with and without cholesterol using far IR spectroscopy.

3.1 The temperature dependence of lipids in the mid infrared domain

The mid infrared absorption spectra of thin films of pure EPC, EPE, cardiolipin and mixtures with cholesterol in a mole ratio of 2:1 (lipid/cholesterol) are recorded upon heating from 0 to 90 °C on a ZnSe/Si crystal. These spectra include the characteristic absorbance of the acyl chains part (CH vibrations) and the head group (phosphate and carbonyl stretching)⁽²⁶⁴⁾ as shown in Figure 48. For analysis, the spectrum is divided into four different spectral domains.

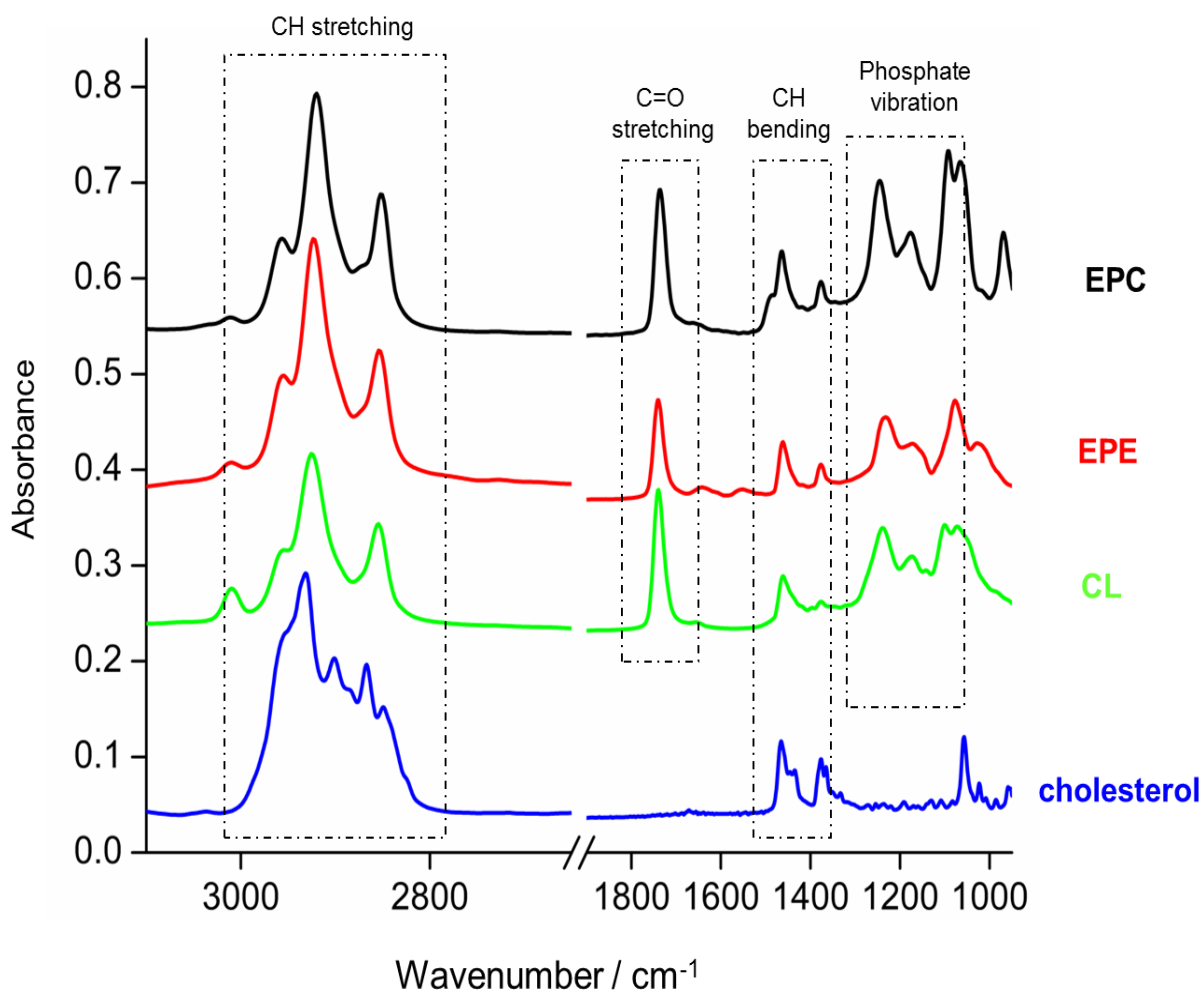


Figure 48. The ATR absorption spectra of EPC (black), EPE (red), CL (green) and cholesterol (blue).

3.1.1 Spectral features characteristics of the tail part

3.1.1.1 CH stretching vibration

The carbon-hydrogen stretching vibrations give rise to strong bands in the spectral region 2800-3100 cm^{-1} (Figure 49). These infrared absorption bands correspond to the asymmetric ($\nu_{\text{as}} \text{CH}_2$) and symmetric ($\nu_{\text{s}} \text{CH}_2$) stretching vibrations of the methylene groups. The frequencies of these vibrations are sensitive to the static order of the acyl chains. Thus, the increase in hydrocarbon chain conformational disorder causes an increase in their frequencies (18, 248, 265-270).

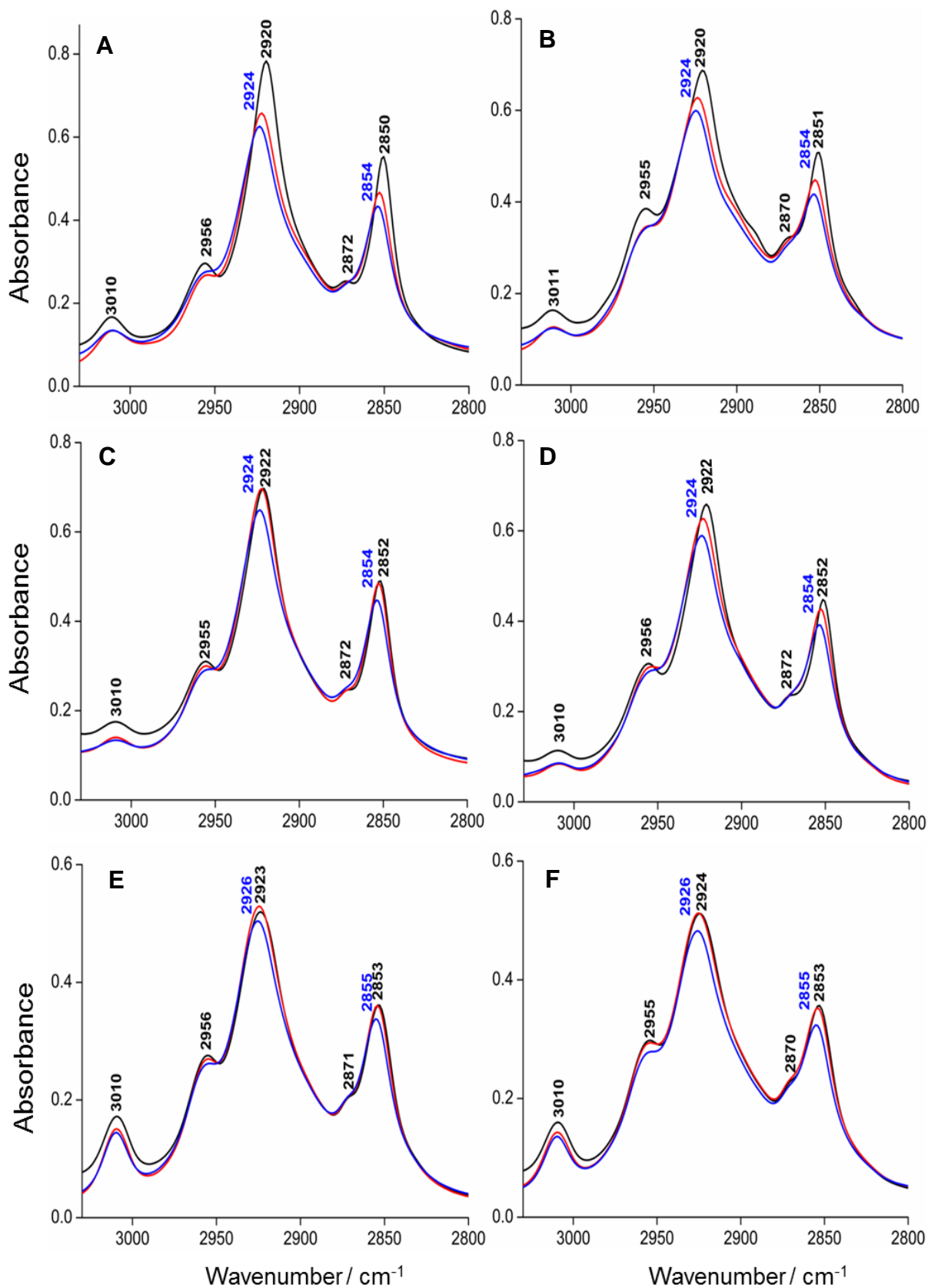


Figure 49. Temperature dependent ATR absorbance spectra of pure EPE (A), EPE/cholesterol (2:1) (B), EPC (C), EPC/cholesterol (2:1) (D), CL (E) and CL/cholesterol (2:1) (F). Line assignments: 0 °C (back), 40 °C (red), 90 °C (blue).

Figure 49 shows the asymmetric stretching ν_{as} CH₂ and symmetric stretching ν_s CH₂ vibrations near 2920 cm⁻¹ and 2850 cm⁻¹ respectively, for pure EPC, EPE, cardiolipin and their mixtures with cholesterol. Further vibrational modes originating from the terminal methyl groups (symmetric/asymmetric stretch; at 2870/2956 cm⁻¹) and from the =C–H stretching bands of unsaturated acyl chains at 3010 cm⁻¹ can be seen⁽²⁶⁹⁾.

The CH₂ symmetric and asymmetric vibrations exhibit temperature dependent variations in the peak position, height and bandwidth. For instance, the symmetric vibrational mode of the CH₂ group of pure EPE film is shifted from 2850 cm⁻¹ to 2854 cm⁻¹ at 0 °C and 90 °C respectively. Similar observations are made for other lipids (Figures 49C, 49E). In comparison, the incorporation of cholesterol to these lipid layers causes subtle changes in the CH vibrations inducing an upshift of the CH₂ symmetric vibration from 2850 (EPE) to 2851 cm⁻¹ (EPE/cholesterol) (Figures 49A, 49B), as well as for CH₂ asymmetric vibration where it shifts from 2923 (CL) to 2924 cm⁻¹ (CL/cholesterol) (Figures 49E, 49F). Furthermore, cardiolipin exhibits an intense peak assigned to =C–H at 3010 cm⁻¹ as compared to other lipids and this originates from the high percentage of unsaturation (18:2, 92%).

As a result, the temperature increase is accompanied by an upshift of the ν_{as} CH₂ and ν_s CH₂ vibrations by 2-3 cm⁻¹, the broadening of the bands and an overall decrease in their amplitudes⁽²⁷⁰⁾. These shifts reflect the high disorder and mobility of hydrocarbon chain indicating changes of the trans/gauche ratio in the lipid acyl chains which causes the transition from a gel (ordered) phase (L_β) to a liquid crystalline (disordered) phase (L_α)⁽²⁴⁸⁾.

3.1.1.2 Phase transition temperature

In order to determine the phase transition temperatures of the studied lipids and lipid/cholesterol systems, a series of spectra are recorded and averaged at each temperature. Then the wavenumber of symmetric CH₂ vibration is followed similarly to what have been reported for most FTIR studies on phospholipid gel to liquid crystalline transitions^(248, 266). The presented work allows the characterization of lipid systems and the examination of the influence of cholesterol on transition temperatures.

The infrared absorption bands at 2850 and 2920 cm⁻¹ can be used to monitor the phase transition temperature of lipid. The 2920 cm⁻¹ signal is rarely used in practice because it contains overlapping contributions from CH₃ groups. This band could also be perturbed by Fermi resonance interactions with the first overtones of the CH₂ scissoring vibration⁽²⁴⁸⁾. The

band near 2850 cm^{-1} is usually less perturbed by such effects and it originates mostly from the symmetric C-H stretching vibrations of the CH_2 groups⁽²⁴⁸⁾. This CH_2 vibration is a very sensitive indicator of the hydrocarbon chain melting phase transition. Sometimes the CH rocking modes are used to examine the phase transition temperature. For instance, Mendelsohn *et al.*⁽²⁷¹⁾ used the CD_2 rocking modes of the lipid specifically deuterated at various positions along the hydrocarbon chain to determine the conformational disorder (trans/gauche isomerisation) and to probe the transition temperature.

- **EPE and EPE/cholesterol (2:1)**

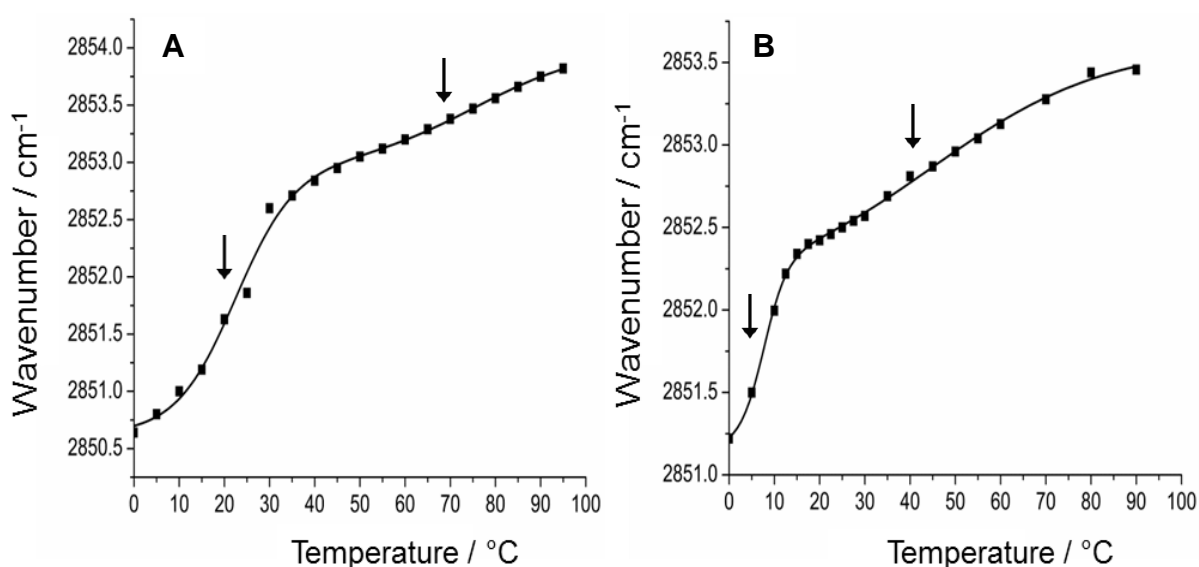


Figure 50. Plot of CH_2 wavenumber as function of temperature of pure EPE (A) and EPE/cholesterol (2:1) (B).

A first analysis of EPE lipid (Figure 50A) shows one main transition temperature at 22 °C and a second transition temperature which is difficult to determine at 70 °C (indicated by arrows). These obtained results are in good agreement with a previous study done by Pare *et al.*⁽⁸⁰⁾ on POPE system. These two temperatures correspond to the transition from a bilayer phase to a non-bilayer phase (Figure 51) where the conformational disorder of the acyl chains is the driving force behind this transition⁽⁴⁷⁾.

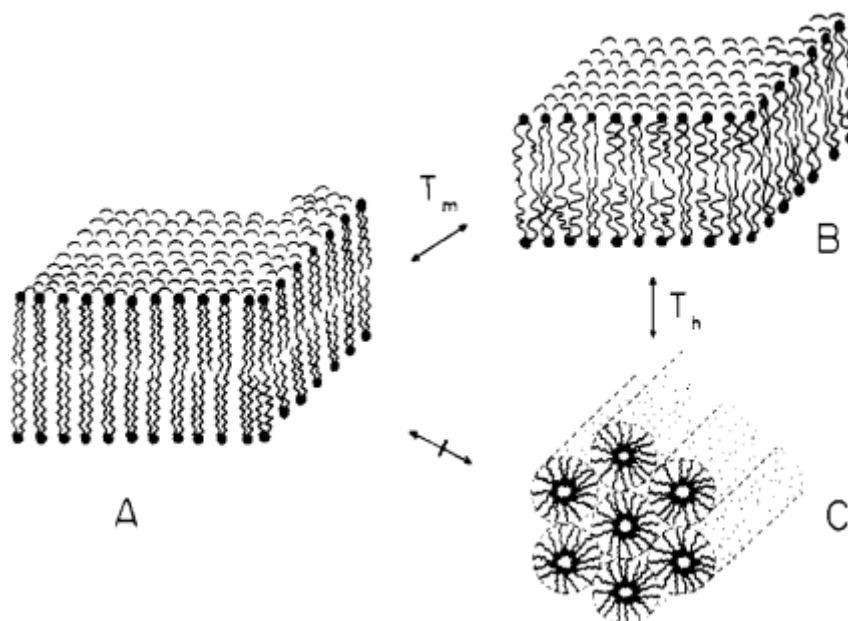


Figure 51. Description of the different lipid phases: the gel phase (A) the liquid crystalline phase (B) and the hexagonal non-bilayer structure (C). The phase transition temperatures are T_m (m for melting) and T_h (h for hexagonal) ⁽⁴⁷⁾.

The first transition temperature at 22 °C, called the T_m , involves the conversion of a relatively ordered gel state bilayer, where the hydrocarbon chains exist in their extended, rigid, all *trans* conformation, to a disordered liquid crystalline bilayer in which the hydrocarbon chains contain a number of *gauche* conformers.

The second transition temperature at 70 °C, called the T_h , shows the transition from liquid crystalline bilayer phase into an inverted hexagonal (H_{II}) phase non-bilayer structure. This phase is promoted by the unsaturated acyl chains. The amplitude of the shift of CH_2 between different phases is smaller than that observed for the gel to liquid crystalline phase transition because the acyl chain order is less perturbed during the lamellar to hexagonal phase transition.

In the presence of cholesterol (EPE/cholesterol 2:1 mixture (Figure 50B)), the L_β to L_α phase transition and L_α to H_{II} are both shifted toward lower temperatures. The T_m is decreased to 8 °C because cholesterol addition leads to looser lipid packing. Cholesterol is reported to disorder the L_β phase whereas it orders the phospholipids in the L_α phase. Between 12 and 30 °C, the system is in the fluid phase and cholesterol now has an ordering effect on the acyl chains of EPE. It causes a decrease in the frequency shift amplitude which can be interpreted as a reduction of the conformational disorder introduced during this transition.

The T_h transition temperature is shifted from 70 °C of pure EPE to 45 °C for EPE/cholesterol mixture which is in agreement with the results obtained by Pare *et al.* and Epand *et al.* ^(47, 80, 82) on POPE system where they reported a decrease in the T_h temperature between 0 and 30 mol % cholesterol. Cholesterol affects the transition from the liquid crystalline lamellar to hexagonal phase because of its small head group which is considered as a cone shaped molecule that promotes hexagonal phase formation ⁽⁸²⁾.

Indeed, this study allows probing the properties of EPE lipid and examining the influence of cholesterol on the EPE lipid propensities to form non lamellar phases.

- **EPC and EPC/cholesterol (2:1)**

The temperature dependencies of the frequencies of the symmetric CH_2 stretching mode in pure EPC film and in the EPC/cholesterol system are displayed in Figure 52. In both plots there is an increase in the frequency with increasing temperature. The main phase transition is found at 29 °C for EPC (Figure 52A) which is lower by around 10 °C from the value reported by Popova *et al.* for dry EPC ^(48, 249).

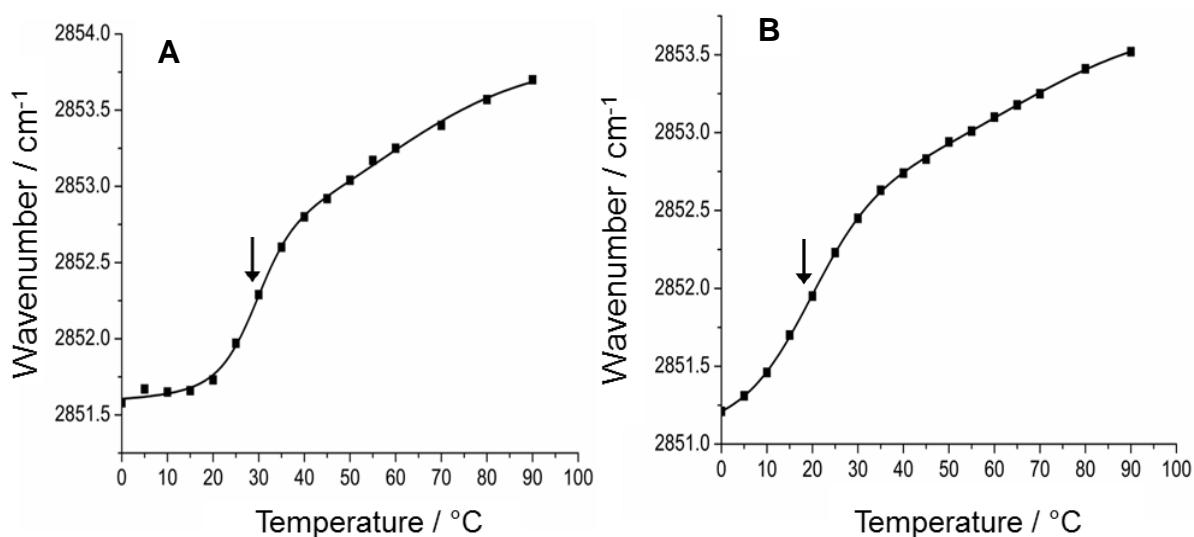


Figure 52. Plot of CH_2 wavenumber as function of temperature of pure EPC (A) and EPC/cholesterol (2:1) (B).

Figure 52A reveals the presence of one main transition temperature where EPC moves from the gel bilayer phase to the liquid disordered bilayer phase. This finding is consistent with the literature where it was suggested that EPC is stabilized in bilayer form due to the cylindrical shape of the molecule. In contrast, EPE exhibits two transition temperatures (Figure 50A) necessary for its stabilization in the hexagonal phase owing to its conical shape⁽²⁷²⁻²⁷⁴⁾.

Concerning EPC/cholesterol (2:1) (Figure 52B), the transition temperature is 19 °C (indicated by arrow), it decreases by 10 °C in comparison to EPC. The decrease in T_m after the incorporation of cholesterol is in line with previous reported studies using differential scanning calorimetry on cholesterol /phosphatidylcholine mixtures^(76, 275, 276). Usually, the cholesterol/phosphatidylcholine interaction depends on the hydrophobic mismatch effect. Previous studies showed that cholesterol stabilizes the gel phase of PC with acyl chains shorter than 17 carbon atoms while it destabilizes the gel phase of longer chain (longer than 18 carbon atoms)⁽⁷⁶⁾. So, as long as the hydrophobic steroid part of cholesterol is comparable with that of phosphatidylcholine chains this causes a strong interaction.

- **CL and CL/cholesterol (2:1)**

Cardiolipin has a unique chemical structure and this structure determines its physical properties. Few studies were performed on the organization and the thermotropic phase behavior of cardiolipin systems^(53, 54, 277). Hubner *et al.*⁽⁵³⁾ reported the transition temperatures of two cardiolipins (16:0) and (18:0) probing the effect of hydrocarbon chain length on the phase transition of saturated cardiolipins. Besides it was demonstrated that there is a clear effect of the monovalent and divalent cations on the L_β/L_α phase transition temperature of cardiolipin^(54, 277-280). The following section discusses the frequency versus temperature plots of pure cardiolipin in comparison to cardiolipin/cholesterol mixture (Figure 53) to see the influence of cholesterol.

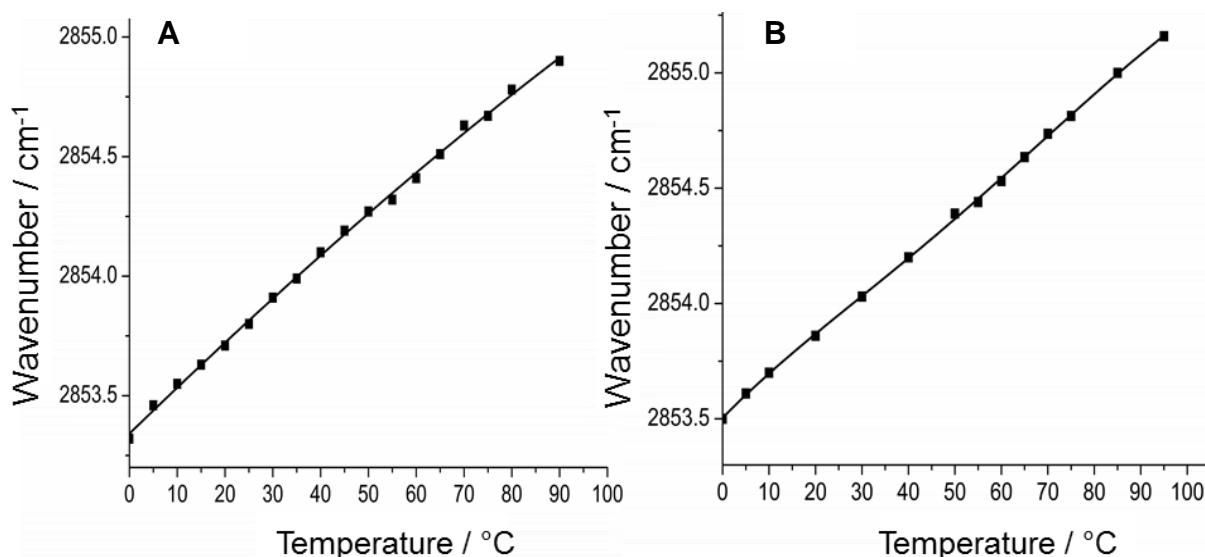


Figure 53. Plot of CH₂ wavenumber as function of temperature of pure CL (A) and CL/cholesterol (2:1) (B).

In both cases, there are no steep sigmoidal frequency curves. The frequency increases in a linear manner as function of temperature indicating that there is no transition from one phase to another. The results observed revealed that the high degree of unsaturation in beef heart cardiolipin does not allow the formation of a lamellar bilayer structure leading to the absence of a transition from gel to liquid crystalline phase. This unsaturated cardiolipin only forms a hexagonal (H_{II}) nonlamellar structure in which the C-OH and PO₄⁻ groups are buried⁽⁵³⁾. For CL/cholesterol, very little work has been reported on the role of cholesterol on cardiolipin polymorphism. Lu. *et al.*⁽⁸⁶⁾ found that cholesterol promotes the formation of hexagonal structure in cardiolipin.

In summary, our results on EPE, EPC and cardiolipin indicate that the presence of cholesterol in lipid systems induces conformational changes, downshifts the transition temperatures (Table 13) and affects lipid polymorphisms.

Table 13. The transition temperatures of EPC, EPE lipids and their mixtures with cholesterol.

Transition Temperature	EPE	EPE/cholesterol	EPC	EPC/cholesterol
T _m	22 °C	8 °C	29°C	19°C
T _h	70 °C	45 °C		

3.1.1.3 Bending modes: CH₂ wagging, rocking and scissoring vibrational modes

The bending vibrations of methylene and methyl groups are usually seen in the 1500-1350 cm⁻¹ region. The CH₂ scissoring vibration is located at 1465 cm⁻¹ and this band is sensitive to the acyl chain packing and conformation⁽²⁴⁸⁾. The CH₂ wagging band is observed between 1300-1400 cm⁻¹ in a region free of interferences of other IR active groups with the exception of CH₃ bending band. The CH₂ rocking modes are found in the region 1150-700 cm⁻¹.

In some cases, the CH₂ rocking and wagging vibrations are coupled to vibrations of polar groups as in the lipid membranes and this leads to the enhancement of the intensities of these bands. Upon heating, the introduction of gauche conformers leads to uncoupling of these vibrations from the polar group. The overall effect is the large decrease in the intensity and the increase of band width which could be interpreted as the conformational disorder in the acyl chains that occurs at hydrocarbon chain melting transitions.

Sometimes the chain melting transitions causes the decrease in the intensities of CH₂ wagging and rocking modes to the extent that they disappear from the infrared spectra of lipids. Thus the changes in the intensities of CH₂ rocking and wagging vibrations could be a useful indicator of hydrocarbon chain melting phase transition and conformational changes that affect the orientation of polar groups.

The infrared spectra of EPC, EPE, cardiolipin and the lipid mixtures with cholesterol show strong absorption bands near 1465 cm⁻¹ and 1377 cm⁻¹ that correspond to CH₂ scissoring mode and CH₃ umbrella band respectively (Figure 54). There is a weak band at 1417 cm⁻¹ which arises from the $\delta(\alpha\text{-CH}_2)$ group of the acyl chains next to the ester group. For EPC and EPC/cholesterol (Figures 54C, 54D), there is an additional peak at 1485 cm⁻¹ which is attributed to $\delta_{\text{as}}(\text{N}^+(\text{CH}_3)_3)$ of the choline group. Interestingly, the common feature between all these figures is the decrease in their amplitudes and increase of the width at higher temperature indicating the increasing disorder (Figure 54).

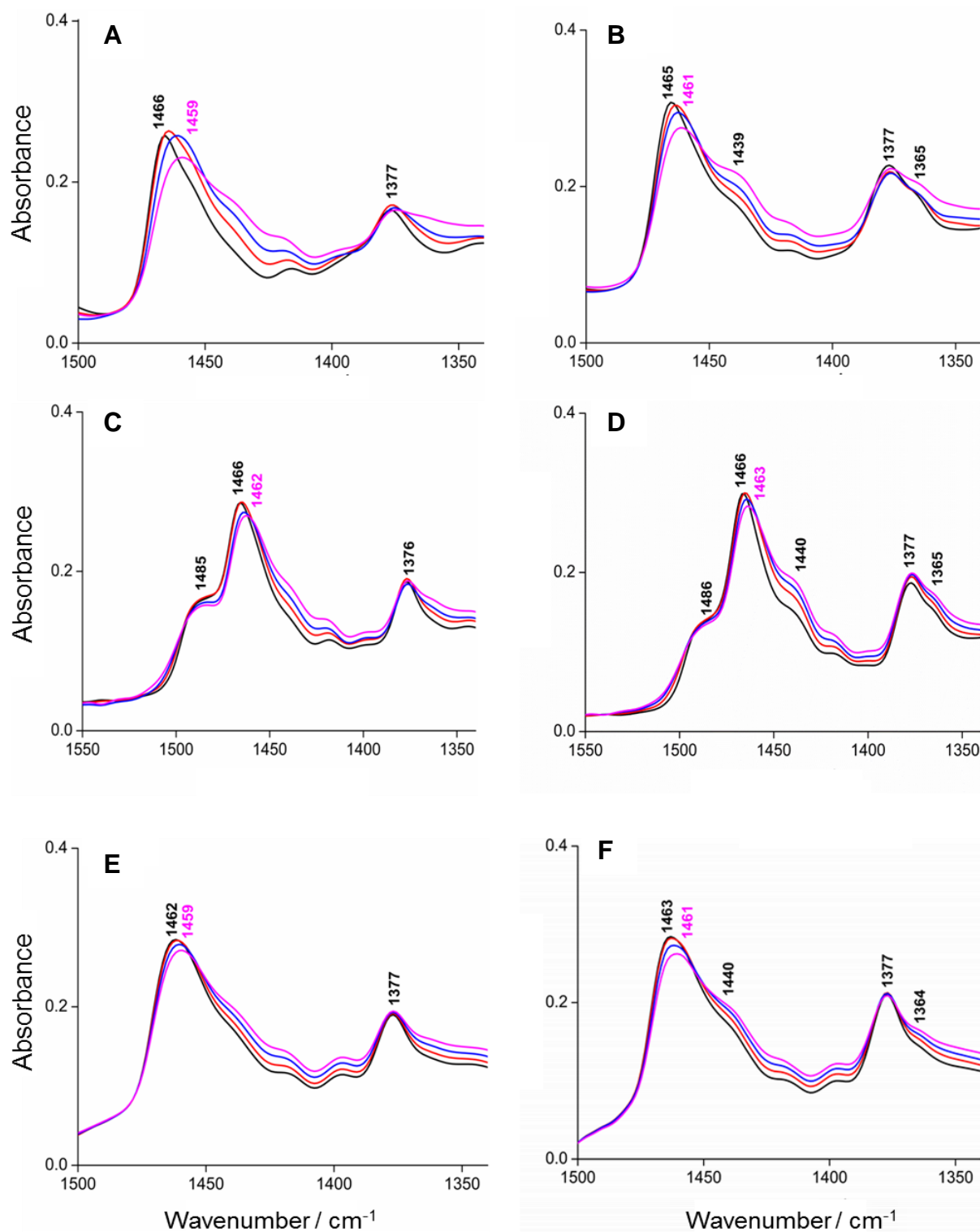


Figure 54. The CH bending region of EPE (A), EPE/cholesterol (2:1) (B), EPC (C), EPC/cholesterol (2:1) (D), CL (E), CL/cholesterol (2:1) (F) under the effect of temperature. Line assignments: 5 °C (back), 20 °C (red), 40 °C (blue) and 60 °C (magenta).

3.1.2 Spectral features characteristics of the lipid head group

The head group of the lipid gives rise to a number of infrared bands that are assigned to the phosphate and the CO vibrations. These bands reflect the level of hydration and conformational changes taking place around the head group.

3.1.2.1 CO vibration

The properties of lipids are often studied on the basis of the carbonyl absorption band which arises from the stretching vibrations of two ester carbonyl (C=O) groups. The position and the shape of the CO absorption band are sensitive to the hydrogen bonding interaction. It usually includes two underlying peaks: a higher wavenumber component which originates from C=O groups that are not hydrogen bonded and the second component corresponds to C=O groups that are involved in hydrogen bonding^(281, 282).

Furthermore, there are C-O stretching bands of the ester groups between 1200 and 1000 cm⁻¹ but these vibrational modes are less informative since they are coupled to C-C stretching vibrations. The C=O stretching vibration has a broad and intense signal around 1738 cm⁻¹ in a region free from contributions of other infrared active groups, making it useful for the interpretation of the structural changes in the local environments⁽²⁴⁸⁾.

Figure 55 presents an enlarged view of the CO stretching band of the pure lipids and different mixtures of lipids/cholesterol under the effect of temperature. The absorbance spectra upon heating and cooling are perfectly reversible (see appendix 2 for cooling step). The C=O absorption bands are seen at 1737 cm⁻¹, 1736 cm⁻¹ and 1739 cm⁻¹ for EPE, EPC and cardiolipin respectively (Figures 55A, 55C, 55E). Upon heating, the CO vibration is shifted to a higher wavenumber accompanied by an increase in the amplitude and a decrease of the band width. The shape of the CO band changes when the lipid passes from the gel phase to the liquid disordered phase since the relative intensities of the high and low frequency components change.

The amplitude of the CO vibration is sensitive towards the degree of hydration, revealing the presence of the intramolecular hydrogen bonds with large proton polarizability. The intensity of this band decreases at low temperatures caused by the interaction of these polarizable hydrogen bonds with their hydration water environment^(283, 284).

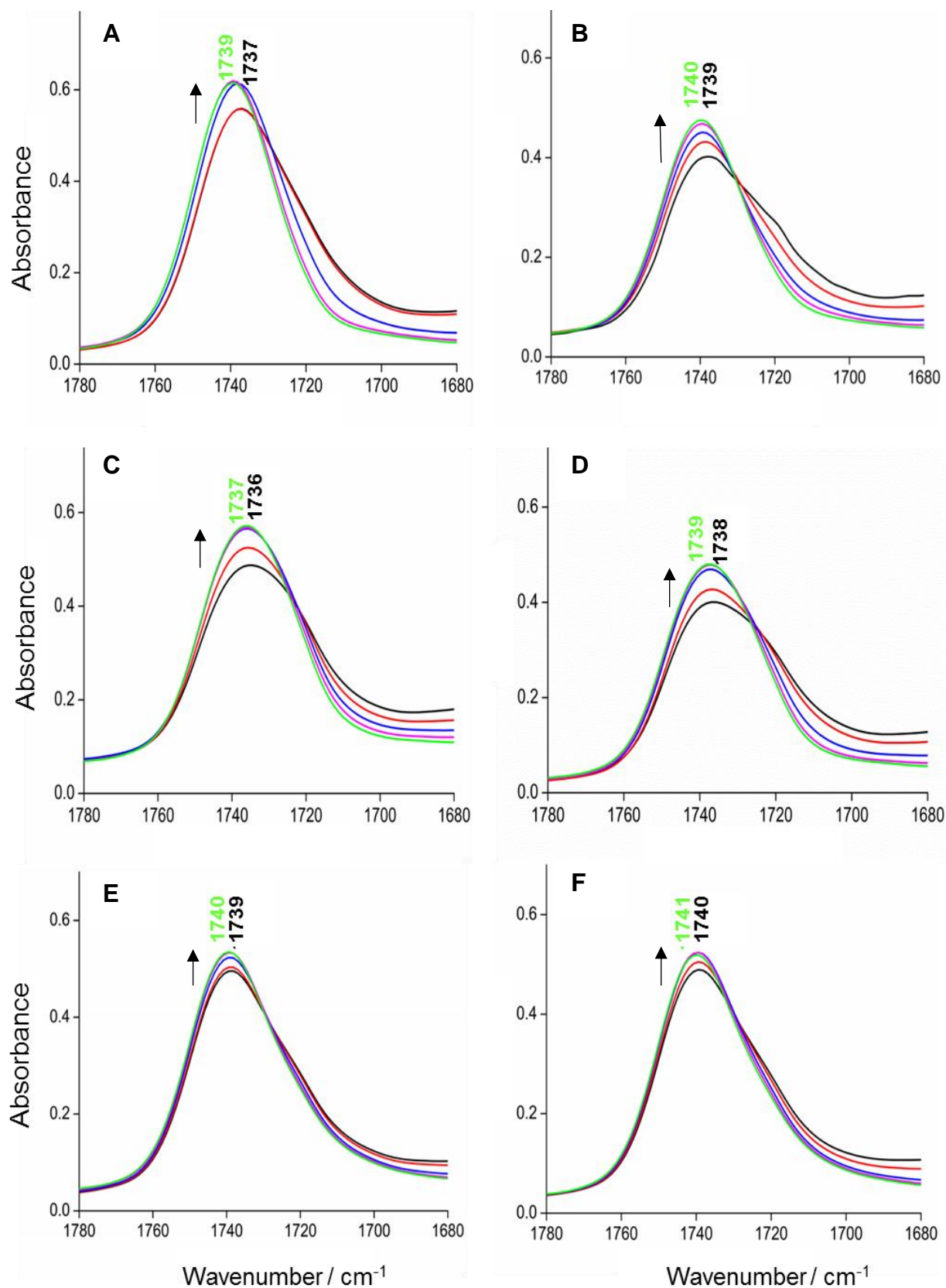


Figure 55. The temperature dependent C=O band of EPE (A), EPE/cholesterol (2:1) (B), EPC (C), EPC/cholesterol (2:1) (D), CL (E), CL/cholesterol (2:1) (F). Line assignment: 5 °C (back), 10 °C (red), 20 °C (blue), 30 °C (magenta) and 40°C (green).

The addition of cholesterol affects the shape of the C=O stretching signal which becomes highly asymmetric and shows a larger bandwidth in comparison to the data of the pure lipid. This asymmetry decreases at high temperatures as can be seen in (Figures 55B, 55D and 55F). Additionally, the carbonyl bands shift to higher frequencies in the presence of cholesterol and is now found at 1737 cm^{-1} for EPE and at 1739 cm^{-1} for EPE/cholesterol. The small upshift of 2 cm^{-1} indicates that the insertion of cholesterol perturbs the system leading to increased lipid spacing between lipid molecules (Figure 56) and thus interrupting the hydrogen bonding interaction of CO.

It is noted that cholesterol has no absorption bands in the spectral zone characteristic for the CO vibration (see Figure 48), so any effects seen here are correlated to the interaction between cholesterol and lipid either in a direct way by the formation of hydrogen bonding between CO group of the lipid and hydroxyl group of cholesterol or indirectly through conformational effects.

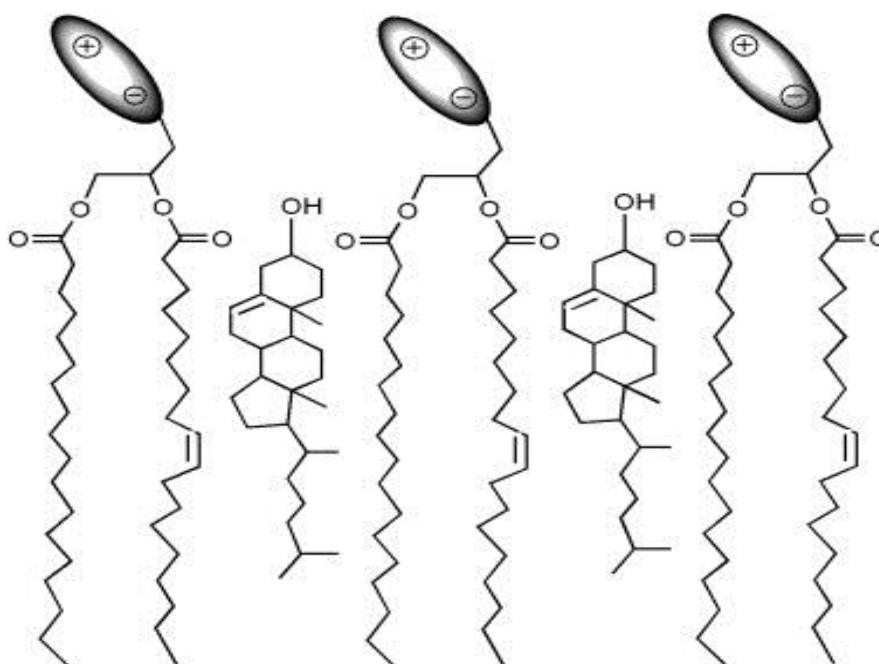


Figure 56. Schematic representation of cholesterol insertion between acyl chains of lipids ⁽⁹⁶⁾.

- **Carbonyl bands of EPC and EPC/cholesterol (2:1)**

The carbonyl bands with their fitted components for EPC and EPC/cholesterol are depicted in Figure 57 showing a high frequency component and a low frequency component at around 1740 cm^{-1} and 1730 cm^{-1} respectively (Table 14). The deconvolution is carried out for data obtained at 5 and 40 °C where EPC exists in the gel phase and in the liquid crystalline phase respectively (T_m for EPC is 29 °C as indicated in section 3.1.1.2).

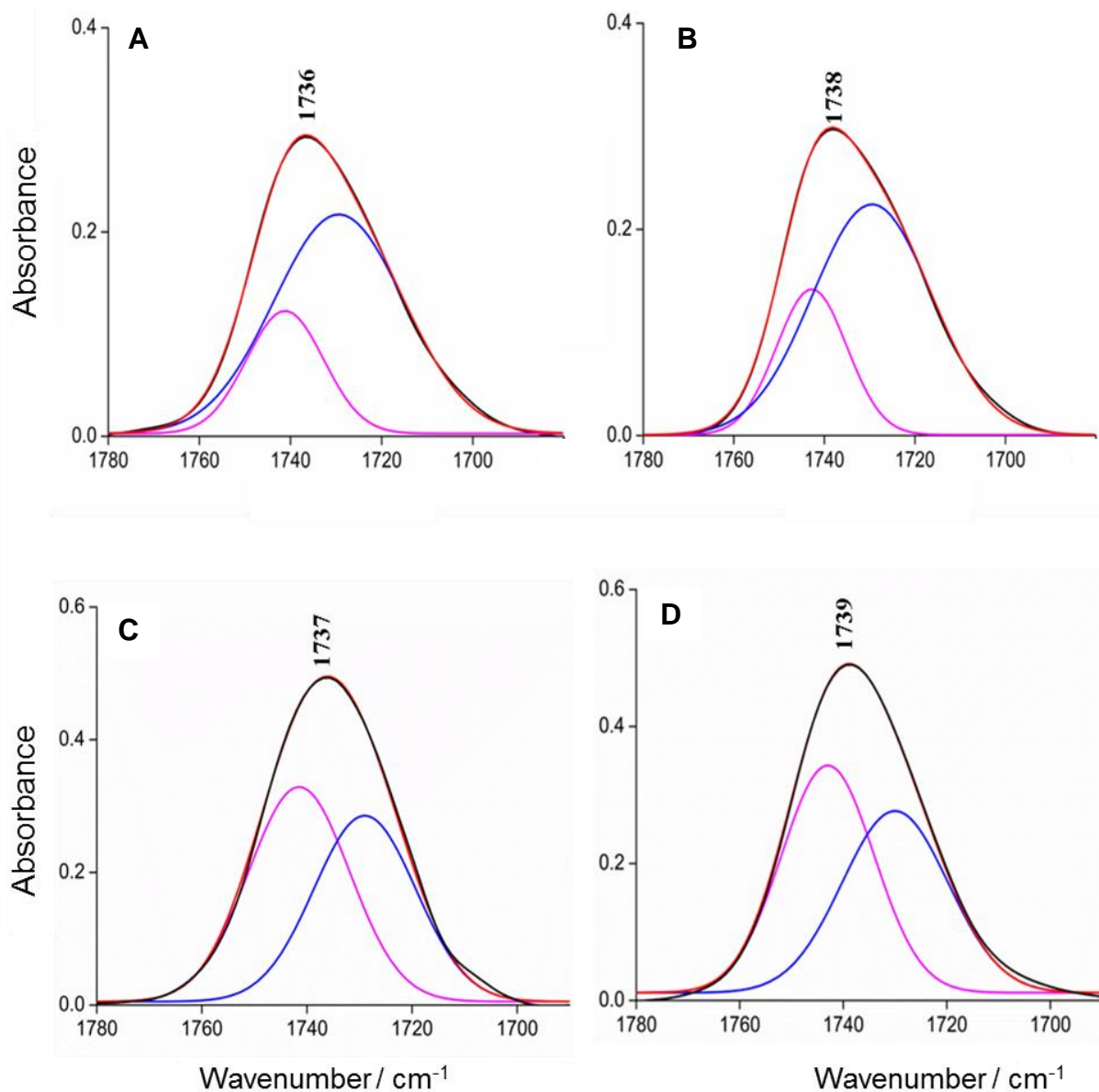


Figure 57. Comparison of the carbonyl band of EPC 5 °C (A), EPC/cholesterol 5 °C (B), EPC 40 °C (C) and EPC/cholesterol 40 °C (D). CO band experimental (black line), fitted curve (red line), low frequency component (blue line) and high frequency component (magenta line).

Table 14. Positions of the low and high frequency components of carbonyl band obtained by deconvolution at a temperature of 5 °C and 40 °C for EPC and EPC/cholesterol. The error on the peak positions is 0.1-0.4 cm⁻¹ and it results from the calculation.

	Low frequency component (cm ⁻¹)	High frequency component (cm ⁻¹)
EPC 5 °C	1729.3	1741.2
EPC/Cholesterol 5 °C	1729.4	1742.7
EPC 40 °C	1729.5	1741.5
EPC/Cholesterol 40 °C	1730.0	1743.0

At 5 °C, the carbonyl band is dominated by the low frequency component. The position of the low frequency component is the same for both EPC and EPC/cholesterol. The high frequency component is shifted up by 1.5 cm⁻¹ in the presence of cholesterol. At 40 °C, the carbonyl band looks highly symmetric for both EPC and EPC/cholesterol (Figures 57C, 57D). The intensity of the high frequency component at 40 °C is higher than at 5 °C. This indicates that at higher temperature part of the free water that is not specifically bound in the lipid film evaporates, so the population of non-hydrogen bonded carbonyl groups is higher. Thus, the transition from the gel phase to the liquid crystalline phase causes an increase in the high frequency component and a decrease in the low frequency component. In addition, the insertion of cholesterol leads to an up shift of the high frequency component due to the conformational effects.

Zoran *et al.* ⁽²⁸⁵⁾ analyzed the effect of cholesterol on phosphatidylcholines based on the difference of the peak positions of the high and low frequency components. Here, the difference between the high and low frequency components in the case of pure EPC and EPC/cholesterol (Table 14) is very close in both cases (13 cm⁻¹), indicating that the effect of cholesterol is indirect and it is mainly influencing the access of interfacial water to the carbonyl group as suggested by Zoran *et al.* ⁽²⁸⁵⁾. On the contrary, if the difference is large between EPC and EPC/cholesterol, this means that cholesterol forms stronger hydrogen bonds with carbonyl groups than water molecules.

- **Carbonyl bands of EPE and EPE/cholesterol (2:1)**

The deconvolution of CO stretching vibration in the gel phase, liquid crystalline phase and in the hexagonal phase of EPE and EPE/cholesterol is illustrated in Figure 58. The CO band is constituted of two frequency components as described before for EPC (Table 15).

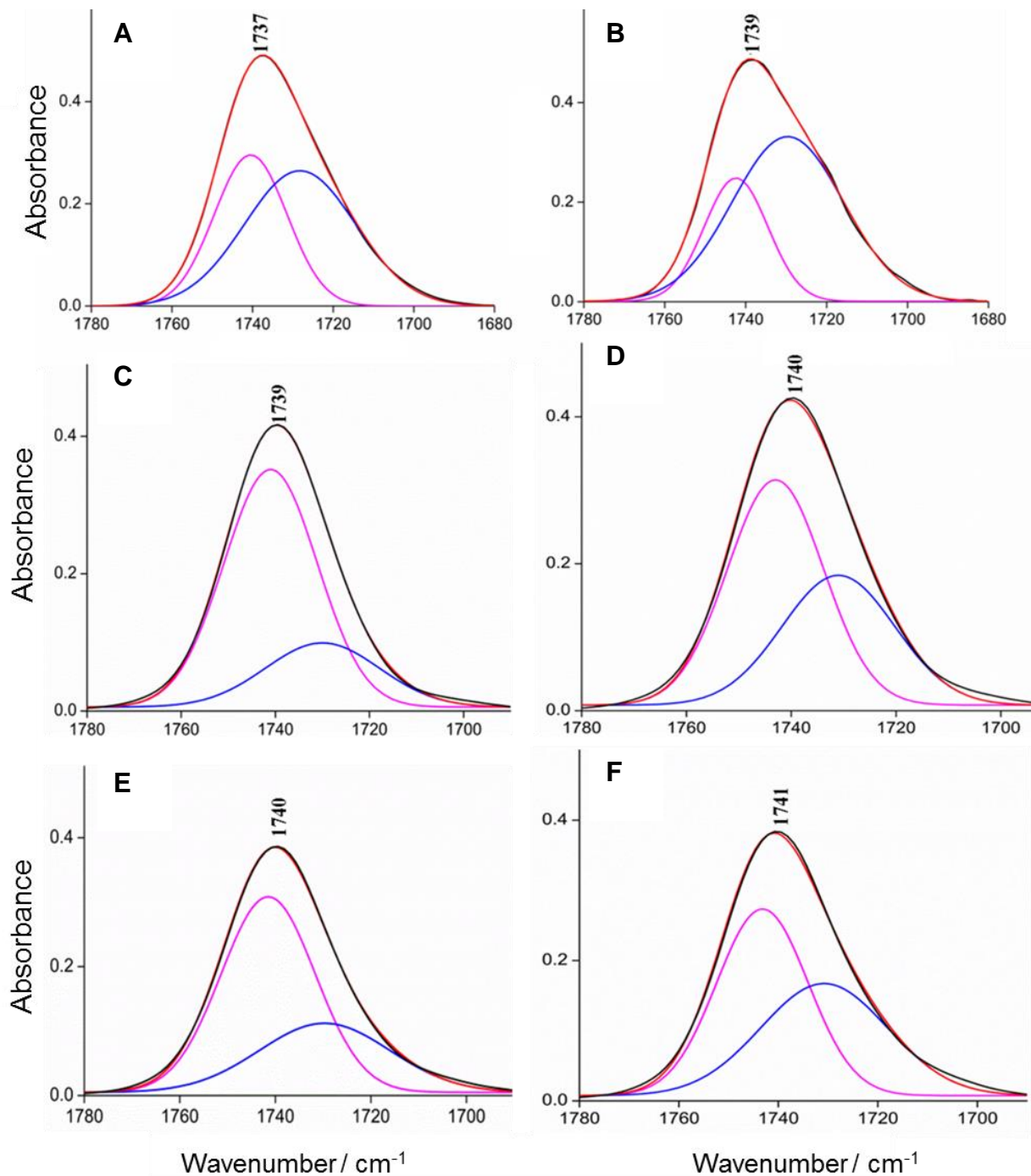


Figure 58. Comparison of the carbonyl band for EPE 5 °C (A), EPE/cholesterol 5 °C (B), EPE 40 °C (C), EPE/cholesterol 40 °C (D), EPE 80 °C (E) and EPE/cholesterol 80 °C (F). CO band experimental (black line), fitted curve (red line), low frequency component (blue line) and high frequency component (magenta line).

Table 15. Positions of the low and high frequency components of carbonyl band obtained by deconvolution at a temperature of 5 °C, 40 °C and 80 °C of EPE and EPE/cholesterol.

	Low frequency component (cm ⁻¹)	High frequency component (cm ⁻¹)
EPE 5 °C	1729.0	1740.4
EPE/Cholesterol 5 °C	1729.5	1742.4
EPE 40 °C	1730.0	1741.0
EPE/Cholesterol 40 °C	1730.4	1743.0
EPE 80 °C	1729.7	1741.5
EPE/Cholesterol 80 °C	1730.0	1743.2

Comparing both EPE and EPE/cholesterol in the gel phase at 5 °C, the high frequency component is higher in intensity in case of EPE indicating a tight lipid packing (Figure 58A). When cholesterol is added there is a decrease in the intensity of the high frequency component and an increase in the low frequency component (Figure 58B) suggesting that the presence of cholesterol at low temperatures causes looser lipid packing, where carbonyl groups can interact with free water⁽⁸⁰⁾.

The carbonyl bands for both EPE and EPE/cholesterol in the fluid phase at 40 °C and in the hexagonal phase at 80 °C are highly symmetric (Figures 58C, 58D, 58E and 58F). At high temperature, the high frequency component dominates over the low frequency component. Probably, this is due to the loss of free water from the lipid film which leads to the decrease of hydrogen bonding.

- **Carbonyl bands of cardiolipin and cardiolipin/cholesterol (2:1)**

The beef heart cardiolipin exhibits a broad ester C=O stretching band around 1740 cm^{-1} (Figure 59). As demonstrated throughout the previous sections, the deconvolution of the carbonyl bands as function of temperature yields two different components. The frequencies of these components are summarized in Table 16.

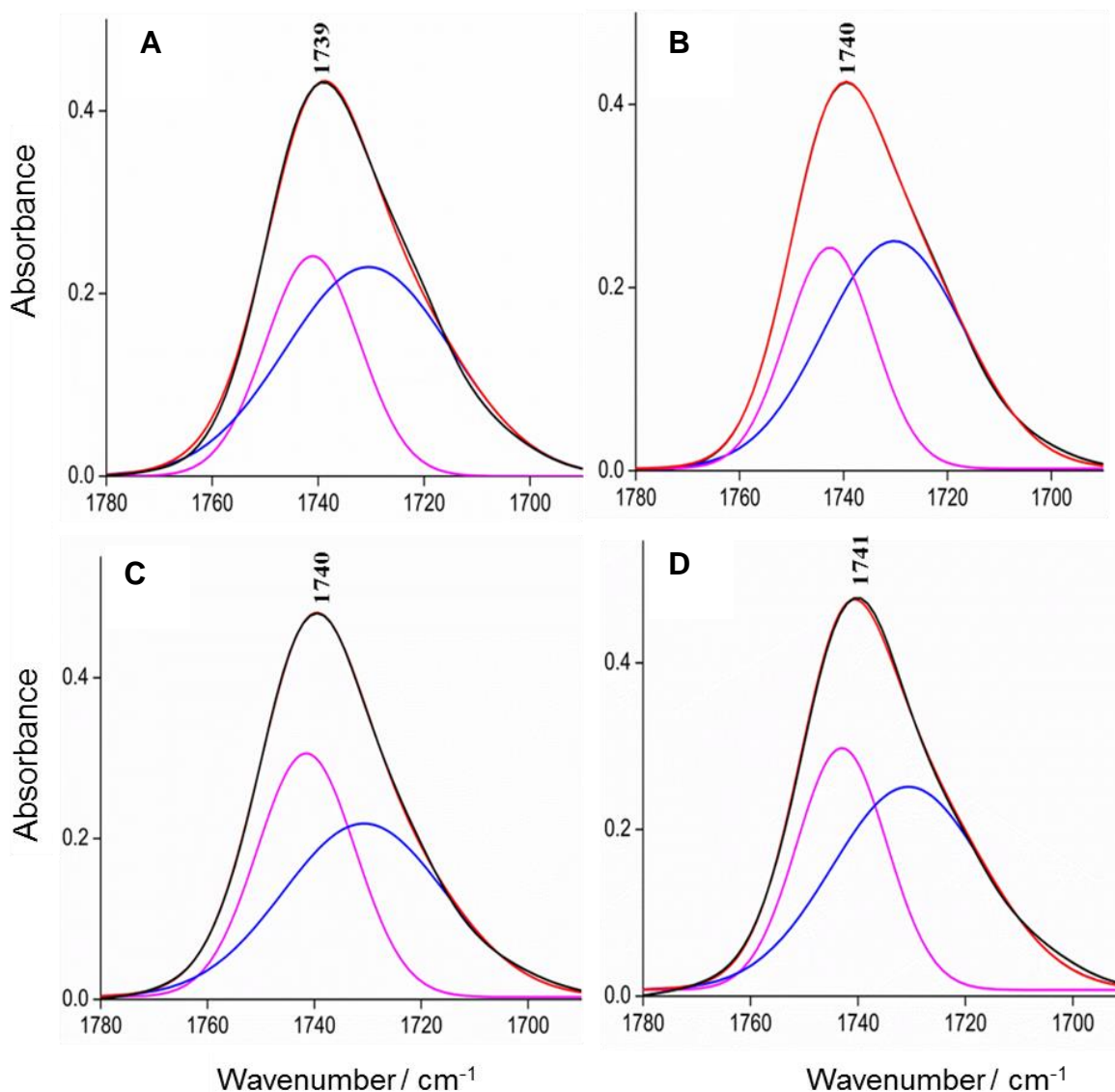


Figure 59. Comparison of the carbonyl band for CL $5\text{ }^{\circ}\text{C}$ (A), CL/cholesterol $5\text{ }^{\circ}\text{C}$ (B), CL $40\text{ }^{\circ}\text{C}$ (C) and CL/cholesterol $40\text{ }^{\circ}\text{C}$ (D). CO band experimental (black line), fitted curve (red line), low frequency component (blue line) and high frequency component (magenta line).

Table 16. Positions of the low and high frequency components of carbonyl band obtained by deconvolution at a temperature of 5 °C and 40 °C of CL and CL/cholesterol.

	Low frequency component (cm ⁻¹)	High frequency component (cm ⁻¹)
CL 5 °C	1730.5	1741.0
CL/Cholesterol 5 °C	1730.3	1742.6
CL 40 °C	1730.7	1741.5
CL/Cholesterol 40 °C	1730.6	1743.0

The increase in the temperature from 5 to 40 °C causes a decrease in the low frequency component and increase in the high frequency component (Figures 59A, 59C) as described for EPC and EPE lipids (Figures 57, 58). These results indicate that there is a decrease in the hydrogen bonding interaction of the fatty acid carbonyl groups at high temperature. In addition, the incorporation of cholesterol causes the small upshift of the high frequency component by 1.5 cm⁻¹. For instance, it is shifted from 1741.0 cm⁻¹ to 1742.6 cm⁻¹ for CL and CL/cholesterol respectively (Table 16). This could be attributed to the conformational effects induced by cholesterol.

The results observed here for the CL alone are in good agreement with the study of Hubner *et al.*⁽⁵³⁾ who discussed the properties of C=O band in beef heart unsaturated CL (as used here). They found that the absence of the shoulder at 1712 cm⁻¹ in beef heart CL indicates weak hydrogen bonding and they correlated this to the different spatial arrangement of C-OH/P-OH and C=O groups in the hexagonal II phase.

3.1.2.2 Phosphate region

Beside the analysis of CO band, there is another group of infrared bands characteristic of phospholipids head groups. The dominant peaks from 1300-1000 cm⁻¹ originate mainly from the vibrations of phosphate moiety; there is no contribution from cholesterol in this region (see Figure 48).

- Phosphate group absorptions of EPC and EPC/cholesterol (2:1)

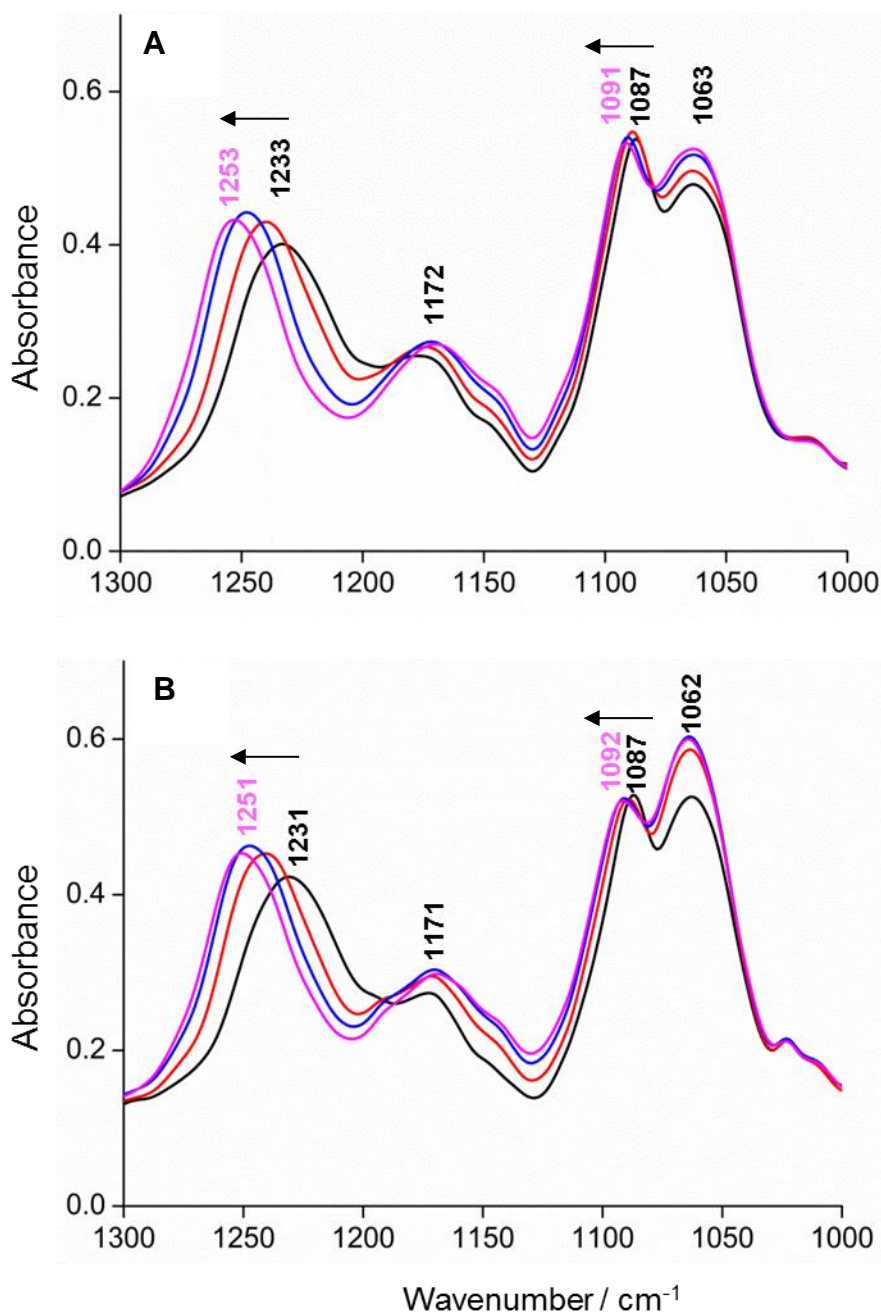


Figure 60. Enlarged view of the temperature dependent $\nu_{as}(\text{PO}_2^-)$ and $\nu_s(\text{PO}_2^-)$ stretching modes of EPC (A), EPC/cholesterol (2:1) (B). Line assignments: 5 °C (back), 20 °C (red), 40 °C (blue) and 60 °C (magenta).

Figure 60 illustrates the temperature dependence of phosphate stretching vibrations in EPC and EPC/cholesterol. The two strong bands around 1087 and 1233 cm⁻¹ correspond to the phosphate symmetric and asymmetric stretching modes, respectively. The latter mode can be used to obtain structural information about the interfacial region of the lipid bilayer. Furthermore, its position is sensitive to the formation of hydrogen bonds and it shifts to lower frequencies with increased hydrogen bonding^(270, 286).

The $\nu_{\text{as}}(\text{PO}_2^-)$ stretching vibration for EPC and EPC/cholesterol at 5 °C are found at 1233 and 1231 cm^{-1} respectively (Figures 60A, 60B). With increasing temperature, a shift to higher frequencies is observed. The formation of the liquid crystalline phase induces an upshift of the $\nu_{\text{as}}(\text{PO}_2^-)$ to 1253 cm^{-1} for EPC and 1251 cm^{-1} for EPC/cholesterol. The shift of about 20 cm^{-1} to higher wavenumber indicates less strong hydrogen bonding since the amount of free water is reduced at higher temperatures. These results are consistent with studies done by Hielscher *et al.* ⁽¹⁸¹⁾ and Lewis *et al.* ⁽²⁷⁰⁾ where they reported a similar temperature dependence of different lipids.

Furthermore, the $\nu_{\text{as}}(\text{PO}_2^-)$ of EPC/cholesterol is seen at lower wavenumber in comparison to EPC, indicating a higher degree of hydrogen bonding interaction. The insertion of cholesterol between the acyl chains of the lipids causes an increase in the average distance between the lipid molecules. In the headgroup region, the increase in spacing in the structure results in a less tightly packed headgroup and thus increases its hydration level (see Figure 56). This finding is in agreement with the results obtained by Chen *et al.* ⁽²⁸⁷⁾ where the $\nu_{\text{as}}(\text{PO}_2^-)$ vibration is seen at 2-3 cm^{-1} lower wavenumber after the incorporation of cholesterol. In addition, this observation is consistent with the study done by Verma *et al.* ⁽²⁶²⁾ who reported a shift to lower frequency in the phosphate vibration of lecithin in the presence of 50 mole percent cholesterol suggesting the formation of hydrogen bonding interaction between PO and hydroxyl group of cholesterol.

- **Phosphate group absorptions of EPE and EPE/cholesterol (2:1)**

The spectral region of the symmetric and asymmetric (PO_2^-) stretching modes of EPE and EPE/cholesterol is depicted in Figure 61. The comparison between EPE and EPC at 5 °C (Figures 61A and 60A) shows that the frequency of the asymmetric (PO_2^-) vibration varies from 1233 cm^{-1} in EPC to 1221 cm^{-1} in EPE. The shift toward lower frequencies in EPE lipid can be explained by the intra and intermolecular hydrogen bonding of NH_3^+ with PO_2^- ⁽²⁸⁸⁻²⁹⁰⁾. Therefore, the frequency of PO_2^- depends on the nature of the polar head group.

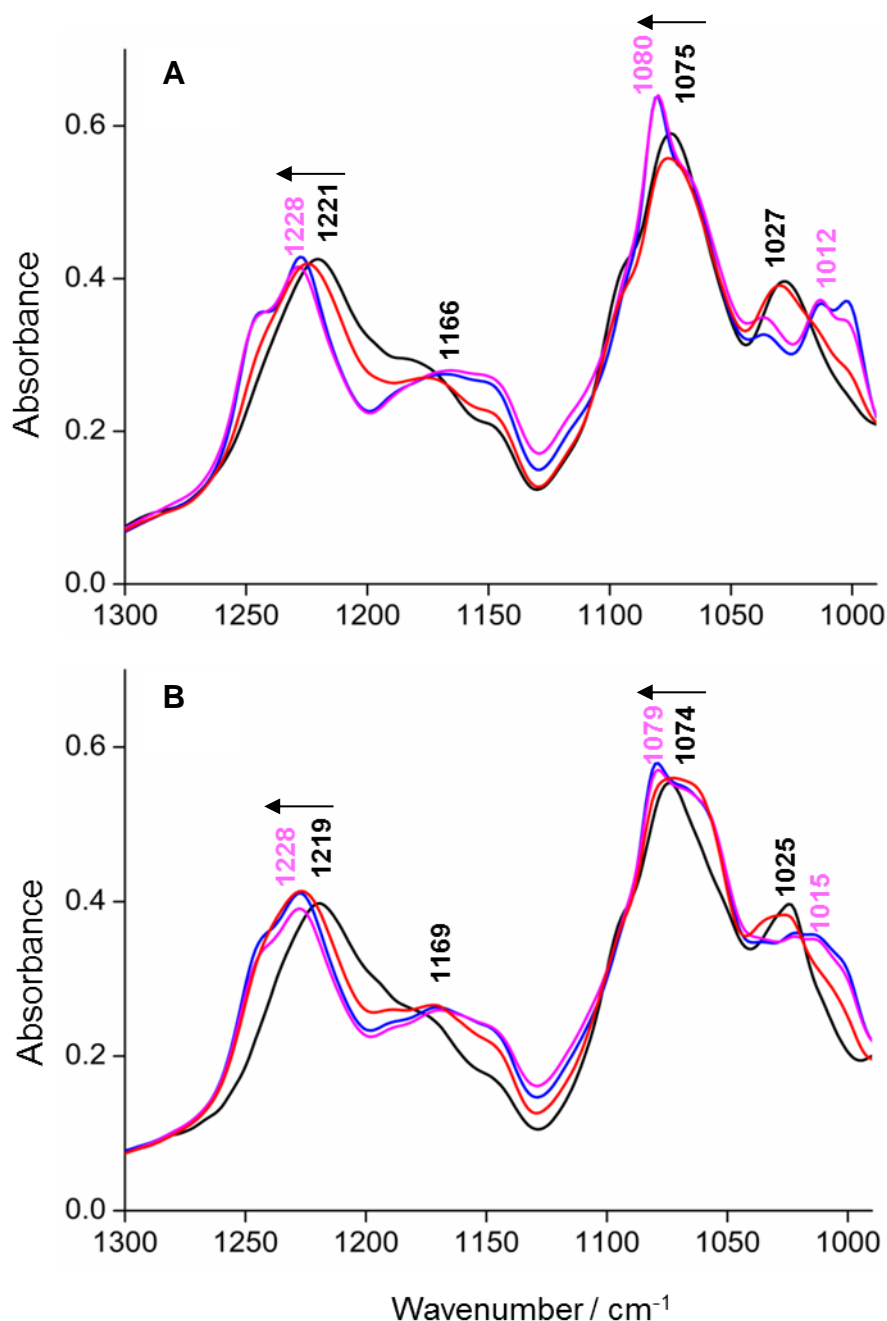


Figure 61. Enlarged view of the temperature dependent $\nu_{\text{as}}(\text{PO}_2^-)$ and $\nu_{\text{s}}(\text{PO}_2^-)$ stretching modes of EPE (A), EPE/cholesterol (B). Line assignments: 5 °C (back), 20 °C (red), 40 °C (blue) and 60 °C (magenta).

The temperature increase causes a shift of $\nu_{\text{as}}(\text{PO}_2^-)$ of EPE from 1221 cm⁻¹ (5 °C) to 1228 cm⁻¹ (40 °C) (Figure 61A). The observed shift is explained by the increased lipid spacing and lower hydrogen bonding between water and phosphate at high temperatures. This finding is in contrast with the study done by Goni *et al.* ⁽²⁹¹⁾ where they reported no changes in the asymmetric phosphate vibration of bacterial phosphatidylethanolamine at different

temperatures. Another useful feature is clearly seen where the asymmetric and symmetric phosphate bands are splitted in two peaks. This indicates the presence of two different populations of phosphate groups: one is free and the other is hydrogen bonded.

The interaction of cholesterol with EPE is similar to that described for EPC, where the addition of cholesterol leads to a decrease of the $\nu_{as}(\text{PO}_2^-)$ from 1221 cm^{-1} (EPE $5\text{ }^\circ\text{C}$) to 1219 cm^{-1} (EPE/cholesterol $5\text{ }^\circ\text{C}$) (Figures 61A, 61B). This is attributed to the increase in the hydration level around the head group after incorporation of cholesterol.

- **Phosphate group absorptions of CL and CL/cholesterol (2:1)**

The study of temperature dependence of the phosphate vibrations in the case of beef heart cardiolipin which contains two phosphate groups is examined in Figure 63. Two main bands are seen at 1216 and 1091 cm^{-1} that correspond to the asymmetric and symmetric stretching vibration of PO_2^- respectively (Figure 63A). The low frequency of $\nu_{as}(\text{PO}_2^-)$ corresponds to the high degree of hydrogen bonding which could be attributed to the intramolecular hydrogen bonding between the C-OH and PO of cardiolipin (Figure 62) as postulated by Hubner *et al.* ⁽⁵³⁾.

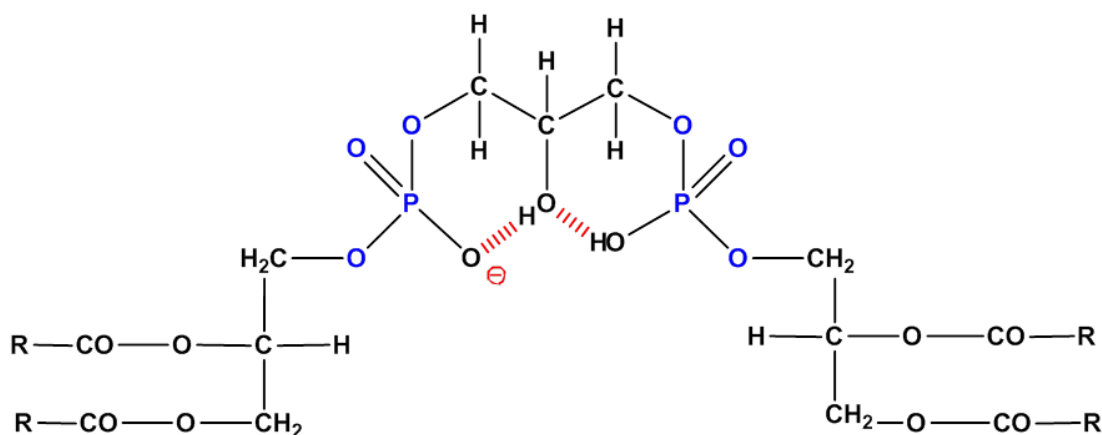


Figure 62. The intramolecular hydrogen bonding (red color) of cardiolipin structure (18:0).

The spectra reveal the contribution of the four C-O-P vibrations in the region around 1050 cm^{-1} (Figure 63). The major shifts upon heating are seen in the asymmetric and symmetric phosphate vibrations. However, in contrast to EPC and EPE, in this case the insertion of cholesterol causes an up shift of the asymmetric vibration from 1216 (CL) to 1219 cm^{-1} (CL/cholesterol). This leads to the suggestion that cholesterol insertion induces a

reorientation and rearrangement of the cardiolipin molecules in a certain way causing a decrease in the hydrogen bonding interaction.

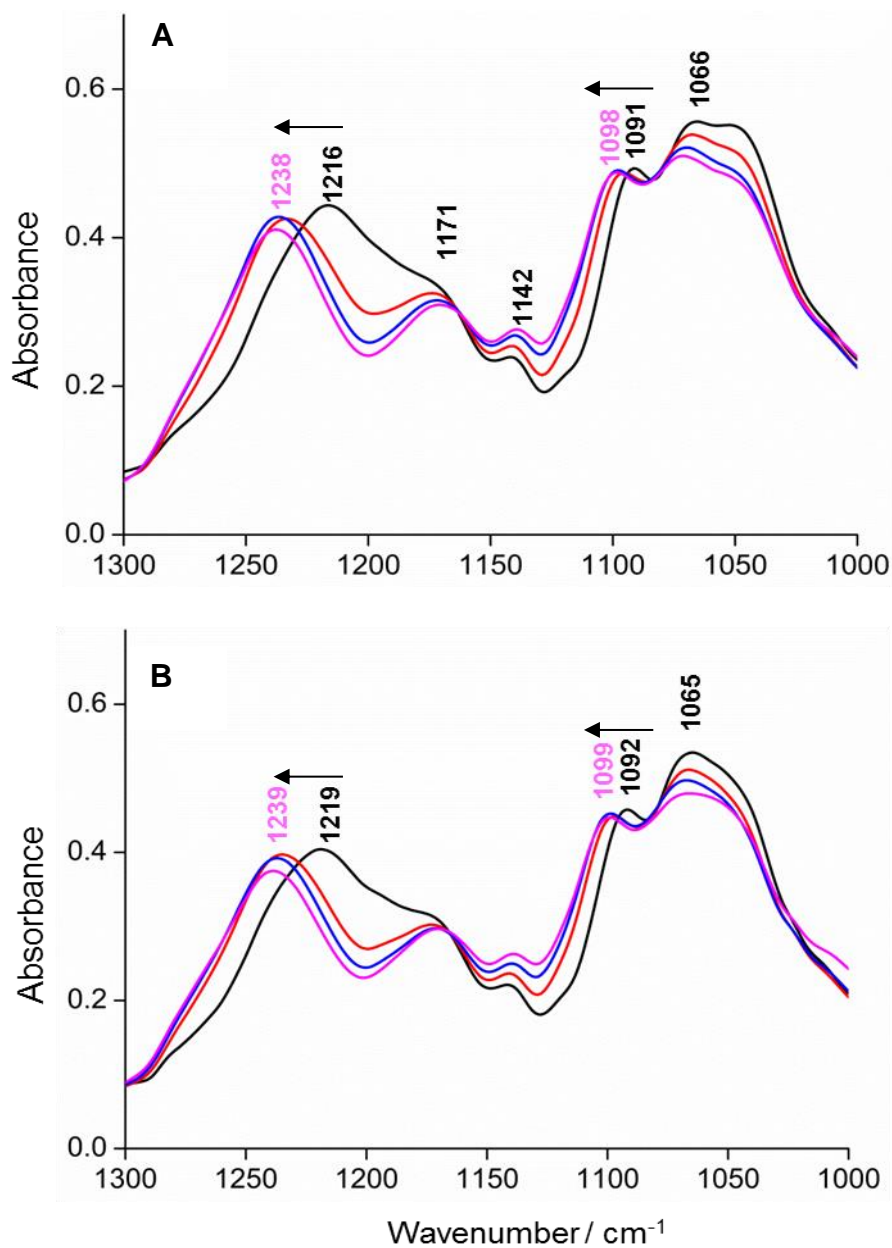


Figure 63. Enlarged view of the temperature dependent $\nu_{as}(\text{PO}_2^-)$ and $\nu_s(\text{PO}_2^-)$ stretching modes of CL (A), CL/cholesterol (B). Line assignments: 5 °C (back), 20 °C (red), 40 °C (blue) and 60 °C (magenta).

3.2 The temperature dependence of lipids in the far infrared domain

To get a better understanding about the changes observed in the mid infrared, the far infrared region is studied. In this part, the hydrogen bonding behaviour of the lipids and lipid mixtures with cholesterol using far infrared spectroscopy is presented. The far infrared absorption spectra are recorded upon heating using an absorbance cell in transmission mode (section 2.3.3).

- **EPC and EPC/cholesterol (2:1)**

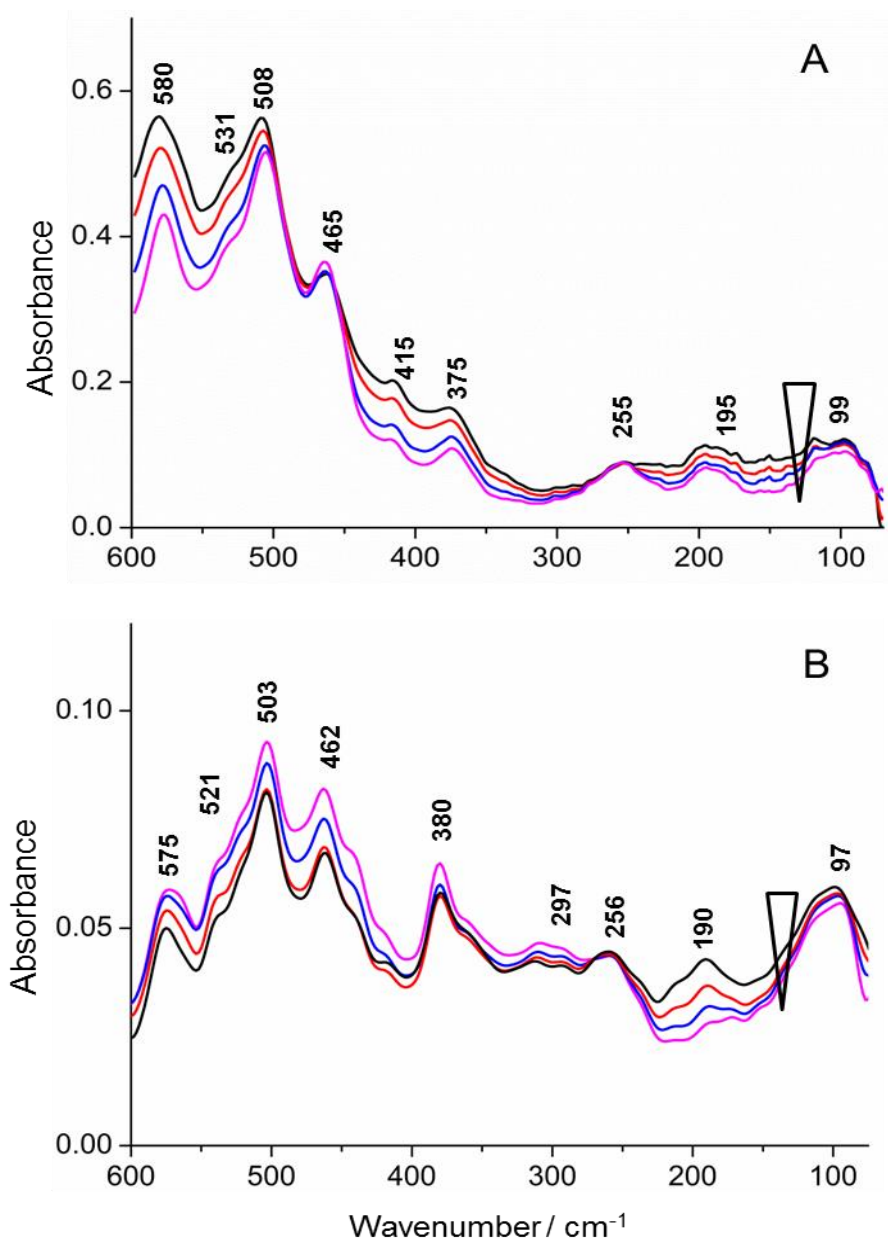


Figure 64. Far IR absorbance spectra as a function of temperature of EPC (A) and EPC/cholesterol (B). Line assignments: 10 °C (black), 20 °C (red), 30 °C (blue), 40 °C (magenta). The spectra have been normalized at 255 cm^{-1} .

Figure 64 illustrates the temperature dependent spectroscopic properties of EPC from egg yolk (trace A) and EPC/cholesterol (2:1) (trace B) in the far infrared domain from 600 to 50 cm^{-1} . The far infrared spectra of EPC and EPC/cholesterol clearly show significant changes between 10 °C and 40 °C.

The signals observed between 600-480 cm^{-1} originate from the head group. In case of EPC, the peaks at 531 and 508 cm^{-1} correspond to the O-P-O wagging and rocking vibrations from the phosphate moiety^(284, 292, 293). The intensity of these two peaks is reduced at higher temperature in contrast to EPC/cholesterol where the intensity is increased upon heating (Figure 64B).

The peaks at 580 and 375 cm^{-1} originate from the deformation vibration and the $\tau(\text{C-CN})$ torsion vibration of the choline $\text{CN}^+(\text{CH}_3)_3$ head group respectively^(241, 293). In addition, the peak at 195 cm^{-1} , which is assigned to the torsion motion of CH_2 , decreases upon heating in EPC. This may be interpreted in terms of less tightly packed hydrocarbon chains. However this CH_2 vibration is almost absent at high temperature in case of EPC/cholesterol. Furthermore, the signal observed at 297 cm^{-1} (Figure 64B) originates from the contribution of cholesterol (see far infrared spectrum of cholesterol in Appendix 3).

The most interesting signal in the low frequency region is the connectivity mode which includes the hydrogen bonding signature of water and any other hydrogen bonds, it is located below 200 cm^{-1} (Figure 64)^(294, 295). As illustrated in both cases in Figure 64, the hydrogen bonding feature is reduced upon heating. This can be correlated with the H_2O vibrational modes in the mid infrared (see Appendix 4) where the water content in the lipid film is reduced at high temperature causing a lower hydrogen bonding interaction.

- **EPE and EPE/cholesterol (2:1)**

The temperature dependent far infrared spectra of pure EPE and EPE/cholesterol are described in Figure 65. The deformation vibration $\delta(\text{CN}^+\text{H}_3)$ (ethanol amine group) is seen at 551 cm^{-1} in both cases (Figures 65A, 65B). The $\delta(\text{O-P=O})$ vibration is seen at 534 cm^{-1} , it increases upon heating due to the intra and intermolecular hydrogen bonding of NH_3^+ with the PO_2^- ⁽²⁸⁸⁾. Additional signals observed at 458, 397, 246 and 197 cm^{-1} are attributed to $\tau(\text{C-C})$, $\tau(\text{C-CN})$, $\tau(\text{C-CH}_3)$ and $\tau(\text{C-CH}_2)$ respectively⁽²⁹³⁾. The signal at 504 cm^{-1} (Figure 65B) may originate from cholesterol (see Appendix 3).

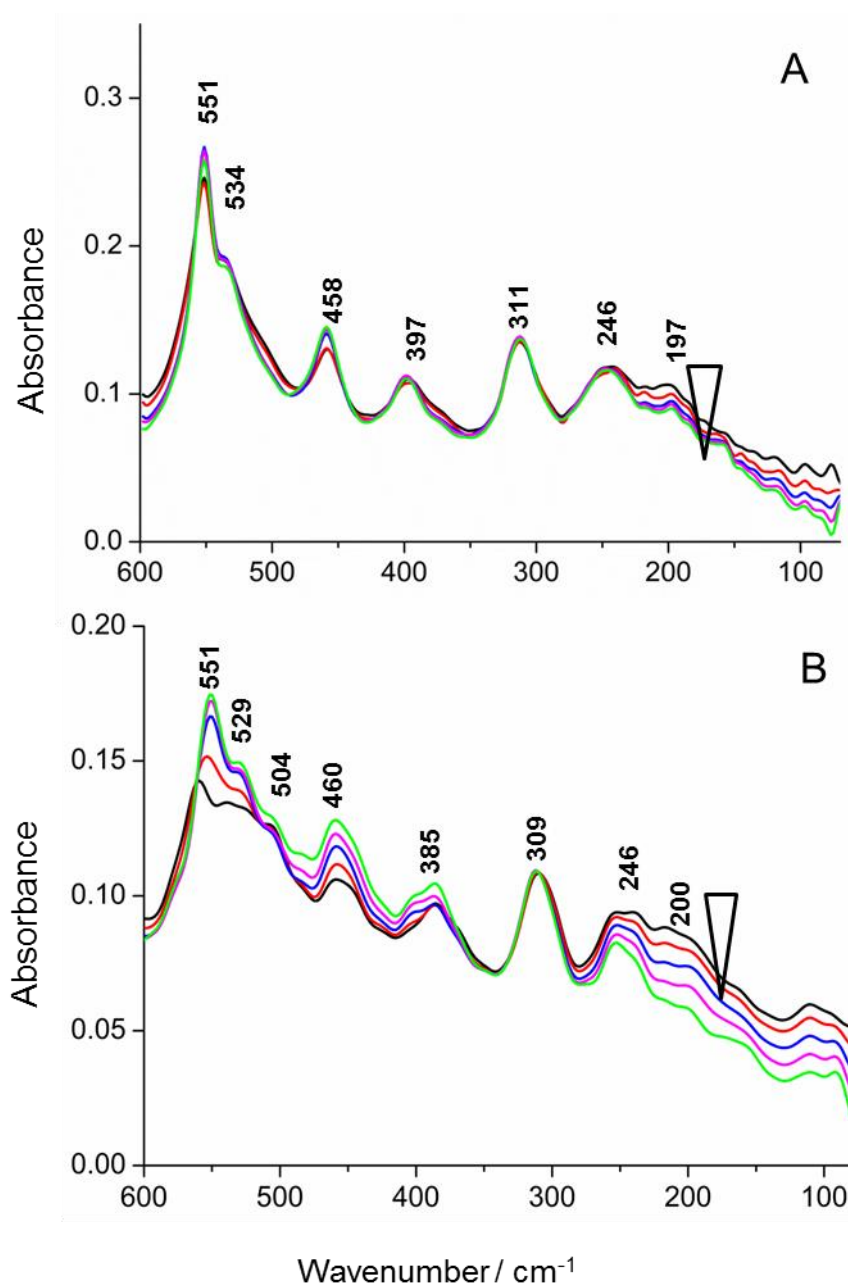


Figure 65. Far IR absorbance spectra as a function of temperature of EPE (A) and EPE/cholesterol (B). Line assignments: 10 °C (black), 20 °C (red), 30 °C (blue), 40 °C (magenta), 50 °C (green). The spectra have been normalized at 311 cm^{-1} peak.

In EPE and EPE/cholesterol, the hydrogen bonding feature below 200 cm^{-1} is decreased upon heating. This finding is in line with the results observed in the mid infrared region where upon heating the amount of water is lower (see Appendix 4). The comparison between EPC and EPE reveals that the behaviour of $\delta(\text{O-P=O})$ under temperature effect is different in these

two lipids. One possible explanation could be the higher positive charge density of ethanolamine in comparison to choline which may lead to different solvation of the polar head group and thus a difference in the size and possible interactions^(37, 274).

- **CL and CL/cholesterol (2:1)**

Figure 66 displays the temperature dependent behaviour of pure CL and CL/cholesterol. This lipid has two protonable phosphate groups⁽³⁰⁾ and it shows a broad hydrogen bonding feature between 300 and 100 cm^{-1} .

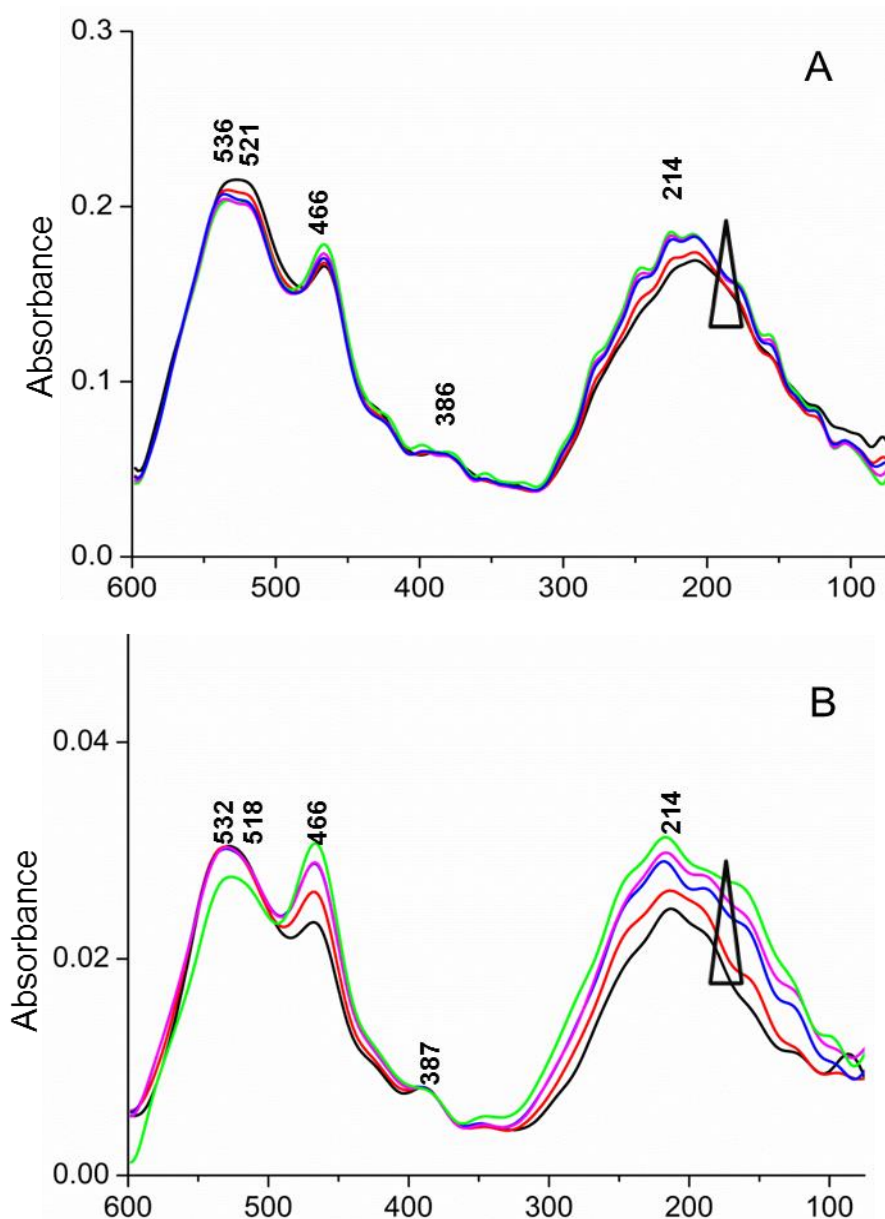


Figure 66. Far IR absorbance spectra as a function of temperature of CL (A) and CL/cholesterol (B). Line assignments: 10 °C (black), 20 °C (red), 30 °C (blue), 40 °C (magenta) and 50 °C (green). The spectra have been normalized at 387 cm^{-1} .

The two significant peaks at 536 and 521 cm^{-1} originate from the phosphate head group. The intensity of these 2 peaks decreases upon heating whereas the hydrogen bonding below 300 cm^{-1} increases. This increase is in contrast to the decrease of the water modes observed in the mid infrared (see Appendix 4) and of the other lipids and it is probably attributed to the intermolecular or intramolecular hydrogen bonding. As a result, the difference in the behavior between mid and far is correlated with the different hydrogen bonding modes. The assignments of the different peaks seen in the mid and far infrared region for the different lipids and their mixtures with cholesterol are summarized in Table 17.

Table 17. Summary of the tentative assignments presented in the text ⁽²⁹³⁾.

EPC	EPC/cholesterol	EPE	EPE/cholesterol	CL	Cl/cholesterol	Tentative assignments
2852	2852	2850	2851	2853	2853	$\nu_s(\text{CH}_2)$
2922	2922	2920	2920	2923	2924	$\nu_{as}(\text{CH}_2)$
1466	1466	1466	1465	1462	1463	CH bending
1736	1738	1737	1739	1739	1740	C=O stretching
1233	1231	1221	1219	1216	1219	$\nu_{as}(\text{PO}_2^-)$
1087	1087	1075	1074	1091	1092	$\nu_s(\text{PO}_2^-)$
580	575					$\delta(\text{CN}^+(\text{CH}_3)_3)$
		551	551			$\delta(\text{CN}^+\text{H}_3)$
531	521	534	529	536	532	$\delta(\text{O-P=O})$
				521	518	$\delta(\text{O-P-O})$
508	503					$\delta(\text{O-P-O})$
465	460	458	460	466	466	$\tau(\text{C-C})_n$
375	380	397	385			$\tau(\text{C-CN})$
		311	309			?
255	257	246	246			$\tau(\text{C-CH}_3)$
195	190	197	200	214	214	$\tau(\text{C-CH}_2)$,
						Hydrogen bonds
99	97					Hydrogen bonds

3.3 Raman spectroscopic study of lipids

Beside mid and far infrared spectroscopies, Raman is used to further improve the analysis of lipids. There is a large body of reported literature on the spectral characterization of lipids, oils and fats by applying Raman spectroscopy⁽²⁹⁶⁻²⁹⁸⁾. Indeed it helps in the determination of the chemical composition and physical structure parameters such as cis/trans isomer ratio⁽²⁹⁹⁾, molar unsaturation (C=C per molecule)⁽³⁰⁰⁾, mass unsaturation (C=C per unit mass)⁽³⁰¹⁾, conjugated double bond content⁽³⁰²⁾ and chain length⁽³⁰³⁾.

Krafft *et al.*⁽³⁰⁴⁾ recorded the Raman spectra of some phospholipids, sphingolipids and cholesterol on gold coated glass slides. The work presented here is an attempt to study the lipids EPC, EPE, cardiolipin thin films and their mixtures with cholesterol using Raman spectroscopy in order to follow the structural changes between the free and the mixture forms. To the best of our knowledge, these lipid/cholesterol mixtures have not been studied before. In addition, SERS is applied on these lipids to probe the enhancement effect using octadecanethiol modifier on silicon substrates.

Figure 67 illustrates the Raman spectra of the pure lipid films which are recorded using the calcium fluoride window (CaF₂) and the 514 nm laser. The position of the bands are compared and correlated with specific functional groups. The assignments of these bands are presented in Table 18. The region from 400 to 1800 cm⁻¹ in the Raman spectra of lipids creates a fingerprint for each component whereas the second region from 2700 to 3500 cm⁻¹ corresponds to the less informative region where broad Raman bands originating from CH, NH and OH stretching vibrations overlap⁽³⁰⁴⁾ (data not shown).

The Raman spectrum of egg phosphatidylcholine (EPC) (Figure 67A) shows a band at 1736 cm⁻¹ which is diagnostic for the CO vibration. The bands near 1267 and 1657 cm⁻¹ correspond to C=C groups in unsaturated fatty acid chains. Moreover, the bands located at 716 and 873 cm⁻¹ are attributed to the symmetric and asymmetric stretching vibrations of the choline group (N⁺(CH₃)₃) respectively⁽³⁰⁴⁾.

The Raman spectrum of egg phosphatidylethanolamine (Figure 67B) is very similar to that of EPC with the exception of minor band shifts. The bands in the wavenumber region from 1000 to 1700 cm⁻¹ are dominated by the C-C and CH groups of saturated and unsaturated chains. Furthermore, the peak at 759 cm⁻¹ is assigned to the ethanolamine head group of EPE. In few

words, the comparison between EPC and EPE indicates that the lower wavenumber region below 800 cm^{-1} allows the distinction of these two phospholipids.

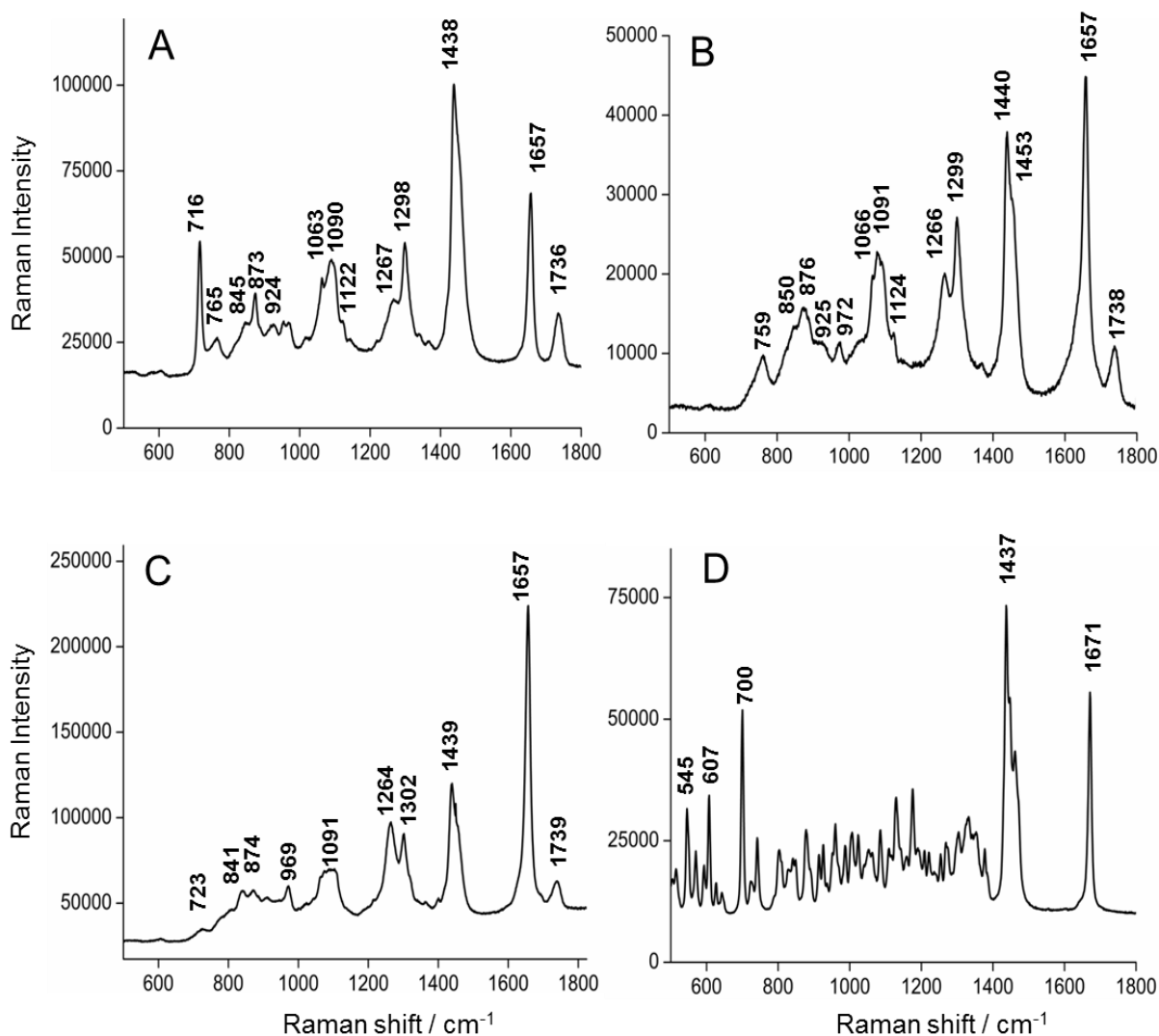


Figure 67. Raman spectra from 400 to 1800 cm^{-1} of EPC (A), EPE (B), CL (C) and cholesterol (D) with an excitation of 514 nm .

Moving to trace C which presents the Raman spectrum of cardiolipin, it exhibits two intense band at 1657 and 1264 cm^{-1} , in comparison to EPC and EPE, that correspond to $\text{C}=\text{C}$ vibration due to its high degree of unsaturation (98%, 18:2). Another useful band at 1091 cm^{-1} is correlated to the phosphate groups PO_2^- . The shape of this band is different from the one seen for EPC and EPE because of the presence of two phosphate groups.

Trace D of Figure 67 describes the Raman spectrum of cholesterol. Cholesterol has no strong absorption in Raman and the spectrum is thus very noisy. Sharp bands are observed between 500 and 1200 cm^{-1} with the most intensive ones at 545, 607 and 700 cm^{-1} . Additional bands at 1437 and 1671 cm^{-1} are obtained and they are assigned to CH deformation vibration and C=C vibration respectively^(304, 305).

Table 18. Assignments of Raman modes in EPC, EPE, CL and cholesterol^(301, 306).

EPC (cm^{-1})	EPE (cm^{-1})	CL (cm^{-1})	Cholesterol (cm^{-1})	Tentative assignment
1736	1738	1739		ν (C=O) stretch
1657	1657	1657	1671	ν (C=C) stretch
1438	1440	1439	1437	$\delta(\text{CH}_2)_{\text{sc}}$ methylene scissor deformations
1298	1299	1302		$\delta(\text{CH}_2)_{\text{tw}}$ methylene twisting deformations
1267	1266	1264		ν (C=C) stretch
800-1200	800-1200	800-1200		ν (C-C) stretch, ν (C-O), CH ₃ rocking mode , ν (PO)
	759			Symmetric $\nu(\text{NH}_3^+)$
		723		=CH planar bending
716				Symmetric $\nu(\text{N}^+(\text{CH}_3)_3)$
			700	?
			607	?
			545	?

3.3.1 Raman spectroscopic study of mixture of lipids with cholesterol

Figure 68 illustrates the Raman spectra of pure lipids (EPC, EPE and cardiolipin) and their corresponding lipid/cholesterol system (2:1). The comparison between EPC (Figure 68A, black) and EPC/cholesterol (Figure 68A, red) shows three additional bands at 544, 605 and 700 cm^{-1} arising from cholesterol (indicated by symbols). Similar observation is clearly visualized for EPE and cardiolipin (Figures 68B, 68C).

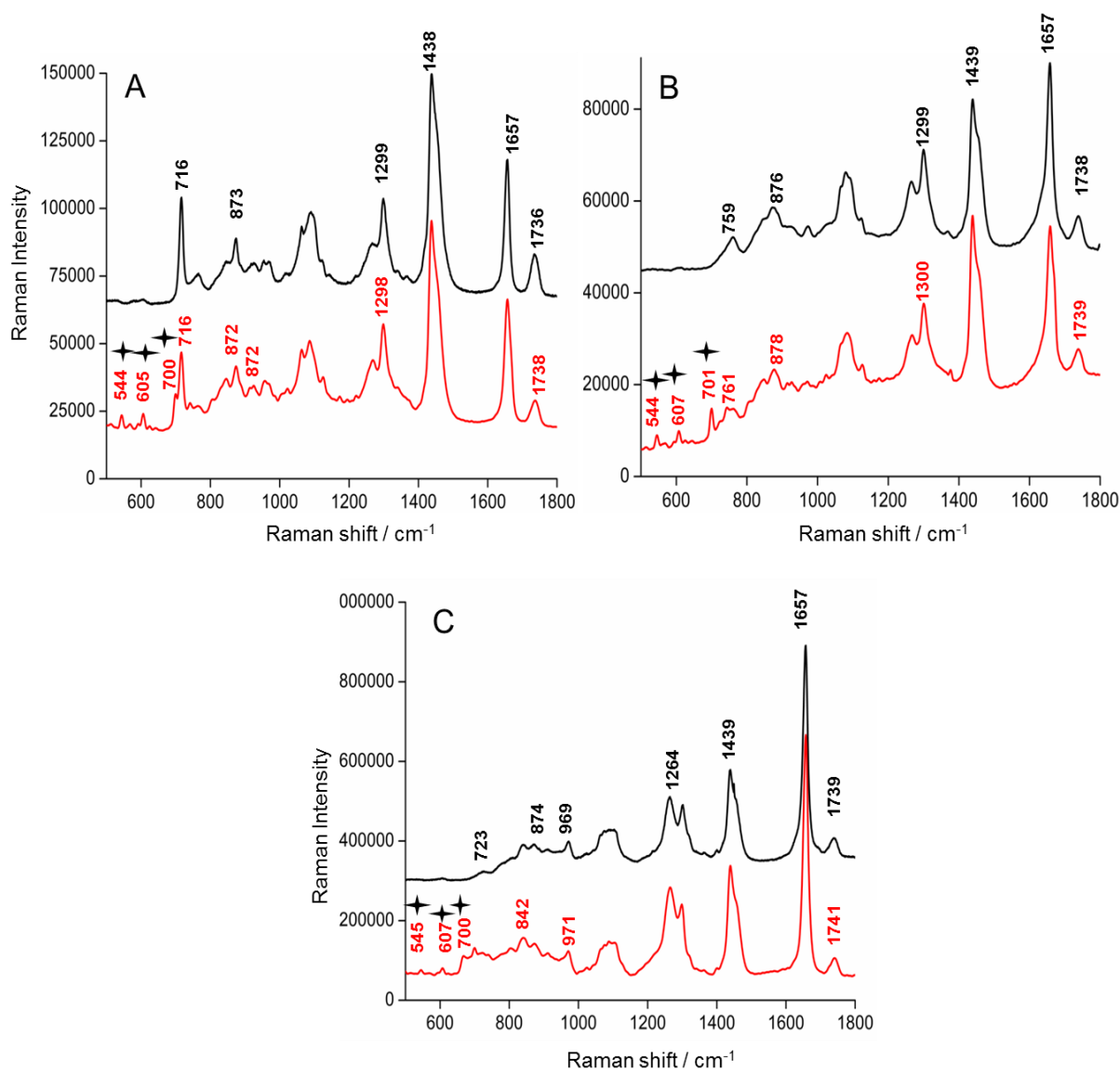


Figure 68. Raman spectra from 400 to 1800 cm^{-1} of EPC and EPC/cholesterol (A), EPE, EPE/cholesterol (B), CL and CL/cholesterol (C), Line assignments: pure lipid (black), lipid/cholesterol (red).

Another interesting feature to compare between the Raman spectra of lipids and lipid/cholesterol systems is the CO vibration. For instance, the CO stretching vibration is

observed at 1736, 1738 and 1739 cm^{-1} for EPC, EPE and cardiolipin respectively. After addition of cholesterol, these carbonyl vibrations are shifted toward higher frequencies. They are found now at 1738, 1739 and 1741 cm^{-1} for EPC/cholesterol, EPE/cholesterol and CL/cholesterol respectively. The upshift of 1-2 cm^{-1} is in agreement with the results obtained in the mid infrared study where cholesterol addition disorders the system inducing an upshift in the wavenumber. The results are summarized briefly in Table 19 in combination with the far and mid infrared data.

Table 19. Tentative assignments of phospholipids vibrations in the mid, far infrared as well as Raman domains.

EPC (cm^{-1})	EPC/ cholesterol (cm^{-1})	EPE (cm^{-1})	EPE/ cholesterol (cm^{-1})	CL (cm^{-1})	CL/ Cholesterol (cm^{-1})	Tentative assignment	
1736	1738	1737	1739	1739	1740	ν (C=O) stretch	M I D
1233	1231	1221	1219	1216	1219	ν_{as} (PO_2^-) stretch	
1087	1087	1075	1074	1091	1092	ν_{s} (PO_2^-) stretch	
580	575	551	551			$\delta(\text{CN}^+(\text{CH}_3)_3)$	F A R
						$\delta(\text{CN}^+ \text{H}_3)$	
531	521	534	529	536	532	$\delta(\text{O-P=O})$	
508	503					$\delta(\text{O-P-O})$	
465	462	458	460	466	466	τ (C-C) _n	}
99	97	197	198	214	214	Hydrogen bonds	
1736	1738	1738	1739	1739	1741	ν (C=O) stretch	R a m a n
		759	761			$\nu_{\text{s}}(\text{NH}_3^+)$	
716	716					$\nu_{\text{s}}(\text{N}^+(\text{CH}_3)_3)$	

3.3.2 Surface enhanced Raman spectroscopy

As mentioned above, Raman spectroscopy has been widely used for the characterization of lipids⁽²⁹⁶⁻²⁹⁸⁾; however some of the Raman signals are weak. For this reason, the assertion to enhance the intensity of weak Raman signatures led to the development of powerful surface enhanced Raman spectroscopy method. Few studies have been reported for SERS measurements of lipids unlike infrared and conventional Raman spectroscopy. This is because the nanocolloids solution used for SERS analysis is immiscible with lipid phases. To overcome this problem the nanoparticles are dried onto the solid surface and then lipid molecules are applied on the top.

Li *et al.*⁽³⁰⁷⁾ used silver dendrites as SERS substrates to test the enhancement ability toward canola oil and α -tocopherol. Weldon *et al.*⁽³⁰⁸⁾ reported the SERS of model sebum lipids and they described the usage of silicon substrates with silver microprobes to resolve classes of lipids. In addition, Driver *et al.*⁽³⁰⁹⁾ used gold nanoparticles for SERS studies to provide information about lipids in diluted oils and to monitor lipids oxidation. In this study, we reported the SERS using silver nanoparticles solution on silicon substrate to test the enhancement of EPC, EPE and cardiolipin as presented in Figure 69.

The signals observed between 2800 and 3100 cm^{-1} (Figures 69B, 69D, 69F) correspond to the symmetric and asymmetric stretching vibrations from the CH_2 and CH_3 groups. For EPC (Figure 69A), the peak at 716 cm^{-1} , assigned to symmetric stretching of the choline group representing a marker band for EPC, is enhanced using SERS. Similarly, the marker band of EPE seen at 757 cm^{-1} is enhanced after SERS (Figure 69C). Subsequently, this method can enhance Raman signals however it has some limitations due to the contribution from the modifier such as the peak seen at 974 cm^{-1} (see appendix 5). The comparison between normal Raman and SERS spectra of EPC, EPE and cardiolipin reveals similar features (Figure 69) with the enhancement of CH and CO stretching vibrations. The assignments are summarized in Table 20.

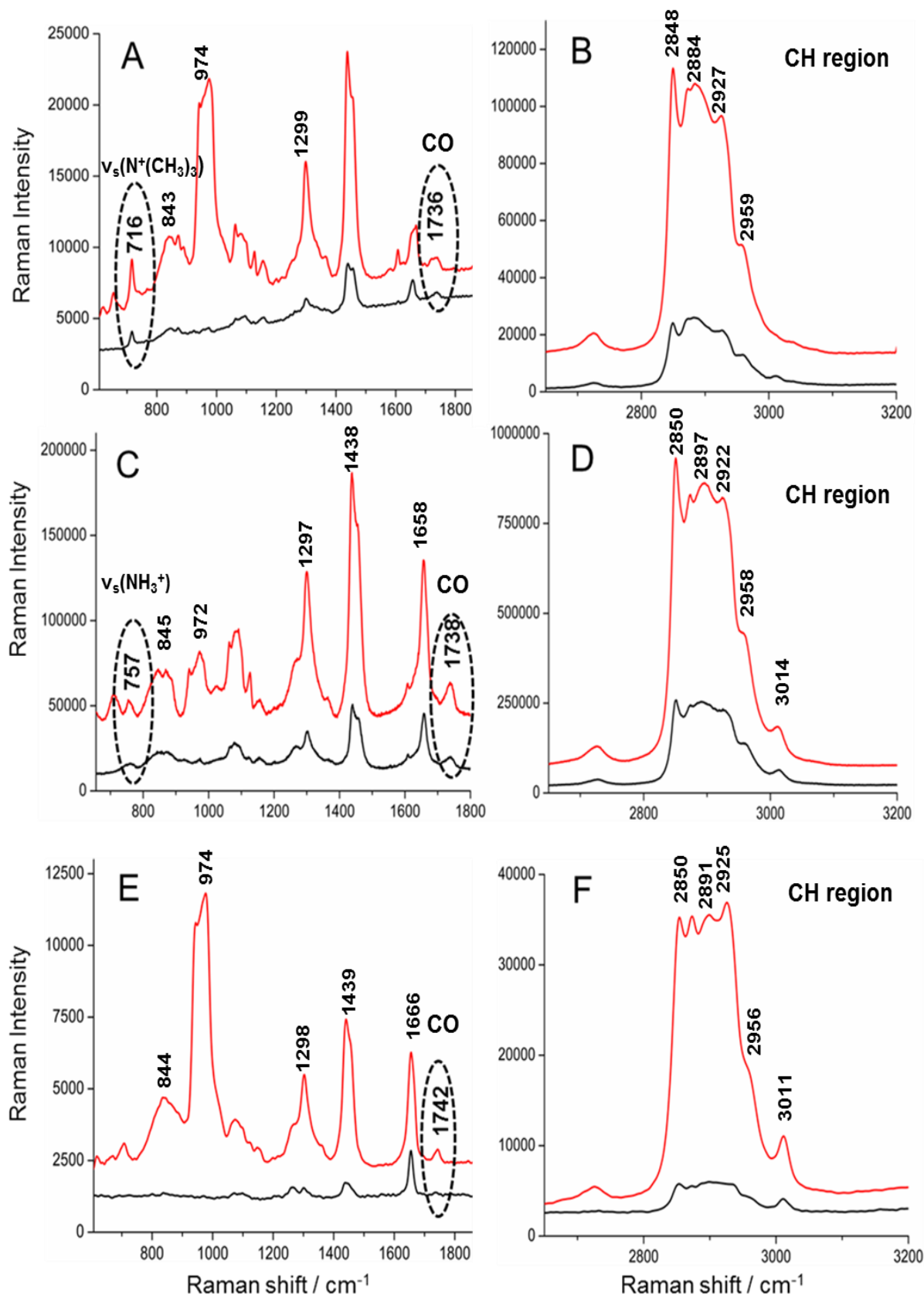


Figure 69. The low frequency and CH stretching regions of EPC (A, B), EPE (C, D) and CL (E, F). Line assignments: pure lipid before (black) and after SERS (red).

Table 20. The assignments of EPC, EPE and CL Raman peaks after SERS.

EPC	EPE	CL	Tentative assignments
2959	2958	2956	CH ₃ asymmetric stretching
2927	2922	2925	CH ₃ symmetric stretching
2884	2897	2891	CH ₂ asymmetric stretching
2848	2850	2850	CH ₂ symmetric stretching
1736	1738	1742	CO stretching
1658	1658	1666	C=C stretching
1437	1438	1439	CH ₂ bending
1299	1297	1298	= CH bending
974	972	974	C-C stretching (modifier)
	757		(NH ₃ ⁺) symmetric stretching
716			N ⁺ (CH ₃) ₃ symmetric stretching

3.4 The far infrared spectroscopic properties of EPC/EPE mixtures

This part summarizes the FTIR studies on the temperature dependence of phosphatidylcholine-phosphatidylethanolamine mixtures in different ratios in the far infrared region (600-50 cm⁻¹). EPC and EPE phospholipids have been selected because phospholipids with choline and ethanolamine head groups constitute major portions of the biological membrane. Three EPC/EPE mixtures (1:1, 2:1 and 4:1) are used as simple model systems in order to analyze the different thermotropic behaviour of mixture of phospholipids together and to probe the effect of the head group composition on the hydrogen bonding behaviour and the phase transition temperature.

3.4.1 Far infrared ATR absorbance spectra of EPC, EPE and EPC/EPE mixtures

Figure 70 shows the far infrared spectroscopic properties of EPC, EPE, EPC/ EPE mixtures of 1:1, 2:1, and 4:1 ratios. The spectra between 600 and 50 cm⁻¹ are divided into three main domains: the head group domain, the torsion motion of hydrocarbon chain and the hydrogen bonding feature.

The lipids EPC (trace B) and EPE (trace A) can be clearly distinguished from each other in the far infrared data due to the presence of two peaks at 576 cm^{-1} and 552 cm^{-1} (highlighted by symbols) which correspond to deformation vibration of choline and ethanolamine head groups respectively.

For the mixtures of EPC/EPE (traces C, D and E) the bands at 561 cm^{-1} and 305 cm^{-1} as well as 241 cm^{-1} originate from EPE and will be used as marker bands whereas the bands at 574 cm^{-1} and 506 cm^{-1} dominate from EPC. It is obvious that the hydrogen bonding signature in the mixture of lipids is less intense than in the spectra of the isolated lipids. This may be based on the reduced formation of intermolecular hydrogen bonds in the interfacial region between EPC and EPE.

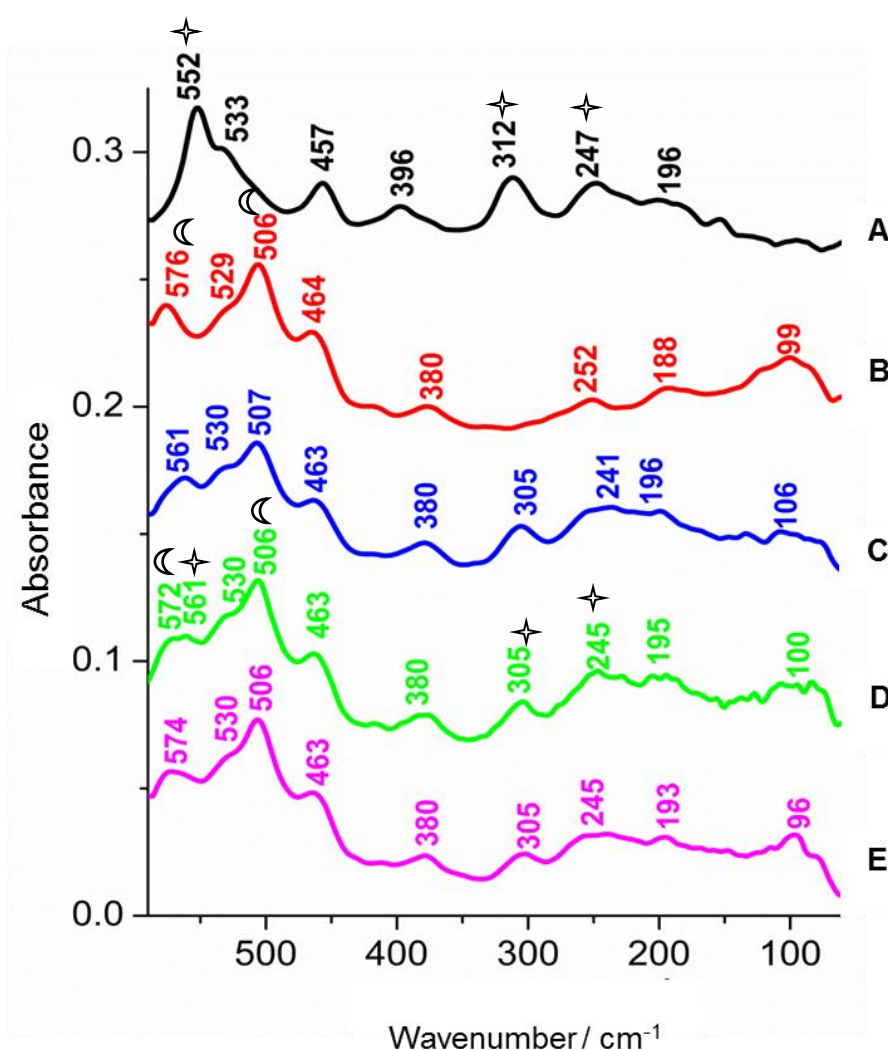


Figure 70. Far infrared absorbance spectra of EPE (A), EPC (B) and the mixture of EPC/EPE ratio of 1:1 (C), 2:1 (D) and 4:1(E). The marker bands of each lipid are highlighted by symbols.

3.4.2 Temperature dependent far infrared absorbance spectra of pure phospholipids (DMPC and DMPE in comparison to EPC and EPE respectively).

The spectroscopic properties and the thermotropic behaviour of the phospholipids DMPC and DMPE containing saturated hydrocarbon chains only are compared with their variants from egg yolk containing a mixture of saturated and unsaturated hydrocarbon chain (Figure 71).

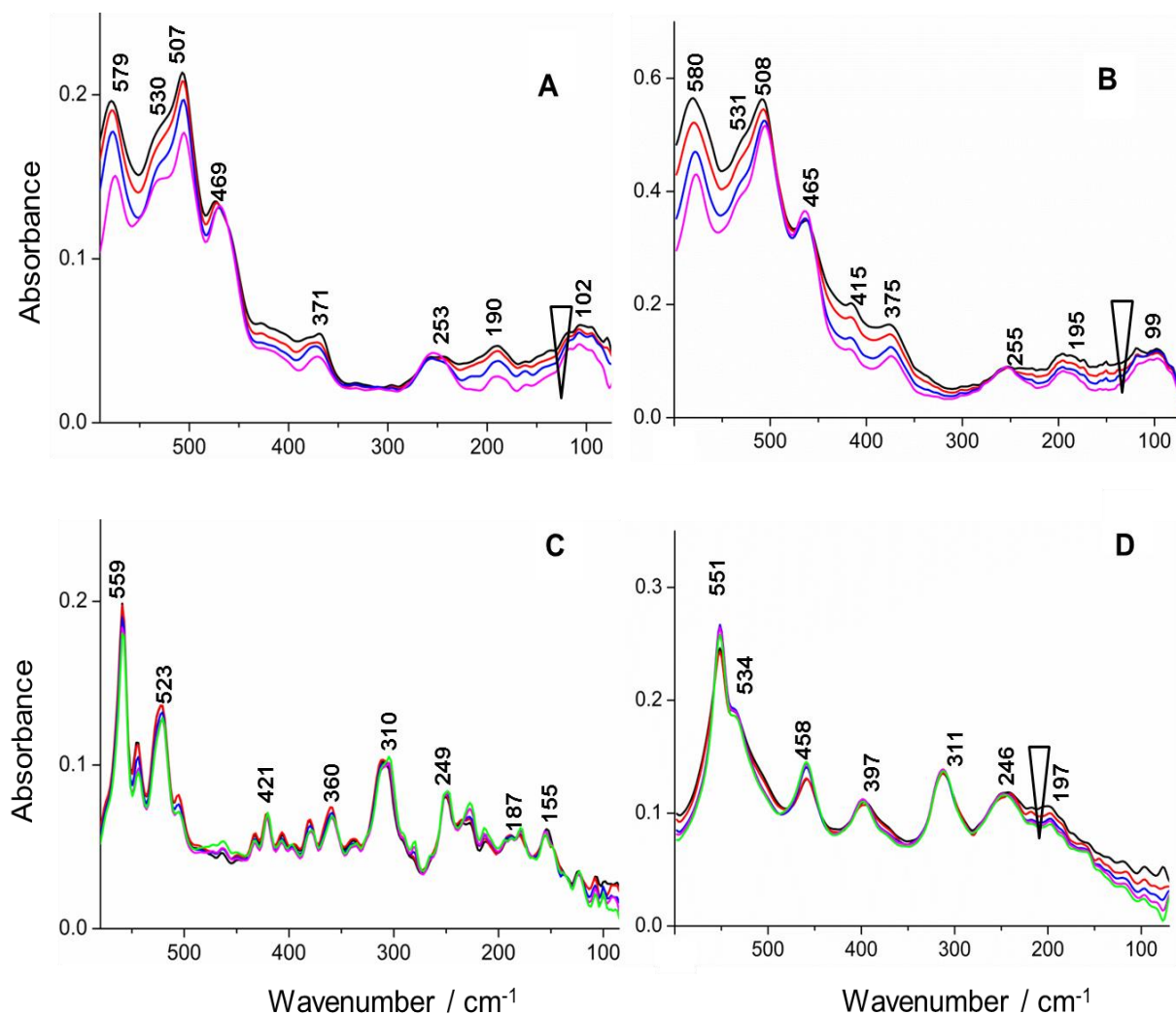


Figure 71. Temperature dependent far infrared absorbance spectra of DMPC (A), EPC (B), DMPE (C) and EPE (D) lipids upon heating from 10 to 40 °C (DMPC and EPC) and from 10 to 50 °C (DMPE and EPE) where 10 °C (black), 20 °C (red), 30 °C (blue), 40 °C (magenta) and 50 °C (green).

Figure 71 illustrates the temperature dependent spectroscopic properties of saturated PC (trace A), EPC from egg yolk (trace B), saturated PE (trace C), and EPE from egg yolk (trace

D) in the far infrared domain from 600 to 50 cm^{-1} . The far infrared spectra of DMPC and EPC clearly show temperature shifts between 10 $^{\circ}\text{C}$ and 40 $^{\circ}\text{C}$. These changes are based on the transition from the gel to liquid crystalline phase ^(19, 310). In both traces, the temperature dependent far infrared absorbance spectra of the head group domain, the hydrocarbon chains and the hydrogen bonding signature decrease upon heating. This may be based on weaker hydrogen bonding at higher temperature ⁽²⁴¹⁾. The intensity of O-P-O wagging and rocking vibrations at 505 and 532 cm^{-1} is reduced in DMPC as well as in EPC (traces A and B).

Trace C (Figure 71) describes the temperature dependent far infrared spectra of pure DMPE. No alterations are seen in the temperature range between 10 $^{\circ}\text{C}$ and 50 $^{\circ}\text{C}$. In comparison, for EPE lipid (trace D) the peaks at 551 cm^{-1} and 533 cm^{-1} which are assigned to $\delta(\text{CN}^+\text{H}_3)$ and $\delta(\text{O-P=O})$, respectively, increase upon heating and this could be attributed to the intra and intermolecular hydrogen bonding of NH_3^+ with the PO_2^- . The broad signature between 247 and 100 cm^{-1} decreases upon heating. The difference in the behaviour of DMPE and EPE could be correlated to the fact that the transition from the gel to liquid crystalline in these two lipids is different. For DMPE the phase transition temperature is expected at about 48 $^{\circ}\text{C}$ ⁽⁴⁷⁾ whereas for EPE it is observed around 20 $^{\circ}\text{C}$.

3.4.3 Temperature dependent far infrared absorbance spectra of mixture of phospho-lipids

After studying the behaviour of EPC as well as of EPE lipid alone, the temperature dependent far infrared spectra of the lipid titration from EPC and EPE are described in Figure 72. The assignments of the different peaks of these lipid mixtures are summarized in Table 21.

Trace A illustrates the temperature dependent far infrared absorbance spectra of the mixture of 1:1 EPC to EPE ratio. In the head group region an alteration upon heating is clearly seen at 506 cm^{-1} . The intensity of the wagging vibration of O-P-O at 506 cm^{-1} increase upon heating and the broad feature below 200 cm^{-1} , which is assigned to the hydrogen bonding feature decreases upon heating. This broad signal cannot be exactly determined due to the large half band width ⁽²¹¹⁾.

In trace B (Figure 72), the temperature dependent far infrared absorbance spectra of the mixture of 2:1 EPC to EPE ratio is displayed. As also found for the mixture 1:1, the band at 506 cm^{-1} increases upon heating and the broad hydrogen bonding signature below 200 cm^{-1} decreases.

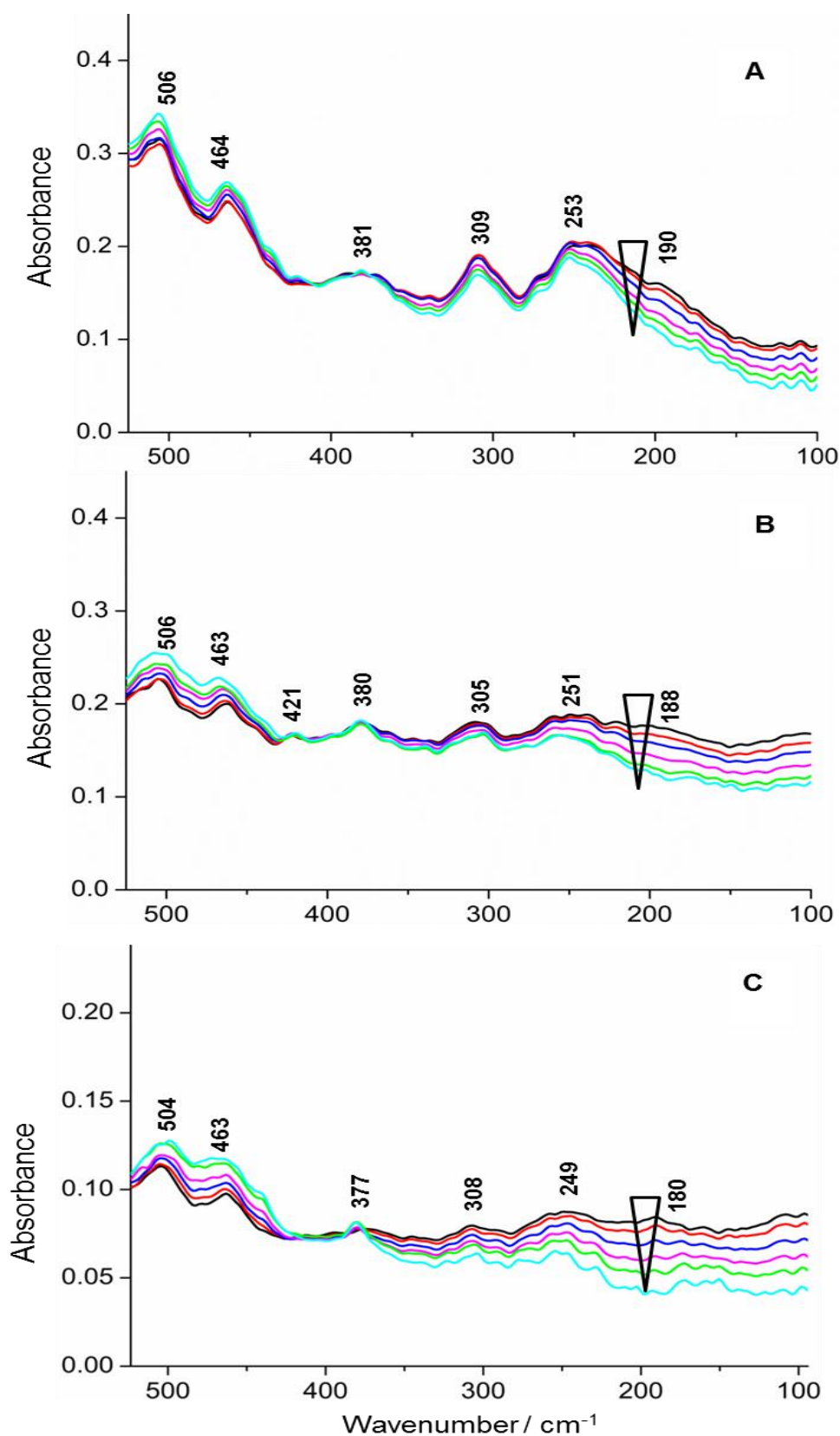


Figure 72. Temperature dependent far infrared absorbance spectra of a varying ratio of phosphatidylcholine and phosphatidylethanolamine: in a ratio of 1:1 (A), 2:1 (B) and 4:1 (C) in the temperature range from 10 °C (black), 20 °C (red), 30 °C (blue), 40 °C (magenta), 50 °C (green) and 60 °C (cyan). The spectra have been normalized at 380 cm^{-1} peak.

Furthermore, trace C shows signals with a similar behaviour as 1:1 and 2:1 mixtures where O-P-O wagging vibration at 504 cm^{-1} increases and hydrogen bonding continuum decreases. The overall temperature dependent change of the broad hydrogen bonding signature is different when comparing the intensity change of the 1:1, 2:1, and 4:1 mixtures. This indicates that hydrogen bonding pattern is different for these mixtures depending on the way of reorganization and rearrangement of the PE with PC lipid, which in turn facilitates or prohibits the formation of inter and intramolecular hydrogen bonds, where the amine group of EPE can interact strongly with the phosphate/carbonyl groups or water. These strong intermolecular interactions cause an alteration in the liquid crystalline phase transition temperature⁽³¹¹⁾.

Table 21. The tentative assignments of all the phospholipids studied in the far infrared region^(241, 312).

EPC (cm^{-1})	DMPC (cm^{-1})	EPE (cm^{-1})	DMPE (cm^{-1})	EPC/EPE 1:1 (cm^{-1})	EPC/EPE 2:1 (cm^{-1})	EPC/EPE 4:1 (cm^{-1})	Tentative assignment
580	579						$\delta(\text{CN}^+(\text{CH}_3)_3)$
		551	559				$\delta(\text{CN}^+\text{H}_3)$
531	530	535	523				$\delta(\text{O-P=O})$
508	507			506	506	504	$\delta(\text{O-P-O})$
465	469	458	421	464	463	463	$\tau(\text{C-C})_n$
375	371	398	360	381	380	377	$\tau(\text{CCN})$
255	253	247	249	253	251	249	$\tau(\text{C-CH}_3)$
195	190	196	187	190	188	189	$\tau(\text{C-CH}_2)$, Hydrogen bonds
99	102		155				Hydrogen bonds

3.4.4 Temperature dependent mid infrared absorbance spectra of mixture of phospholipids

For the analysis of the intermolecular interactions, three functional groups may be taken into account: the hydrocarbon bonds, the carbonyl groups and the phosphate group. In a general way, the C-H torsion is sensitive to tail packing and the C=O and PO to their hydrogen bonding environment ⁽²⁷⁰⁾.

The CH₂/CH₃ stretching vibrations seen from 3000 cm⁻¹ to 2800 cm⁻¹ and the phase transition temperature of these three lipid mixtures are depicted in Figure 73. Between 5 °C and 60 °C the phase transition from the gel to the liquid crystalline can be expected for EPC and for EPE and this transition leads to the perturbation of the tail groups which causes the shift in the wavenumber of CH₂ upon heating.

For the EPC/EPE (1:1) mixture (trace A) and EPC/EPE (2:1) (trace B), the phase transition temperature from gel to liquid crystalline is found at about 23 °C whereas for EPC/EPE (4:1) (trace C) it is 25 °C. This difference denotes that the small contribution of EPE is necessary to influence the thermotropic behaviour of mixed phospholipids and modulates the surface properties of the PC bilayer.

The transition temperature of EPC/EPE (4:1) around 25 °C is far from the results obtained by Quin *et al.* ⁽⁵⁰⁾ where they reported a phase transition temperature from gel to liquid crystalline bilayer at approximately 40 °C for DPPC/DPPE (4:1 fully hydrated sample). This discrepancy probably arises from the mixtures of the acyl chains presented in EPC and EPE lipids. Furthermore, the T_m observed here for EPC/EPE (1:1) at about 23 °C is significantly higher than that determined by Popova *et al.* ⁽⁴⁸⁾ where they reported a T_m at 0 °C for EPC/EPE (1:1) ratio in a dry state. This could be attributed to the difference in the hydration state of the lipid mixtures.

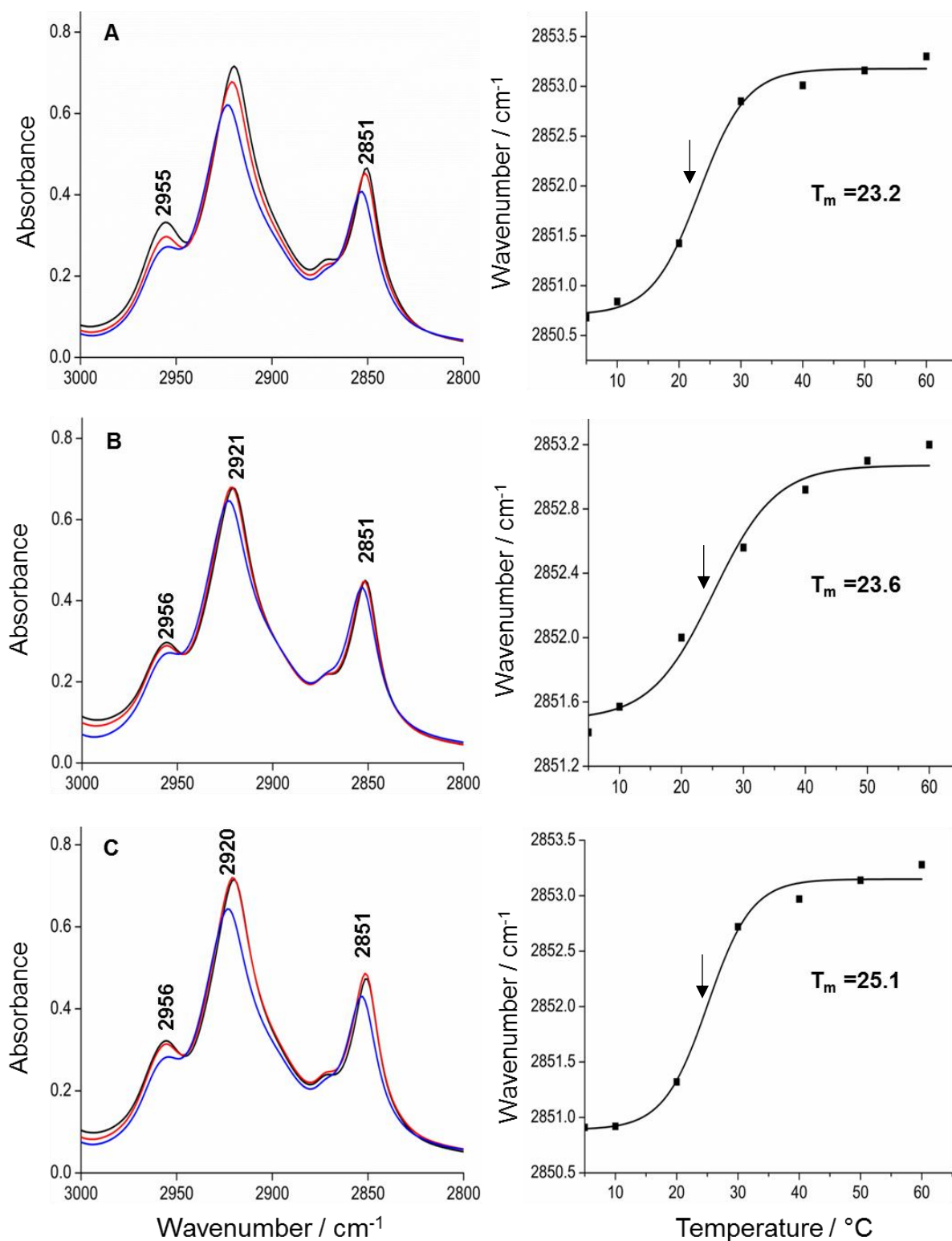


Figure 73. The temperature dependent mid IR absorbance spectra and the transition temperature of EPC /EPE mixture (1:1) (A), EPC/EPE mixture (2:1) (B) and EPC /EPE mixture (4:1) (C) at 5 °C (black), 20 °C (red) and 60 °C (blue).

Concerning the spectral range from 1800 to 900 cm⁻¹, it includes the characteristic absorbance of the phospholipids head group and the C=O stretching vibration of the ester

carbonyl groups. Interestingly, the phosphate vibration is also sensitive to the phase transition temperature and it shifts by around 20 cm^{-1} to higher wavenumber upon heating indicating less strong hydrogen bonding (Figure 74)⁽¹⁸¹⁾.

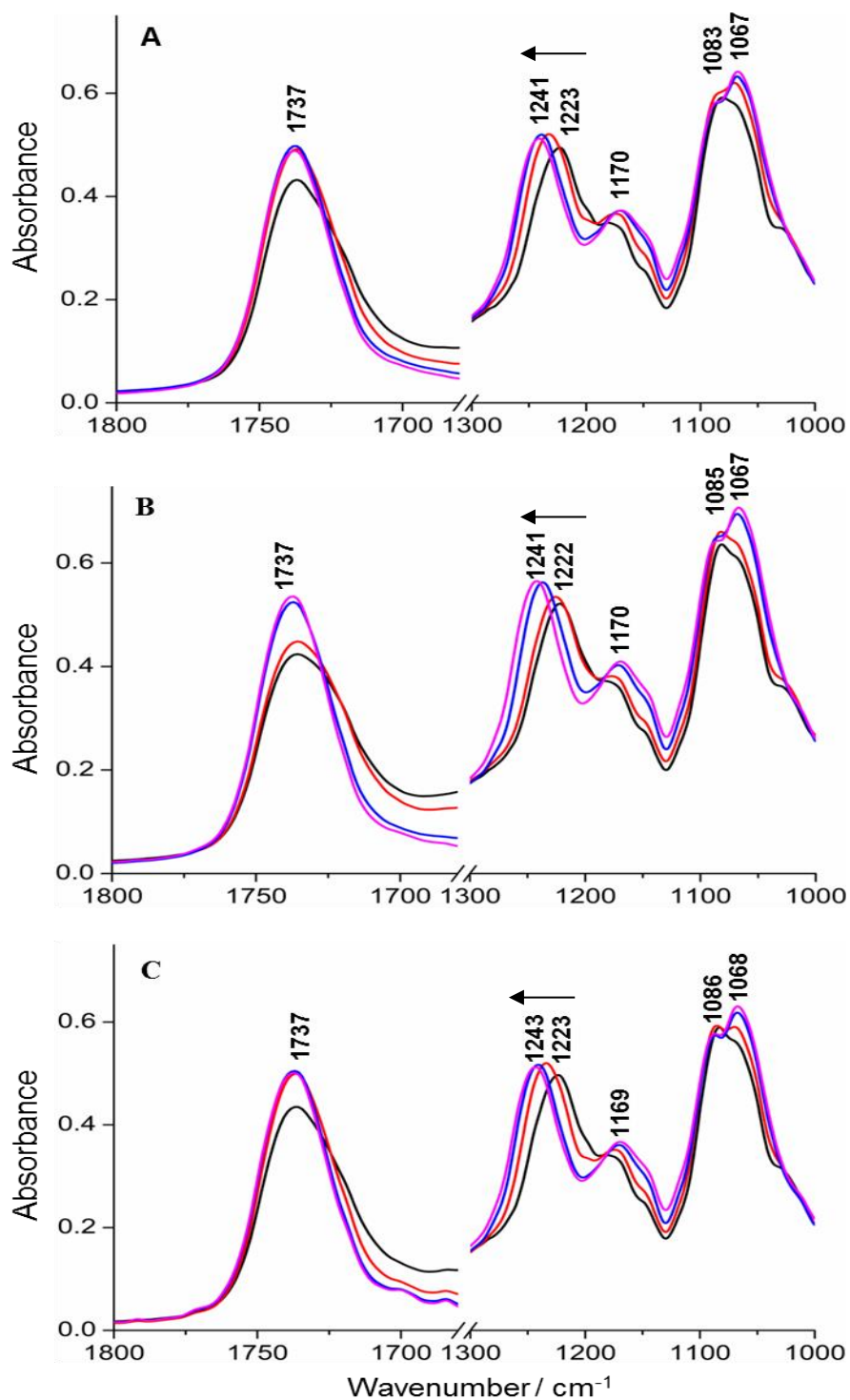


Figure 74. Enlarged view of the studied spectral range $900\text{--}1800\text{ cm}^{-1}$ of EPC /EPE (1:1) mixture (A), EPC/EPE mixture (2:1) (B) and EPC /EPE mixture (4:1) (C) at $5\text{ }^{\circ}\text{C}$ (black), $20\text{ }^{\circ}\text{C}$ (red), $40\text{ }^{\circ}\text{C}$ (blue) and $60\text{ }^{\circ}\text{C}$ (magenta).

3.4.5 Temperature dependence of the water mode in mixed phospholipids

Figure 75 shows the temperature dependence of the ν (OH) stretching vibration from 3700 to 3050 cm^{-1} and the δ (HOH) bending vibration from 1700 to 1550 cm^{-1} of EPC mixed with EPE. The maximum at about 3380 cm^{-1} and the strong shoulder at 3250 cm^{-1} are attributed to OH stretches of water molecules within hydrogen bonded structure whereas the weak high frequency shoulder at 3580 cm^{-1} is assigned to water with the typical absorption for a structure with disrupted hydrogen bonds⁽³¹³⁾.

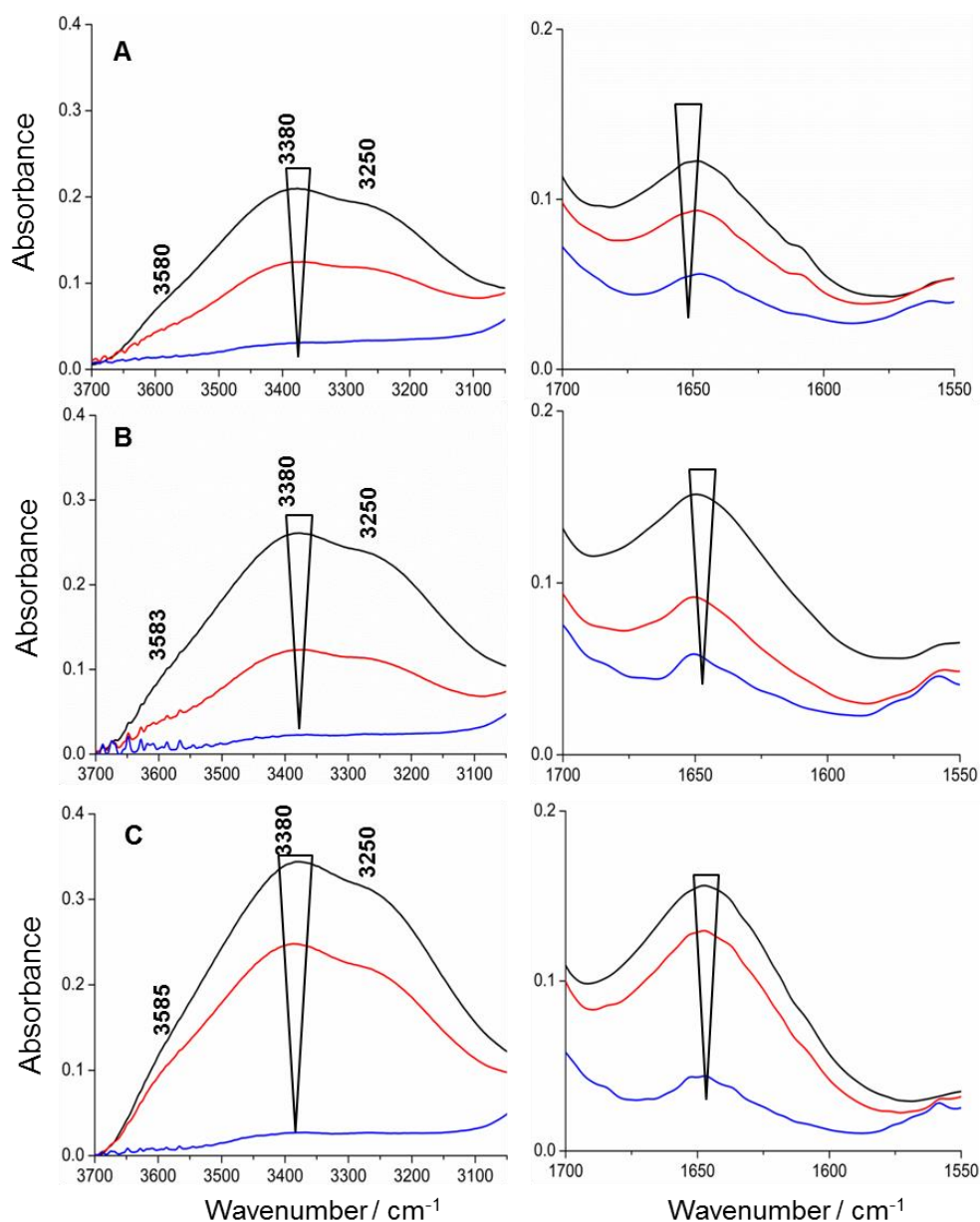


Figure 75. Temperature dependent behaviour of the mid infrared spectra of the (OH) stretching vibration from 3700 to 3050 cm^{-1} and δ (HOH) bending vibrations from 1700 and 1550 cm^{-1} of 1:1 EPC/EPE mixture (A), 2:1 EPC/EPE mixture (B) and 4:1 EPC/EPE mixture (C), 5 °C (black), 20 °C (red) and 60 °C (blue).

The intensity of the OH stretching vibration ($3700\text{-}3100\text{ cm}^{-1}$) decreases with increasing temperature in all cases of mixed EPC/EPE studied here. In addition, the overall intensity of the water modes gets higher when the amount of EPC is higher. This may be caused by the different contribution of EPE which has a smaller head group. Indeed the EPC lipids decrease the intermolecular interactions between the polar head groups of PE and increase the hydration layer of the membrane. Finally the broad feature at 1645 cm^{-1} is assigned to the HOH bending vibration of bound water⁽³¹⁴⁾. The intensity of the HOH vibrational mode decreases upon heating as described above for the OH stretching vibration.

3.5 Liposomes

After studying the pure and mixtures of lipids using mid and far infrared spectroscopies, this part of work deals with the characterization of a typical type of pH sensitive liposomes made of dioleoylphosphatidylethanolamine and cholesterol hemisuccinate (DOPE/CHEMS) (3:2) ratio (for structure see introduction section 1.2).

3.5.1 pH sensitive liposomes

Over the past decade, many studies concerning pH sensitive liposomes have been reported^(103, 315-317) and different classes of pH sensitive liposomes had been proposed^(89, 102). The most commonly established class involves the phosphatidylethanolamine with compounds containing acidic groups (carboxyl groups) that act as a stabilizer at neutral pH^(109, 318-321).

Until now, few data has been obtained about the correlation between the composition of pH sensitive liposome and the pH where the liposomes start to release. This promoted us to investigate the fusion mechanism of these liposomes and provide an exact pH value at which this destabilization occurs. For this reason, six different pH (DOPE/CHEMS) liposomes are studied by mid and far infrared spectroscopies.

3.5.1.1 DOPE/CHEMS liposomes

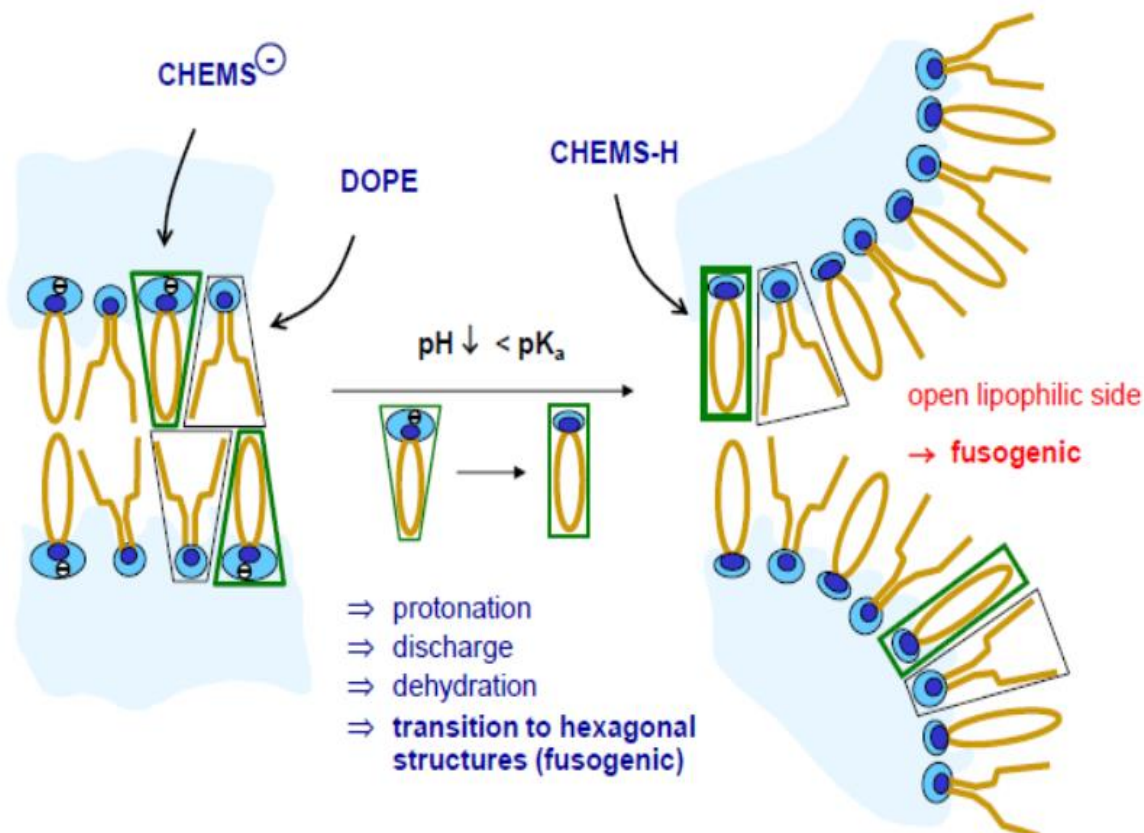


Figure 76. pH sensitive liposomes: fusion with endosomal membrane. Adapted from Prof. Regine Suss with permission.

Figure 76 shows a schematic representation on how the ionization state of the CHEMS determines the phase and fusogenic behaviour of the DOPE/CHEMS liposomes. At $\text{pH} > \text{pK}_a$, the negative charge of CHEMS reduces the intermolecular repulsion of DOPE head groups and stabilizes the structure in a bilayer lamellar phase. On the contrary, the neutral form of CHEMS promotes the fusion property and DOPE can adopt the inverted H_{II} phase it prefers in isolation^(322, 323).

3.5.1.2 Mid infrared ATR absorbance spectra of CHEMS

As asserted by different authors that the polymorphic phase behavior of CHEMS depends on its protonation state which changes around its pK_a value. Hafez *et al.* reported a pK_a value around 5.8 whereas Panzner *et al.* measured a pK_a of 5.4 in vesicles consisting of DMPC and CHEMS in ratio 7:3^(322, 324, 325, 326).

Here, the behaviour of CHEMS in Hepes buffer at two pH values (pH < 5.8 and pH > 5.8) is analyzed with mid infrared spectroscopy (Figure 77) in order to get insight into the spectral properties of the protonated and deprotonated forms.

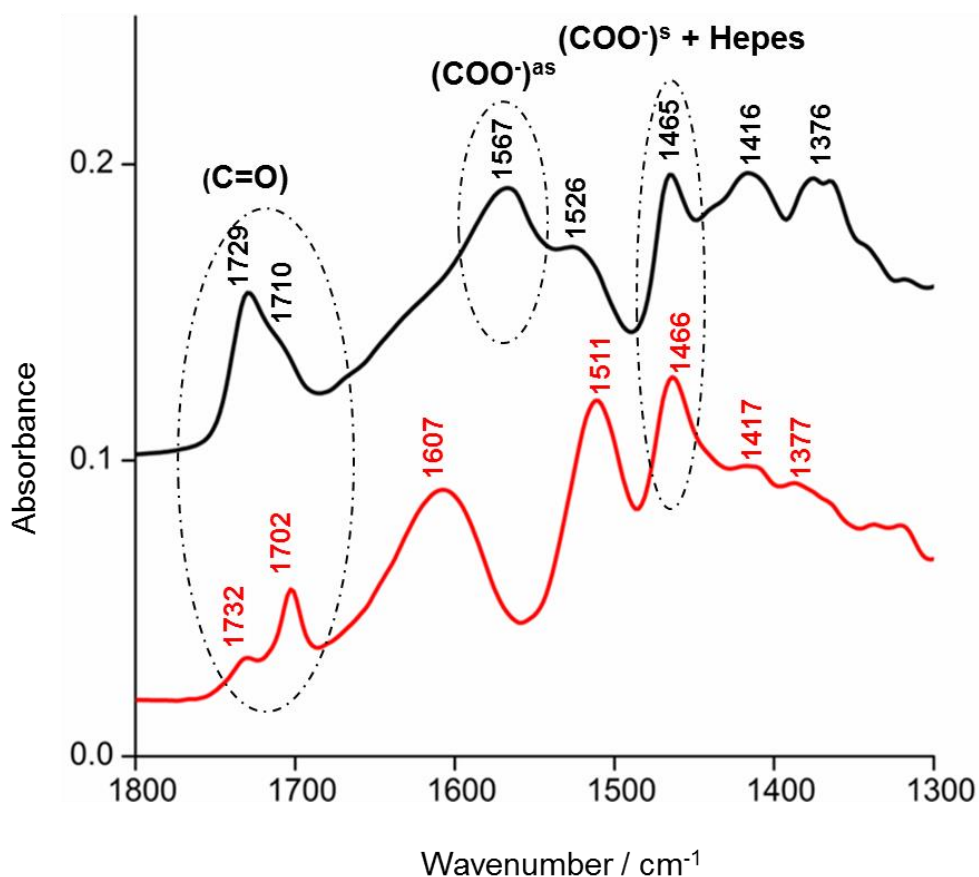


Figure 77. The mir ATR absorbance spectra of CHEMS at pH 7.4 (black) and pH 4.5 (red line).

The ATR absorbance spectra of CHEMS in the 900-1300 cm^{-1} spectral region is not shown here since it contains the contribution from Hepes buffer where the symmetric and asymmetric stretching vibrations of the sulfate group are presented (see appendix 6 and 7 for spectra of Hepes at different pH and the assignments).

Interestingly, the comparison between the two spectra reveals an additional peak at 1567 cm^{-1} which can be assigned to the asymmetric stretch of the COO^- group in the deprotonated state of CHEMS head group at pH 7.4. The carbonyl region between 1680 and 1780 cm^{-1} is considered of particular importance. Figure 78 shows an enlarged view of the CO band at pH 4.5 and 7.4. The presence of two separated bands at 1732 and 1702 cm^{-1} at pH 4.5

corresponds to the CO of ester and carboxylic acid parts respectively present in CHEMS (Figure 78B).

On the other hand, at pH 7.4 the deconvolution of the CO band leads to two peaks at 1710 and 1730 cm^{-1} , the latter peak is assigned to the CO of ester group whereas the former to CO of carboxyl group indicating that a small fraction of CO are still protonated at pH 7.4.

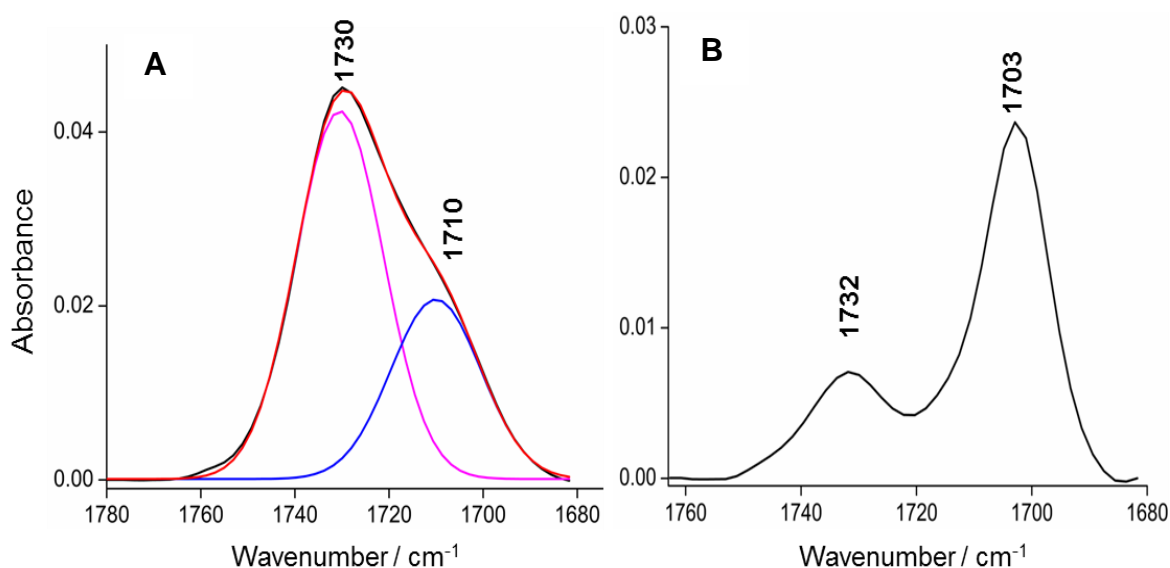


Figure 78. An enlarged view of the carbonyl band of CHEMS at pH 7.4 (A) and pH 4.5 (B).

3.5.1.3 Mid infrared ATR absorbance spectra of DOPE/CHEMS

The mid ATR absorbance spectra of the DOPE/CHEMS liposomes at different pH are recorded using the ZnSe/Si crystal modified with TiO_2 . All the spectra are normalized with respect to CH_2 scissoring band at 1465 cm^{-1} (Figure 79A). The spectra show mainly shifts in the region of the phosphate head group (1100-1300 cm^{-1}) and in the CO stretching vibration (1700-1800 cm^{-1}) upon pH change which gives an idea about the principle interactions taking place around the head group (Figure 79A). Additionally, the spectra of DOPE/CHEMS liposomes seem to correspond to the DOPE spectrum where the contributions from CHEMS are essentially overlapped (Figures 79B, 79C). The assignments of the different peaks are presented in Table 22.

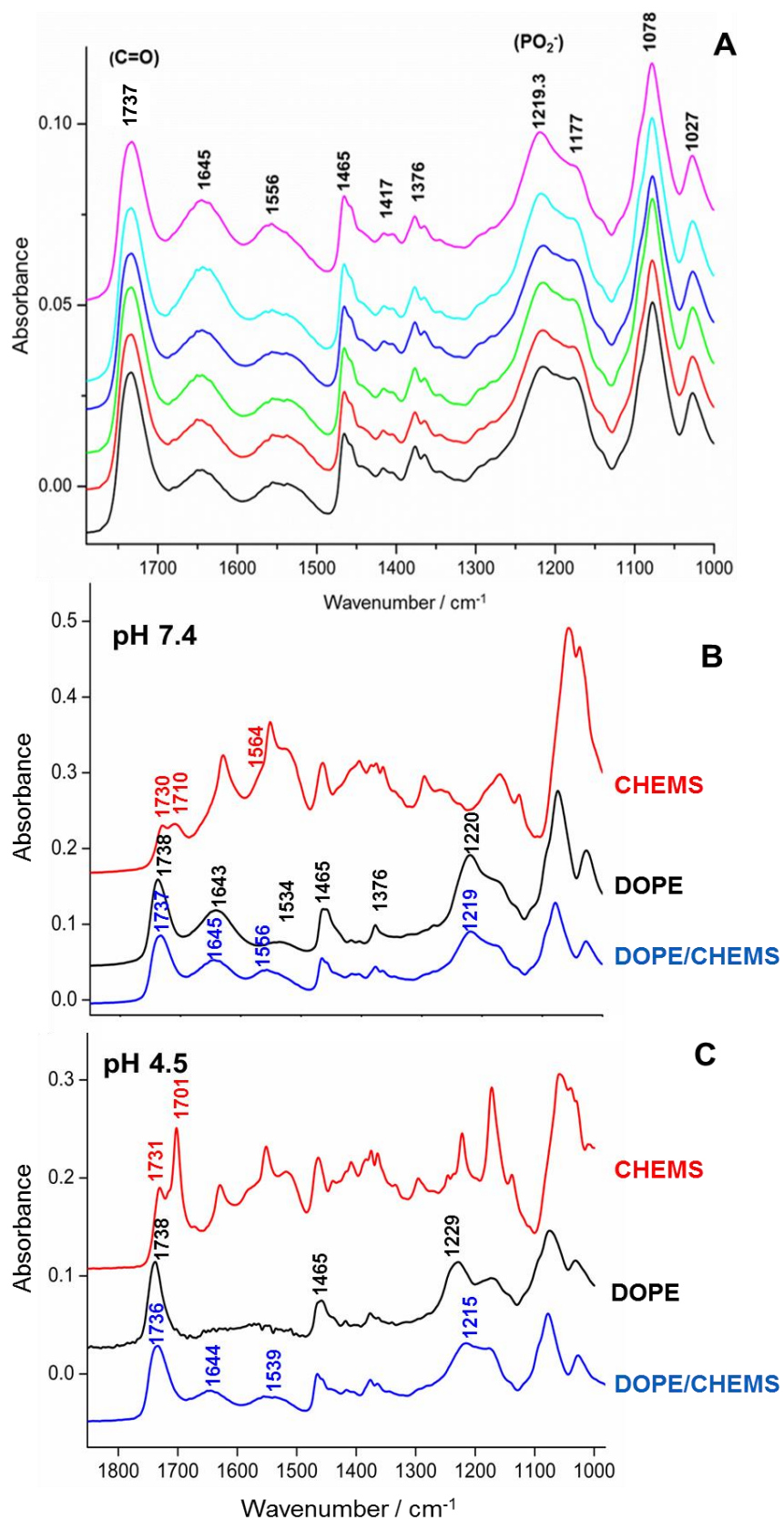


Figure 79. The mid ATR absorbance spectra of the DOPE/CHEMS liposomes (A) at pH 4.5 (black), 5 (red), 5.5 (green), 6 (blue), 6.5 (cyan) and 7.4 (magenta). The ATR spectrum of DOPE lipid (black) and CHEMS (red) and liposomes (blue) at pH 7.4 (B) and 4.5 (C).

Table 22. Detailed band assignments of DOPE/CHEMS liposomes, DOPE lipid, CHEMS at pH 7.4.

DOPE (pH7.4)	CHEMS pH7.4	DOPE/CHEMS pH 7.4	Tentative Assignments
1738	1730	1737	C=O stretch
	1710		C=O stretch
1643		1645	NH ₃ ⁺
	1564		$\nu_{as}(\text{COO}^-)$
		1556	NH ₃ ⁺ and $\nu_{as}(\text{COO}^-)$
1534			NH ₃ ⁺
1465	1466	1465	CH ₂ bend
		1417	CH ₂ bend and $\nu_s(\text{COO}^-)$
1376	1376	1376	CH ₃ bend
1220		1219.3	PO ₂ ⁻ asymmetric stretching
< 1220		< 1219.3	PO ₂ ⁻ symmetric stretching, buffer contribution, ester C-O-C symmetric and asymmetric stretch and $\delta(\text{OH})$
	<1200		C-O-C stretch

3.5.1.4 Effect of pH on phosphate head group

Figure 80A illustrates the phosphate region of DOPE/CHEMS (3:2) liposomes at different pH values. The asymmetric stretching vibration of phosphate is found at 1215.2 and 1219.3 cm⁻¹ at pH 4.5 and 7.4 respectively. The shift of 4 cm⁻¹ to a higher wavenumber, at pH higher than pK_a of CHEMS (5.8), indicates that the phosphate group is involved in less hydrogen bonding interaction. The plot of the wavenumber of the asymmetric stretching phosphate vibration as function of pH is presented in Figure 80B. Between pH 4.5 and 5.5, the curve exhibits a plateau. At pH around 5.6, the wavenumber starts to increase rapidly forming a sigmoidal curve. This pH value (5.6) is very close to the pK_a of CHEMS (5.8).

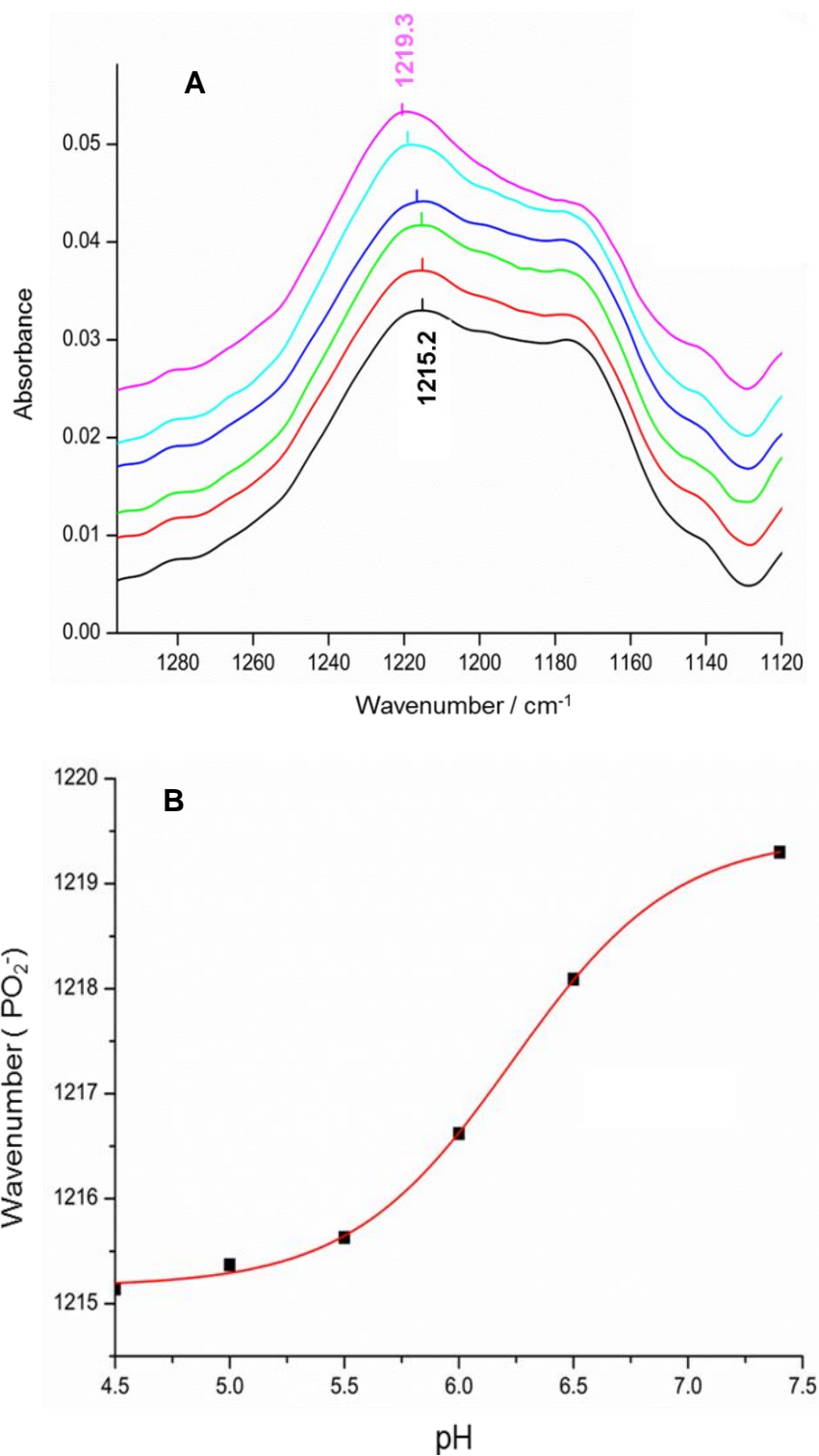


Figure 80. The phosphate region of DOPE/CHEMS liposomes (A), 4.5 (black), 5 (red), 5.5 (green), 6 (blue), 6.5 (cyan) 7.4 (magenta) and its pH dependence (B).

Figure 81 presents the proposed mechanism of interaction between CHEMS and DOPE. In this mechanism, we suggest that the sterol ring of CHEMS fits in the same position as the fatty acid chains of DOPE and the succinic group fits into the polar head of DOPE lipid.

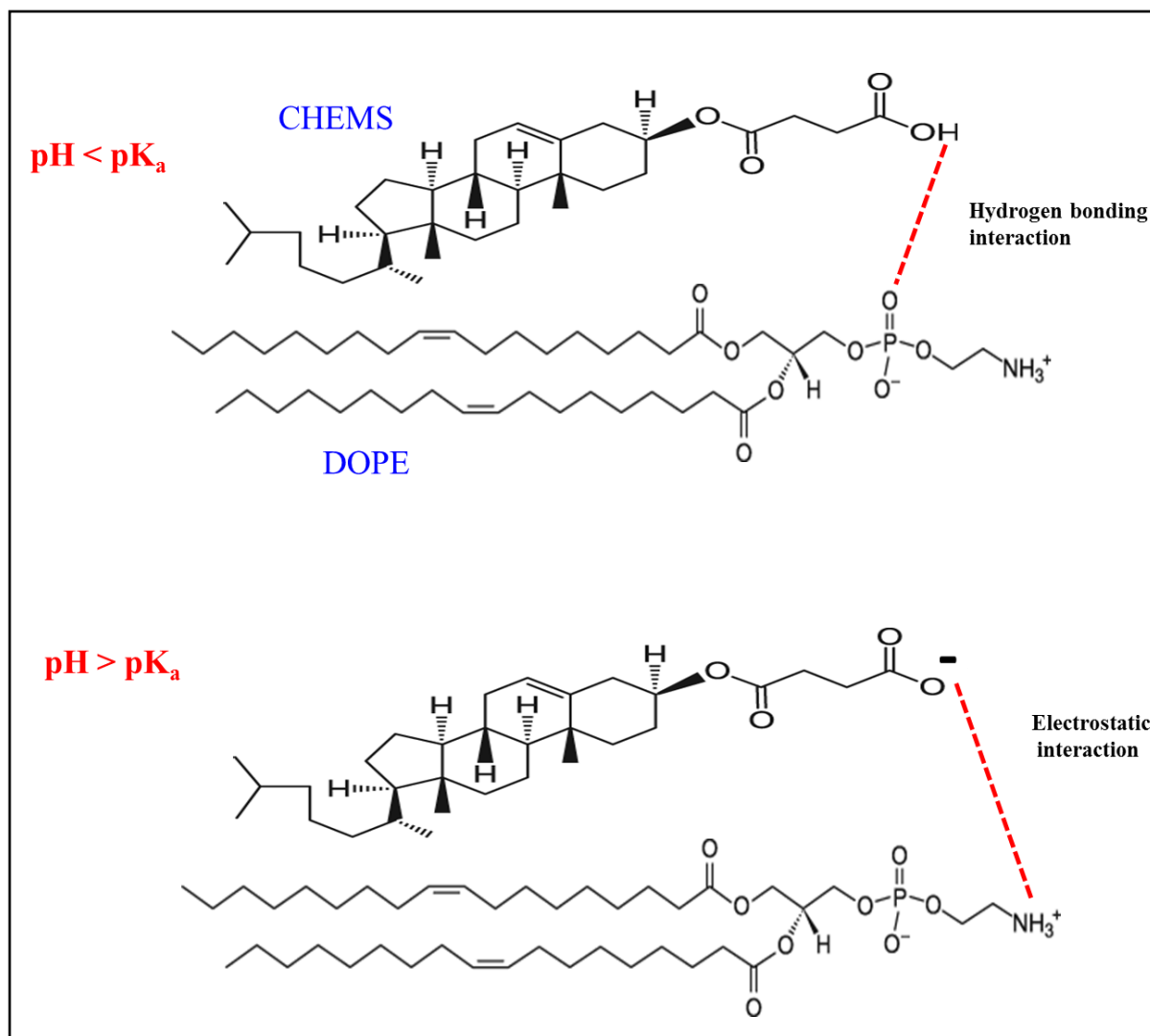


Figure 81. Schematic diagram of the different kinds of interaction between CHEMS and DOPE lipid.

At $\text{pH} < \text{pK}_a$, CHEMS exists in its protonated form, so the OH group could be hydrogen bonded to phosphate group of DOPE and thus shifting it to lower wavenumber. Whereas when $\text{pH} > \text{pK}_a$, the head group of CHEMS will be deprotonated (COO⁻), thus there is no possibility for hydrogen bonding interaction. However, this allows for different kind of interaction as electrostatic between COO⁻ of CHEMS and NH₃⁺ of DOPE lipid⁽³²⁷⁾.

3.5.1.5 Effect of pH on the CO band

The CO stretching vibration of DOPE/ CHEMS liposomes is observed at 1736 and 1737 cm^{-1} at pH 4.5 and 7.4 respectively (Figure 82). The deconvolution of CO band at pH 4.5 reveals the contribution of four components whereas at pH 7.4 three components are presented. The characteristics of these peaks are summarized in Table 23.

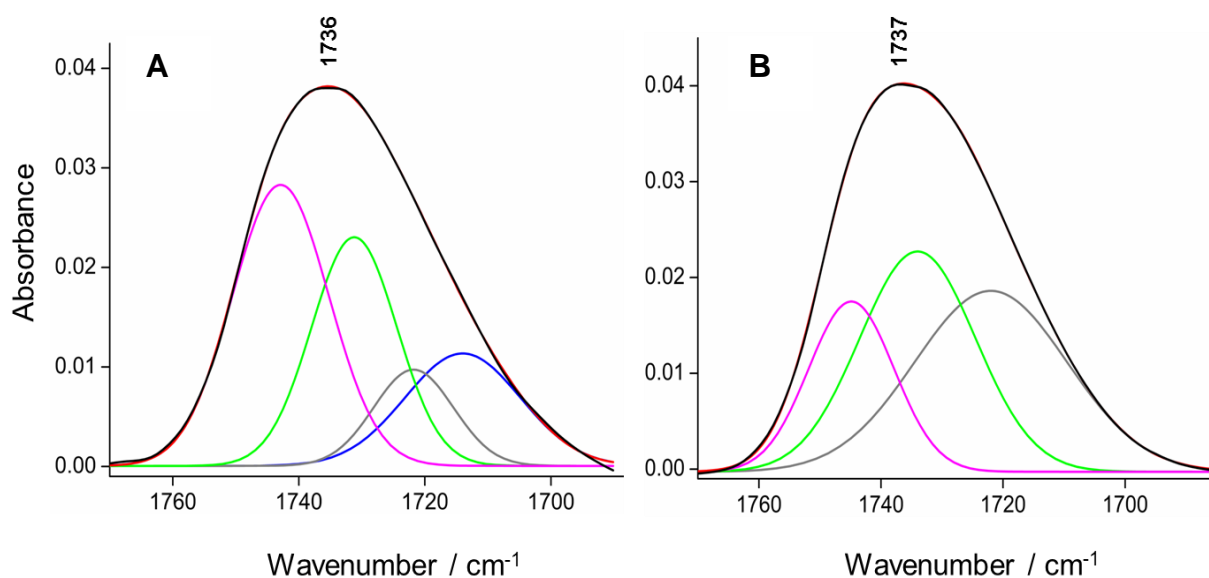


Figure 82. Deconvolution of the CO stretching band at pH 4.5 (A) and pH 7.4 (B). CO band experimental (black line), fitted curve (red line), different components (blue, gray, green, magenta).

Table 23. The deconvolution of the CO vibration of DOPE/CHEMS liposomes at pH 4.5 and 7.4.

CO band	Wavenumber (cm^{-1}) of different components			
pH 4.5	1714.0	1721.8	1731.2	1742.8
pH 7.4	--	1722.0	1734.0	1744.8

Basically the comparison between the CO bands at pH 7.4 and 4.5 reveals the presence of an additional peak at 1714 cm^{-1} in the latter, which is assigned to the CO vibration of the carboxylic group (COOH) of CHEMS. The other peaks at 1722, 1734 and 1745 cm^{-1} originate mainly from the ester groups of DOPE and CHEMS. All the components at pH 4.5

are observed at lower wavenumber indicating that they are highly involved in hydrogen bonding interaction.

3.5.1.6 Far infrared ATR absorbance spectra of DOPE/CHEMS

To confirm the results obtained in the mid infrared region on the different behaviour of DOPE/CHEMS liposomes at different pHs, some far infrared measurements are done in order to probe the effect of pH on the hydrogen bonding interaction. In the FIR region the most significant signals in the spectra of DOPE/CHEMS (Figure 83) are the phosphate vibrations between $580\text{-}500\text{ cm}^{-1}$, and the collective modes of hydrogen bonding found below 300 cm^{-1} .

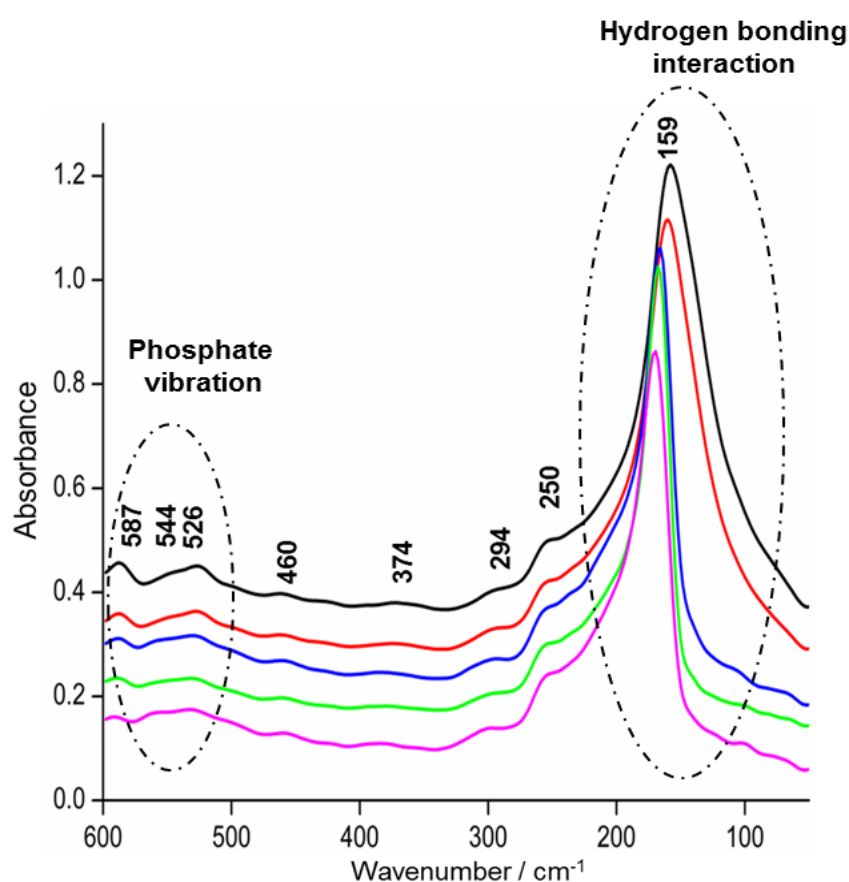


Figure 83. ATR far infrared absorbance spectra of DOPE/CHEMS liposomes at pH 4.5 (black), pH 5 (red), pH 5.5 (blue), pH 6.5 (green) and pH 7.4 (magenta).

In order to see the individual contribution of DOPE and CHEMS in the liposomes, the far infrared spectra of DOPE lipid, CHEMS and liposomes are studied (Figure 84). The peaks observed at 560 and 531 cm^{-1} in the liposomes are attributed to the wagging and rocking modes of phosphate head group and they originate mainly from the DOPE lipid. The band at 456 cm^{-1} corresponds to $\tau(\text{C-C})_n$ and it comes from the contribution of both DOPE and

CHEMS. In addition the peaks seen at 385, 301 and 250 cm^{-1} are attributed to τ (CCN), τ (C-CH₃) and τ (CH₂ chain) respectively. The band at 170 cm^{-1} corresponds to the hydrogen bonding signature.

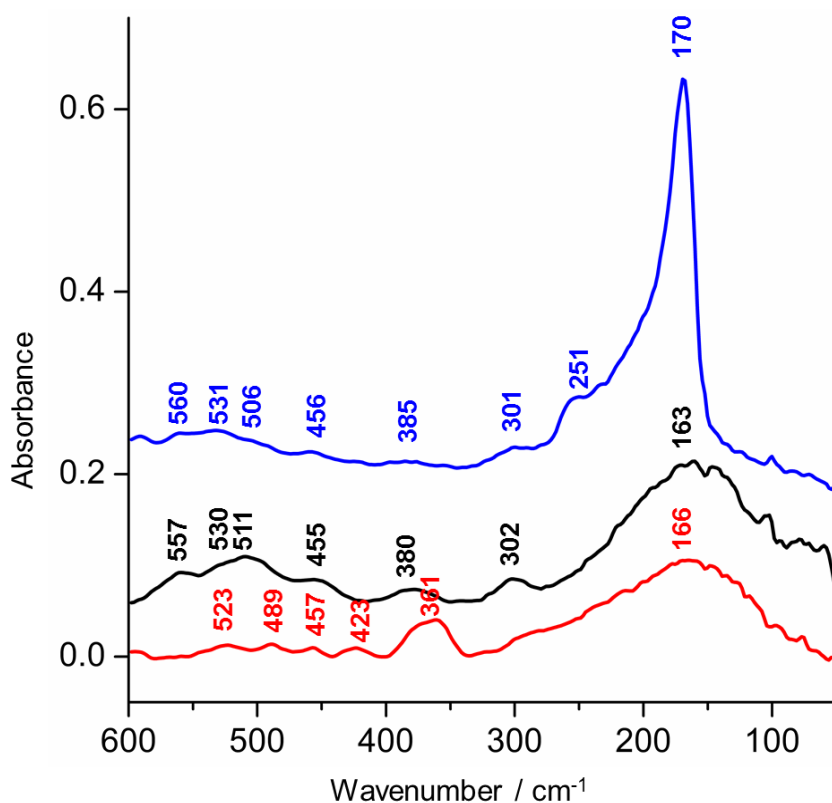


Figure 84. The far infrared spectra of DOPE/CHEMS liposomes (blue), DOPE lipid (black), CHEMS (red) at pH 7.4.

The hydrogen bonding feature is also called the connectivity band ⁽²⁹⁴⁾. The position and the half-band width of this hydrogen bonding signature, may be strongly influenced by its polarizability.

The enlarged view of the hydrogen bonding of DOPE/CHEMS liposomes and their corresponding shifts with different pH are given in Figure 85. This hydrogen bonding is located at 159 and 170 cm^{-1} for pH 4.5 and 7.4 respectively. Obviously, the 11 cm^{-1} shift to higher wavenumber indicate that the hydrogen bonding interaction is affected. In addition, the band at pH 4.5 is very broad in contrast to pH 7.4 where it is very sharp. These findings are consistent with what obtained in the mid infrared.

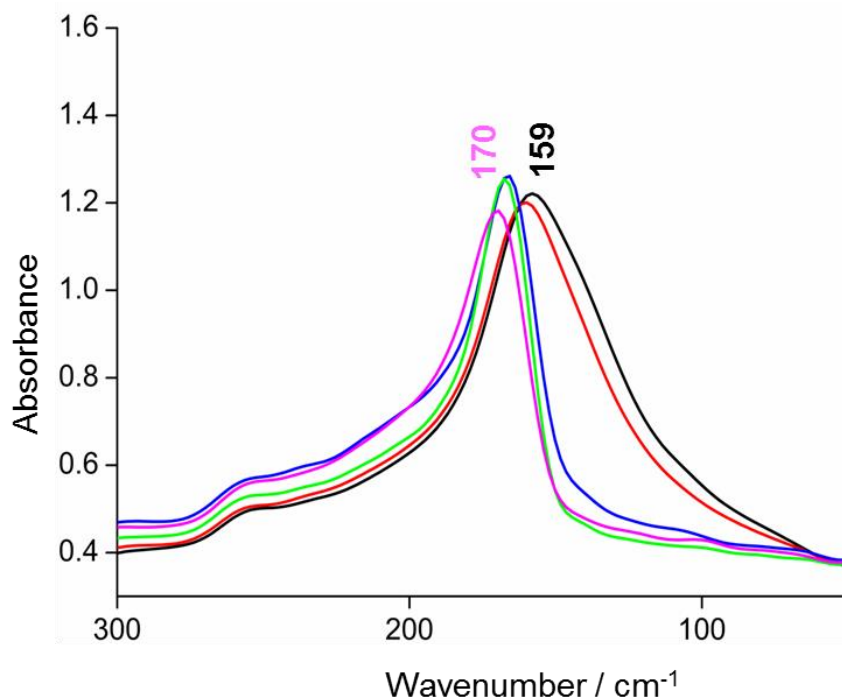


Figure 85. Enlarged view of the hydrogen bonding continuum of DOPE/CHEMS liposomes at pH 4.5 (black), pH 5 (red), pH 5.5 (blue), pH 6.5 (green) and pH 7.4 (magenta).

3.6 Conclusion

Temperature dependent studies aim to answer questions on the presence and the strength of hydrogen bonds, since they are highly influenced by the temperature. Studies of the temperature dependence of IR spectra make it possible to compare the spectra in various phase states and to clarify the role of intermolecular forces.

The temperature dependence behaviour of EPC, EPE, CL and the lipid/cholesterol (2:1) systems allowed the determination of the transition temperature of lipids and the examination of the clear effect of cholesterol. The transition temperatures of EPC and EPE decreased from 29 °C and 22 °C to 19 °C and 8 °C, respectively, after the incorporation of cholesterol. Cardiolipin showed no transition temperature because it is stabilized in the hexagonal (H_{II}) nonlamellar structure.

For EPC, EPE and CL, the CO vibration as well as the phosphate vibration was sensitive to the temperature dependent phase transition. They were shifted to higher wavenumber upon heating indicating the lower hydrogen bonding interaction. Furthermore, the far infrared spectra of these lipids were presented. The hydrogen bonding behavior (below 300 cm^{-1}) of

EPC and EPE was in good agreement with the observation in the mid infrared range whereas cardiolipin showed a different behavior. Then the far infrared spectral properties of mixture of EPC and EPE with different ratios were probed to see the influence of the head group composition on the spectral properties.

Finally, the study of DOPE/CHEMS liposomes revealed their pH dependence behavior. The change in pH induced a clear shift in the asymmetric stretching of phosphate and in the hydrogen bonding continuum. Thus the findings of mid and far infrared spectroscopy allowed us to propose a mechanism for the interaction between DOPE and CHEMS via both hydrogen bonding and electrostatic interaction.

Chapter IV

**Study of complex I protein using infrared,
Raman and UV-visible spectroscopies**

4 Complex I

The specific interaction of lipids with membrane proteins is well accepted to be crucial as mentioned before in section 1.3. However an understanding of this phenomenon on the molecular level is missing. In this chapter, the ability of artificial lipid (PMOXA₁₆-PDMS₇₂-PMOXA₁₆ block copolymer) with designed chemical properties of the hydrophilic and hydrophobic moieties to replace natural lipids is determined ⁽¹⁸²⁾. The interaction between polymer and protein is probed using infrared spectroscopy in order to monitor the conformational changes and protonation/deprotonation states of amino acids during the protein redox reactions.

In the second part of this chapter, the study of different complex I mutants by FTIR and Raman spectroscopies are considered to get further insight into the structure, proton translocation mechanism and different properties of the iron sulfur clusters.

4.1 Complex I protein and polymer

In order to study the effect of polymer, complex I was provided, by the group of Prof. Dr. Thorsten Friedrich, as isolated in detergent solution devoid of endogenous lipids. The polymer was added to the protein sample and the activity was measured. The activity measurements have been carried by Marius Schulte (Freiburg) and the results obtained are summarized in Table 24.

The NADH: decylubiquinone (DQ) oxidoreductase activity depends on the incubation time and the temperature. For instance, the optimum conditions for complex I NADH: DQ activity are obtained by 30 min incubation time at 0 °C whereas in the case of phospholipids it needs 20 min incubation at 0 °C.

Table 24. The activity measurements of delipidated complex I protein in the presence of *E. coli* polar lipids (PL), cardiolipin (CL) and block copolymer (BCP).

Sample	Absolute value $\mu\text{mol}\cdot\text{min}^{-1}\cdot\text{mg}^{-1}$	Activity 100 %
Delipidated KI + PL	3.45	100
Delipidated KI	0.9	26
Delipidated KI + CL	2.65	77
Delipidated KI + BCP	1.93	56

As illustrated in the table above, the enzymatic activity is highly enhanced in the presence of *E. coli* polar lipids and cardiolipin. The recovery in the activity is in agreement with the previously reported studies where the activity of complex I is strongly dependent on the presence of phospholipids that provide an appropriate environment for the active conformation of the complex I protein^(179, 328).

Concerning the addition of block copolymer, the activity is enhanced twice in comparison to the delipidated sample indicating that the block copolymer activates complex I to a similar extent as phospholipids. This finding is in line with the results obtained on delipidated complex I by Graff *et al.*⁽¹⁸²⁾ using the PMOXA₁₃-PDMS₁₁₀-PMOXA₁₃.

Graff *et al.*⁽¹⁸²⁾ investigated the effect of the molecular properties of the block copolymer on the physiological activity of complex I. They found that increasing the length of the hydrophobic block leads to stronger activation of complex I whereas increasing the hydrophilic block length causes an inverse effect on the activity and increases the thickness of the membrane.

The enhancement in the activity could be explained by the amphipathic nature of the block copolymer that leads to the formation of various structures as unordered structures or bilayers where the membrane arm of complex I resides (Figure 86). Thus the polymer can interact with the outer surface of the protein or even diffuse into the inside. The hydrophilic and the hydrophobic blocks of the copolymer system are related to intermolecular forces acting between polymer and the protein and might favour a more active conformation of complex I.

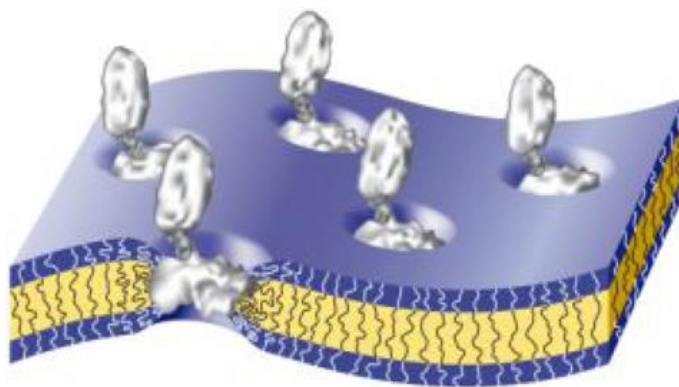


Figure 86. Graphical representation of complex I incorporated in copolymer membrane ⁽¹⁸²⁾.

4.1.1 Electrochemical cell

To get a clearer idea on the effect of the polymer on the complex I function, the electrochemically induced differential FTIR spectra have been obtained for the delipidated complex I from *E. coli* with and without polymer to get a better understanding about the changes occurring upon oxidation and reduction of the protein. Figure 87 presents the spectra for a potential step from 0 to -650 mV in the spectral region from 1800-1200 cm^{-1} .

The differential spectrum presents positive and negative signals that are associated with the oxidized and reduced forms of the protein respectively. Contributions from the cofactors, conformational changes of the protein backbone as well as the protonation and deprotonation states of the individual amino acids are expected.

The oxidized minus reduced FTIR spectrum of delipidated complex I (Figure 87, red spectrum) involves intense signals from 1700 to 1610 cm^{-1} and from 1570 to 1500 cm^{-1} which are attributed to amide I and amide II respectively. Contributions from FMN (1547 cm^{-1}) and ubiquinone (1264 and 1255 cm^{-1}) are also observed. The signals from the phosphate buffer occur mainly below 1200 cm^{-1} (see Appendix 8). The contribution from the polymer is mainly observed above 2800 cm^{-1} and below 1258 cm^{-1} (see Appendix 9).

The addition of the polymer induces a large reorganization of the peptide backbone where the peaks in the amide I and amide II regions (1648, 1622 and 1505 cm^{-1}) are highly perturbed revealing that the secondary structure components undergo certain modifications (Figure 87, black spectrum). This indicates that the conformational movements associated with the functioning of the enzyme are altered by the presence of the polymer.

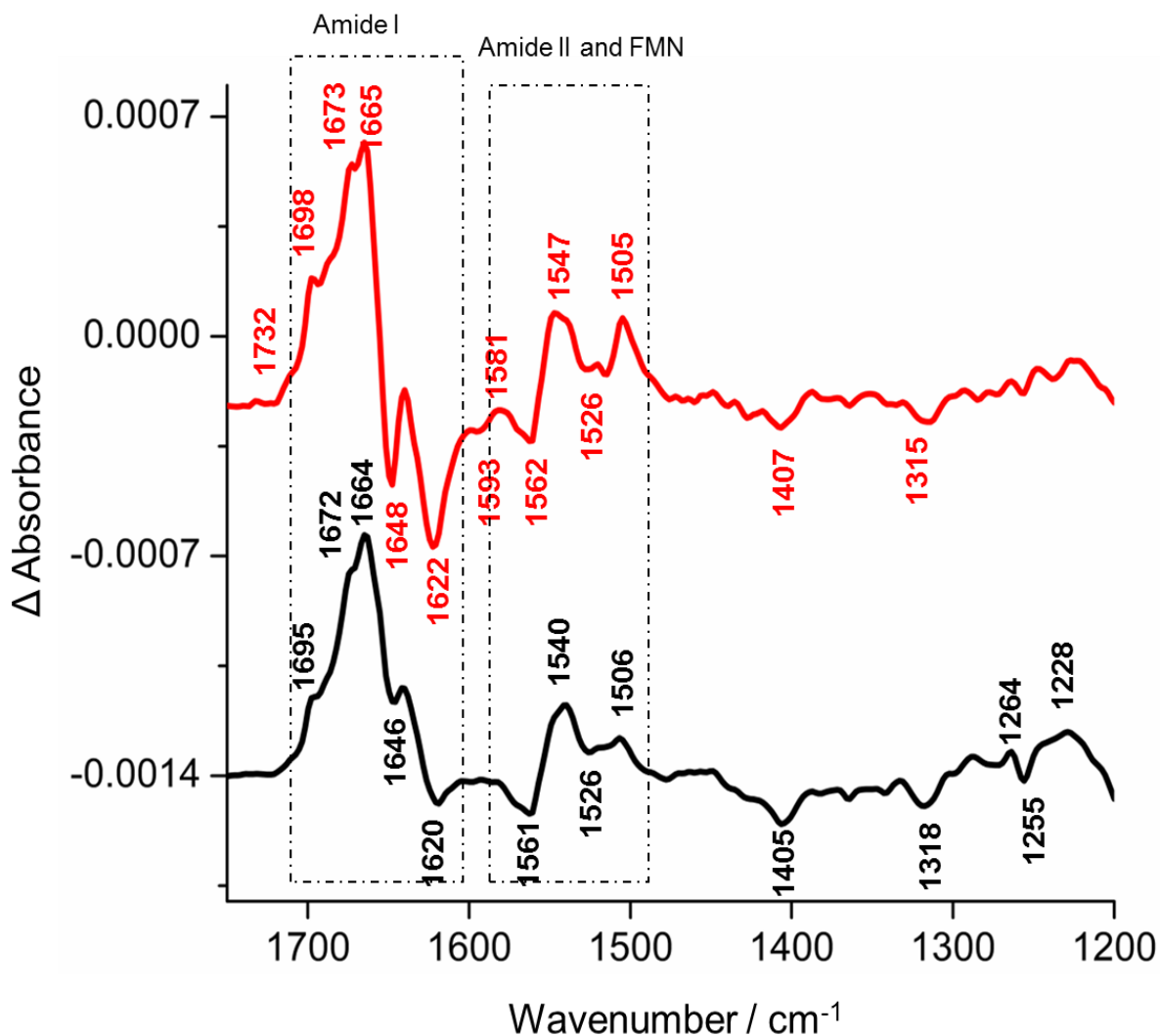


Figure 87. Oxidized minus reduced FTIR difference spectra of the delipidated wild type complex I (red) with polymer (black), MES buffer pH 6.3.

4.1.2 Far infrared spectroscopic investigation

Figure 88 shows the far infrared of delipidated complex I from *E. coli* with and without polymer between 600-50 cm^{-1} . The most relevant spectral difference between both spectra is the hydrogen bonding collective mode which is sensitive to the structure of the molecules and to intermolecular interactions. This band is characterized by an intense peak below 300 cm^{-1} (329, 330).

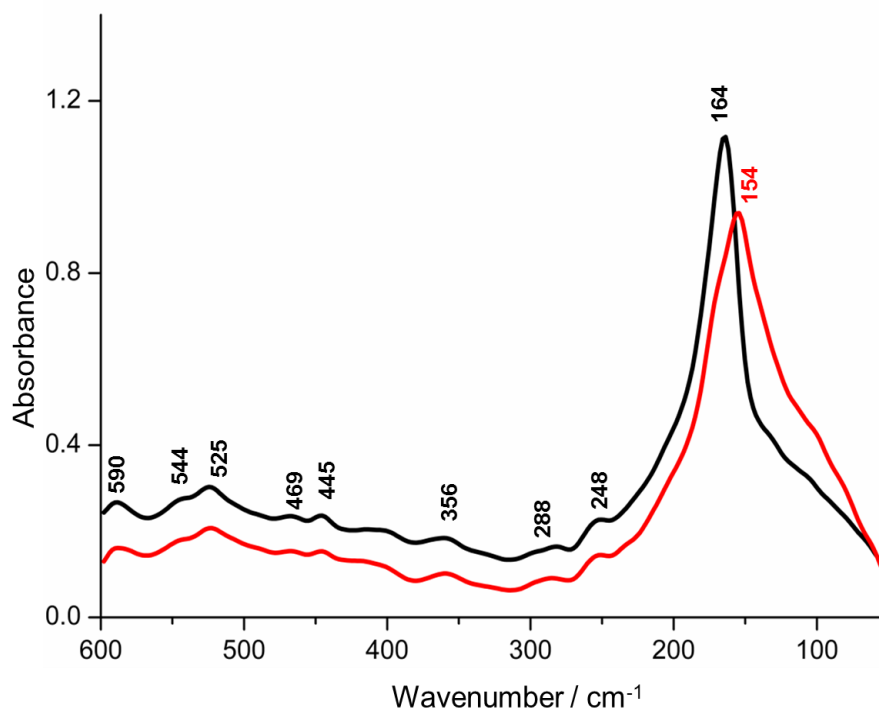


Figure 88. ATR absorbance spectra of delipidated complex I (red) with polymer (black) from *E. coli* in the far infrared domain from 600 to 50 cm^{-1} .

The far infrared absorbance spectrum of delipidated complex I (red spectrum) includes the contribution from the amide VII (N-H out of plane) at 288 cm^{-1} as well as the metal ligand vibrations. In particular, the Fe-S vibrations of the binuclear [2Fe-2S] and tetranuclear [4Fe-4S] clusters can be expected at 455 and 469 cm^{-1} for complex I⁽²¹⁰⁾.

The hydrogen bonding mode is seen at 154 and 164 cm^{-1} for the pure delipidated sample and with polymer respectively. None of the observed signals arises from the polymer alone (see Appendix 10).

Interestingly, the hydrogen bonding shows changes not only in the position but also in the shape (broadness). Thus the shift to the lower wavenumber in the case of pure sample indicates that the hydrogen bonding is stronger. This could be explained by the different environments between both samples where the interaction with the backbone of the protein and the stabilization of the structure is higher in the case of the pure delipidated sample. In few words, the results from this part clearly demonstrated the strong influence of the ABA polymer on the complex I protein. This block copolymer is responsible for the regulation of the catalytic activity and the formation of a suitable environment for the active conformation of this protein.

4.2 NuoL mutants

As mentioned before in the introduction part, the subunits NuoL, M, N, A, J, K in the membrane part are involved in proton translocation mechanism. The NuoL subunit is characterized by the presence of a 110 Å long horizontal amphipathic helix aligning the membrane arm ⁽³³¹⁾ (Figure 89). Charged amino acids on the horizontal helix of the *E. coli* complex I have been mutated to investigate their roles in proton translocation. Steimle *et al.* ⁽¹⁷⁵⁾ mutated the amino acids in position D542, D546 and D563. They found that D563 residue has a functional role in the proton pumping of the *E. coli* complex I.

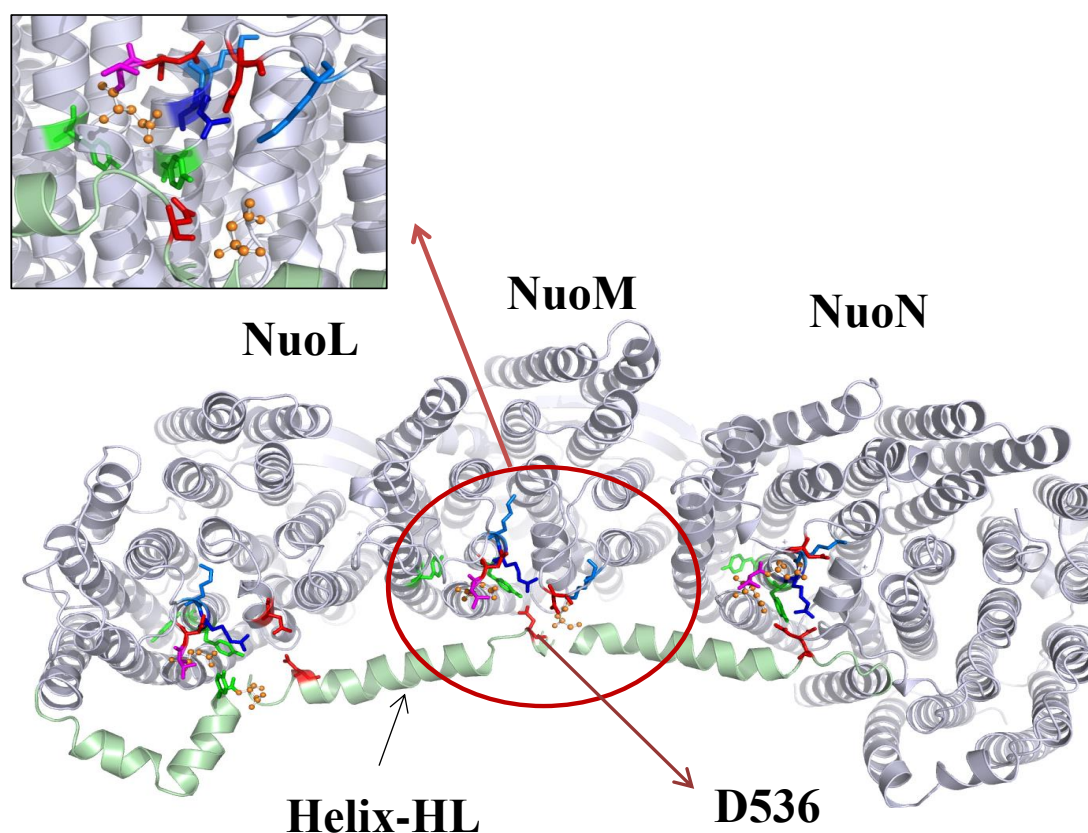


Figure 89. The subunits NuoL, M, N of the membrane arm of complex I from *E. coli* (PDB ID: 3RKO). The residues are colored as follows: Gln, Asn - Orange (balls and sticks); Asp, Glu and Gly- Red; Arg - Deep Blue; Lys - Light Blue; Tyr - Green; Thr - Magenta. Helix HL is colored in pale green.

The recently described D563N variant showed a slightly reduced NADH:ubiquinone oxidoreductase activity of $1.2 \pm 0.2 \mu\text{mol}\cdot\text{min}^{-1}\cdot\text{mg}^{-1}$ in proteoliposomes that is 75% of the activity of the wild type complex in proteoliposomes ⁽¹⁷⁵⁾. The H^+/e^- stoichiometry was found to be about 3. Since the wild type complex has a stoichiometry of 4, it was suggested that at

least one of the proton pathways is perturbed in the mutant. The conservative substitution D563E led to the same H^+/e^- stoichiometry demonstrating not only, that the presence of this acidic residue is required for full proton translocation but also, that the spatial position of the carboxylic group is essential.

To collect further information about the general effects induced by mutating these residues on the complex I protein, electrochemically induced FTIR difference spectroscopy was performed. Figure 90 displays the fully oxidized (0 mV) minus fully reduced (-650 mV) FTIR spectra in the 1800-1200 cm^{-1} region. Figure 90A presents the oxidized minus reduced FTIR difference spectrum of the wild type complex I from 0 to -650 mV. This spectrum includes the contribution from the reorganization of secondary structure elements, from FMN, individual amino acids and quinone⁽¹⁵⁹⁾. The obtained result for wild type is in line with Hellwig *et al.*⁽¹⁵⁹⁾ where they reported the difference spectrum of the whole protein and for the NADH dehydrogenase fragment.

The spectrum (Figure 90A) is dominated by strong positive signals in the amide I region at 1698, 1673 and 1665 cm^{-1} as well as strong negative modes at 1648 and 1623 cm^{-1} in the amide I region reflecting the large reorganization of the peptide backbone upon oxidation and reduction. These peaks are characteristic of the secondary structure components. Peaks at 1560, 1538 and 1529 cm^{-1} are seen in the amide II region where signals from the bending (N-H) and stretching (C-N) modes are expected to contribute. Furthermore, this spectrum includes the contributions from FMN, ubiquinone and amino acid side chains. Usually the FMN modes including the $\nu(C=C)$ mode and $\nu(C=O)$ vibration appear at 1540 and 1710 cm^{-1} respectively. Other FMN modes are involved in signals at 1226, 1698 and 1673 cm^{-1} .

The signals observed for FMN are in good agreement with the redox FTIR spectra of FMN described in details in both H_2O and D_2O by Hellwig *et al.*⁽¹⁵⁹⁾. Moreover, the $\delta(C-OCH_3)$ modes of ubiquinone appear at 1264 and 1256 cm^{-1} and the $\nu(C=O)$ modes of protonated aspartic and glutamic acid side chains contribute at 1735 cm^{-1} . Further contributions of several amino acids appear at frequencies within the amide I and amide II range. For example glutamine, lysine, arginine, and asparagine have strong vibrations in the 1690 to 1620 cm^{-1} range⁽³³²⁾. At 1540/1535 and 1406 cm^{-1} the $\nu_{s/as}(COO^-)$ mode of deprotonated residues are expected. Additionally, the signal at 1514 cm^{-1} is attributed to $\nu(C=C)$ ring mode of tyrosine. The tentative assignments are summarized in Table 25.

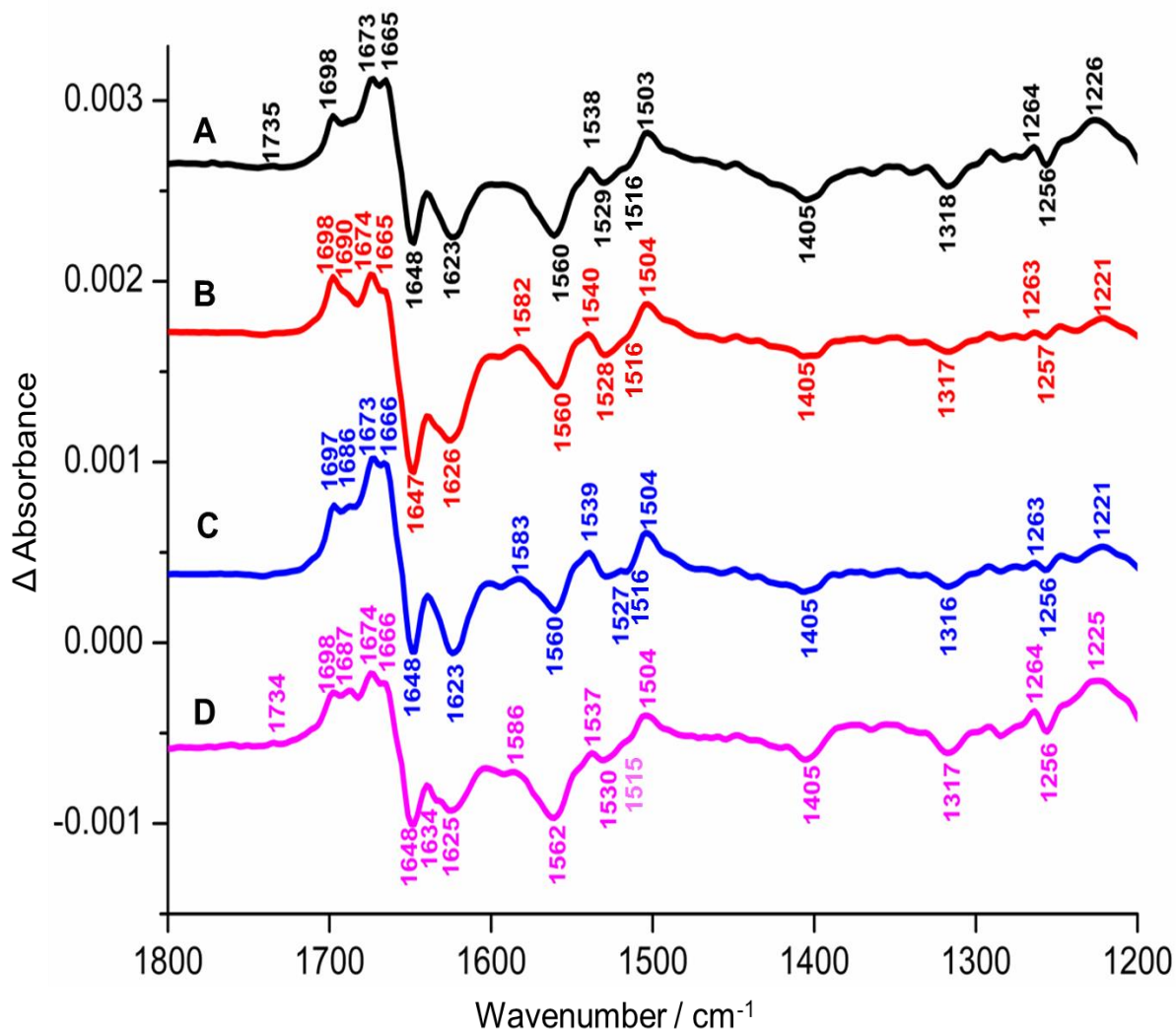


Figure 90. Oxidized minus reduced FTIR spectra of complex I (A, black line), D563E (B, red), D563N (C, blue) and Y594F (D, magenta).

Figures 90B and 90C show the oxidized minus reduced FTIR difference spectra of the D563E and D563N mutants respectively. The signals dominating in the spectral range from 1600-1700 cm^{-1} and 1500-1580 cm^{-1} correspond to the amide I and amide II regions respectively. The spectra of these variants do not show strong differences in comparison to the wild type complex I (Figure 90A) indicating that the variants are properly assembled and stable which is in accordance with their only mildly changed electron transfer rate⁽¹⁷⁵⁾. Shifts in the amide I range around 1665/1625 cm^{-1} reveal a change in the conformational reorganization upon redox transfer. Figure 90D describes the oxidized minus reduced spectrum of Y594F. In comparison with the other spectra, small changes including the amide I and amide II regions can be seen. In addition, the peak at 1515 cm^{-1} which corresponds to the $\nu(\text{C}=\text{C})$ TyrOH is affected.

Table 25. Detailed band assignments of the FTIR electrochemically induced oxidized minus reduced difference spectra of the complex I from *E. coli*, D563N, D563E and Y594F mutants in 50mM MES, 50mM NaCl and pH 6.3 (207, 246, 333, 212).

Wild type	Nuo L D563 E	Nuo L D563N	Nuo L Y594F	Assignments
1735	----	----	1734	$\nu(\text{C=O})_{\text{asp,glu}}$
1698	1698	1697	1698	$\nu(\text{C=O})$ FMN, amide I
-----	1690	1686	1687	amide I
1673	1674	1673	1674	Amide I, $\nu(\text{C=O})_{\text{UQ}}$, $\nu_{\text{as}}(\text{CN}_3\text{H}_5^+)_{\text{arg}}$
1665	1665	1666	1666	amide I, Ubiquinone
1648	1647	1648	1648	amide I, α -helix, $\nu(\text{C=O})_{\text{asn,gln}}$
1623	1626	1623	1625	amide I, β -sheet, $\nu_{\text{s}}(\text{CN}_3\text{H}_5^+)_{\text{arg}}$
----	1582	1583	1586	$\nu(\text{C=N})$ FMN, amide II
1560	1560	1560	1562	amide II
1538	1540	1539	1537	$\nu_{\text{as}}(\text{COO}^-)_{\text{asp,glu}}$, $\nu(\text{C=C})$ FMN
1529	1528	1527	1530	Amide II
1516	1516	1516	1515	$\nu(\text{C=C})_{\text{TyrOH}}$
1503	1504	1504	1504	C-C stretching, bending CH, Tyr
1405	1405	1405	1405	$\nu_{\text{s}}(\text{COO}^-)_{\text{asp,glu}}$
1264	1263	1263	1263	$\delta(\text{C-OCH}_3)_{\text{UQ}}$, $\nu(\text{CO})_{\text{tyr}}$
1256	1257	1256	1256	$\delta(\text{C-OCH}_3)_{\text{UQ}}$
1226	1221	1221	1225	$\nu(\text{S=O})$ MES, ring FMN isoalloxazine

4.2.1 Zinc inhibition

Zn^{2+} is known to be the first inhibitor for the membrane arm of the complex I protein. The presence of zinc perturbs the proton translocation. Schulte *et al.* ⁽¹⁷⁸⁾ reported through detailed kinetic analysis the presence of several binding sites of Zn^{2+} in *E. coli* complex I. They also showed that the coordination of Zn^{2+} ions clearly involves acidic residues by using FTIR difference spectroscopy. The D563N mutant was studied and it is considered an excellent candidate for investigating the interaction of Zn^{2+} with complex I. To obtain more information about the interaction, the electrochemically induced FTIR difference spectroscopy was performed.

Figure 91 shows the oxidized minus reduced FTIR difference spectra of D563N mutant with and without zinc in the spectral region from 1800 to 1000 cm^{-1} . The two spectra are obtained from samples of the same preparation.

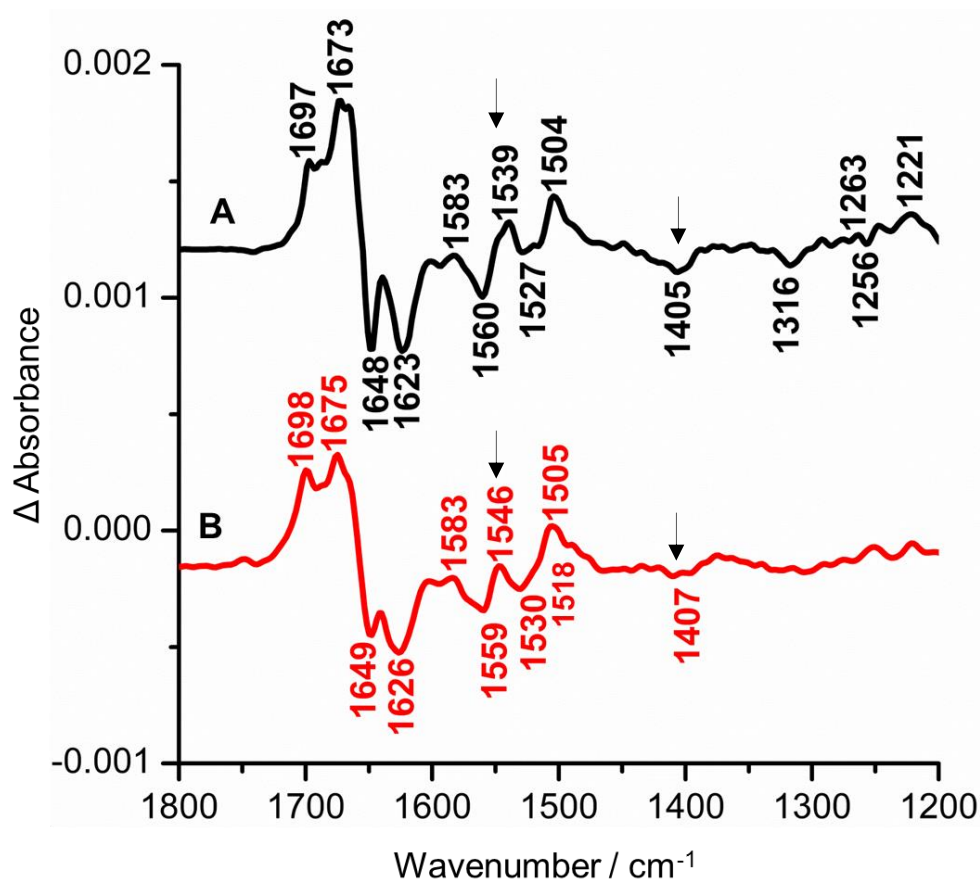


Figure 91. The fully oxidized minus fully reduced difference spectra of untreated (A) and Zn^{2+} incubated (B) D563N complex I mutant for the step from -650 to 0 mV.

The presence of zinc ions causes small changes in the difference spectrum of the D563N mutant. Particularly, the signals from the protonable residues such as aspartic and glutamic acids are modified (indicated by arrows). To highlight the perturbation induced by zinc binding, the double difference spectrum of D563N *minus* D563N+Zn²⁺ was calculated via interactive subtraction (Figure 92B). The changes induced by the Zn²⁺ binding to the variant are directly compared to the Zn²⁺ induced shifts detected for wild type complex I in H₂O (Adapted from Sebastien Kriegel thesis strasbourg, with permission⁽¹³⁰⁾).

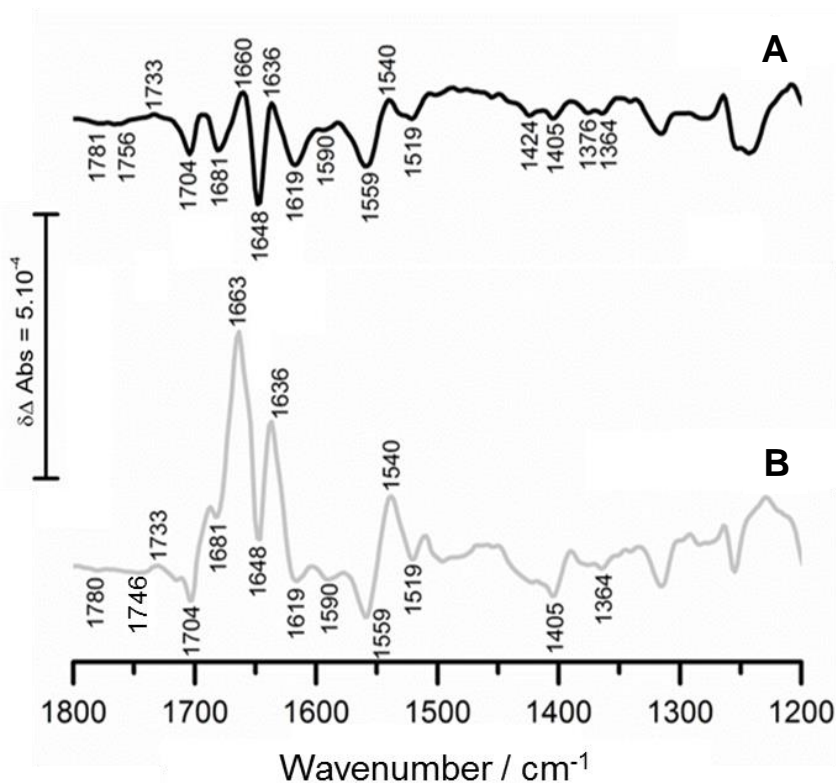


Figure 92. Double difference spectra of complex I *minus* complex I treated with Zn²⁺ of the wild type protein (A) and the D563N variant (B).

The double difference spectrum of D563N (Figure 92B) shows changes in the amide I and amide II regions from 1700 to 1500 cm⁻¹. The peaks seen at 1681, 1663 and 1648 cm⁻¹ indicate that the secondary structure components (α -helices, β -sheets and random) are perturbed by zinc binding. In addition, the vibrational modes from the acidic residues Asp and Glu are altered as the $\nu(\text{C}=\text{O})$, $\nu_{\text{as}}(\text{COO}^-)$ and $\nu_{\text{s}}(\text{COO}^-)$ modes of protonated and deprotonated Asp and Glu residues. The attribution of the peaks is summarized in Table 26.

The presence of the peaks at 1746 and 1780 cm⁻¹ correspond to the $\nu(\text{C}=\text{O})$ modes of protonated acidic residues in increasingly hydrophobic environments. These 2 peaks

represent two populations of protonated acidic residues: one is not hydrogen bonded and the other is hydrogen bonded. Moreover, the signal seen at 1733 cm^{-1} is assigned to the protonation of one or more aspartic or glutamic acid residues.

Table 26. Tentative attribution of the signals of the oxidized minus reduced FTIR difference spectra of the WT complex I and D563N in presence of Zn^{2+} (130).

WT $^1\text{H}_2\text{O}$	D563N	Tentative Attributions
1781	1780	$\nu(\text{C}=\text{O})_{\text{COOH}}$, no H-bond
1756	1746	$\nu(\text{C}=\text{O})_{\text{COOH}}$, H-bond
1733	1733	$\nu(\text{C}=\text{O})_{\text{protonated Asp, Glu}}$
1704	1704	$\nu(\text{C}=\text{O})_{\text{Asn, Gln}}$
1681	1681	$\nu(\text{C}=\text{O})_{\text{Asn, Gln}}$, $\nu(\text{C}=\text{O})_{\text{SQ}}$, $\nu_{\text{as}}(\text{CN}_3\text{H}_5^+)_{\text{Arg}}$, Amide I β -turns
1660	1663	$\nu_{\text{as}}(\text{CN}_3\text{H}_5^+)_{\text{Arg}}$, Amide I α -helices
1648	1648	$\nu(\text{C}=\text{O})_{\text{Asn, Gln}}$ bound to Zn^{2+} , $\nu(\text{C}=\text{O})_{\text{Q or SQ}}$, Amide I random
1636	1636	$\nu_{\text{s}}(\text{CN}_3\text{H}_5^+)_{\text{Arg}}$, $\delta(\text{NH}_3^+)_{\text{Lys}}$, Amide I β -sheets
1619	1619	$\delta(\text{NH}_2)_{\text{Asn, Gln}}$
1590	1590	$\nu_{\text{as}}(\text{COO}^-)_{\text{Asp, Glu}}$ bound to Zn^{2+} , monodentate
1559	1559	$\nu_{\text{as}}(\text{COO}^-)_{\text{Asp, Glu}}$, Amide II
1540	1540	$\nu(\text{C}=\text{C})_{\text{FMN}}$, $\nu_{\text{as}}(\text{COO}^-)_{\text{asp, glu}}$
1519	1519	$\nu(\text{C}=\text{C})_{\text{TyrOH}}$
1424		$\nu_{\text{s}}(\text{COO}^-)_{\text{Asp, Glu}}$ bound to Zn^{2+} , monodentate
1405	1405	$\nu_{\text{s}}(\text{COO}^-)_{\text{Asp, Glu}}$
1376	1376	$\nu_{\text{s}}(\text{COO}^-)_{\text{Asp, Glu}}$ bound to Zn^{2+} , monodentate
		$\nu_{\text{s}}(\text{COO}^-)_{\text{Asp, Glu}}$ bound to Zn^{2+} , bidentate

From the results obtained, it is obvious that zinc binding to D563N induces changes in the vibrational modes from the acidic residues Asp and Glu. This is in agreement with the results of Schulte *et al.* ⁽¹⁷⁸⁾ where they proposed direct Zn^{2+} binding to acidic residues and to Gln/Asn residues.

When comparing the double differential spectra of wild type (Figure 92A) with that of D563N (Figure 92B), several differences are commonly found for both samples. For instance, the signal at 1704 cm^{-1} which is associated to the perturbation of the $\nu(C=O)$ mode from gating Asn (or Gln) residues upon Zn^{2+} binding decreases in case of D563N. In addition the absence of the signal at 1681 cm^{-1} can be noticed together with changes in the amide I and amide II range. The complex signal pattern in the amide I range reveals small shifts and changes in intensity indicating changes of the structural rearrangement in the variant upon electron transfer in the presence of Zn^{2+} . Furthermore changes occur in the important spectral region above 1720 cm^{-1} . For instance, the signal at 1756 cm^{-1} , where CO vibration from protonated COOH are expected, is shifted to 1746 cm^{-1} . At least one of the acidic residues in a hydrophobic environment discussed above seems to be influenced in this variant. Thus the D563N can be considered as one of the residues where the interaction with Zn^{2+} occurs.

In this study, we reported that the inhibition of the enzyme with zinc produces complex changes in the conformational reorganization in the D563N that may be part of the proton translocation machinery as judged by the modifications in the infrared signals typical for deeply buried acidic residues and probably other charged residues as well. The data presented here are nevertheless an important first step to understand the mechanism of proton translocation.

4.3 NuoB mutants

As mentioned before in the introduction part, NuoB subunit contains the tetranuclear iron sulfur cluster N2. This cluster is bound to four cysteines (Figure 93) with two of them located vicinal as confirmed by molecular dynamic simulation studies ^(334, 335). This ligand coordination induces an unusual geometry and higher flexibility around the cluster ⁽¹⁴⁹⁾. It was suggested that the unusual redox potential is regulated by this structural arrangement. Previous reported studies have shown that the mutation of certain amino acids has a great influence on the midpoint potential of the cluster ^(157, 336, 337).

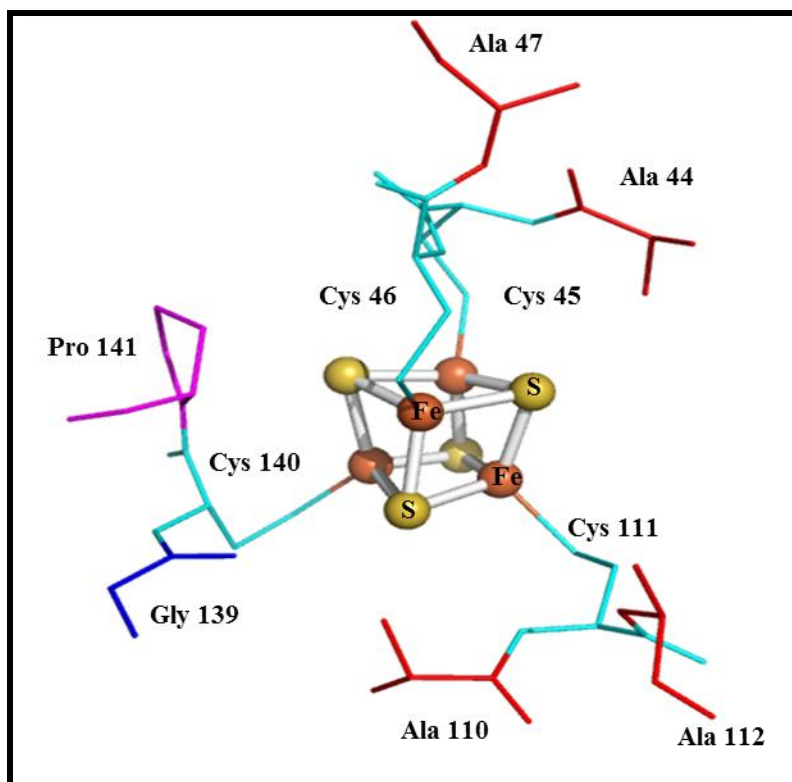


Figure 93. The tetranuclear iron sulfur cluster N2 with Fe (red balls), sulfur (yellow), cysteine (cyan), alanine (red), proline (magenta) and glycine (blue); PDB (4HEA).

This cluster N2 plays a crucial role in coupling electron transfer with proton translocation⁽³³⁷⁾. Furthermore, it possesses special properties because of its location near the surface of peripheral arm of complex I where it is connected by a hydrogen bond network with amino acids in NuoB and NuoD. The redox reaction of this cluster is coupled with protonation and deprotonation of amino acids surrounding it⁽¹⁵⁹⁾ and it is suggested to be the direct reductant for the substrate quinone. Thus the site directed mutagenesis of some amino acids around N2 cluster help to probe their roles in tuning the cluster redox properties⁽³³⁷⁾. Flemming *et al.*⁽³³⁸⁾ mutated the conserved acidic amino acids in NuoB and characterized them by their enzymatic activity and by means of EPR and FTIR spectroscopies. They found that Glu67, Asp77 and Asp94 are essential for electron transfer and they discussed the importance of Glu67 which is protonated by the oxidation of N2 for proton translocation.

Here mutagenesis have been introduced in NuoB to change the vicinal ligation pattern to a normal ligation. The mutation involves two amino acids (Figure 94) (Cysteine 46 and Glycine 82 with respect to *T. thermophilus*).

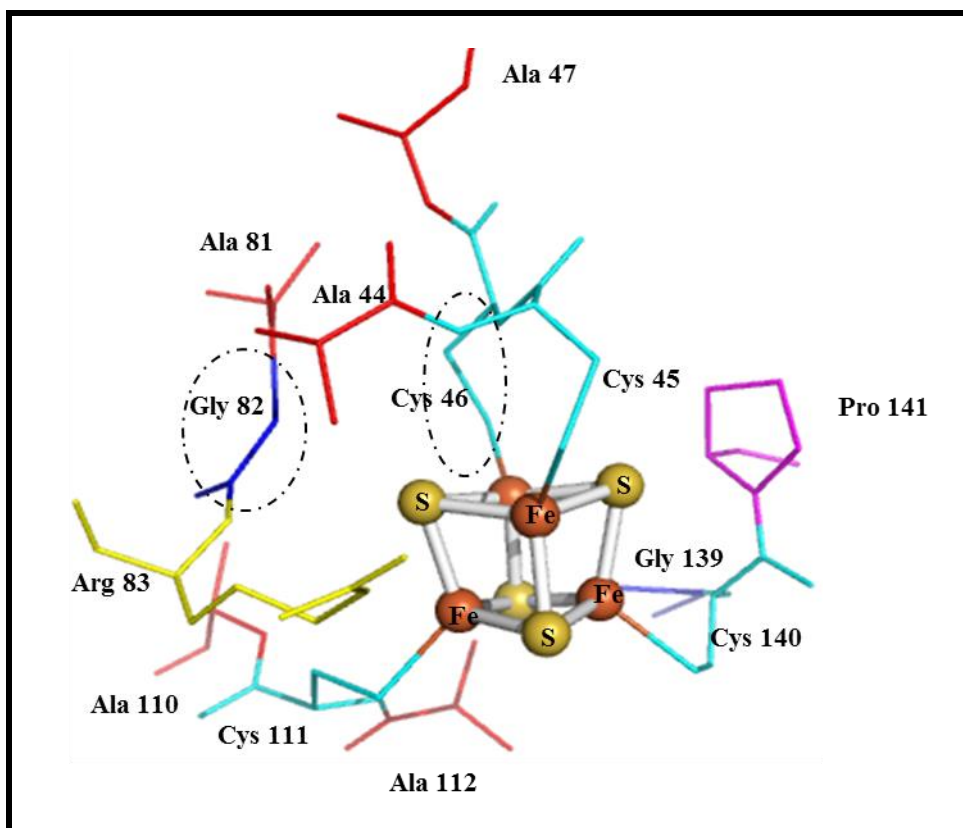


Figure 94. The tetranuclear iron sulfur cluster N2 with Fe (red balls), sulfur (yellow), cysteine (cyan), alanine (red), proline (magenta), glycine (blue) and arginine (yellow); PDB (4HEA). Numbering for *T. thermophilus*. (The mutation sites are highlighted by circles).

4.3.1 UV-visible titration

The redox properties of the cofactors found in complex I protein from *E. coli* are studied by the means of UV-visible spectroscopy. The titrations of NuoB mutants at pH 6.5 and 7 between -650 to -100 mV are presented in Figure 95.

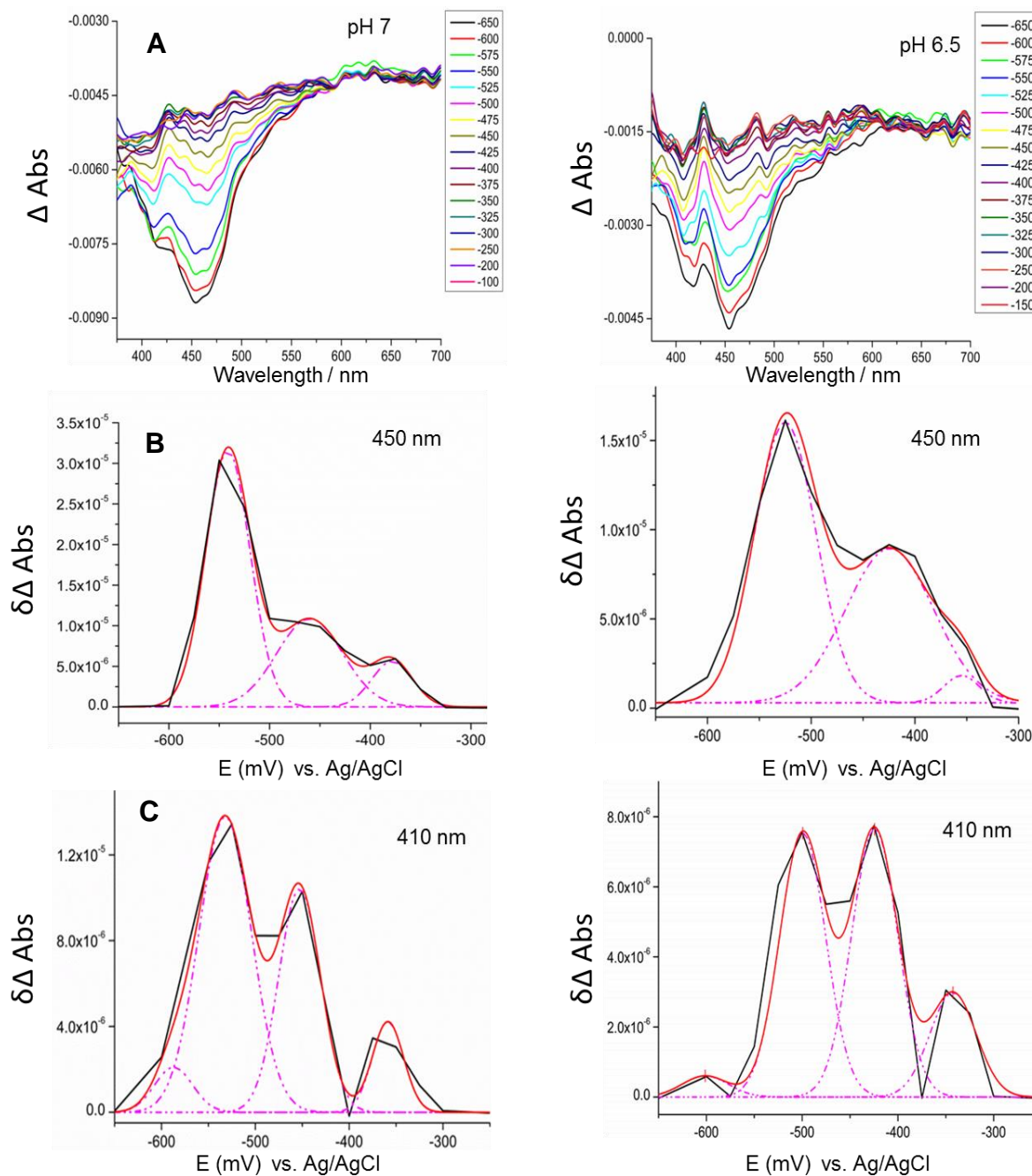


Figure 95. UV-vis titrations of the NuoB mutants at pH 7 and 6.5 (A). First derivative of the absorption difference at 450 (B) and 410 (C) nm and fitted curves representing the redox transitions of FeS clusters and FMN. E is given vs. Ag/AgCl (3M KCl).

The spectra recorded at different potentials and the corresponding $\delta\Delta$ Abs_{450 nm} and $\delta\Delta$ Abs_{410 nm} are shown. At 450 nm both the iron sulfur clusters and FMN absorb, however the molar extinction coefficient of FMN ($\epsilon_{450 \text{ nm}} = 12.800 \text{ M}^{-1} \cdot \text{cm}^{-1}$) is about three times larger than individual extinction coefficient of Fe-S ($\epsilon_{450 \text{ nm}} = 4.100 \text{ M}^{-1} \cdot \text{cm}^{-1}$). Following the first derivative of the absorbance at 450 nm vs. the applied potential (E) allows determining the midpoint potential of FMN. In addition, the first derivative of the absorption at 412 nm is

used to estimate the contributions from Fe-S centers⁽³³⁹⁻³⁴¹⁾. From the derivative curves and the fitting to Gaussian form, the midpoint potentials of FMN and iron sulfur clusters are estimated and summarized in Table 27.

Table 27. The estimated midpoint potentials of FMN and iron sulfur redox cofactors of the NuoB mutants at pH 7 and 6.5 versus SHE.

Wavelength	Attribution	E_m at pH 7 (NuoB mutant)	E_m at pH 6.5 (NuoB mutant)	E_m at pH 7 (wild type)
At 450 nm	FMN midpoint potential	-334 mV	-315 mV	-350 mV (literature by Euro <i>et al.</i> ⁽³⁴²⁾)
At 410 nm	Iron sulfur clusters	-378,-324, -245, -152	-392, -292, -216, -134	

The midpoint potential (E_m) of FMN in the NuoB mutant at pH 7 is -334 mV versus SHE (Table 27). The obtained value is in agreement with the study of Euro *et al.*⁽³⁴²⁾ where they reported the midpoint redox potential (E_m) of the FMN cofactor in the wild type complex I protein at pH 7 ~ -350 mV. Thus the midpoint potential seems not to be affected by the mutation. This is not surprising because of the long distance between the site of mutation and the position of FMN.

At pH 6.5, the E_m of FMN in the NuoB mutant becomes -315 mV thus it decreases by 19 mV with 0.5 pH change. This is consistent with the literature where FMN in solution shows a pH dependency of -52 mV/pH unit, thus if a lower pH value is used, the obtained E_m FMN would be less negative⁽¹³⁰⁾.

Concerning the iron sulfur clusters, their major contributions are typically included at 410 nm. It is well known that most of the Fe-S clusters are equipotential with E_m values close to -270 mV with two exceptions (N1a and N2 clusters). The cluster N2 exhibits the highest midpoint potential because of its high polar environment. The reported values range from -220 mV in the wild type complex I from *E. coli* to (-50/-150 mV) in the mitochondrial complex⁽³⁴³⁾. The other one, is N1a whose midpoint potential is very uncertain and varies with the source of the enzyme within the range from -150 to -400 mV⁽³⁴²⁾.

The midpoint potential seen at -152 mV (vs. SHE) for the NuoB mutant at pH 7 could be attributed to the iron sulfur cluster N2. This obtained E_m is shifted in comparison to the values reported for this N2 cluster from wild type protein (*E. coli*) upon redox titration by Leif *et al.* ⁽³⁴³⁾ and Euro *et al.* ⁽³⁴²⁾ where they found a midpoint potential of -220 mV and -200/-300 mV respectively. The comparison between these values reveals a shift of around 70 mV which could be correlated to the change in the environment around this iron sulfur cluster induced by mutating one of the cysteine residues connected directly to the cluster to alanine.

At pH 6.5, the midpoint potential of the iron sulfur cluster N2 (NuoB mutant) is -134 mV in comparison to -152 mV at pH 7 (Table 27). The change in the E_m of N2 is in line with the study of Ohnishi *et al.* ⁽³⁴⁴⁾ where they reported about the pH dependency of this cluster. However, the shift of 18 mV is a little lower than expected since it is well known that the E_m of the cluster N2 changes by -60 mV per pH unit (-60mV/pH) ⁽¹⁵⁷⁾, thus the change should be around 30 mV. This indicates that N2 undergoes small conformational changes induced by protonation and deprotonation upon pH change.

Because of the complexity of the titration data, which is caused by multiple redox interactions and overlapping signals, further studies including resonance Raman spectroscopy will be required for the detailed analysis of the redox cofactors and clear examination of the effect of pH and mutation on the environment of the clusters.

4.3.2 Raman spectroscopy of Complex I wild type and NuoB mutants

The Raman spectra of complex I and NuoB mutants from *E. coli* are recorded after the excitation with a 514.5 nm laser. The spectra are divided into three main regions based on the nature of the observed vibrational modes:

- (i) 100-700 cm^{-1} corresponds to the region where the metal ligand vibrations and their overtones appear.
- (ii) 700-1800 cm^{-1} the vibration of amino acid side chain and FMN are seen in this region.
- (iii) 2700-3200 cm^{-1} corresponds to the last region where the vibrations $\nu(\text{C-H})$ of the protein backbone are expected.

Since the mutations in the NuoB subunit involve the amino acids around N2 cluster, we focused on the low frequency region (100-900 cm^{-1}) which is characterized by the Fe-S vibrational modes. The spectra are directly correlated to the properties of the Fe-S clusters,

their close environment and to the polypeptide backbone. To the best of our knowledge, the first description of the enhancement of the Fe-S clusters in complex I using resonance Raman spectroscopy is reported in our lab (Yegres *et al.*, manuscript in preparation). They studied the subcomplex NuoEF (N1a and N3 clusters), the dehydrogenase fragment NDF (N1b, N4, N5 and N7), the quinone reductase fragment QRF (N6a, N6b and N2) and complex I. The comparison between all of them led to a detailed analysis of each cluster and its environment and to a full assignment of the metal ligand vibrations of complex I.

4.3.2.1 Fe-S modes for Complex I and NuoB mutants at different pH

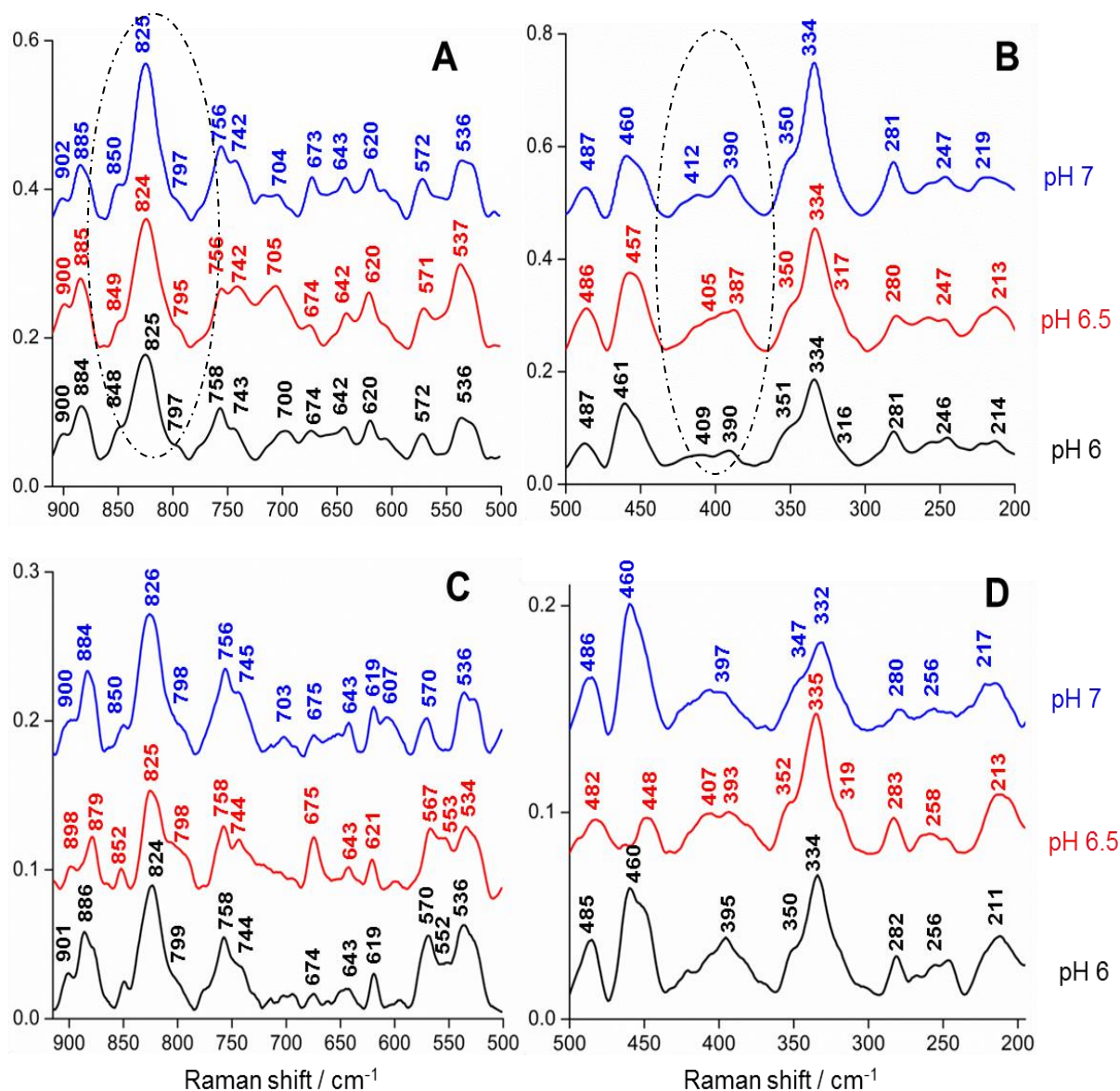


Figure 96. Low frequency resonance Raman spectra of NuoB mutants (C64A G100C with respect to *E. coli*) (A and B) and complex I wild type (C and D). The blue color corresponds to pH 7, red to pH 6.5 and black to pH 6.

The low frequency spectra of complex I and NuoB mutants are shown in Figure 96. Two spectral regions are distinguished: the first one corresponds to the low frequency region ($500\text{-}200\text{ cm}^{-1}$), it is characterized by the Fe-S vibrational modes. In comparison, the second region ($500\text{-}900\text{ cm}^{-1}$) includes a combination of modes corresponding to amino acids side chains and overtones related to the environment of the cofactors. The assignment of the iron sulfur clusters in a huge protein having nine Fe-S is a difficult task. However, the previous reported studies on the [2Fe-2S] and [4Fe-4S] model complexes and their extinction profiles^(152, 339, 345) help to attribute the peaks to given clusters. In addition, isotope labeling supports these assignments^(339, 346, 347).

The Raman spectrum of complex I includes the contribution of the binuclear iron sulfur clusters [2Fe-2S] (N1a and N1b) and tetranuclear [4Fe-4S] (N2, N3, N4, N5, N7, N6a and N6b). Interestingly, the binuclear and the tetranuclear clusters exhibit different forms of symmetry such as D_{2h} distortion which applies only for [2Fe-2S] and T_d for [4Fe-4S] leading to the clear differentiation between the Fe-S stretching modes^(225, 345, 346).

Figure 99A describes the Raman spectra of the NuoB mutants at pH 6, 6.5 and 7. The peaks seen between $900\text{-}880\text{ cm}^{-1}$ corresponds to tryptophan residue(s), the signal at 885 cm^{-1} can be used as structural marker for the examination of the environment and solvent exposure of tryptophan residues indicating the strength of the hydrogen bonding⁽³⁴⁸⁾. The signals observed between $820\text{-}855\text{ cm}^{-1}$ originate from tyrosine residues⁽³⁴⁹⁾. The ratio of the intensity of these two signals gives an idea about the average of the “exposed” or “buried” tyrosine residues present near the cofactors. The ratio of the tyrosine signals I_{850}/I_{825} is influenced by the pH⁽³⁴⁹⁾ as suggested by Siamwiza *et al.*⁽³⁵⁰⁾ where they used the intensity ratio of I_{854}/I_{832} as an indicator for the degree of protonation.

In Figure 99A this ratio decreases as pH increases. Thus pH is considered as a factor which affects the environment of the benzene ring and the conformation of the amino acid side chain. Besides, the peaks at 797 and 742 cm^{-1} are attributed to the isoalloxazine ring from the flavin mode⁽³⁵¹⁾. Additionally the signals seen at 756 and 675 cm^{-1} are assigned probably to C-S stretching modes associated with four cysteine ligands whose frequency varies depending on the cysteine conformations^(224, 339). Furthermore, the signal observed at 643 cm^{-1} could be attributed to the C-S stretching modes for a [4Fe-4S] with incomplete cysteine ligation. This is typical for the cluster N5 in NuoG subunit which is connected to three cysteine amino acids and to histidine as the fourth amino acid⁽³⁵²⁾. The band at 620 cm^{-1} is a

candidate for C-S stretching⁽²²⁴⁾. The peaks at 572 and 536 cm⁻¹ are identified as the iron sulfur overtones combined with Fe-S stretching modes^(224, 339).

Figure 99B presents the second spectral region from 500-200 cm⁻¹ of the NuoB mutants at the different pHs. This region is characterized mainly by the Fe-S stretching and bending vibrations. The peak at 460 cm⁻¹ describes the bending modes C-C-N⁽²²⁶⁾ and the peak at 487 cm⁻¹ could be attributed to the iron sulfur bending modes. The peak at 412 cm⁻¹ describes the iron sulfur bridging modes with B_{2u} which has no terminal contribution in D_{2h} symmetry⁽³³⁹⁾. In addition, the peak observed at 390 cm⁻¹ is correlated with Fe-S^b with A_g symmetry⁽³³⁹⁾. The signal at 219 cm⁻¹ is described by the metal-metal stretching modes, thus it is related to the A_g mode of the Fe-Fe interaction⁽³³⁹⁾. The resonance Raman band at 247 cm⁻¹ corresponds to the iron sulfur bridging vibration from clusters in complex I. This band involves the contribution of B₂ and E, thus it is described as T₂ mode⁽³⁴⁵⁾. Furthermore, the peak at 281 cm⁻¹ could be attributed to the stretching and bending vibrations of the iron sulfur clusters: Fe-S^t and Fe-S^b vibrations according to the B_{1u} and B_{3u} modes^(227, 339).

The signal at 334 cm⁻¹ is intense; it is correlated to the bridging modes of the cluster Fe-S^b stretching. It exhibits a total symmetric A₁ breathing mode⁽³⁴⁶⁾. Moreover, the Raman band at 350 cm⁻¹ corresponds to the terminal stretching Fe-S with T₂ mode⁽³⁴⁵⁾. Other study done by Meyer *et al.*⁽³⁵³⁾ assigned this band at 350 cm⁻¹ to the terminal stretching Fe-S^t according to B_{1u} and B_{2g} modes. The attribution of the different Raman peaks is summarized in Table 28.

As shown in Figure 99B, small differences in the NuoB mutants at different pH are seen in the low frequency region (500-200 cm⁻¹) where the iron sulfur bridging modes seem to be affected by the pH change. These changes could be attributed to the conformational reorganization occurring upon pH changes.

Now the comparison between wild type and NuoB mutants reveals a great difference in the low frequency region (Figures 99B and 99D). In the spectrum of NuoB mutant at pH 7, the peak at 390 cm⁻¹ which is correlated with bridging mode Fe-S^b is shifted to 397 cm⁻¹ in the case of wild type. Similar shifts are obtained in the case of pH 6.5 and 6. This could be related to the mutation effect where one cysteine residue is replaced by alanine thus causing a perturbation in the bridging mode and giving rise to a new conformation of the N2 cluster. These observed changes are consistent with the redox titration results where the midpoint potential of the N2 cluster shifts from -220 mV (vs. SHE) in case of wild type to -152 mV (vs. SHE) for the NuoB mutant. Thus coupling the results of UV redox titration and Raman

spectroscopy helps to investigate the properties and the environment of the iron sulfur clusters and pointing toward a better understanding of the respiratory complex I protein.

Table 28. Frequencies modes (cm^{-1}) of the different samples and their assignments ⁽³³⁹⁾.

Modes		Nuo B mutant / cm^{-1}	WT / cm^{-1}
Fe-S stretching	A_g Fe-Fe	219	217
	Bridging (T_2 : B_2/E)	247	256
	Terminal(B_{3u})	281	280
	Bridging (B_{1u})		
	Terminal(A_g)		320
	Bridging (A_1 breathing)	334	332
	Terminal B_{1u} and B_{2g}	350	347
Fe-S bridging A_g		390	397
Fe-S bridging B_{2u}		412	
C-C-N Bending mode		460	460
Fe-S bending modes		487	486
Fe-S overtones		536	536
		572	570
C-S Stretching		620	619
		643	643
		673	675
		756	756
FMN		742	745
isoalloxazine		797	798
Tyrosine		825	826
Fermi doublet		850	850
Tryptophan		885	--

Chapter V

Conclusion and Perspectives

5 Conclusion and future work

This thesis contains two main projects: lipid-lipid interaction and the complex I protein from the respiratory chain. In the first part, the temperature dependence of pure EPC, EPE, cardiolipin and mixed lipid/cholesterol was presented. Using mid infrared spectroscopy, it was possible to look deeply into the hydrocarbon chain conformation and to determine the effect of cholesterol on the transition temperatures. The hydration and polarity of the phosphate head groups were also examined. In addition, information was obtained from the far infrared data concerning the description and the characterization of head groups, hydrocarbon chain and hydrogen bonding in a very specific way.

The examination of the transition temperature in the case of EPC and EPE revealed that EPC is stabilized in a bilayer form whereas EPE in a hexagonal non-bilayer form. The insertion of cholesterol caused a decrease in the transition temperature since cholesterol disorders the gel phase of lipid leading to a less packed system. Furthermore, the characterization of these lipids and lipid/cholesterol systems using far infrared spectroscopy revealed that the position of wagging and rocking vibrations of the phosphate group was altered upon heating indicating a change of the hydrogen bonding network in the polar head group region. In addition, the hydrogen bonding signature below 300 cm^{-1} was strongly perturbed upon heating in a quite interesting way. It decreased in the case of EPC and EPE and this can be correlated with H_2O vibrational modes in the mid infrared. In cardiolipin, the signal increased in contrast to the decrease of the water signature in the mid infrared domain pointing towards different hydrogen bonding interactions and interaction with water molecules in CL.

Raman spectroscopy measurements were performed on the lipids and lipid/cholesterol systems. The results showed that the low frequency region is informative because of the presence of marker bands which constituted a fingerprint for each lipid as for EPC and EPE lipids and the data were complementary to IR. In contrast the higher frequency region gave no valuable information. In addition, the possibility to enhance the Raman signals was probed.

The temperature dependent measurements performed on EPC and EPE lipids showed that the transition temperature is different due to the presence of different head groups which include choline and ethanolamine respectively. Within this context, the far infrared spectra of EPC, EPE were studied and the marker bands for each lipid were depicted. Then the properties of EPC in the presence of different amounts of EPE were analyzed as function of temperature. Well defined lipid titrations were performed using three EPC/EPE mixtures. For the 1:1 and 2:1 and 4:1 mixtures, the bands of the wagging and rocking vibrations of phosphate group increased upon heating. This could be explained by the presence of PE which modulates the properties of the PC layer causing a strong interaction between the two components of the mixture giving place to a different geometry in the organization of the lipid head group. In addition the hydrogen bonding signature was altered. Furthermore, the study of pH sensitive DOPE/CHEMS (3:2) liposomes revealed huge structural changes under the effect of pH. These changes were clearly investigated by mid and far infrared spectroscopies in order to better understand the mechanism of destabilization of these liposomes. In conclusion, mid and far infrared offered great opportunities to investigate the structure and organization of lipid systems.

In the second part, complex I protein was studied. The interaction of the block copolymer (PMOXA-PDMS-PMOXA) with complex I, whose activity depends on the presence of lipids, was probed. The activity of the delipidated enzyme was enhanced twice after addition of polymer. The conformational changes and the perturbation of the hydrogen bonding behavior were seen clearly using the mid and far infrared spectroscopies respectively.

Additionally, the study of the different NuoL mutants (D563N, D563E, Y594F) by means of redox induced FTIR difference spectroscopy was demonstrated. The oxidized minus reduced FTIR difference spectra included the contribution of individual amino acids, cofactors, redox-dependent changes in the protein structure. These spectra did not show strong differences in comparison to that of the parental enzyme confirming that the variants were properly assembled and stable which is in accordance with their mildly changed electron transfer rate. Moreover, the effect of Zn^{2+} inhibition on the D563N mutant was studied. The direct comparison of electrochemically induced FTIR difference spectra from the wild type and the D563N variant revealed that the infrared signals attributed to Asn, Asp and/or Gln residues were perturbed. As this variant exhibited reduced proton pumping activity, the participation of this residue in one of the proposed proton pathways is thus very likely. However, this residue can only be one of the interaction partners of Zn^{2+} . To further investigate the different

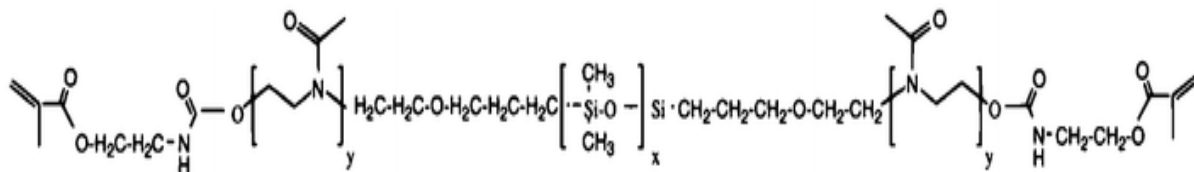
aminoacids involved in zinc binding, the study of different complex I mutants seems to be the next step of this work.

Finally, NuoB mutants (C64AG100C with respect to *E. coli*) at different pH were studied. The vibrations of the iron sulfur clusters as well as their midpoint potentials were probed using Raman and UV-vis spectroscopies. The midpoint potential of the cluster N2 was downshifted by 70 mV in comparison to the wild type. On the contrary, the E_m of FMN was not affected. This could be explained by the distance between the site of the mutation and the cofactor. From the Raman results, it can be concluded that the bridging mode Fe-S^b was shifted toward lower frequency revealing that the mutation causes a perturbation and new cluster conformation.

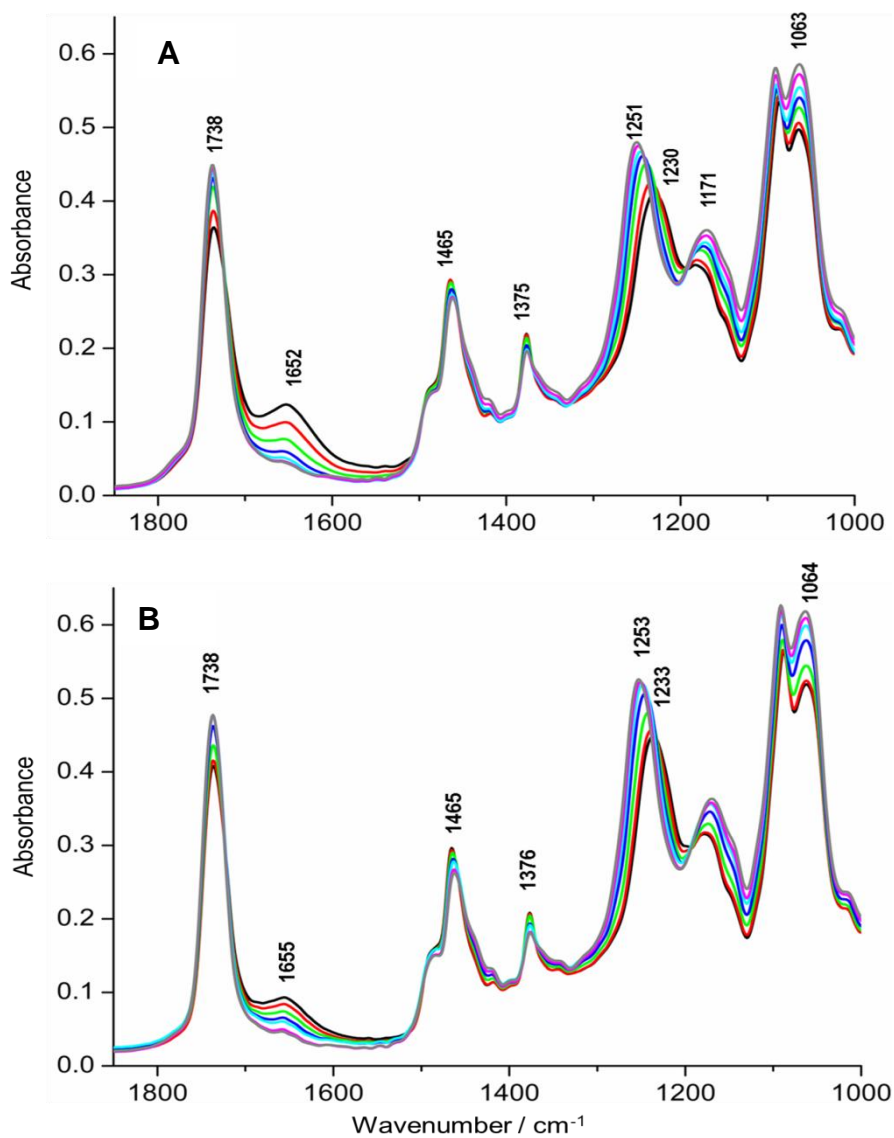
In conclusion, crucial amino acids in complex I have been identified together with the importance of lipids for the conformational change during redox reaction. In future, mutants in the putative proton pathways will be correlated with studies in the absence or presence of lipids and polymers.

6 Appendix

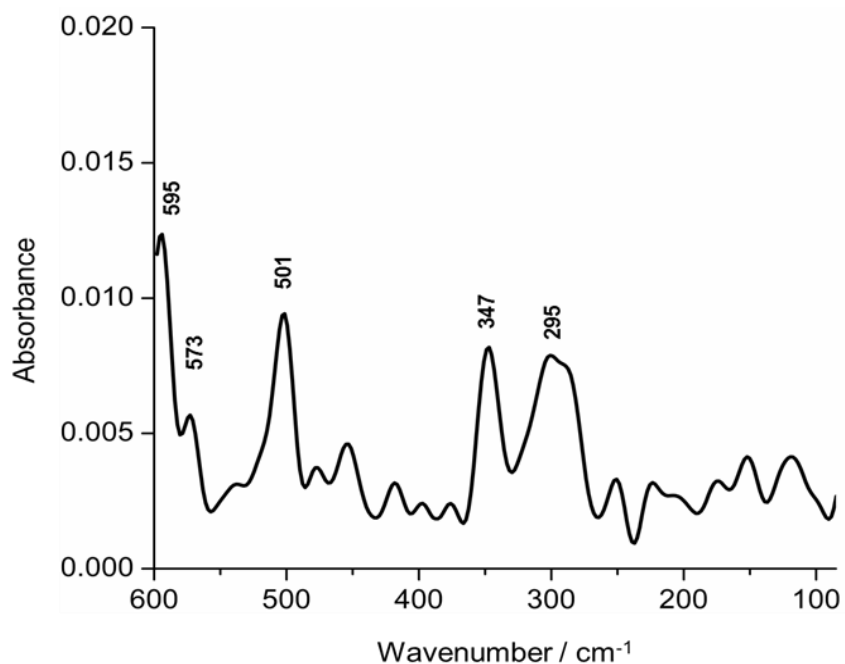
6.1 Results and discussion appendix



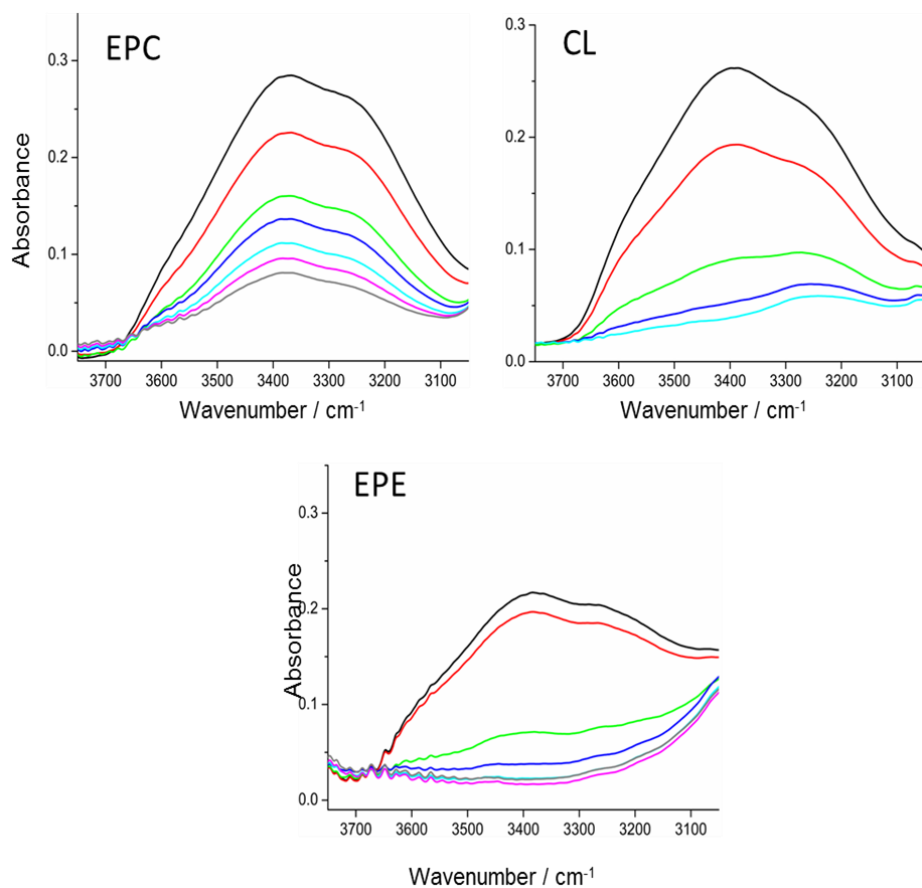
Appendix 1. chemical structure of the PMOXA_y-PDMS_x-PMOXA_y triblock copolymer.



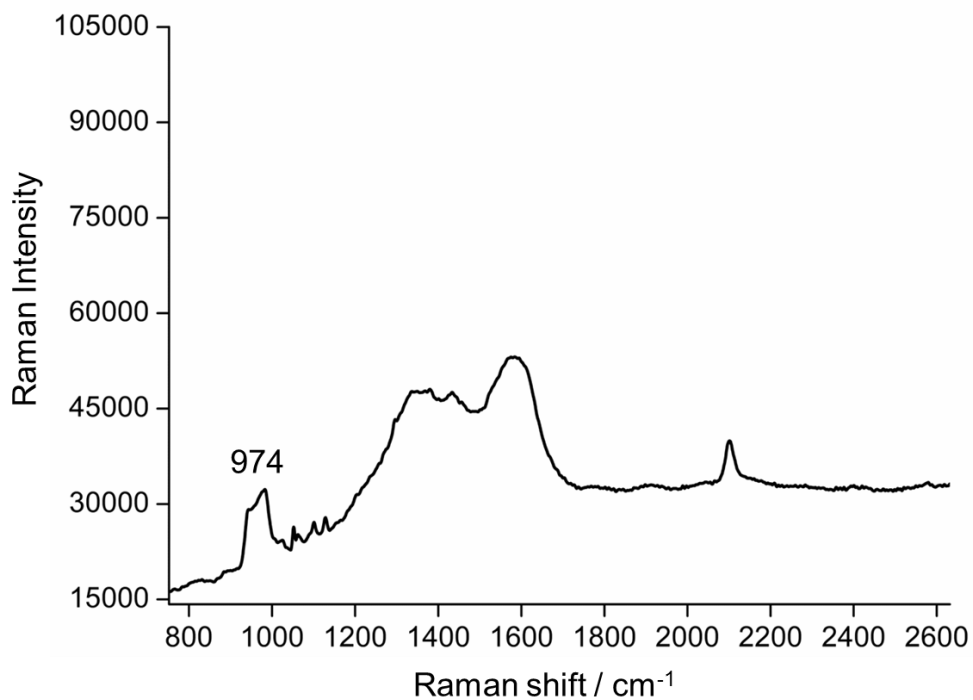
Appendix 2. Temperature dependent ATR absorbance spectra of EPC in H₂O in heating (A) and cooling (B) steps. Line assignment: 5 °C black, 10 °C red, 20 °C green, 30 °C blue, 40 °C cyan, 50 °C magenta, 60 °C gray.



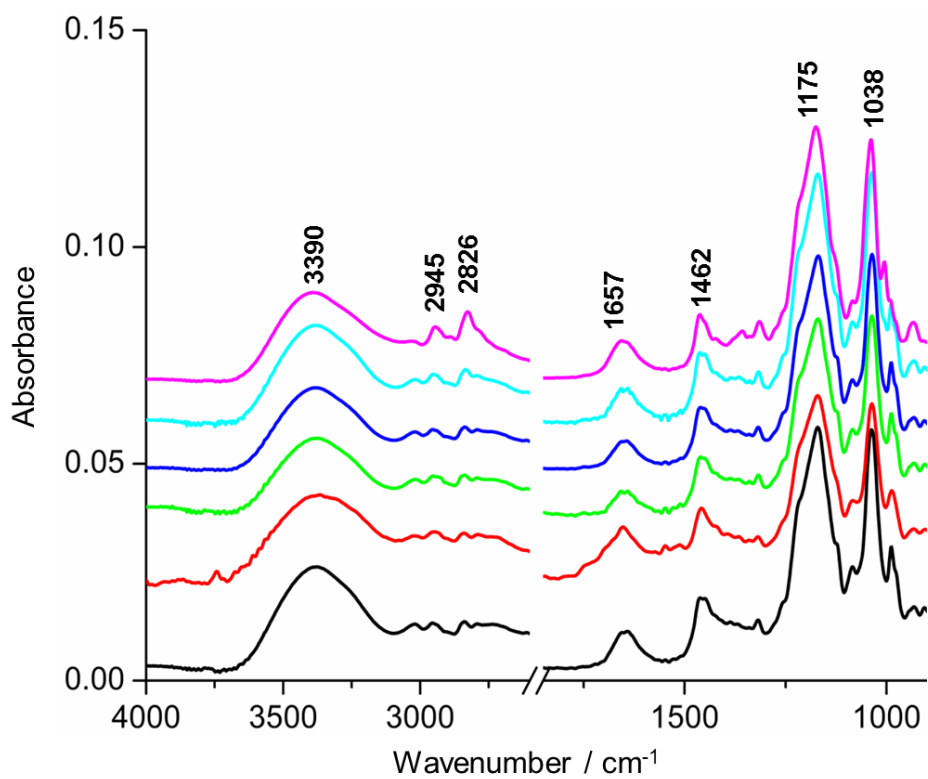
Appendix 3. ATR-FTIR absorption spectrum of cholesterol in the far infrared region.



Appendix 4. The OH stretching vibration mode of EPC, EPE and CL. Line assignment: 5 °C black, 10 °C red, 20 °C green, 30 °C blue, 40 °C cyan, 50 °C magenta, 60 °C gray.



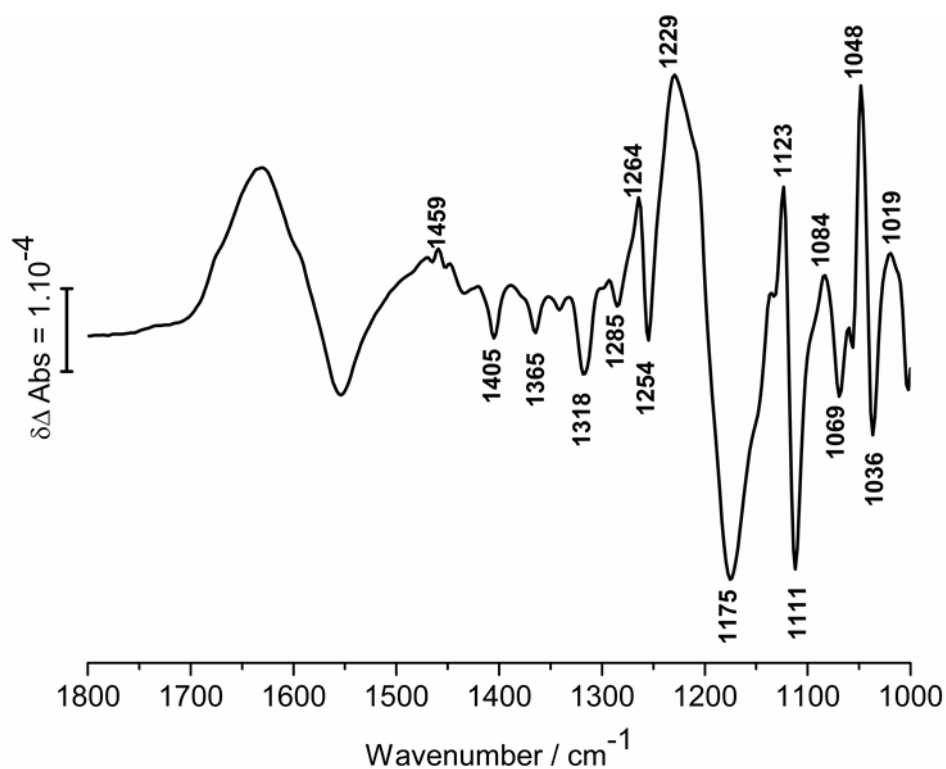
Appendix 5. The Raman spectrum of the octadecanethiol modifier.



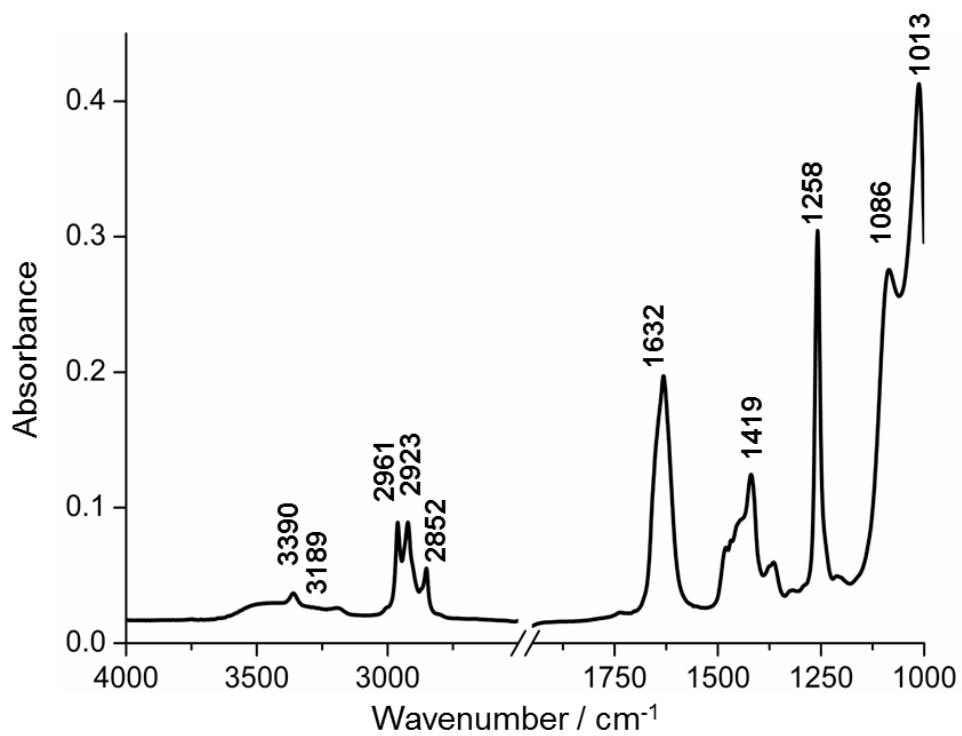
Appendix 6. The MIR ATR absorbance spectra of HEPES buffer at different pH. Line assignment: pH 4.5 (black), pH 5 (red), pH 5.5 (green), pH 6 (blue), pH 6.5 (cyan), pH 7.4 (magenta).

Wavenumber/cm ⁻¹	Assignments
3200-3600	OH stretch
2800-3100	CH stretch
1650	OH bending
1457	CH ₂ bending
1314	Asymmetric S=O stretch
1172	Symmtric S=O stretch
1035	C-O stretch
1000-875	S-O and C-N stretch

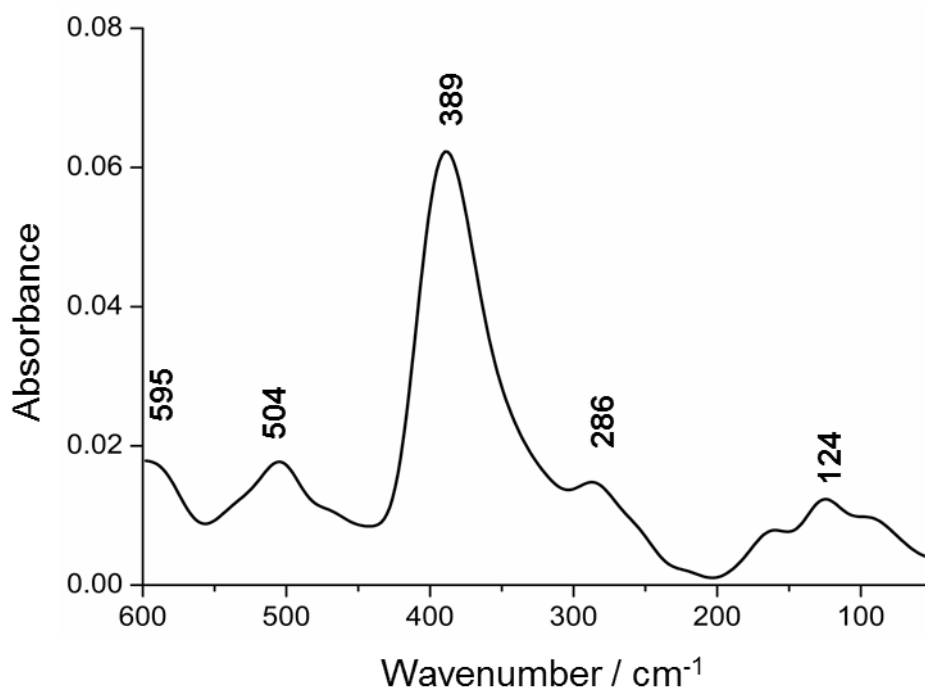
Appendix 7. The tentative assignments of the peaks obtained for Hepes buffer at different pH values.



Appendix 8. The Oxidized *minus* reduced FTIR difference spectrum of MES buffer (MES 50 mM, NaCl 50 mM, DDM 0.01 %, pH 6.3).



Appendix 9. ATR-FTIR absorption spectrum of PMOXA-PDMS-PMOXA in the mid infrared region.



Appendix 10. ATR-FTIR absorption spectrum of PMOXA-PDMS-PMOXA in the far infrared region.

7 References

1. Singer, S. J.; Nicolson, G. L., The fluid mosaic model of the structure of cell membranes. *Science* **1972**, *175* (4023), 720-731.
2. Simons, K.; Ikonen, E., Functional rafts in cell membranes. *Nature* **1997**, *387* (6633), 569-572.
3. Brown, D. A.; London, E., Structure of Detergent-Resistant Membrane Domains: Does Phase Separation Occur in Biological Membranes?. *Biochemical and Biophysical Research Communications* **1997**, *240* (1), 1-7.
4. Eeman, M.; Deleu, M., From biological membranes to biomimetic model membranes. *Biotechnol. Agron. Soc. Environ.* **2010** *14* (4), 719-736.
5. Karp, G., *Cell and Molecular Biology*, 5th Edition; John Wiley & Sons **2008**.
6. Merz, K.; Roux, B. t.; Biological membranes, A Molecular Perspective from computation and experiment. *Birkhäuser BioSciences* **1996**, Boston.
7. Brown, B. S., Biological membranes. *Biochemical Society* **1996**.
8. Fahy, E.; Subramaniam, S.; Brown, H. A.; Glass, C. K.; Merrill, A. H.; Murphy, R. C.; Raetz, C. R.; Russell, D. W.; Seyama, Y.; Shaw, W., A comprehensive classification system for lipids. *Journal of lipid research* **2005**, *46* (5), 839-862.
9. Lipid Maps link: Lipid Metabolites And Pathways Strategy.
10. Tanford, C., The Hydrophobic Effect: Formation of Micelles and Biological Membranes *2d Ed.* J. Wiley.: **1980**.
11. Mouritsen, O. G.; Jorgensen, K., Dynamical order and disorder in lipid bilayers. *Chemistry and Physics of Lipids* **1994**, *73* (1-2), 3-25.
12. McLaughlin, S.; Wang, J.; Gambhir, A.; Murray, D., PIP2 and proteins: interactions, organization, and information flow. *Annual review of biophysics and biomolecular structure* **2002**, *31* (1), 151-175.
13. Michel, M. Fonctionnalisation de films multicouches de polyélectrolytes avec des liposomes enfouis: création de reacteurs immobilisés. Strasbourg 1, **2005**.
14. Stoenescu, R. Asymmetric amphiphilic triblock copolymers: synthesis, characterization and self-assembly. University of Basel, **2004**.
15. Hamley, I. W., Introduction to soft matter: Polymers, colloids, amphiphiles and liquid crystals. John Wiley.: New York, **2000**.
16. Alberts, B. B., D.; Lewis, J.; Raff, M.; Roberts, K. et al., Molecular biology of the cell. 2nd. ed. ed.; Garland Publishing Inc.: New York, **1989**.
17. Binder, W. H.; Barragan, V.; Menger, F. M., Domains and rafts in lipid membranes. *Angewandte Chemie International Edition* **2003**, *42* (47), 5802-5827.
18. Lewis R.N.A.H., M. R. N., Fourier transform infrared spectroscopy in the study of hydrated lipids and lipid bilayer membranes. *Infrared spectroscopy of biomolecules*. **1996**, 159-202.
19. Boggs, J. M., Lipid intermolecular hydrogen bonding: influence on structural organization and membrane function. *Biochimica et Biophysica Acta (BBA) - Reviews on Biomembranes* **1987**, *906* (3), 353-404.
20. Eibl, H. r., Phospholipids as functional constituents of biomembranes. *Angewandte Chemie International Edition in English* **1984**, *23* (4), 257-271.
21. Avanti Polar Lipid, I. Phase Transition Temperatures for Glycerophospholipids. . <http://www.avantilipids.com>.
22. Litman, B. J.; Lewis, E. N.; Levin, I. W., Packing characteristics of highly unsaturated bilayer lipids: Raman spectroscopic studies of multilamellar phosphatidylcholine dispersions. *Biochemistry* **1991**, *30* (2), 313-319.

23. Keough, K. M. W.; Giffin, B.; Matthews, P. L. J., Phosphatidylcholine-cholesterol interactions: bilayers of heteroacid lipids containing linoleate lose calorimetric transitions at low cholesterol concentration. *Biochimica et Biophysica Acta (BBA) - Biomembranes* **1989**, *983* (1), 51-55.
24. Dowhan, W., Molecular basis for membrane phospholipid diversity: why are there so many lipids? *Annual review of biochemistry* **1997**, *66* (1), 199-232.
25. Birner, R.; Bürgermeister, M.; Schneider, R.; Daum, G. n., Roles of phosphatidylethanolamine and of its several biosynthetic pathways in *Saccharomyces cerevisiae*. *Molecular biology of the cell* **2001**, *12* (4), 997-1007.
26. Jahn, R.; Grubmüller, H., Membrane fusion. *Current Opinion in Cell Biology* **2002**, *14* (4), 488-495.
27. Uran, S.; Larsen, A. s.; Jacobsen, P. B.; Skotland, T., Analysis of phospholipid species in human blood using normal-phase liquid chromatography coupled with electrospray ionization ion-trap tandem mass spectrometry. *Journal of Chromatography B: Biomedical Sciences and Applications* **2001**, *758* (2), 265-275.
28. Campbell, N. A. R., J.B, *Biology*. 6th ed.; Benjamin Cummings: San Francisco, **2002**.
29. Blume, A.; Wittebort, R. J.; Das Gupta, S. K.; Griffin, R. G., Phase equilibria, molecular conformation, and dynamics in phosphatidylcholine/phosphatidylethanolamine bilayers. *Biochemistry* **1982**, *21* (24), 6243-6253.
30. Haines, T. H.; Dencher, N. A., Cardiolipin: a proton trap for oxidative phosphorylation. *FEBS Letters* **2002**, *528* (1-3), 35-39.
31. Daum, G. n., Lipids of mitochondria. *Biochimica et Biophysica Acta (BBA)-Reviews on Biomembranes* **1985**, *822* (1), 1-42.
32. Ratledge, C.; Wilkinson, S., Fatty acids, related and derived lipids. *Microbial lipids* **1988**, *1*, 23-52.
33. O'leary, W.; Wilkinson, S., Gram-positive bacteria. *Microbial lipids* **1988**, *1*, 117-201.
34. Hoch, F. L., Cardiolipins and biomembrane function. *Biochimica et Biophysica Acta (BBA)-Reviews on Biomembranes* **1992**, *1113* (1), 71-133.
35. Nagle, J. F.; Zhang, R.; Tristram-Nagle, S.; Sun, W.; Petrache, H. I.; Suter, R. M., X-ray structure determination of fully hydrated L alpha phase dipalmitoylphosphatidylcholine bilayers. *Biophysical Journal* **1996**, *70* (3), 1419-1431.
36. Lewis, B. A.; Engelman, D. M., Lipid bilayer thickness varies linearly with acyl chain length in fluid phosphatidylcholine vesicles. *Journal of molecular biology* **1983**, *166* (2), 211-217.
37. Rand, R. P.; Parsegian, V. A., Hydration forces between phospholipid bilayers. *Biochimica et Biophysica Acta (BBA) - Reviews on Biomembranes* **1989**, *988* (3), 351-376.
38. Lis, L.; McAlister, M.; Fuller, N.; Rand, R.; Parsegian, V., Interactions between neutral phospholipid bilayer membranes. *Biophysical Journal* **1982**, *37* (3), 657.
39. Schindler, H.; Seelig, J., Deuterium order parameters in relation to thermodynamic properties of a phospholipid bilayer. Statistical mechanical interpretation. *Biochemistry* **1975**, *14* (11), 2283-2287.
40. De Young, L. R.; Dill, K. A., Solute partitioning into lipid bilayer membranes. *Biochemistry* **1988**, *27* (14), 5281-5289.
41. Büldt, G.; Gally, H.; Seelig, J.; Zaccai, G., Neutron diffraction studies on phosphatidylcholine model membranes: I. Head group conformation. *Journal of molecular biology* **1979**, *134* (4), 673-691.
42. Wiener, M. C.; White, S. H., Structure of a fluid dioleoylphosphatidylcholine bilayer determined by joint refinement of x-ray and neutron diffraction data. II. Distribution and packing of terminal methyl groups. *Biophysical Journal* **1992**, *61* (2), 428-433.

43. Tristram-Nagle, S.; Petrache, H. I.; Nagle, J. F., Structure and interactions of fully hydrated dioleoylphosphatidylcholine bilayers. *Biophysical Journal* **1998**, *75* (2), 917-925.
44. Petrache, H. I.; Tristram-Nagle, S.; Nagle, J. F., Fluid phase structure of EPC and DMPC bilayers. *Chemistry and Physics of Lipids* **1998**, *95* (1), 83-94.
45. Nagle, J. F.; Wilkinson, D. A., Lecithin bilayers. Density measurement and molecular interactions. *Biophysical Journal* **1978**, *23* (2), 159-175.
46. Hitchcock, P. B.; Mason, R.; Shipley, G. G., Phospholipid arrangements in multilayers and artificial membranes: Quantitative analysis of the X-ray diffraction data from a multilayer of 1,2-dimyristoyl-phosphatidylethanolamine. *Journal of molecular biology* **1975**, *94* (2), 297-299.
47. Mantsch, H. H.; Martin, A.; Cameron, D. G., Characterization by infrared spectroscopy of the bilayer to nonbilayer phase transition of phosphatidylethanolamines. *Biochemistry* **1981**, *20* (11), 3138-3145.
48. Popova, A. V.; Hinch, D. K., Thermotropic phase behavior and headgroup interactions of the nonbilayer lipids phosphatidylethanolamine and monogalactosyldiacylglycerol in the dry state. *BMC Biophysics* **2011**, *4* (1).
49. Dyck, M.; Krüger, P.; Lösche, M., Headgroup organization and hydration of methylated phosphatidylethanolamines in Langmuir monolayers. *Physical Chemistry Chemical Physics* **2005**, *7* (1), 150-156.
50. Quinn, P. J.; Lis, L. J.; Cunningham, B. A., A time-resolved study of phase transitions in phosphatidylcholine-phosphatidylethanolamine mixtures. *Journal of Colloid and Interface Science* **1988**, *125* (2), 437-443.
51. Mendelsohn, R.; Koch, C. C., Deuterated phospholipids as raman spectroscopic probes of membrane structure: Phase diagrams for the dipalmitoyl phosphatidylcholine (and its d62 derivative)-dipalmitoyl phosphatidylethanolamine system. *Biochimica et Biophysica Acta (BBA) - Biomembranes* **1980**, *598* (2), 260-271.
52. Blume, A.; Ackermann, T., A calorimetric study of the lipid phase transitions in aqueous dispersions of phosphorylcholine-phosphorylethanolamine mixtures. *FEBS Letters* **1974**, *43* (1), 71-74.
53. Hübner, W.; Mantsch, H. H.; Kates, M., Intramolecular hydrogen bonding in cardiolipin. *Biochimica et Biophysica Acta (BBA) - Biomembranes* **1991**, *1066* (2), 166-174.
54. Lewis, R. N. A. H.; Zweytick, D.; Pabst, G.; Lohner, K.; McElhaney, R. N., Calorimetric, X-Ray Diffraction, and Spectroscopic Studies of the Thermotropic Phase Behavior and Organization of Tetramyristoyl Cardiolipin Membranes. *Biophysical Journal* **2007**, *92* (9), 3166-3177.
55. Powell, G. L.; Marsh, D., Polymorphic phase behavior of cardiolipin derivatives studied by phosphorus-31 NMR and x-ray diffraction. *Biochemistry* **1985**, *24* (12), 2902-2908.
56. Damodaran, K.; Merz Jr, K. M., Head group-water interactions in lipid bilayers: a comparison between DMPC-and DLPE-based lipid bilayers. *Langmuir* **1993**, *9* (5), 1179-1183.
57. Stouch, T. R., Lipid membrane structure and dynamics studied by all-atom molecular dynamics simulations of hydrated phospholipid bilayers. *Molecular Simulation* **1993**, *10* (2-6), 335-362.
58. Robinson, A. J.; Richards, W. G.; Thomas, P. J.; Hann, M. M., Head group and chain behavior in biological membranes: a molecular dynamics computer simulation. *Biophysical Journal* **1994**, *67* (6), 2345-2354.
59. Shinoda, W.; Fukada, T.; Okazaki, S.; Okada, I., Molecular dynamics simulation of the dipalmitoylphosphatidylcholine (DPPC) lipid bilayer in the fluid phase using the Nosé-Parrinello-Rahman NPT ensemble. *Chemical physics letters* **1995**, *232* (3), 308-312.

60. Tieleman, D.; Berendsen, H., Molecular dynamics simulations of a fully hydrated dipalmitoylphosphatidylcholine bilayer with different macroscopic boundary conditions and parameters. *The Journal of Chemical Physics* **1996**, *105* (11), 4871-4880.
61. Berger, O.; Edholm, O.; Jähnig, F., Molecular dynamics simulations of a fluid bilayer of dipalmitoylphosphatidylcholine at full hydration, constant pressure, and constant temperature. *Biophysical Journal* **1997**, *72* (5), 2002-2013.
62. Ceccarelli, M.; Marchi, M., Molecular dynamics simulation of POPC at low hydration near the liquid crystal phase transition. *Biochimie* **1998**, *80* (5), 415-419.
63. Pasenkiewicz-Gierula, M.; Murzyn, K.; Róg, T.; Czaplewski, C., Molecular dynamics simulation studies of lipid bilayer systems. *Acta Biochimica polonica-English edition* **2000**, *47* (3), 601-612.
64. Chiu, S. W.; Jakobsson, E.; Subramaniam, S.; Scott, H. L., Combined Monte Carlo and Molecular Dynamics Simulation of Fully Hydrated Dioleoyl and Palmitoyl-oleoyl Phosphatidylcholine Lipid Bilayers. *Biophysical Journal* **1999**, *77* (5), 2462-2469.
65. Damodaran, K. V.; Merz Jr, K. M., A comparison of DMPC- and DLPE-based lipid bilayers. *Biophysical Journal* **1994**, *66* (4), 1076-1087.
66. Murzyn, K.; Róg, T.; Pasenkiewicz-Gierula, M., Phosphatidylethanolamine-phosphatidylglycerol bilayer as a model of the inner bacterial membrane. *Biophysical Journal* **2005**, *88* (2), 1091-1103.
67. Shi, Q.; Voth, G. A., Multi-Scale Modeling of Phase Separation in Mixed Lipid Bilayers. *Biophysical Journal* **2005**, *89* (4), 2385-2394.
68. Dahlberg, M.; Maliniak, A., Molecular Dynamics Simulations of Cardiolipin Bilayers. *The Journal of Physical Chemistry B* **2008**, *112* (37), 11655-11663.
69. Dahlberg, M., Polymorphic Phase Behavior of Cardiolipin Derivatives Studied by Coarse-Grained Molecular Dynamics. *The Journal of Physical Chemistry B* **2007**, *111* (25), 7194-7200.
70. Poznansky, M. J.; Czekanski, S., Cholesterol exchange as a function of cholesterol/phospholipid mole ratios. *Biochemical Journal* **1979**, *177* (3), 989.
71. Hjort Ipsen, J.; Karlström, G.; Mourtisen, O. G.; Wennerström, H.; Zuckermann, M. J., Phase equilibria in the phosphatidylcholine-cholesterol system. *Biochimica et Biophysica Acta (BBA)- Biomembranes* **1987**, *905* (1), 162-172.
72. Vist, M. R.; Davis, J. H., Phase equilibria of cholesterol /dipalmitoylphosphatidylcholine mixtures: deuterium nuclear magnetic resonance and differential scanning calorimetry. *Biochemistry* **1990**, *29* (2), 451-464.
73. McMullen, T. P. W.; McElhaney, R. N., New aspects of the interaction of cholesterol with dipalmitoylphosphatidylcholine bilayers as revealed by high-sensitivity differential scanning calorimetry. *Biochimica et Biophysica Acta (BBA) - Biomembranes* **1995**, *1234* (1), 90-98.
74. McIntosh, T. J., The effect of cholesterol on the structure of phosphatidylcholine bilayers. *Biochimica et Biophysica Acta (BBA) - Biomembranes* **1978**, *513* (1), 43-58.
75. Lippert, J. L.; Peticolos, W. L., Laser Raman Investigation of the Effect of Cholesterol on Conformational Changes in Dipalmitoyl Lecithin Multilayers. *Proceedings of the National Academy of Sciences* **1971**, *68* (7), 1572-1576.
76. McMullen, T. P. W.; Lewis, R. N. A. H.; McElhaney, R. N., Differential scanning calorimetric study of the effect of cholesterol on the thermotropic phase behavior of a homologous series of linear saturated phosphatidylcholines. *Biochemistry* **1993**, *32* (2), 516-522.
77. Almeida, P. F. F.; Vaz, W. L. C.; Thompson, T. E., Lateral diffusion in the liquid phases of dimyristoylphosphatidylcholine/cholesterol lipid bilayers: a free volume analysis. *Biochemistry* **1992**, *31* (29), 6739-6747.

78. Chen, Y.-f., Phase Behavior Of Cardiolipin, Cornell University **2012**.
79. de Meyer, F. d. r.; Smit, B., Effect of cholesterol on the structure of a phospholipid bilayer. *Proceedings of the National Academy of Sciences* **2009**, *106* (10), 3654-3658.
80. Paré, C.; Lafleur, M., Polymorphism of POPE/Cholesterol System: A ²H Nuclear Magnetic Resonance and Infrared Spectroscopic Investigation. *Biophysical Journal* **1998**, *74* (2), 899-909.
81. McMullen, T. P. W.; Lewis, R. N. A. H.; McElhaney, R. N., Calorimetric and spectroscopic studies of the effects of cholesterol on the thermotropic phase behavior and organization of a homologous series of linear saturated phosphatidylethanolamine bilayers. *Biochimica et Biophysica Acta (BBA) - Biomembranes* **1999**, *1416* (1-2), 119-134.
82. Epanand, R. M.; Bottega, R., Modulation of the phase transition behavior of phosphatidylethanolamine by cholesterol and oxysterols. *Biochemistry* **1987**, *26* (7), 1820-1825.
83. Blume, A., Thermotropic behavior of phosphatidylethanolamine-cholesterol and phosphatidylethanolamine-phosphatidylcholine-cholesterol mixtures. *Biochemistry* **1980**, *19* (21), 4908-4913.
84. Gallay, J.; Vincent, M., Cardiolipin-cholesterol interactions in the liquid-crystalline phase: a steady-state and time-resolved fluorescence anisotropy study with cis- and trans-parinaric acids as probes. *Biochemistry* **1986**, *25* (9), 2650-2656.
85. Boggs, J. M.; Hsia, J. C., Structural Characteristics of Hydrated Glycerol- and Sphingo-lipids. A Spin Label Study. *Canadian Journal of Biochemistry* **1973**, *51* (11), 1451-1459.
86. Lu, Q.-w.; Wen, D.-c.; Zhao, B.-z.; Huang, F., Effect of cholesterol on the polymorphism in cardiolipin liposomes. *Kexue tongbao, Scientia* **1989**, *34* (11), 946-948.
87. Bangham, A. D.; Horne, R. W., Negative staining of phospholipids and their structural modification by surface-active agents as observed in the electron microscope. *Journal of molecular biology* **1964**, *8* (5), 660-IN10.
88. Reimhult, E.; Höök, F.; Kasemo, B., Intact Vesicle Adsorption and Supported Biomembrane Formation from Vesicles in Solution: Influence of Surface Chemistry, Vesicle Size, Temperature, and Osmotic Pressure. *Langmuir* **2002**, *19* (5), 1681-1691.
89. Drummond, D. C.; Zignani, M.; Leroux, J.-C., Current status of pH-sensitive liposomes in drug delivery. *Progress in Lipid Research* **2000**, *39* (5), 409-460.
90. Fröhlich, M.; Brecht, V.; Peschka-Süss, R., Parameters influencing the determination of liposome lamellarity by ³¹P-NMR. *Chemistry and Physics of Lipids* **2001**, *109* (1), 103-112.
91. Berger, N.; Sachse, A.; Bender, J.; Schubert, R.; Brandl, M., Filter extrusion of liposomes using different devices: comparison of liposome size, encapsulation efficiency, and process characteristics. *International Journal of Pharmaceutics* **2001**, *223* (1), 55-68.
92. Allen, T. M.; Cullis, P. R., Drug delivery systems: entering the mainstream. *Science* **2004**, *303* (5665), 1818-1822.
93. Costello, M. J.; Viitanen, P.; Carrasco, N.; Foster, D.; Kaback, H., Morphology of proteoliposomes reconstituted with purified lac carrier protein from Escherichia coli. *Journal of Biological Chemistry* **1984**, *259* (24), 15579-15586.
94. Egelhaaf, S.; Wehrli, E.; Adrian, M.; Schurtenberger, P., Determination of the size distribution of lecithin liposomes: a comparative study using freeze fracture, cryoelectron microscopy and dynamic light scattering. *Journal of Microscopy* **1996**, *184* (3), 214-228.
95. Ingebrigtsen, L.; Brandl, M., Determination of the size distribution of liposomes by SEC fractionation, and PCS analysis and enzymatic assay of lipid content. *AAPS PharmSciTech* **2002**, *3* (2), 9-15.

96. Chen, C. A Molecular Study of Membrane Structure in Liposomes. *Electronic Theses and Dissertations*, **2009**.
97. Lingler, S.; Rubinstein, I.; Knoll, W.; Offenhäusser, A., Fusion of Small Unilamellar Lipid Vesicles to Alkanethiol and Thiolipid Self-Assembled Monolayers on Gold. *Langmuir* **1997**, *13* (26), 7085-7091.
98. Sofou, S.; Thomas, J. L., Stable adhesion of phospholipid vesicles to modified gold surfaces. *Biosensors and Bioelectronics* **2003**, *18* (4), 445-455.
99. Jung, H.; Kim, J.; Park, J.; Lee, S.; Lee, H.; Kuboi, R.; Kawai, T., Atomic force microscopy observation of highly arrayed phospholipid bilayer vesicle on a gold surface. *Journal of bioscience and bioengineering* **2006**, *102* (1), 28-33.
100. Jiang, C.; Gamarnik, A.; Tripp, C. P., Identification of Lipid Aggregate Structures on TiO₂ Surface Using Headgroup IR Bands. *The Journal of Physical Chemistry B* **2005**, *109* (10), 4539-4544.
101. Reimhult, E.; Zäch, M.; Höök, F.; Kasemo, B., A multitechnique study of liposome adsorption on Au and lipid bilayer formation on SiO₂. *Langmuir* **2006**, *22* (7), 3313-3319.
102. Torchilin, V. P.; Zhou, F.; Huang, L., pH-Sensitive Liposomes. *Journal of Liposome Research* **1993**, *3* (2), 201-255.
103. Cho, S.; Lee, H.; Kim, J.-C., pH-dependent release property of dioleoylphosphatidyl ethanolamine liposomes. *Korean Journal of Chemical Engineering* **2008**, *25* (2), 390-393.
104. Straubinger, R. M.; Düzgünes, N.; Papahadjopoulos, D., pH-sensitive liposomes mediate cytoplasmic delivery of encapsulated macromolecules. *FEBS Letters* **1985**, *179* (1), 148-154.
105. Liu, D.; Huang, L., pH-sensitive, plasma-stable liposomes with relatively prolonged residence in circulation. *Biochimica et Biophysica Acta (BBA) - Biomembranes* **1990**, *1022* (3), 348-354.
106. Litzinger, D. C.; Huang, L., Phosphatidylethanolamine liposomes: drug delivery, gene transfer and immunodiagnostic applications. *Biochimica et Biophysica Acta (BBA) - Reviews on Biomembranes* **1992**, *1113* (2), 201-227.
107. Ellens, H.; Bentz, J.; Szoka, F. C., pH-Induced destabilization of phosphatidylethanolamine-containing liposomes: role of bilayer contact. *Biochemistry* **1984**, *23* (7), 1532-1538.
108. Sudimack, J. J.; Guo, W.; Tjarks, W.; Lee, R. J., A novel pH-sensitive liposome formulation containing oleyl alcohol. *Biochimica et Biophysica Acta (BBA) - Biomembranes* **2002**, *1564* (1), 31-37.
109. Simões, S. r.; Moreira, J. o. N.; Fonseca, C.; Düzgünes, N.; Pedroso de Lima, M. C., On the formulation of pH-sensitive liposomes with long circulation times. *Advanced Drug Delivery Reviews* **2004**, *56* (7), 947-965.
110. Zignani, M.; Drummond, D. C.; Meyer, O.; Hong, K.; Leroux, J.-C., In vitro characterization of a novel polymeric-based pH-sensitive liposome system. *Biochimica et Biophysica Acta (BBA) - Biomembranes* **2000**, *1463* (2), 383-394.
111. de Groot, B. L.; Grubmüller, H., Water permeation across biological membranes: mechanism and dynamics of aquaporin-1 and GlpF. *Science* **2001**, *294* (5550), 2353-2357.
112. Ronson, C. W.; Nixon, B. T.; Ausubel, F. M., Conserved domains in bacterial regulatory proteins that respond to environmental stimuli. *Cell* **1987**, *49* (5), 579-581.
113. Higgins, C. F., ABC transporters: physiology, structure and mechanism-an overview. *Research in Microbiology* **2001**, *152*, 205-210.
114. Bogdanov, M.; Dowhan, W., Lipid-assisted protein folding. *Journal of Biological Chemistry* **1999**, *274* (52), 36827-36830.

115. Fyfe, P. K.; Isaacs, N. W.; Cogdell, R. J.; Jones, M. R., Disruption of a specific molecular interaction with a bound lipid affects the thermal stability of the purple bacterial reaction centre. *Biochimica et Biophysica Acta (BBA) - Bioenergetics* **2004**, *1608* (1), 11-22.
116. Bogdanov, M.; Sun, J.; Kaback, H. R.; Dowhan, W., A phospholipid acts as a chaperone in assembly of a membrane transport protein. *Journal of Biological Chemistry* **1996**, *271* (20), 11615-11618.
117. Pfeiffer, K.; Gohil, V.; Stuart, R. A.; Hunte, C.; Brandt, U.; Greenberg, M. L.; Schägger, H., Cardiolipin stabilizes respiratory chain supercomplexes. *Journal of Biological Chemistry* **2003**, *278* (52), 52873-52880.
118. Zimmerberg, J.; Gawrisch, K., The physical chemistry of biological membranes. *Nat Chem Biol* **2006**, *2* (11), 564-567.
119. Lee, A. G., How lipids affect the activities of integral membrane proteins. *Biochimica et Biophysica Acta (BBA) - Biomembranes* **2004**, *1666* (1-2), 62-87.
120. Vrije, T. d.; Swart, R. d.; Dowhan, W.; Tommassen, J.; Kruijff, B. d., Phosphatidylglycerol is involved in protein translocation across Escherichia coli inner membranes. *Nature: international weekly journal of science* **1988**, *334* (6178), 173-175.
121. van Klompenburg, W.; Nilsson, I.; von Heijne, G.; de Kruijff, B., Anionic phospholipids are determinants of membrane protein topology. *The EMBO journal* **1997**, *16* (14), 4261-4266.
122. Wenz, T.; Hielscher, R.; Hellwig, P.; Schägger, H.; Richers, S.; Hunte, C., Role of phospholipids in respiratory cytochrome bc₁ complex catalysis and supercomplex formation. *Biochimica et Biophysica Acta (BBA) - Bioenergetics* **2009**, *1787* (6), 609-616.
123. Hielscher, R.; Wenz, T.; Hunte, C.; Hellwig, P., Monitoring the redox and protonation dependent contributions of cardiolipin in electrochemically induced FTIR difference spectra of the cytochrome bc₁ complex from yeast. *Biochimica et Biophysica Acta (BBA) - Bioenergetics* **2009**, *1787* (6), 617-625.
124. Chicco, A. J.; Sparagna, G. C., Role of cardiolipin alterations in mitochondrial dysfunction and disease. *American Journal of Physiology-Cell Physiology* **2007**, *292* (1), C33-C44.
125. Hakizimana, P.; Masureel, M.; Gbaguidi, B. n. d.; Ruyschaert, J.-M.; Govaerts, C. d., Interactions between Phosphatidylethanolamine Headgroup and LmrP, a Multidrug Transporter: a conserved mechanism for proton gradient sensing?. *Journal of Biological Chemistry* **2008**, *283* (14), 9369-9376.
126. Bertero, M. G.; Rothery, R. A.; Palak, M.; Hou, C.; Lim, D.; Blasco, F.; Weiner, J. H.; Strynadka, N. C., Insights into the respiratory electron transfer pathway from the structure of nitrate reductase A. *Nature Structural & Molecular Biology* **2003**, *10* (9), 681-687.
127. Sazanov, L. A.; Carroll, J.; Holt, P.; Toime, L.; Fearnley, I. M., A role for native lipids in the stabilization and two-dimensional crystallization of the Escherichia coli NADH-ubiquinone oxidoreductase (complex I). *Journal of Biological Chemistry* **2003**, *278* (21), 19483-19491.
128. Shinzawa-Itoh, K.; Seiyama, J.; Terada, H.; Nakatsubo, R.; Naoki, K.; Nakashima, Y.; Yoshikawa, S., Bovine Heart NADH-ubiquinone Oxidoreductase Contains One Molecule of Ubiquinone with Ten Isoprene Units as One of the Cofactors. *Biochemistry* **2009**, *49* (3), 487-492.
129. Mitchell, P., Coupling of Phosphorylation to Electron and Hydrogen Transfer by a Chemi-Osmotic type of Mechanism. *Nature* **1961**, *191* (4784), 144-148.
130. Kriegel, S. Transformation of a membrane protien from the respiratory chain into a sensor for the analysis of the analysis of its interaction with substrates, inhibitors and lipids. Université de Strasbourg, **2013**.

131. Sazanov, L. A., Respiratory complex I: mechanistic and structural insights provided by the crystal structure of the hydrophilic domain. *Biochemistry* **2007**, *46* (9), 2275-2288.
132. Dawson, T. M.; Dawson, V. L., Molecular pathways of neurodegeneration in Parkinson's disease. *Science* **2003**, *302* (5646), 819-822.
133. Balaban, R. S.; Nemoto, S.; Finkel, T., Mitochondria, oxidants, and aging. *Cell* **2005**, *120* (4), 483-495.
134. Weiss, H.; Friedrich, T.; Hofhaus, G. t.; Preis, D., The respiratory-chain NADH dehydrogenase (complex I) of mitochondria. In *EJB Reviews 1991*, Springer: **1992**, 55-68.
135. Efremov, R. G.; Sazanov, L. A., Structure of the membrane domain of respiratory complex I. *Nature* **2011**, *476* (7361), 414-420.
136. Hatefi, Y.; Haavik, A.; Griffiths, D. E., Studies on the electron transfer system XL. Preparation and properties of mitochondrial DPNH-coenzyme Q reductase. *Journal of Biological Chemistry* **1962**, *237* (5), 1676-1680.
137. Brandt, U., Energy converting NADH: quinone oxidoreductase (complex I). *Annu. Rev. Biochem.* **2006**, *75*, 69-92.
138. Hirst, J., Mitochondrial complex I. *Annual review of biochemistry* **2013**, *82*, 551-575.
139. Verkhovskaya, M.; Bloch, D. A., Energy-converting respiratory Complex I: on the way to the molecular mechanism of the proton pump. *The international journal of biochemistry & cell biology* **2013**, *45* (2), 491-511.
140. Walker, J. E., The NADH: ubiquinone oxidoreductase (complex I) of respiratory chains. *Quarterly reviews of biophysics* **1992**, *25* (03), 253-324.
141. Hatefi, Y.; Sidney, F.; Lester, P., [3] Preparation and properties of NADH: Ubiquinone oxidoreductase (complex I), EC 1.6.5.3. In *Methods in Enzymology*, Academic Press: **1978**, *53*, 11-14.
142. Yagi, T.; Matsuno-Yagi, A., The proton-translocating NADH-quinone oxidoreductase in the respiratory chain: the secret unlocked. *Biochemistry* **2003**, *42* (8), 2266-2274.
143. Carroll, J.; Fearnley, I. M.; Skehel, J. M.; Shannon, R. J.; Hirst, J.; Walker, J. E., Bovine complex I is a complex of 45 different subunits. *Journal of Biological Chemistry* **2006**, *281* (43), 32724-32727.
144. Friedrich, T.; Steinmüller, K.; Weiss, H., The proton-pumping respiratory complex I of bacteria and mitochondria and its homologue in chloroplasts. *FEBS Letters* **1995**, *367* (2), 107-111.
145. Friedrich, T.; Scheide, D., The respiratory complex I of bacteria, archaea and eukarya and its module common with membrane-bound multisubunit hydrogenases. *FEBS Letters* **2000**, *479* (1), 1-5.
146. Baradaran, R.; Berrisford, J. M.; Minhas, G. S.; Sazanov, L. A., Crystal structure of the entire respiratory complex I. *Nature* **2012**, *494* (7438), 443-448.
147. Guénebat, V.; Schlitt, A.; Weiss, H.; Leonard, K.; Friedrich, T., Consistent structure between bacterial and mitochondrial NADH: ubiquinone oxidoreductase (complex I). *Journal of molecular biology* **1998**, *276* (1), 105-112.
148. Friedrich, T., The NADH: ubiquinone oxidoreductase (complex I) from *Escherichia coli*. *Biochimica et Biophysica Acta (BBA)-Bioenergetics* **1998**, *1364* (2), 134-146.
149. Sazanov, L. A.; Hinchliffe, P., Structure of the hydrophilic domain of respiratory complex I from *Thermus thermophilus*. *Science* **2006**, *311* (5766), 1430-1436.
150. Radermacher, M.; Ruiz, T.; Clason, T.; Benjamin, S.; Brandt, U.; Zickermann, V., The three-dimensional structure of complex I from *Yarrowia lipolytica*: A highly dynamic enzyme. *Journal of structural biology* **2006**, *154* (3), 269-279.
151. Mathiesen, C.; Hägerhäll, C., The antiporter module of respiratory chain Complex I includes the MrpC/NuoK subunit - a revision of the modular evolution scheme. *FEBS Letters* **2003**, *549* (1-3), 7-13.

152. Spiro, T. G.; Czernuszewicz, R. S.; Kenneth, S., Resonance Raman spectroscopy of metalloproteins. In *Methods in Enzymology*, Academic Press: **1995**, 246, 416-460.
153. Birrell, J. A.; Hirst, J., Investigation of NADH Binding, Hydride Transfer, and NAD⁺ Dissociation during NADH Oxidation by Mitochondrial Complex I Using Modified Nicotinamide Nucleotides. *Biochemistry* **2013**, 52 (23), 4048-4055.
154. Baranova, E. A.; Holt, P. J.; Sazanov, L. A., Projection Structure of the Membrane Domain of Escherichia coli Respiratory Complex I at 8 Å Resolution. *Journal of molecular biology* **2007**, 366 (1), 140-154.
155. Verkhovskaya, M. L.; Belevich, N.; Euro, L.; Wikström, M. r.; Verkhovsky, M. I., Real-time electron transfer in respiratory complex I. *Proceedings of the National Academy of Sciences* **2008**, 105 (10), 3763-3767.
156. Braun, M.; Bungert, S.; Friedrich, T., Characterization of the overproduced NADH dehydrogenase fragment of the NADH: ubiquinone oxidoreductase (complex I) from Escherichia coli. *Biochemistry* **1998**, 37 (7), 1861-1867.
157. Ohnishi, T., Iron-sulfur clusters/semiquinones in complex I. *Biochimica et Biophysica Acta (BBA)-Bioenergetics* **1998**, 1364 (2), 186-206.
158. Tocilescu, M. A.; Fendel, U.; Zwicker, K.; Dröse, S.; Kerscher, S.; Brandt, U., The role of a conserved tyrosine in the 49-kDa subunit of complex I for ubiquinone binding and reduction. *Biochimica et Biophysica Acta (BBA)-Bioenergetics* **2010**, 1797 (6), 625-632.
159. Hellwig, P.; Scheide, D.; Bungert, S.; Mäntele, W.; Friedrich, T., FT-IR spectroscopic characterization of NADH: ubiquinone oxidoreductase (complex I) from Escherichia coli: oxidation of FeS cluster N2 is coupled with the protonation of an aspartate or glutamate side chain. *Biochemistry* **2000**, 39 (35), 10884-10891.
160. Flemming, D.; Stolpe, S.; Schneider, D.; Hellwig, P.; Friedrich, T., A possible role for iron-sulfur cluster N2 in proton translocation by the NADH: ubiquinone oxidoreductase (complex I). *Journal of molecular microbiology and biotechnology* **2006**, 10 (2-4), 208-222.
161. Sled, V. D.; Rudnitzky, N. I.; Hatefi, Y.; Ohnishi, T., Thermodynamic Analysis of Flavin in Mitochondrial NADH:Ubiquinone Oxidoreductase (Complex I). *Biochemistry* **1994**, 33 (33), 10069-10075.
162. Kussmaul, L.; Hirst, J., The mechanism of superoxide production by NADH: ubiquinone oxidoreductase (complex I) from bovine heart mitochondria. *Proceedings of the National Academy of Sciences* **2006**, 103 (20), 7607-7612.
163. Hayashi, T.; Stuchebrukhov, A. A., Electron tunneling in respiratory complex I. *Proceedings of the National Academy of Sciences* **2010**, 107 (45), 19157-19162.
164. Hirst, J., Towards the molecular mechanism of respiratory complex I. *Biochem. J* **2009**, 425, 327-339.
165. Page, C. C.; Moser, C. C.; Chen, X.; Dutton, P. L., Natural engineering principles of electron tunnelling in biological oxidation-reduction. *Nature* **1999**, 402 (6757), 47-52.
166. Ohnishi, T.; Ohnishi, S. T.; Shinzawa-Itoh, K.; Yoshikawa, S.; Weber, R. T., EPR detection of two protein-associated ubiquinone components (SQ(Nf) and SQ(Ns)) in the membrane in situ and in proteoliposomes of isolated bovine heart complex I. *Biochimica et Biophysica Acta (BBA)-Bioenergetics* **2012**, 1817 (10), 1803-1809.
167. Euro, L.; Bloch, D. A.; Wikström, M. r.; Verkhovsky, M. I.; Verkhovskaya, M., Electrostatic Interactions Between FeS Clusters in NADH: Ubiquinone Oxidoreductase (Complex I) from Escherichia coli *Biochemistry* **2008**, 47 (10), 3185-3193
168. Pohl, T.; Bauer, T.; Dörner, K.; Stolpe, S.; Sell, P.; Zocher, G.; Friedrich, T., Iron-sulfur cluster N7 of the NADH: ubiquinone oxidoreductase (complex I) is essential for stability but not involved in electron transfer. *Biochemistry* **2007**, 46 (22), 6588-6596.
169. Roessler, M. M.; King, M. S.; Robinson, A. J.; Armstrong, F. A.; Harmer, J.; Hirst, J., Direct assignment of EPR spectra to structurally defined iron-sulfur clusters in complex I by

- double electron-electron resonance. *Proceedings of the National Academy of Sciences* **2010**, *107* (5), 1930-1935.
170. Fearnley, I. M.; Walker, J. E., Conservation of sequences of subunits of mitochondrial complex I and their relationships with other proteins. *Biochimica et Biophysica Acta (BBA)-Bioenergetics* **1992**, *1140* (2), 105-134.
171. Mathiesen, C.; Hägerhäll, C., Transmembrane topology of the NuoL, M and N subunits of NADH: quinone oxidoreductase and their homologues among membrane-bound hydrogenases and bona fide antiporters. *Biochimica et Biophysica Acta (BBA)-Bioenergetics* **2002**, *1556* (2), 121-132.
172. Sazanov, L. A.; Baradaran, R.; Efremov, R. G.; Berrisford, J. M.; Minhas, G., A long road towards the structure of respiratory complex I, a giant molecular proton pump. *Biochem Soc Trans* **2013**, *41* (5), 1265-71.
173. Friedrich, T., Complex I: a chimaera of a redox and conformation-driven proton pump? *Journal of bioenergetics and biomembranes* **2001**, *33* (3), 169-177.
174. Steimle, S.; Bajzath, C.; Dörner, K.; Schulte, M.; Bothe, V.; Friedrich, T., Role of Subunit NuoL for Proton Translocation by Respiratory Complex I. *Biochemistry* **2011**, *50* (16), 3386-3393.
175. Steimle, S.; Willistein, M.; Hegger, P.; Janoschke, M.; Erhardt, H.; Friedrich, T., Asp563 of the horizontal helix of subunit NuoL is involved in proton translocation by the respiratory complex I. *FEBS Letters* **2012**, *586* (6), 699-704.
176. Sharpley, M. S.; Hirst, J., The inhibition of mitochondrial complex I (NADH: ubiquinone oxidoreductase) by Zn^{2+} . *Journal of Biological Chemistry* **2006**, *281* (46), 34803-34809.
177. Link, T. A.; von Jagow, G., Zinc ions inhibit the QP center of bovine heart mitochondrial bcl complex by blocking a protonatable group. *Journal of Biological Chemistry* **1995**, *270* (42), 25001-25006.
178. Schulte, M.; Mattay, D.; Kriegel, S.; Hellwig, P.; Friedrich, T., Inhibition of Escherichia coli Respiratory Complex I by Zn^{2+} . *Biochemistry* **2014**, *53* (40), 6332-6339.
179. S Sharpley, M. S.; Shannon, R. J.; Draghi, F.; Hirst, J., Interactions between Phospholipids and NADH:Ubiquinone Oxidoreductase (Complex I) from Bovine Mitochondria. *Biochemistry* **2005**, *45* (1), 241-248.
180. Hielscher, R.; Wenz, T.; Stolpe, S.; Hunte, C.; Friedrich, T.; Hellwig, P., Monitoring redox-dependent contribution of lipids in Fourier transform infrared difference spectra of complex I from Escherichia coli. *Biopolymers* **2006**, *82* (4), 291-294.
181. Hielscher, R. G. The role of lipids and nucleotides in the catalytic mechanism of proteins from the respiratory chain (an electrochemical and infrared spectroscopic approach. Université de Strasbourg, **2009**.
182. Graff, A.; Fraysse-Ailhas, C.; Palivan, C. G.; Grzelakowski, M.; Friedrich, T.; Vebert, C.; Gescheidt, G.; Meier, W., Amphiphilic Copolymer Membranes Promote NADH:Ubiquinone Oxidoreductase Activity: Towards an Electron-Transfer Nanodevice. *Macromolecular Chemistry and Physics* **2010**, *211* (2), 229-238.
183. Neehaul, Y. Study of protien interactions in the resparatory chain by IR spectroscopy and electrochemistry. Université de Strasbourg **2012**.
184. Hammes, G. G., Spectroscopy for the Biological Sciences. John Wiley & Sons, Inc: United State of America, **2006**.
185. Hans-Ulrich Gremlich, G. H., Handbook of Spectroscopy. Wiley-VCH GmBH and Co. KGaA: Weinheim, **2003**.
186. khoury, Y. E. Mid and far spectroelectrochemical studies on the metal ligand interactionin respiratory chain enzymes. University of Strasbourg **2010**.

187. A Munro, A.; Girvan, H.; McLean, K.; Cheesman, M.; Leys, D., Chapter 10 heme and heme proteins. *Landes Biosciences and Springer Science* **2009**.
188. Wyer, J. A.; Nielsen, S. B. n., Absorption in the Q-band region by isolated ferric heme+ and heme+(histidine)in vacuo. *The Journal of Chemical Physics* **2010**, *133* (8).
189. Friedrich, T.; Hofhaus, G.; Ise, W.; Nehls, U.; Schmitz, B.; Weiss, H., A small isoform of NADH: ubiquinone oxidoreductase (complex I) without mitochondrially encoded subunits is made in chloramphenicol-treated *Neurospora crassa*. *European Journal of Biochemistry* **1989**, *180* (1), 173-180.
190. Friedrich, T.; Brors, B.; Hellwig, P.; Kintscher, L.; Rasmussen, T.; Scheide, D.; Schulte, U.; Mäntele, W.; Weiss, H., Characterization of two novel redox groups in the respiratory NADH:ubiquinone oxidoreductase (complex I). *Biochimica et Biophysica Acta (BBA) - Bioenergetics* **2000**, *1459* (2-3), 305-309.
191. Hellwig, P.; Scheide, D.; Bungert, S.; Mäntele, W.; Friedrich, T., FT-IR Spectroscopic Characterization of NADH:Ubiquinone Oxidoreductase (Complex I) from *Escherichia coli*: Hellwig Oxidation of FeS Cluster N2 is Coupled with the Protonation of an Aspartate or Glutamate Side Chains *Biochemistry* **2000**, *39* (35), 10884-10891.
192. Siebert, F.; Hildebrandt, P., *Vibrational Spectroscopy in Life Science*. Wiley-VCH Verlag GmbH & Co. KGaA: **2008**.
193. Stuart, B., *Infrared Spectroscopy: Fundamentals and Applications*. John Wiley & Sons **2004**.
194. Stuart, B., *Modern Infrared Spectroscopy*. Wiley, Chichester: UK, **1996**.
195. Larkin, P., *IR and Raman Spectroscopy : principles and spectral interpretation, 1st Edition ed.* Elsevier Inc: Oxford, UK, **2011**.
196. Chalmers, J. M., and Griffiths, P, *Handbook of vibrational spectroscopy (Vol 1-5)*. Wiley: **2002**.
197. Siegfried, W., *IR and Raman Spectroscopy*. Wiley-VCH Verlag GmbH and Co: Germany, **2003**.
198. Yegres, M. Probing the effect of conformational changes in protein complexes by vibrational spectroscopy : bioenergetics and allostery. University of Strasbourg, **2014**.
199. Smith, G. D., and Palmer, R. A. , *Fast Time-resolved Mid-infrared Spectroscopy Using an Interferometer*, In *Time-resolved spectroscopy*, 625-640. John Wiley & Sons Ltd: **2002**.
200. Gallagher, W., *FTIR analysis of protein structure, Course manual Chem*, **2009**.
201. Freeman, H., *Molecular Cell Biology*, sixth edition. **2008**.
202. Hellwig, P.; Mogi, T.; Tomson, F. L.; Gennis, R. B.; Iwata, J.; Miyoshi, H.; Mäntele, W., Vibrational Modes of Ubiquinone in Cytochrome bo3 from *Escherichia coli* Identified by Fourier Transform Infrared Difference Spectroscopy and Specific ¹³C Labeling. *Biochemistry* **1999**, *38* (44), 14683-14689.
203. Hellwig, P.; Grzybek, S.; Behr, J.; Ludwig, B.; Michel, H.; Mäntele, W., Electrochemical and Ultraviolet/Visible/Infrared Spectroscopic Analysis of Heme a and a₃ Redox Reactions in the Cytochrome c Oxidase from *Paracoccus denitrificans*: Separation of Heme a and a₃ Contributions and Assignment of Vibrational Modes. *Biochemistry* **1999**, *38* (6), 1685-1694.
204. Hellwig, P.; Pfitzner, U.; Behr, J.; Rost, B.; Pesavento, R. P.; Donk, W. v.; Gennis, R. B.; Michel, H.; Ludwig, B.; Mäntele, W., Vibrational Modes of Tyrosines in Cytochrome c Oxidase from *Paracoccus denitrificans*: FTIR and Electrochemical Studies on Tyr-D4-labeled and on Tyr280His and Tyr35Phe Mutant Enzymes. *Biochemistry* **2002**, *41* (29), 9116-9125.
- Oxidase from *Paracoccus denitrificans*: FTIR and Electrochemical Studies on Tyr-D4-labeled and on Tyr280His and Tyr35Phe Mutant Enzymes *Biochemistry* **2002**, *41* (29), 9116-9125.

205. Hellwig, P.; Behr, J.; Ostermeier, C.; Richter, O.-M. H.; Pfitzner, U.; Odenwald, A.; Ludwig, B.; Michel, H.; Mäntele, W., Involvement of Glutamic Acid 278 in the Redox Reaction of the Cytochrome c Oxidase from *Paracoccus denitrificans* Investigated by FTIR Spectroscopy. *Biochemistry* **1998**, *37* (20), 7390-7399.
206. Kong, J.; Yu, S., Fourier Transform Infrared Spectroscopic Analysis of Protein Secondary Structures. *Acta Biochimica et Biophysica Sinica* **2007**, *39* (8), 549-559.
207. Barth, A., Infrared spectroscopy of proteins. *Biochimica et Biophysica Acta (BBA) - Bioenergetics* **2007**, *1767* (9), 1073-1101.
208. Surewicz, W. K.; Mantsch, H. H.; Chapman, D., Determination of protein secondary structure by Fourier transform infrared spectroscopy: A critical assessment. *Biochemistry* **1993**, *32* (2), 389-394.
209. Zscherp, C.; Barth, A., Reaction-Induced Infrared Difference Spectroscopy for the Study of Protein Reaction Mechanisms. *Biochemistry* **2001**, *40* (7), 1875-1883.
210. El Khoury, Y.; Hellwig, P., A Combined Far-Infrared Spectroscopic and Electrochemical Approach for the Study of Iron-Sulfur Proteins. *ChemPhysChem* **2011**, *12* (14), 2669-2674.
211. El Khoury, Y.; Trivella, A.; Gross, J.; Hellwig, P., Probing the Hydrogen Bonding Structure in the Rieske Protein. *ChemPhysChem* **2010**, *11* (15), 3313-3319.
212. Wolpert, M.; Hellwig, P., Infrared spectra and molar absorption coefficients of the 20 alpha amino acids in aqueous solutions in the spectral range from 1800 to 500 cm⁻¹. *Spectrochimica Acta Part A: Molecular and Biomolecular Spectroscopy* **2006**, *64* (4), 987-1001.
213. Goormaghtigh, E.; Raussens, V.; Ruyschaert, J.-M., Attenuated total reflection infrared spectroscopy of proteins and lipids in biological membranes. *Biochimica et Biophysica Acta (BBA) - Reviews on Biomembranes* **1999**, *1422* (2), 105-185.
214. Harrick, N. J., *Internal reflection spectroscopy*. John Wiley & Sons: ,New York **1967**.
215. Sevenou, O.; Hill, S. E.; Farhat, I. A.; Mitchell, J. R., Organisation of the external region of the starch granule as determined by infrared spectroscopy. *International Journal of Biological Macromolecules* **2002**, *31* (1-3), 79-85.212.
216. <http://www.semrock.com/uv-raman-spectroscopy.aspx>.
217. Ewen Smith, G. D., *Modern Raman spectroscopy - A Practical Approach*. John Wiley and Sons: Ltd, England, **2005**
218. J John R. Ferraro, K. N. a. C. W. B., *Introductory Raman Spectroscopy* (Second edition). *Elsevier*: **2003**.
219. Streckas, T. C.; Packer, A. J.; Spiro, T. G., Resonance Raman spectra of ferri-hemoglobin fluoride: Three scattering regimes. *Journal of Raman Spectroscopy* **1973**, *1* (2), 197-206.
220. Streckas, T. C.; Spiro, T. G., Hemoglobin: Resonance Raman spectra. *Biochimica et Biophysica Acta (BBA) - Protein Structure* **1972**, *263* (3), 830-833.
221. Morikis, D.; Champion, P. M.; Springer, B. A.; Sligar, S. G., Resonance Raman investigations of site-directed mutants of myoglobin: effects of distal histidine replacement. *Biochemistry* **1989**, *28* (11), 4791-4800.
222. Walters, M. A.; Spiro, T. G., Resonance Raman spectroscopic studies of axial ligation in oxyhemoglobin and oxymyoglobin, and nitrosylmyoglobin. *Biochemistry* **1982**, *21* (26), 6989-6995.
223. Kitagawa, T.; Nagai, K.; Tsubaki, M., Assignment of the Fe-Nepsilon (His F8) stretching band in the resonance Raman spectra of deoxy myoglobin. *FEBS Letters* **1979**, *104* (2), 376-378.

224. Yachandra, V. K.; Hare, J.; Gewirth, A.; Czernuszewicz, R. S.; Kimura, T.; Holm, R. H.; Spiro, T. G., Resonance Raman spectra of spinach ferredoxin and adrenodoxin and of analog complexes. *Journal of the American Chemical Society* **1983**, *105* (21), 6462-6469.
225. Han, S.; Czernuszewicz, R. S.; Kimura, T.; Adams, M. W. W.; Spiro, T. G., Fe₂S₂ protein resonance Raman spectra revisited: structural variations among adrenodoxin, ferredoxin, and red paramagnetic protein. *Journal of the American Chemical Society* **1989**, *111* (10), 3505-3511.
226. Kilpatrick, L. K.; Kennedy, M. C.; Beinert, H.; Czernuszewicz, R. S.; Spiro, T. G.; Qiu, D., Cluster Structure and H-Bonding in Native, Substrate-Bound, and 3Fe Forms of Aconitase as Determined by Resonance Raman Spectroscopy. *Journal of the American Chemical Society* **1994**, *116* (9), 4053-4061.
227. Mino, Y.; Loehr, T. M.; Wada, K.; Matsubara, H.; Sanders-Loehr, J., Hydrogen bonding of sulfur ligands in blue copper and iron-sulfur proteins: detection by resonance Raman spectroscopy. *Biochemistry* **1987**, *26* (25), 8059-8065.
228. Iwasaki, T.; Kounosu, A.; Kolling, D. R. J.; Lhee, S.; Crofts, A. R.; Dikanov, S. A.; Uchiyama, T.; Kumasaka, T.; Ishikawa, H.; Kono, M.; Imai, T.; Urushiyama, A., Resonance Raman characterization of archaeal and bacterial Rieske protein variants with modified hydrogen bond network around the [2Fe-2S] center. *Protein Science* **2006**, *15* (8), 2019-2024.
229. Kuila, D.; Schoonover, J. R.; Dyer, R. B.; Batie, C. J.; Ballou, D. P.; Fee, J. A.; Woodruff, W. H., Resonance Raman studies of Rieske-type proteins. *Biochimica et Biophysica Acta (BBA) - Bioenergetics* **1992**, *1140* (2), 175-183.
230. Willis, L. J.; Loehr, T. M., Resonance Raman studies of the flavin and iron-sulfur centers of milk xanthine oxidase. *Biochemistry* **1985**, *24* (11), 2768-2772.
231. Fleischmann, M.; Hendra, P. J.; McQuillan, A. J., Raman spectra of pyridine adsorbed at a silver electrode. *Chemical Physics Letters* **1974**, *26* (2), 163-166.
232. Hicks, C. J., Surface Enhanced Raman Spectroscopy. MSU CEM 924: **2001**.
233. Moskovits, M., Surface-enhanced spectroscopy. *Reviews of Modern Physics* **1985**, *57* (3), 783-826.
234. Campion, A.; Kambhampati, P., Surface-enhanced Raman scattering. *Chem. Soc. Rev.* **1998**, *27* (4), 241-250.
235. Cotton, T. M.; Schultz, S. G.; Van Duyne, R. P., Surface-enhanced resonance Raman scattering from cytochrome c and myoglobin adsorbed on a silver electrode. *Journal of the American Chemical Society* **1980**, *102* (27), 7960-7962.
236. Pohl, T.; Uhlmann, M.; Kaufenstein, M.; Friedrich, T., Lambda Red-Mediated Mutagenesis and Efficient Large Scale Affinity Purification of the Escherichia coli NADH:Ubiquinone Oxidoreductase (Complex I) *Biochemistry* **2007**, *46* (37), 10694-10702.
237. Gill, S. C.; von Hippel, P. H., Calculation of protein extinction coefficients from amino acid sequence data. *Analytical Biochemistry* **1989**, *182* (2), 319-326.
238. Maestrelli, F.; González-Rodríguez, M. L.; Rabasco, A. M.; Mura, P., Effect of preparation technique on the properties of liposomes encapsulating ketoprofen-cyclodextrin complexes aimed for transdermal delivery. *International Journal of Pharmaceutics* **2006**, *312* (1-2), 53-60.
239. Maestrelli, F.; González-Rodríguez, M. L.; Rabasco, A. M.; Mura, P., Effect of preparation technique on the properties of liposomes encapsulating ketoprofen-cyclodextrin complexes aimed for transdermal delivery. *International Journal of Pharmaceutics* **2006**, *312* (1-2), 53-60.
240. Sharata, H. H.; Katz, K. H., Liposomes. *International Journal of Dermatology* **1996**, *35* (11), 761-769.
241. Hielscher, R.; Hellwig, P., The Temperature-Dependent Hydrogen-Bonding Signature of Lipids Monitored in the Far-Infrared Domain. *ChemPhysChem* **2010**, *11* (2), 435-441.

242. Ninness, B. J. A molecular investigation of adsorption onto mineral pigments. Electronic thesis, University of Maine, **2001**.
243. Moss, D.; Nabedryk, E.; Breton, J.; Mäntele, W., Redox-linked conformational changes in proteins detected by a combination of infrared spectroscopy and protein electrochemistry. *European Journal of Biochemistry* **1990**, *187* (3), 565-572.
244. Baymann, F.; Moss, D. A.; Mäntele, W., An electrochemical assay for the characterization of redox proteins from biological electron transfer chains. *Analytical Biochemistry* **1991**, *199* (2), 269-274.
245. Voicescu, M.; Rother, D.; Bardischewsky, F.; Friedrich, C. G.; Hellwig, P., A Combined Fluorescence Spectroscopic and Electrochemical Approach for the Study of Thioredoxins. *Biochemistry* **2011**, *50* (1), 17-24.
246. Hellwig, P.; Rost, B.; Kaiser, U.; Ostermeier, C.; Michel, H.; Mäntele, W., Carboxyl group protonation upon reduction of the *Paracoccus denitrificans* cytochrome c oxidase: direct evidence by FTIR spectroscopy. *FEBS Letters* **1996**, *385* (1-2), 53-57.
247. Neehaul, Y.; Juárez, O.; Barquera, B.; Hellwig, P., Thermodynamic Contribution to the Regulation of Electron Transfer in the Na⁺-Pumping NADH:Quinone Oxidoreductase from *Vibrio cholerae*. *Biochemistry* **2012**, *51* (19), 4072-4077.
248. Lewis, R. N. A. H.; McElhaney, R. N., Membrane lipid phase transitions and phase organization studied by Fourier transform infrared spectroscopy. *Biochimica et Biophysica Acta (BBA) - Biomembranes* **2013**, *1828* (10), 2347-2358.
249. Popova, A. V.; Hinch, D. K., Intermolecular Interactions in Dry and Rehydrated Pure and Mixed Bilayers of Phosphatidylcholine and Digalactosyldiacylglycerol: A Fourier Transform Infrared Spectroscopy Study. *Biophysical Journal* **2003**, *85* (3), 1682-1690.
250. Casal, H. L.; McElhaney, R. N., Quantitative determination of hydrocarbon chain conformational order in bilayers of saturated phosphatidylcholines of various chain lengths by Fourier transform infrared spectroscopy. *Biochemistry* **1990**, *29* (23), 5423-5427.
251. Hübner, W.; Mantsch, H. H., Orientation of specifically ¹³C=O labeled phosphatidylcholine multilayers from polarized attenuated total reflection FT-IR spectroscopy. *Biophysical Journal* **1991**, *59* (6), 1261-1272.
252. Snyder, R. G.; Liang, G. L.; Strauss, H. L.; Mendelsohn, R., IR spectroscopic study of the structure and phase behavior of long-chain diacylphosphatidylcholines in the gel state. *Biophysical Journal* **1996**, *71* (6), 3186-3198.
253. Ladbrooke, B. D.; Williams, R. M.; Chapman, D., Studies on lecithin-cholesterol-water interactions by differential scanning calorimetry and X-ray diffraction. *Biochimica et Biophysica Acta (BBA) - Biomembranes* **1968**, *150* (3), 333-340.
254. Franks, N. P., Structural analysis of hydrated egg lecithin and cholesterol bilayers I. X-ray diffraction. *Journal of Molecular Biology* **1976**, *100* (3), 345-358.
255. Worcester, D. L.; Franks, N. P., Structural analysis of hydrated egg lecithin and cholesterol bilayers II. Neutron diffraction. *Journal of Molecular Biology* **1976**, *100* (3), 359-378.
256. Stockton, G. W.; Polnaszek, C. F.; Tulloch, A. P.; Hasan, F.; Smith, I. C. P., Molecular motion and order in single-bilayer vesicles with multilamellar dispersions of egg lecithin and lecithin-cholesterol mixtures. A deuterium nuclear magnetic resonance study of specifically labeled lipids. *Biochemistry* **1976**, *15* (5), 954-966.
257. Yeagle, P. L.; Bruce Martin, R., Hydrogen-bonding of the ester carbonyls in phosphatidylcholine bilayers. *Biochemical and Biophysical Research Communications* **1976**, *69* (3), 775-780.
258. Brown, M. F.; Seelig, J., Influence of cholesterol on the polar region of phosphatidylcholine and phosphatidylethanolamine bilayers. *Biochemistry* **1978**, *17* (2), 381-384.

259. Oldfield, E.; Meadows, M.; Rice, D.; Jacobs, R., Spectroscopic studies of specifically deuterium labeled membrane systems. Nuclear magnetic resonance investigation of the effects of cholesterol in model systems. *Biochemistry* **1978**, *17* (14), 2727-2740.
260. Mailer, C.; Taylor, C. P. S.; Schreier-Muccillo, S.; Smith, I. C. P., The influence of cholesterol on molecular motion in egg lecithin bilayers- A variable-frequency electron spin resonance study of a cholestane spin probe. *Archives of Biochemistry and Biophysics* **1974**, *163* (2), 671-678.
261. Mendelsohn, R., Laser-Raman spectroscopic study of egg lecithin and egg lecithin-cholesterol mixtures. *Biochimica et Biophysica Acta (BBA) - Biomembranes* **1972**, *290* (0), 15-21.
262. Verma, S. P.; Hoelzl Wallach, D. F., Effects of cholesterol on the infrared dichroism of phosphatide multibilayers. *Biochimica et Biophysica Acta (BBA) - Biomembranes* **1973**, *330* (2), 122-131.
263. Asher, I. M.; Levin, I. W., Effects of temperature and molecular interactions on the vibrational infrared spectra of phospholipid vesicles. *Biochimica et Biophysica Acta (BBA) - Biomembranes* **1977**, *468* (1), 63-72.
264. Lee, D.; Chapman, D., Infrared spectroscopic studies of biomembranes and model membranes. *Bioscience Reports* **1986**, *6* (3), 235-256.
265. Ruthven N.A.H. Lewis, R. N. M., Lewis, R. N., McElhaney, R. N, Vibrational Spectroscopy of Lipids. Handbook of Vibrational Spectroscopy, **2006**.
266. Dopico, A.; Lewis, R. A. H.; McElhaney, R., Fourier Transform Infrared Spectroscopy in the Study of Lipid Phase Transitions in Model and Biological Membranes. In *Methods in Membrane Lipids*, Humana Press: **2007**; 400, 207-226.
267. Mendelsohn, R.; Moore, D. J., Vibrational spectroscopic studies of lipid domains in biomembranes and model systems. *Chemistry and Physics of Lipids* **1998**, *96* (1-2), 141-157.
268. Mendelsohn, R., IR spectroscopy of lipid chains: theoretical background and applications to phase transitions, membranes, cells and tissues. *The Structure of Biological Membranes*. **2012**; 91-118.
269. Mantsch, H. H.; McElhaney, R. N., Phospholipid phase transitions in model and biological membranes as studied by infrared spectroscopy. *Chemistry and Physics of Lipids* **1991**, *57* (2-3), 213-226.
270. Lewis, R. N. A. H.; McElhaney, R. N., The structure and organization of phospholipid bilayers as revealed by infrared spectroscopy. *Chemistry and Physics of Lipids* **1998**, *96* (1-2), 9-21.
271. Mendelsohn, R.; Davies, M. A.; Brauner, J. W.; Schuster, H. F.; Dluhy, R. A., Quantitative determination of conformational disorder in the acyl chains of phospholipid bilayers by infrared spectroscopy. *Biochemistry* **1989**, *28* (22), 8934-8939.
272. Seddon, J. M., Structure of the inverted hexagonal (HII) phase, and non-lamellar phase transitions of lipids. *Biochimica et Biophysica Acta (BBA) - Reviews on Biomembranes* **1990**, *1031* (1), 1-69.
273. Seddon, J. M.; Cevc, G.; Kaye, R. D.; Marsh, D., X-ray diffraction study of the polymorphism of hydrated diacyl and dialkylphosphatidylethanolamines. *Biochemistry* **1984**, *23* (12), 2634-2644.
274. Cullis, P. R.; De Kruijff, B., Lipid polymorphism and the functional roles of lipids in biological membranes. *Biochimica et Biophysica Acta (BBA) - Reviews on Biomembranes* **1979**, *559* (4), 399-420.
275. Chong, P. L.; Choate, D., Calorimetric studies of the effects of cholesterol on the phase transition of C(18):C(10) phosphatidylcholine. *Biophysical Journal* **1989**, *55* (3), 551-556.

276. Umemura, J.; Cameron, D. G.; Mantsch, H. H., A Fourier transform infrared spectroscopic study of the molecular interaction of cholesterol with 1,2-dipalmitoyl-sn-glycero-3-phosphocholine. *Biochimica et Biophysica Acta (BBA) - Biomembranes* **1980**, 602 (1), 32-44.
277. Lewis, R. N. A. H.; McElhaney, R. N., The physicochemical properties of cardiolipin bilayers and cardiolipin-containing lipid membranes. *Biochimica et Biophysica Acta (BBA) - Biomembranes* **2009**, 1788 (10), 2069-2079.
278. Rainier, S.; Jain, M. K.; Ramirez, F.; Ioannou, P. V.; Marecek, J. F.; Wagner, R., Phase transition characteristics of diphosphatidylglycerol (cardiolipin) and stereoisomeric phosphatidylglycerol bilayers: Mono- and divalent metal ion effects. *Biochimica et Biophysica Acta (BBA) - Biomembranes* **1979**, 558 (2), 187-198.
279. Nagamachi, E.; Kariyama, R.; Kanemasa, Y., The effect of head group structure on phase transition of phospholipid membranes as determined by differential scanning calorimetry. *Physiological chemistry and physics and medical NMR* **1985**, 17 (3), 255-260.
280. Sankaram, M. B.; Powell, G. L.; Marsh, D., Effect of acyl chain composition on salt-induced lamellar to inverted hexagonal phase transitions in cardiolipin. *Biochimica et Biophysica Acta (BBA) - Biomembranes* **1989**, 980 (3), 389-392.
281. Blume, A.; Huebner, W.; Messner, G., Fourier transform infrared spectroscopy of ^{13}C :O labeled phospholipids hydrogen bonding to carbonyl groups. *Biochemistry* **1988**, 27 (21), 8239-8249.
282. Lewis, R. N.; McElhaney, R. N.; Pohle, W.; Mantsch, H. H., Components of the carbonyl stretching band in the infrared spectra of hydrated 1,2-diacylglycerol bilayers: a reevaluation. *Biophysical Journal* **1994**, 67 (6), 2367-2375.
283. Eckert, M.; Zundel, G., Proton polarizability, dipole moment, and proton transitions of an AH...B .dblharw. A-...H+B proton-transfer hydrogen bond as a function of an external electrical field: an ab initio SCF treatment. *The Journal of Physical Chemistry* **1987**, 91 (20), 5170-5177.
284. Leberle, K.; Kempf, I.; Zundel, G., An intramolecular hydrogen bond with large proton polarizability within the head group of phosphatidylserine. An infrared investigation. *Biophysical Journal* **1989**, 55 (4), 637-648.
285. Arsov, Z.; Quaroni, L., Direct interaction between cholesterol and phosphatidylcholines in hydrated membranes revealed by ATR-FTIR spectroscopy. *Chemistry and Physics of Lipids* **2007**, 150 (1), 35-48.
286. Wong, P. T. T.; Mantsch, H. H., High-pressure infrared spectroscopic evidence of water binding sites in 1,2-diacyl phospholipids. *Chemistry and Physics of Lipids* **1988**, 46 (3), 213-224.
287. Chen, C.; Tripp, C. P., An infrared spectroscopic based method to measure membrane permeance in liposomes. *Biochimica et Biophysica Acta (BBA) - Biomembranes* **2008**, 1778 (10), 2266-2272.
288. Hübner, W.; Blume, A., Interactions at the lipid-water interface. *Chemistry and Physics of Lipids* **1998**, 96 (1-2), 99-123.
289. Bouchet, A. M.; Frías, M. A.; Lairion, F.; Martini, F.; Almaleck, H.; Gordillo, G.; Disalvo, E. A., Structural and dynamical surface properties of phosphatidylethanolamine containing membranes. *Biochimica et Biophysica Acta (BBA) - Biomembranes* **2009**, 1788 (5), 918-925.
290. Fookson, J. E.; Wallach, D. F. H., Structural differences among phosphatidylcholine, phosphatidylethanolamine, and mixed phosphatidylcholine/phosphatidylethanolamine multilayers: An infrared absorption study. *Archives of Biochemistry and Biophysics* **1978**, 189 (1), 195-204.

291. Goni, F. M.; Arrondo, J. L. R., A study of phospholipid phosphate groups in model membranes by Fourier transform infrared spectroscopy. *Faraday Discussions of the Chemical Society* **1986**, *81* (0), 117-126.
292. Klähn, M.; Mathias, G.; Kötting, C.; Nonella, M.; Schlitter, J. r.; Gerwert, K.; Tavan, P., IR Spectra of Phosphate Ions in Aqueous Solution: Predictions of a DFT/MM Approach Compared with Observations. *The Journal of Physical Chemistry A* **2004**, *108* (29), 6186-6194.
293. Hielscher, R.; Hellwig, P., Specific Far Infrared Spectroscopic Properties of Phospholipids. *Spectroscopy: An International Journal* **2012**, *27* (5-6).
294. Brubach, J.-B.; Mermet, A.; Filabozzi, A.; Gerschel, A.; Roy, P., Signatures of the hydrogen bonding in the infrared bands of water. *The Journal of Chemical Physics* **2005**, *122* (18), 184509.
295. Knözinger, E., Far-Infrared Fourier Spectroscopy as a Method for Structure Determination in Chemistry. *Angewandte Chemie International Edition in English* **1976**, *15* (1), 25-39.
296. Yang, H.; Irudayaraj, J., Comparison of near-infrared, fourier transform-infrared, and fourier transform-raman methods for determining olive pomace oil adulteration in extra virgin olive oil. *Journal of the American Oil Chemists' Society* **2001**, *78* (9), 889-895.
297. Baeten, V.; Fernández Pierna, J. A.; Dardenne, P.; Meurens, M.; García-González, D. L.; Aparicio-Ruiz, R. n., Detection of the Presence of Hazelnut Oil in Olive Oil by FT-Raman and FT-MIR Spectroscopy. *Journal of Agricultural and Food Chemistry* **2005**, *53* (16), 6201-6206.
298. Baeten, V.; Hourant, P.; Morales, M. T.; Aparicio, R., Oil and Fat Classification by FT-Raman Spectroscopy. *Journal of Agricultural and Food Chemistry* **1998**, *46* (7), 2638-2646.
299. Bailey, G.; Horvat, R., Raman spectroscopic analysis of the cis/trans isomer composition of edible vegetable oils. *Journal of the American Oil Chemists Society* **1972**, *49* (8), 494-498.
300. Sadeghi-Jorabchi, H.; Wilson, R. H.; Belton, P. S.; Edwards-Webb, J. D.; Coxon, D. T., Quantitative analysis of oils and fats by Fourier transform Raman spectroscopy. *Spectrochimica Acta Part A: Molecular Spectroscopy* **1991**, *47* (9-10), 1449-1458.
301. Sadeghi-Jorabchi, H.; Hendra, P. J.; Wilson, R. H.; Belton, P. S., Determination of the total unsaturation in oils and margarines by fourier transform raman spectroscopy. *Journal of the American Oil Chemists' Society* **1990**, *67* (8), 483-486.
302. Chmielarz, B.; Bajdor, K.; Labudzinska, A.; Klukowska-Majewska, Z., Studies on the double bond positional isomerization process in linseed oil by UV, IR and Raman spectroscopy. *Journal of Molecular Structure* **1995**, *348* (0), 313-316.
303. Beattie, J.; Bell, S.; Moss, B. In Raman Studies of Lipid Structure and Composition, *International Conference on Raman Spectroscopy* **2000**, 708-709
304. Krafft, C.; Neudert, L.; Simat, T.; Salzer, R., Near infrared Raman spectra of human brain lipids. *Spectrochimica Acta Part A: Molecular and Biomolecular Spectroscopy* **2005**, *61* (7), 1529-1535.
305. Krafft, C., Bioanalytical applications of Raman spectroscopy. *Analytical and Bioanalytical Chemistry* **2004**, *378* (1), 60-62.
306. Beattie, J. R.; Bell, S. J.; Moss, B., A critical evaluation of Raman spectroscopy for the analysis of lipids: Fatty acid methyl esters. *Lipids* **2004**, *39* (5), 407-419.
307. Li, Y.; Driver, M.; Decker, E.; He, L., Lipid and lipid oxidation analysis using surface enhanced Raman spectroscopy (SERS) coupled with silver dendrites. *Food Research International* **2014**, *58* (0), 1-6.

308. Weldon, M. K.; Zhelyaskov, V. R.; Morris, M. D., Surface-Enhanced Raman Spectroscopy of Lipids on Silver Microprobes. *Applied Spectroscopy* **1998**, *52* (2), 265-269.
309. Driver, M.; Li, Y.; Zheng, J.; Decker, E.; Julian McClements, D.; He, L., Fabrication of lipophilic gold nanoparticles for studying lipids by surface enhanced Raman spectroscopy (SERS). *Analyst* **2014**, *139* (13), 3352-3355.
310. Laroche, C. I.; Simonin, H. I. n.; Beney, L.; Gervais, P., Phase transitions as a function of osmotic pressure in *Saccharomyces cerevisiae* whole cells, membrane extracts and phospholipid mixtures. *Biochimica et Biophysica Acta (BBA) - Biomembranes* **2005**, *1669* (1), 8-16.
311. Huang, C.-h.; Li, S., Calorimetric and molecular mechanics studies of the thermotropic phase behavior of membrane phospholipids. *Biochimica et Biophysica Acta (BBA) - Reviews on Biomembranes* **1999**, *1422* (3), 273-307.
312. Manner, V. W.; Chellappa, R. S.; Sheffield, S. A.; Liu, Z.; Dattelbaum, D. M., High-Pressure Far-Infrared Spectroscopic Studies of Hydrogen Bonding in Formic Acid. *Applied Spectroscopy* **2013**, *67* (9), 1080-1086.
313. Binder, H., Water near lipid membranes as seen by infrared spectroscopy. *European Biophysics Journal* **2007**, *36* (4-5), 265-279.
314. Venyaminov, S. Y.; Kalnin, N. N., Quantitative IR spectrophotometry of peptide compounds in water (H₂O) solutions. I. Spectral parameters of amino acid residue absorption bands. *Biopolymers* **1990**, *30* (13-14), 1243-1257.
315. Karanth, H.; Murthy, R. S. R., pH-Sensitive liposomes-principle and application in cancer therapy. *Journal of Pharmacy and Pharmacology* **2007**, *59* (4), 469-483.
316. Ferreira, D. d. S.; Lopes, S. v. C. d. A. j.; Franco, M. S.; Oliveira, M. n. C., pH-sensitive liposomes for drug delivery in cancer treatment. *Therapeutic Delivery* **2013**, *4* (9), 1099-1123.
317. Vanić, A. e.; Barnert, S.; Süß, R.; Schubert, R., Fusogenic activity of PEGylated pH-sensitive liposomes. *Journal of Liposome Research* **2012**, *22* (2), 148-157.
318. Ellens, H.; Bentz, J.; Szoka, F. C., Proton- and calcium-induced fusion and destabilization of liposomes. *Biochemistry* **1985**, *24* (13), 3099-3106.
319. Liu, D.; Huang, L., Small, but not large, unilamellar liposomes composed of dioleoylphosphatidylethanolamine and oleic acid can be stabilized by human plasma. *Biochemistry* **1989**, *28* (19), 7700-7707.
320. Torchilin, V. P., Recent advances with liposomes as pharmaceutical carriers. *Nat Rev Drug Discov* **2005**, *4* (2), 145-160.
321. Duzgunes, N.; Straubinger, R.; Baldwin, P.; Papahadjopoulos, D.; Wilschut, J.; Hoekstra, D., pH-sensitive liposomes: introduction of foreign substances into cells. *membrane fusion, Wilschut J and Hoekstra D editor New York Marcel Decker* **1991**, 713-30.
322. Hafez, I. M.; Cullis, P. R., Cholesteryl hemisuccinate exhibits pH sensitive polymorphic phase behavior. *Biochimica et Biophysica Acta (BBA) - Biomembranes* **2000**, *1463* (1), 107-114.
323. Van Bambeke, F. o.; Kerkhofs, A.; Schanck, A.; Remacle, C.; Sonveaux, E.; Tulkens, P.; Mingeot-Leclercq, M.-P., Biophysical studies and intracellular destabilization of pH-sensitive liposomes. *Lipids* **2000**, *35* (2), 213-223.
324. Klasczyk, B.; Panzner, S.; Lipowsky, R.; Knecht, V., Fusion-Relevant Changes in Lipid Shape of Hydrated Cholesterol Hemisuccinate Induced by pH and Counterion Species. *The Journal of Physical Chemistry B* **2010**, *114* (46), 14941-14946.
325. Siepi, E.; Lutz, S.; Meyer, S.; Panzner, S., An Ion Switch Regulates Fusion of Charged Membranes. *Biophysical Journal* **2011**, *100* (10), 2412-2421.

326. Sánchez, M.; Aranda, F. J.; Teruel, J. A.; Ortiz, A., New pH-sensitive liposomes containing phosphatidylethanolamine and a bacterial dirhamnolipid. *Chemistry and Physics of Lipids* **2011**, *164* (1), 16-23.
327. Ding, W.-x.; Qi, X.-r.; Li, P.; Maitani, Y.; Nagai, T., Cholesteryl hemisuccinate as a membrane stabilizer in dipalmitoylphosphatidylcholine liposomes containing saikosaponin-d. *International Journal of Pharmaceutics* **2005**, *300* (1-2), 38-47.
328. Sinagina, L.; Wikström, M. r.; Verkhovskiy, M. I.; Verkhovskaya, M. L., Activation of Isolated NADH:Ubiquinone Reductase I (Complex I) from Escherichia coli by Detergent and Phospholipids. Recovery of Ubiquinone Reductase Activity and Changes in EPR Signals of Iron-Sulfur Clusters, *Biochemistry* **2005**, *44* (23), 8500-8506.
329. El Khoury, Y.; Trivella, A. I.; Hellwig, P., The hydrogen bonding signature of peptides and proteins in the far infrared. *THz Sci. Technol* **2010**, *3*, 183-191.
330. El Khoury, Y.; Hellwig, P., Infrared spectroscopic characterization of copper-polyhistidine from 1,800 to 50 cm⁻¹: model systems for copper coordination. *JBIC Journal of Biological Inorganic Chemistry* **2009**, *14* (1), 23-34.
331. Efremov, R. G.; Baradaran, R.; Sazanov, L. A., The architecture of respiratory complex I. *Nature* **2010**, *465* (7297), 441-445.
332. Marshall, D.; Fisher, N.; Grigic, L.; Zickermann, V.; Brandt, U.; Shannon, R. J.; Hirst, J.; Lawrence, R.; Rich, P. R., ATR-FTIR redox difference spectroscopy of Yarrowia lipolytica and bovine complex I. *Biochemistry* **2006**, *45* (17), 5458-5467.
333. Barth, A.; Zscherp, C., What vibrations tell about proteins. *Quarterly reviews of biophysics* **2002**, *35* (04), 369-430.
334. Flemming, D.; Schlitt, A.; Spehr, V.; Bischof, T.; Friedrich, T., Iron-sulfur cluster N2 of the Escherichia coli NADH: ubiquinone oxidoreductase (complex I) is located on subunit NuoB. *Journal of Biological Chemistry* **2003**, *278* (48), 47602-47609.
335. Gurrath, M.; Friedrich, T., Adjacent cysteines are capable of ligating the same tetranuclear iron-sulfur cluster. *Proteins: Structure, Function, and Bioinformatics* **2004**, *56* (3), 556-563.
336. J James, A. B.; Klaudia, M.; Hannah, R. B.; Thorsten, F.; Judy, H., Investigating the function of [2Fe-2S] cluster N1a, the off-pathway cluster in complex I, by manipulating its reduction potential. *Biochemical Journal* **2013**, *456* (1), 139-146.
337. Friedrich, T.; Hellwig, P., Redox-induced conformational changes within the Escherichia coli NADH ubiquinone oxidoreductase (complex I): An analysis by mutagenesis and FT-IR spectroscopy. *Biochimica et Biophysica Acta (BBA) - Bioenergetics* **2010**, *1797* (6-7), 659-663.
338. Flemming, D.; Hellwig, P.; Lepper, S.; Kloer, D. P.; Friedrich, T., Catalytic importance of acidic amino acids on subunit NuoB of the Escherichia coli NADH: ubiquinone oxidoreductase (complex I). *Journal of Biological Chemistry* **2006**, *281* (34), 24781-24789.
339. Han, S.; Czernuszewicz, R. S.; Spiro, T. G., Vibrational spectra and normal mode analysis for [2Fe-2S] protein analogs using sulfur-34, iron-54 and deuterium substitution: coupling of iron-sulfur stretching and sulfur-carbon-carbon bending modes. *Journal of the American Chemical Society* **1989**, *111* (10), 3496-3504.
340. Burova, T. V.; Beckert, V.; Ristau, O.; Uhlmann, H.; Bernhardt, R.; Pfeil, W., Conformational stability of adrenodoxin mutant proteins. *Protein Science* **1996**, *5* (9), 1890-1897.
341. Grinberg, A. V.; Bernhardt, R., Contribution of a Salt Bridge to the Thermostability of Adrenodoxin Determined by Site-Directed Mutagenesis. *Archives of Biochemistry and Biophysics* **2001**, *396* (1), 25-34.

342. Euro, L.; Bloch, D. A.; Wikström, M. r.; Verkhovsky, M. I.; Verkhovskaya, M., Electrostatic Interactions Between FeS Clusters in NADH:Ubiquinone Oxidoreductase (Complex I) from *Escherichia coli* *Biochemistry* **2008**, *47* (10), 3185-3193.
343. Leif, H.; Sled, V. D.; Ohnishi, T.; Weiss, H.; Friedrich, T., Isolation and Characterization of the Proton-translocating NADH:ubiquinone Oxidoreductase from *Escherichia coli*. *European Journal of Biochemistry* **1995**, *230* (2), 538-548.
344. ngledew, W.; Ohnishi, T., An analysis of some thermodynamic properties of iron-sulphur centres in site I of mitochondria. *Biochemical Journal* **1980**, *186*, 111-117.
345. Czernuszewicz, R. S.; Macor, K. A.; Johnson, M. K.; Gewirth, A.; Spiro, T. G., Vibrational mode structure and symmetry in proteins and analogs containing Fe₄S₄ clusters: resonance Raman evidence that HiPIP is tetrahedral while ferredoxin undergoes a D_{2d} distortion. *Journal of the American Chemical Society* **1987**, *109* (23), 7178-7187.
346. Mitra, D.; Pelmeshnikov, V.; Guo, Y.; Case, D. A.; Wang, H.; Dong, W.; Tan, M.-L.; Ichiye, T.; Jenney, F. E.; Adams, M. W. W.; Yoda, Y.; Zhao, J.; Cramer, S. P., Dynamics of the [4Fe-4S] Cluster in *Pyrococcus furiosus* D14C Ferredoxin via Nuclear Resonance Vibrational and Resonance Raman Spectroscopies, Force Field Simulations, and Density Functional Theory Calculations. *Biochemistry* **2011**, *50* (23), 5220-5235.
347. Madden, J. F.; Han, S.; Siegel, L. M.; Spiro, T. G., Resonance Raman studies of *Escherichia coli* sulfite reductase hemoprotein. 2. Fe₄S₄ cluster vibrational modes. *Biochemistry* **1989**, *28* (13), 5471-5477.
348. Chen, J.; Bender, S. L.; Keough, J. M.; Barry, B. A., Tryptophan as a Probe of Photosystem I Electron Transfer Reactions: A UV Resonance Raman Study. *The Journal of Physical Chemistry B* **2009**, *113* (33), 11367-11370.
349. Fischer, W. B.; Eysel, H. H., Polarized Raman spectra and intensities of aromatic amino acids phenylalanine, tyrosine and tryptophan. *Spectrochimica Acta Part A: Molecular Spectroscopy* **1992**, *48* (5), 725-732.
350. Siamwiza, M. N.; Lord, R. C.; Chen, M. C.; Takamatsu, T.; Harada, I.; Matsuura, H.; Shimanouchi, T., Interpretation of the doublet at 850 and 830 cm⁻¹ in the Raman spectra of tyrosyl residues in proteins and certain model compounds. *Biochemistry* **1975**, *14* (22), 4870-4876.
351. Copeland, R. A.; Spiro, T. G., Ultraviolet resonance Raman spectroscopy of flavin mononucleotide and flavin-adenine dinucleotide. *The Journal of Physical Chemistry* **1986**, *90* (25), 6648-6654.
352. Moulis, J.-M.; Meyer, J.; Lutz, M., Characterization of [4Fe-4S]²⁺, [4Fe-4Se]²⁺ and hybrid (S, Se) clusters in *Clostridium pasteurianum* ferredoxin. A resonance Raman study. *Biochem. J* **1984**, *219*, 829-832.
353. Meyer, J.; Fujinaga, J.; Gaillard, J.; Lutz, M., Mutated Forms of the [2Fe-2S] Ferredoxin from *Clostridium pasteurianum* with Noncysteinylic Ligands to the Iron-Sulfur Cluster. *Biochemistry* **1994**, *33* (46), 13642-13650.

Emerging roles for natural and artificial lipids in shaping the catalytic function, stability and oligomeric state of membrane proteins.

Résumé

L'étude des membranes biologiques nécessite l'examen des différentes propriétés de ses composantes principales: les lipides et les protéines. Dans ce manuscrit, l'interaction lipide-lipide et lipide-protéine ont été suivies par spectroscopie vibrationnelle (Raman, Infrarouge). Nous sommes intéressés en premier lieu à l'étude de la structure et l'organisation des phospholipides dans leur phase gel et leur phase cristalline liquide en utilisant la spectroscopie moyen infrarouge. En outre, l'effet de la composition du groupement hydrophiles des lipides sur le comportement de la liaison hydrogène des mélanges lipidiques a été sondé en utilisant la spectroscopie lointain infrarouge. Dans la seconde partie, l'interaction de la protéine NADH ubiquinone oxydoréductase et du mutant NuoL (D563N) avec le zinc ont été étudiés par spectroscopie différentielle et les changements conformationnels induits par la liaison du zinc avec les protéines ont été examinés. Enfin, les vibrations métal-ligand des groupements fer-soufre dans le mutant de NuoB (C64A G100C) à différents pH ont été analysées par spectroscopie Raman.

Mots-clés: spectroscopie infrarouge différentielle, phospholipides, infrarouge lointain, NADH ubiquinone oxydoréductase, spectroscopie Raman, fer-soufre.

Résumé en anglais

The study of biological membranes involves the examination of the different properties of its main components: as lipids and proteins. In this manuscript, the lipid-lipid interaction and the lipid-protein interaction were monitored by vibrational spectroscopy (Raman and Infrared). We have been interested in the first part in studying the structure and organization of phospholipids in the gel phase and the liquid crystalline phase using mid infrared spectroscopy. In addition, the effect of the head group composition on the hydrogen bonding behaviour of lipid mixtures was probed using far infrared spectroscopy. In the second part, the interaction of the NADH ubiquinone oxidoreductase protein and NuoL mutant (D563N) with zinc was investigated through FTIR difference spectroscopy where the conformational changes upon zinc binding were monitored. Finally, the metal-ligand vibrations of the iron- sulfur clusters in NuoB mutants (C64A G100C) at different pH were analysed using Raman spectroscopy.

Keywords: FTIR difference spectroscopy, phospholipid, far infrared, NADH ubiquinone oxidoreductase, Raman spectroscopy, iron-sulfur clusters.